

A new internet, woven with spooky
quantum threads p. 1026

Summer books
roundup p. 1030

Tera-electron volt observations
of a gamma-ray burst p. 1081

Science

\$15
4 JUNE 2021
sciencemag.org

AAAS

HOW TRANSCRIPTION BEGINS

Human transcription machinery at high resolution p. 1055

2022 AWARDS PRIZES &

AAAS DAVID AND BETTY HAMBURG AWARD FOR SCIENCE DIPLOMACY

SUBMIT A NOMINATION TODAY

Deadline June 30, 2021

The **AAAS David and Betty Hamburg Award for Science Diplomacy** recognizes an individual or a limited number of individuals working together in the scientific and engineering or foreign affairs communities who are making an outstanding contribution to furthering science diplomacy.

Over the past 28 years, AAAS has honored an international cadre of science luminaries for their contributions to international scientific cooperation and science diplomacy. **This year, the award has been renamed for David and Betty Hamburg** to recognize their unparalleled commitment to the significant role of science diplomacy to advance science, human rights, peace, and cooperation.

- The award is open to all regardless of nationality or citizenship.
- We accept self-nominations.
- Nominees must be living at the time of their nomination.

To learn more, visit

aaas.org/awards/science-diplomacy/about

AAAS gratefully acknowledges the Carnegie Corporation of New York for their generous support to launch the AAAS David and Betty Hamburg Award for Science Diplomacy and the individuals and foundations whose contributions have begun an endowment that will allow us to sustain it in perpetuity.



PHOTO CREDIT: DIRCO

2016 WINNER

Minister Naledi Pandor, Ph.D.
South African Minister of
International Relations
and Cooperation

Recognized for using science and technology to support development in South Africa and sub-Saharan Africa.

Winners will receive:

- Monetary prize of \$10,000
- Commemorative plaque
- Worldwide promotion of their achievements through AAAS communication channels, including AAAS publications, member news, website, and social media
- Complimentary registration to the 2022 AAAS Annual Meeting
- Reimbursement for travel and hotel expenses to attend the AAAS Annual Meeting
- The opportunity to publish in *Science & Diplomacy*



AMERICAN ASSOCIATION FOR
THE ADVANCEMENT OF SCIENCE

AAAS AWARDS & PRIZES

AAAS Mani L. Bhaumik Award for Public Engagement with Science

CALL FOR NOMINATIONS

Deadline June 30, 2021

The AAAS Mani L. Bhaumik Award for Public Engagement with Science celebrates notable scientists and engineers who demonstrate excellence in their contribution to public engagement with science. Public engagement emphasizes dialogue and promotes meaningful exchanges with the public about science- and technology- related issues in society.

The recipient receives a monetary prize of \$5,000 and recognition at the 2022 AAAS Annual Meeting.

AAAS is seeking nominations for the 2022 award recipient to join our list of esteemed award winners. For more information and to submit a nomination, visit: aaas.org/PESAward



AAAS is grateful to quantum physicist Mani L. Bhaumik for his generous contribution to endow this award, which will allow AAAS to continue to recognize individuals whose creative methods are engaging the public in significant ways.

PHOTO CREDIT: Mani L. Bhaumik

RECOGNIZING PAST AWARD WINNERS



Esther Ngumbi
2021



J. Marshall Shepherd
2020



Richard Alley
2012



May Berenbaum
2009



Robert Ballard
1989

AMERICAN ASSOCIATION FOR THE ADVANCEMENT OF SCIENCE

PHOTO CREDITS: Esther Ngumbi: Esther Ngumbi / J. Marshall Shepherd: American Meteorological Society / Richard Alley: Richard Alley / May Berenbaum: L. Brian Stauffer / Robert Ballard: Emily Shur/National Geographic /



CONTENTS

4 JUNE 2021 • VOLUME 372 • ISSUE 6546

NEWS

IN BRIEF

1018 News at a glance

IN DEPTH

1020 Applied research gets big role in Biden's budget

2022 spending plan envisions new entities for translating basic research into practical tools *By J. Mervis and D. Malakoff*

1021 Image sleuth faces legal threats

Scientists rally around Elisabeth Bik after accusations of harassment and blackmail *By C. O'Grady*

1022 To study swarming cicadas, it takes a crowd

Cellphone-wielding observers track when and where the insects emerge *By I. Graber-Stiehl*
PODCAST

1024 Mexican funding agency forces out early-career researchers

Conacyt faces at least 145 wrongful termination lawsuits *By R. Pérez Ortega and I. Gutiérrez Jaber*

1025 NAS ousts member for first time, for sexual harassment

Academy removes astronomer Geoffrey Marcy *By J. Kaiser*

FEATURES

1026 The internet goes quantum

A global network that would use quantum "entanglement" to weave intimate ties between far-flung users is beginning to take shape *By G. Popkin*

INSIGHTS

BOOKS ET AL.

1030 Summer reading 2021

PERSPECTIVES

1036 When sharks nearly disappeared

A previously unidentified extinction event in the open ocean decimated pelagic sharks *By C. Pimiento and N. D. Pyenson*
REPORT p. 1105



1037 Calibrating experiments at atom-crushing pressures

Shockless compression of platinum and gold provides pressure standards to >1 terapascal *By R. Jeanloz*
RESEARCH ARTICLE p. 1063

1038 A LoCK at the T cell dock

Topology of T cell receptor–antigen binding constrains T cell activation *By V. Horkova and O. Stepanek*
RESEARCH ARTICLE p. 1056

1040 Rewriting the genetic code

Making room in the genetic code allows the creation of designer proteins with new building blocks *By D. Jewel and A. Chatterjee*
RESEARCH ARTICLE p. 1057

1041 Antibody sugars are bittersweet

Antibodies that lack specific sugar modifications can worsen acute viral diseases *By R. de Alwis and E. Eong Ooi*
REPORT p. 1102

1043 Uncertain effects of the pandemic on respiratory viruses

Expanded genomic and clinical surveillance are needed to understand the spread of respiratory viruses *By G. B. Gomez et al.*

POLICY FORUM

1045 Agricultural productivity must improve in sub-Saharan Africa

The region must pivot from area expansion to increasing crop yields on existing farmland *By T. S. Jayne and P. A. Sanchez*



LETTERS

1048 Protect high seas biodiversity

By R. R. Helm

1049 Trophy hunting undermines public trust

By V. D. Popescu et al.

1049 Brazil's doomed environmental licensing

By R. Ruaro et al.

1050 Technical Comment abstracts

RESEARCH

IN BRIEF

1051 From *Science* and other journals

REVIEW

1054 Gravitational waves

The first 5 years of gravitational-wave astrophysics *S. Vitale*

REVIEW SUMMARY; FOR FULL TEXT: DOI.ORG/10.1126/SCIENCE.ABC7397

RESEARCH ARTICLES

1055 Transcription

Structures of the human Mediator and Mediator-bound preinitiation complex *X. Chen et al.*

RESEARCH ARTICLE SUMMARY; FOR FULL TEXT: DOI.ORG/10.1126/SCIENCE.ABG0635

1056 Immunology

Canonical T cell receptor docking on peptide-MHC is essential for T cell signaling *P. Zareie et al.*

RESEARCH ARTICLE SUMMARY; FOR FULL TEXT: DOI.ORG/10.1126/SCIENCE.ABE9124

PERSPECTIVE p. 1038

1057 Synthetic biology

Sense codon reassignment enables viral resistance and encoded polymer synthesis *W. E. Robertson et al.*

PERSPECTIVE p. 1040; PODCAST

1063 High pressure

Establishing gold and platinum standards to 1 terapascal using shockless compression *D. E. Fratanduono et al.*

PERSPECTIVE p. 1037

1068 Neurodevelopment

Reciprocal repulsions instruct the precise assembly of parallel hippocampal networks *D. T. Pederick et al.*

REPORTS

1074 Electrochemistry

CO₂ electrolysis to multicarbon products in strong acid *J. E. Huang et al.*

1078 Hydrogels

Tough hydrogels with rapid self-reinforcement *C. Liu et al.*

1081 Gamma-ray bursts

Revealing x-ray and gamma-ray temporal and spectral similarities in the GRB 190829A afterglow *H.E.S.S. Collaboration*

1085 Genetics of obesity

Extensive pleiotropism and allelic heterogeneity mediate metabolic effects of *IRX3* and *IRX5* *D. R. Sobreira et al.*

1092 Coronavirus

Household COVID-19 risk and in-person schooling *J. Lessler et al.*

1097 Paleoclimate

Antarctic surface temperature and elevation during the Last Glacial Maximum *C. Buizert et al.*

1102 Immunology

Antibody fucosylation predicts disease severity in secondary dengue infection *S. Bournazos et al.*

PERSPECTIVE p. 1041

1105 Paleontology

An early Miocene extinction in pelagic sharks *E. C. Sibert and L. D. Rubin*

PERSPECTIVE p. 1036

1108 Coronavirus

Prevalent, protective, and convergent IgG recognition of SARS-CoV-2 non-RBD spike epitopes *W. N. Voss et al.*



DEPARTMENTS

1017 Editorial

Come on, CDC, we need you *By H. Holden Thorp*

1118 Working Life

Seeing beyond a test *By Natalia Aristizábal*

ON THE COVER

The human transcription preinitiation complex (PIC; pink and red) and multisubunit Mediator complex (orange, left) are assembled into a supercomplex (76 polypeptides, molecular mass: 4.1 megadaltons) on a promoter region of DNA (orange coil, center) to initiate gene transcription. Mediator binds RNA polymerase II (purple) in the PIC and stimulates phosphorylation of its C-terminal domain (highlighted in white), a critical event in transcription initiation.



See page 1055. *Illustration: V. Altounian/Science; Data: Y. Xu/Fudan University*

Science Staff	1014
New Products	1113
Science Careers	1114

SCIENCE (ISSN 0036-8075) is published weekly on Friday, except last week in December, by the American Association for the Advancement of Science, 1200 New York Avenue, NW, Washington, DC 20005. Periodicals mail postage (publication No. 484460) paid at Washington, DC, and additional mailing offices. Copyright © 2021 by the American Association for the Advancement of Science. The title SCIENCE is a registered trademark of the AAAS. Domestic individual membership, including subscription (12 months): \$165 (\$74 allocated to subscription). Domestic institutional subscription (51 issues): \$2148; Foreign postage extra: Air assist delivery: \$98. First class, airmail, student, and emeritus rates on request. Canadian rates with GST available upon request. GST #125488122. Publications Mail Agreement Number 1069624. Printed in the U.S.A.

Change of address: Allow 4 weeks, giving old and new addresses and 8-digit account number. **Postmaster:** Send change of address to AAAS, P.O. Box 96178, Washington, DC 20090-6178. **Single-copy sales:** \$15 each plus shipping and handling available from backissues.science.org; bulk rate on request. **Authorization to reproduce** material for internal or personal use under circumstances not falling within the fair use provisions of the Copyright Act can be obtained through the Copyright Clearance Center (CCC), www.copyright.com. The identification code for Science is 0036-8075. Science is indexed in the Reader's Guide to Periodical Literature and in several specialized indexes.

Editor-in-Chief Holden Thorp, hthorp@aaas.org

Executive Editor Monica M. Bradford

Editors, Research Valda Vinson, Jake S. Yeston Editor, Insights Lisa D. Chong

DEPUTY EDITORS Julia Fahrenkamp-Uppenbrink (UK), Stella M. Hurlley (UK), Phillip D. Szuroni, Sacha Vignieri SR. EDITORIAL FELLOW Andrew M. Sugden (UK) SR. EDITORS Gemma Alderton (UK), Caroline Ash (UK), Brent Grocholski, Pamela J. Hines, Di Jiang, Marc S. Lavine (Canada), Yevgeniya Nusinovich, Ian S. Osborne (UK), Beverly A. Purnell, L. Bryan Ray, H. Jesse Smith, Keith T. Smith (UK), Jelena Stajic, Peter Stern (UK), Valerie B. Thompson, Brad Wible, Laura M. Zahn ASSOCIATE EDITORS Michael A. Funk, Priscilla N. Kelly, Tage S. Rai, Seth Thomas Scanlon (UK), Yury V. Suleymanov LETTERS EDITOR Jennifer Sills LEAD CONTENT PRODUCTION EDITORS Harry Jach, Lauren Kmec CONTENT PRODUCTION EDITORS Amelia Beyna, Jeffrey E. Cook, Chris Filiatreau, Julia Katris, Nida Masiulis, Abigail Shashikanth, Suzanne M. White SR. EDITORIAL COORDINATORS Carolyn Kyle, Beverly Shields EDITORIAL COORDINATORS Aneera Dobbins, Joi S. Granger, Jeffrey Hearn, Lisa Johnson, Maryrose Madrid, Ope Martins, Shannon McMahon, Jerry Richardson, Hilary Stewart (UK), Alana Warnke, Alice Whaley (UK), Anita Wynn PUBLICATIONS ASSISTANTS Jeremy Dow, Alexander Kief, Ronnel Navas, Brian White EXECUTIVE ASSISTANT Jessica Slater ASI DIRECTOR, OPERATIONS Janet Clements (UK) ASI SR. OFFICE ADMINISTRATOR Jessica Waldoock (UK)

News Editor Tim Appenzeller

NEWS MANAGING EDITOR John Travis INTERNATIONAL EDITOR Martin Enserink DEPUTY NEWS EDITORS Elizabeth Culotta, Lila Guterman, David Grimm, Eric Hand (Europe), David Malakoff SR. CORRESPONDENTS Daniel Clery (UK), Jon Cohen, Jeffrey Mervis, Elizabeth Pennisi ASSOCIATE EDITORS Jeffrey Brinard, Catherine Maticic NEWS REPORTERS Adrian Cho, Jennifer Couzin-Frankel, Jocelyn Kaiser, Rodrigo Pérez Ortega (Mexico City), Kelly Servick, Robert F. Service, Erik Stokstad, Paul Voosen, Meredith Wadman INTERN Sofia Moutinho CONTRIBUTING CORRESPONDENTS Warren Cornwall, Andrew Curry (Berlin), Ann Gibbons, Sam Kean, Eli Kintisch, Kai Kupferschmidt (Berlin), Andrew Lawler, Mitch Leslie, Eliot Marshall, Virginia Morell, Dennis Normile (Tokyo), Elisabeth Pain (Careers), Charles Piller, Michael Price, Tania Rabesandratana (Barcelona), Joshua Sokol, Emily Underwood, Gretchen Vogel (Berlin), Lizzie Wade (Mexico City) CAREERS Donisha Adams, Rachel Bernstein (Editor), Katie Langin (Associate Editor) COPY EDITORS Julia Cole (Senior Copy Editor), Cyra Master (Copy Chief) ADMINISTRATIVE SUPPORT Meagan Weiland

Creative Director Beth Rakouskas

DESIGN MANAGING EDITOR Marcy Atarod GRAPHICS MANAGING EDITOR Alberto Cuadra PHOTOGRAPHY MANAGING EDITOR William Douthitt WEB CONTENT STRATEGY MANAGER Kara Estelle-Powers MULTIMEDIA MANAGING PRODUCER Joel Goldberg DESIGN EDITOR Chrystal Smith DESIGNER Christina Aycock GRAPHICS EDITOR Nirja Desai INTERACTIVE GRAPHICS EDITOR Kelly Franklin SENIOR SCIENTIFIC ILLUSTRATORS Valerie Altounian, Chris Bickel SENIOR GRAPHICS SPECIALISTS Holly Bishop, Nathalie Cary SENIOR PHOTO EDITOR Emily Petersen PHOTO EDITOR Kaitlyn Dolan WEB DESIGNER Jennie Pajkowski SOCIAL MEDIA STRATEGIST Jessica Hubbard VIDEO PRODUCER Meagan Cantwell SENIOR PODCAST PRODUCER Sarah Crespi

Chief Executive Officer and Executive Publisher Sudip Parikh

Publisher, Science Family of Journals Bill Moran

DIRECTOR, BUSINESS SYSTEMS AND FINANCIAL ANALYSIS Randy Yi DIRECTOR, BUSINESS OPERATIONS & ANALYSIS Eric Knott DIRECTOR OF ANALYTICS Enrique Gonzales MANAGER, BUSINESS OPERATIONS Jessica Tierney SENIOR BUSINESS ANALYST Cory Lipman FINANCIAL ANALYST Isacco Fusi ADVERTISING SYSTEM ADMINISTRATOR Tina Burks DIGITAL/PRINT STRATEGY MANAGER Jason Hillman SENIOR MANAGER, PUBLISHING AND CONTENT SYSTEMS Marcus Spiegler ASSISTANT MANAGER DIGITAL/PRINT Rebecca Doshi SENIOR CONTENT SPECIALISTS Steve Forrester, Jacob Hedrick, Antoinette Hodal, Lori Murphy PRODUCTION SPECIALIST Kristin Wowk DIGITAL PRODUCTION MANAGER Lisa Stanford CONTENT SPECIALIST Kimberley Oster ADVERTISING PRODUCTION OPERATIONS MANAGER Deborah Tompkins DESIGNER, CUSTOM PUBLISHING Jeremy Hunsinger SR. TRAFFIC ASSOCIATE Christine Hall SPECIAL PROJECTS ASSOCIATE Sarah Dhere ASSOCIATE DIRECTOR, BUSINESS DEVELOPMENT Justin Sawyers GLOBAL MARKETING MANAGER Allison Pritchard DIGITAL MARKETING MANAGER Aimee Aponte JOURNALS MARKETING MANAGER Shawana Arnold MARKETING ASSOCIATES Tori Velasquez, Mike Romano, Ashley Hyllton DIGITAL MARKETING SPECIALIST Asleigh Rojanavasee SENIOR DESIGNER Kim Huynh

DIRECTOR AND SENIOR EDITOR, CUSTOM PUBLISHING Sean Sanders ASSISTANT EDITOR, CUSTOM PUBLISHING Jackie Oberst

DIRECTOR, PRODUCT & PUBLISHING DEVELOPMENT Chris Reid DIRECTOR, BUSINESS STRATEGY AND PORTFOLIO MANAGEMENT Sarah Whalen ASSOCIATE DIRECTOR, PRODUCT MANAGEMENT Kris Bishop PRODUCT DEVELOPMENT MANAGER Scott Chernoff PUBLISHING TECHNOLOGY MANAGER Michael Di Natale SR. PRODUCT ASSOCIATE Robert Koepke PRODUCT ASSOCIATE Anne Mason SPJ ASSOCIATE Samantha Bruno Fuller

DIRECTOR, INSTITUTIONAL LICENSING Iquo Edim ASSOCIATE DIRECTOR, RESEARCH & DEVELOPMENT Elisabeth Leonard MARKETING MANAGER Kess Knight SENIOR INSTITUTIONAL LICENSING MANAGER Ryan Rexroth INSTITUTIONAL LICENSING MANAGER Marco Castellani MANAGER, AGENT RELATIONS & CUSTOMER SUCCESS Judy Lillibridge SENIOR OPERATIONS ANALYST Lana Guz FULFILLMENT COORDINATOR Melody Stringer SALES COORDINATOR Josh Haverlock

DIRECTOR, GLOBAL SALES Tracy Holmes US EAST COAST AND MID WEST SALES Stephanie O'Connor US WEST COAST SALES Lynne Stickrod US SALES MANAGER, SCIENCE CAREERS Claudia Paulsen-Young US SALES REP. SCIENCE CAREERS Tracy Anderson ASSOCIATE DIRECTOR, ROW Roger Goncalves SALES REP. ROW Sarah Lealre SALES ADMIN ASSISTANT, ROW Bryony Cousins DIRECTOR OF GLOBAL COLLABORATION AND ACADEMIC PUBLISHING RELATIONS, ASIA Xiaoying Chu ASSOCIATE DIRECTOR, INTERNATIONAL COLLABORATION Grace Yao SALES MANAGER Danny Zhao MARKETING MANAGER Kilo Lan ASCA CORPORATION, JAPAN Kaoru Sasaki (Tokyo), Miyuki Tani (Osaka) COLLABORATION/ CUSTOM PUBLICATIONS/JAPAN Adarsh Sandhu

DIRECTOR, COPYRIGHT, LICENSING AND SPECIAL PROJECTS Emilie David RIGHTS AND LICENSING COORDINATOR Jessica Adams RIGHTS AND PERMISSIONS ASSOCIATE Elizabeth Sandler LICENSING ASSOCIATE Virginia Warren

MAIN HEADQUARTERS
Science/AAAS
1200 New York Ave. NW
Washington, DC 20005

SCIENCE INTERNATIONAL
Clarendon House
Clarendon Road
Cambridge, CB2 8FH, UK

SCIENCE CHINA
Room 1004, Culture Square
No. 59 Zhongguancun St.
Haidian District, Beijing, 100872

SCIENCE JAPAN
ASCA Corporation
Sibaura TY Bldg. 4F, 1-14-5
Shibaura Minato-ku
Tokyo, 108-0073 Japan

EDITORIAL
science_editors@aaas.org

NEWS
science_news@aaas.org

INFORMATION FOR AUTHORS
sciencemag.org/authors/
science-information-authors

REPRINTS AND PERMISSIONS
sciencemag.org/help/
reprints-and-permissions

MEDIA CONTACTS
scipak@aaas.org

MULTIMEDIA CONTACTS
SciencePodcast@aaas.org
ScienceVideo@aaas.org

INSTITUTIONAL SALES
AND SITE LICENSES
sciencemag.org/librarian

PRODUCT ADVERTISING
& CUSTOM PUBLISHING
advertising.sciencemag.org/
products-services
science_advertising@aaas.org

CLASSIFIED ADVERTISING
advertising.sciencemag.org/
science-careers

advertise@sciencecareers.org

JOB POSTING CUSTOMER SERVICE
employers.sciencecareers.org

support@sciencecareers.org

MEMBERSHIP AND INDIVIDUAL
SUBSCRIPTIONS
sciencemag.org/subscriptions

MEMBER BENEFITS
aaas.org/membership/benefits

AAAS BOARD OF DIRECTORS
CHAIR Claire M. Fraser

PRESIDENT Susan G. Amara

PRESIDENT-ELECT Gilda A. Barabino

TREASURER Carolyn N. Ainslie

CHIEF EXECUTIVE OFFICER
Sudip Parikh

BOARD Cynthia M. Beall

Rosina M. Bierbaum

Ann Bostrom

Janine Austin Clayton

Laura H. Greene

Kaye Husbands Fealing

Maria M. Klawe

Robert B. Millard

William D. Provine

BOARD OF REVIEWING EDITORS (Statistics board members indicated with \$)

Erin Adams, *U. of Chicago*
Takuzo Aida, *U. of Tokyo*
Leslie Aiello,
Wenner-Gren Foundation
Deji Akinwande, *UT Austin*
Judith Allen, *U. of Manchester*
Marcella Alsan, *Harvard U.*
Sebastian Amigorena,
Institut Curie
James Analytis, *UC Berkeley*
Trevor Archer, *NIH, NIH*
Paola Ariotta, *Harvard U.*
David Awschalom, *U. of Chicago*
Clare Baker, *U. of Cambridge*
Delia Baldassarri, *NYU*
Nenad Ban, *ETH Zürich*
Nandita Basu, *U. of Waterloo*
Franz Bauer,
Pontificia U. Católica de Chile
Ray H. Baughman, *UT Dallas*
Carlo Beenakker, *Leiden U.*
Yasmine Belkaid, *NIH, NIH*
Philip Benfey, *Duke U.*
Kiros T. Berhane, *Columbia U.*
Bradley Bernstein,
Mass. General Hospital
Joseph J. Berry, *NREL*
Alessandra Biffi, *Harvard Med.*
Chris Bowler,
École Normale Supérieure
Ian Boyd, *U. of St. Andrews*
Emily Brodsky, *UC Santa Cruz*
Ron Brookmeyer, *UCLA (\$)*
Christian Büchel, *UKE Hamburg*
Dennis Burton, *Scipps Res.*
Carter Tribble Butts, *US Irvine*
György Buzsáki,
NYU School of Med.
Mariana Byndloss,
Vanderbilt U. Med. Ctr
Annmarie Carlton, *UC Irvine*
Ling-Ling Chen, *SIBCB, CAS*
M. Keith Chen, *UCLA*
Zhijian Chen,
UT Southwestern Med. Ctr.
Ib Chorkendorff, *Denmark TU*
Amander Clark, *UCLA*
James J. Collins, *MIT*
Robert Cook-Deegan,
Arizona State U.
Virginia Cornish, *Columbia U.*
Carolyn Coyne, *Duke U.*
Roberta Croce, *VU Amsterdam*
Ismail Dabo, *Penn State U.*
Jeff L. Dangl, *UNC*
Chiara Daraio, *Caltech*
Nicolas Dauphas, *U. of Chicago*
Christian Davenport, *U. of Michigan*
Frans de Waal, *Emory U.*
Claude Desplan, *NYU*
Sandra Díaz,
U. Nacional de Córdoba
Ulrike Diebold, *TU Wien*
Stefanie Dimmeler,
Goethe-U. Frankfurt
Hong Ding, *Inst. of Physics, CAS*
Dennis Discher, *UPenn*
Jennifer A. Doudna,
UC Berkeley
Ruth Drdla-Schutting,
Med. U. Vienna
Raissa M. D'Souza, *UC Davis*
Bruce Dunn, *UCLA*
William Dunphy, *Caltech*
Scott Edwards, *Harvard U.*
Todd Ehlers, *U. of Tübingen*
Jennifer Eliseiff,
Johns Hopkins U.
Andrea Encalada,
U. San Francisco de Quito
Nader Engheta, *U. of Penn.*
Karen Ersche, *U. of Cambridge*
Beate Escher,
UFZ & U. of Tübingen
Barry Everitt, *U. of Cambridge*
Vanessa Ezenwa, *U. of Georgia*
Michael Feuer, *GWU*
Toren Finkel, *U. of Pitt. Med. Ctr.*
Gwenn Flowers, *Simon Fraser U.*
Peter Fratzl,
Max Planck Inst. Potsdam

Elaine Fuchs, *Rockefeller U.*
Jay Gallagher, *U. of Wisconsin*
Daniel Geschwind, *UCLA*
Ramon Gonzalez,
U. of South Florida
Sandra González-Bailón,
UPenn
Nicolas Gruber, *ETH Zürich*
Hua Guo, *U. of New Mexico*
Taekjip Ha, *Johns Hopkins U.*
Sharon Hammes-Schiffer,
Yale U.
Wolf-Dietrich Hardt, *ETH Zürich*
Louise Harra, *U. Coll. London*
Jian He, *Clensson U.*
Carl-Philipp Heisenberg,
IST Austria
Ykä Helariutta, *U. of Cambridge*
Janet G. Hering, *Eawag*
Heather Hickman, *NIAD, NIH*
Hans Hilgenkamp, *U. of Twente*
Kai-Uwe Hinrichs, *U. of Bremen*
Deirdre Hollingsworth,
U. of Oxford
Randall Hulet, *Rice U.*
Auke Ijspeert, *EPFL*
Akiko Iwasaki, *Yale U.*
Stephen Jackson,
USGS & U. of Arizona
Erich Jarvis, *Rockefeller U.*
Peter Jones, *IST Austria*
Matt Kaeblerlein, *U. of Wash.*
William Kaelin Jr.,
Dana-Farber Cancer Inst.
Daniel Kammen, *UC Berkeley*
V. Narry Kim, *Seoul Nat. U.*
Robert Kingston,
Harvard Med.
Nancy Knowlton,
Smithsonian Institution
Etienne Koechlin,
École Normale Supérieure
Alex L. Kolodkin,
Johns Hopkins U.
Julia Krupic, *U. of Cambridge*
Paul Kubes, *U. of Calgary*
Gabriel Land, *Scipps Res. (\$)*
Mitchell A. Lazar, *UPenn*
Wendell Lim, *UCSF*
Luis Liz-Marzán, *CIC biomaGUNE*
Omar Lizardo, *UCLA*
Jonathan Losos,
Wash. U. in St. Louis
Ke Lu, *Inst. of Metal Res., CAS*
Christian Lüscher, *U. of Geneva*
Jean Lynch-Stieglitz,
Georgia Inst. of Tech.
David Lyons, *U. of Edinburgh*
Fabienne Mackay,
QIMR Berghofer
Anne Magurran, *U. of St. Andrews*
Asifa Majid, *U. of York*
Oscar Marin, *King's Coll. London*
Charles Marshall, *UC Berkeley*
Christopher Marx, *U. of Idaho*
David Masopust, *U. of Minnesota*
Geraldine Masson, *CNRS*
Jason Matheny, *Georgetown U.*
Heidi McBride, *McGill U.*
C. Robertson McClung,
Dartmouth
Rodrigo Medellín,
U. Nacional Autónoma de México
Jane Memmott, *U. of Bristol*
C. Jessica Metcalf, *Princeton U.*
Boxia Mi, *UC Berkeley*
Tom Misteli, *NCI, NIH*
Alison Motsinger-Reif,
NIH, NIH (\$)
Suresh Naidu, *Columbia U.*
Danielle Navarro,
U. of New South Wales
Daniel Nettle, *Newcastle U.*
Daniel Neumark, *UC Berkeley*
Beatriz Noheda, *U. of Groningen*
Helga Nowotny,
Vienna Sci., Res. & Tech. Fund
Rachel O'Reilly, *U. of Birmingham*
Pilar Ossorio, *U. of Wisconsin*
Andrew Oswald, *U. of Warwick*
Isabella Pagano,
Istituto Nazionale di Astrofisica

Elizabeth Levy Paluck,
Princeton U.
Jane Parker,
Max Planck Inst. Cologne
Giovanni Parmigiani,
Dana-Farber Cancer Inst. (\$)
Marcia Paul, *U. of British Columbia*
Ana Pêgo, *U. do Porto*
Samuel Pfaff, *Salk Inst.*
Julie Pfeiffer,
UT Southwestern Med. Ctr.
Philip Phillips, *UIUC*
Matthieu Piel, *Institut Curie*
Kathrin Plath, *UCLA*
Martin Plenio, *Ulm U.*
Katherine Pollard, *UCSF*
Elvira Poloczanska,
Alfred-Wegener-Inst.
Jutta Pongratz,
Ludwig-Maximilians U.
Philippe Poulin, *CNRS*
Jonathan Pritchard, *Stanford U.*
Lei Stanley Qi, *Stanford U.*
Trevor Robbins, *U. of Cambridge*
Amy Rogely, *Imperial Coll. London*
Joeri Rosenzweig,
Northwestern U.
Mike Ryan, *UT Austin*
Miquel Salmeron,
Lawrence Berkeley Nat. Lab
Nitin Samarth, *Penn State U.*
Erica Olmann Saphire,
La Jolla Inst.
Joachim Saur, *U. zu Köln*
Alexander Schier, *Harvard U.*
Wolfram Schlenker, *Columbia U.*
Susannah Scott,
UC Santa Barbara
Anuj Shah, *U. of Chicago*
Vladimir Shalaev, *Purdue U.*
Jie Shan, *Cornell U.*
Beth Shapiro, *UC Santa Cruz*
Jay Shendure, *U. of Wash.*
Steve Sherwood,
U. of New South Wales
Brian Shoichet, *UCSF*
Robert Siliciano,
JHU School of Med.
Lucia Sivilotti, *U. Coll. London*
Alison Smith, *John Innes Centre*
Richard Smith, *UNC (\$)*
Mark Smyth, *QIMR Berghofer*
John Speakman, *U. of Aberdeen*
Tara Spire-Jones,
U. of Edinburgh
Allan C. Spradling,
Carnegie Institution for Sci.
V. S. Subrahmanian,
Dartmouth
Ira Tabas, *Columbia U.*
Eriko Takano, *U. of Manchester*
Patrick Tan,
Duke-NUS Med. School
Sarah Teichmann,
Wellcome Sanger Inst.
Rocio Titunik, *Princeton U.*
Shubha Tole,
Tata Inst. of Fundamental Res.
Maria-Elena Torres Padilla,
Helmholtz Zentrum München
Kimani Toussaint, *Brown U.*
Wim van der Putten,
Netherlands Inst. of Ecology
Henrique Veiga-Fernandes,
Champalimad Fdn
Reinhold Veugelers, *KU Leuven*
Bert Vogelstein, *Johns Hopkins U.*
David Wallach, *Weizmann Inst.*
Jane-Ling Wang, *UC Davis (\$)*
Jessica Ware,
Amer. Mus. of Natural Hist.
David Waxman, *Fudan U.*
Chris Winkle, *U. of Missouri (\$)*
Terrie Williams, *UC Santa Cruz*
Ian A. Wilson, *Scipps Res. (\$)*
Yu Xie, *Princeton U.*
Jan Zaenen, *Leiden U.*
Kenneth Zaret,
UPenn School of Med.
Bing Zhu, *Inst. of Biophysics, CAS*
Xiaowei Zhang, *Harvard U.*
Maria Zubair, *MIT*

An illustration at the top of the page shows two people on the left and two on the right, all working on laptops. Above them are several speech bubbles and a glowing lightbulb icon. In the center, a large red circle contains the text "Where Science Gets Social." in white.

Where
Science
Gets
Social.

AAAS.ORG/COMMUNITY



AAAS' Member Community is a one-stop destination for scientists and STEM enthusiasts alike. It's "Where Science Gets Social": a community where facts matter, ideas are big and there's always a reason to come hang out, share, discuss and explore.

**Member
COMMUNITY**
AAAS

AMERICAN ASSOCIATION FOR THE ADVANCEMENT OF SCIENCE

PUT YOUR RESEARCH OUT IN FRONT

Submit your research:
[cts.ScienceMag.org](https://cts.sciencemag.org)

Come on, CDC, we need you

The US Centers for Disease Control and Prevention (CDC) has had a rough few weeks. At first, it was criticized for being too cautious about its mask guidance for vaccinated individuals. Then, when it abruptly changed its mask recommendation for those who had been vaccinated, it was criticized for acting suddenly and without clearly explaining the reason for the new guidance and what it meant for the unvaccinated. Meanwhile, author Michael Lewis released a bestseller about problems at the CDC that go back decades, with local and state public health officials fighting pandemics in the face of inaction and confusion from the agency. The CDC is in a difficult position: In the course of carrying out its appointed task of communicating science and promoting the best health practices, it can also appear to be making policy—and that is not supposed to be its job. But where do you draw the line between proffering advice and promulgating policy? Maybe the CDC and the administration need to step back and consider if there is a better way for the agency to protect public health.

According to its website, the CDC “conducts critical science *and* provides health information that protects our nation against expensive and dangerous health threats” (*italics mine*). The first part is easy to understand. CDC scientists conduct research and marshal scientific information for public release. Although the muzzling, contradicting, and rebuking of the CDC by the Trump administration made this part of the mission hard to see, there’s no reason to think that the agency isn’t performing this task well.

It’s the second part of the mission where the agency has been getting tripped up. The public cares much less about the details of scientific studies than about the upshot. Do they need to wear a mask? Can they go back to work? Can they hug their grandchildren? To scientists, it makes perfect sense that the answer to these questions is “it depends, and there is still some risk.” But caveats are hard to sell to a public hungering for specific directions.

The CDC has been occupying a gray zone somewhere between the very different worlds of science and politics. Threading this needle requires serious

chops in both communications and politics. Scientists get penalized—perhaps unfairly and unproductively—for reporting a finding that must be modified relatively quickly because of new results. The nature of science includes an unstated qualification that findings are subject to change. Political leaders, on the other hand, must often act on incomplete information. In the face of uncertainty, they are expected to make clearcut decisions. They get penalized if they get it wrong, but also if they fail to take action. So, is the CDC director a scientist or a political leader? If a scientist, then there are some pretty straightforward things to say. COVID-19 is a deadly disease caused by an airborne virus, so masks work. Period. The vaccines are

expected to provide outstanding protection and slow viral transmission, though we won’t know with absolute certainty until studies are done in humans. The vaccines perform extremely well against the variants that have emerged so far, but there could always be a new one that changes the game.

The politics—how to use the science to formulate public policy—are a trickier matter. Will seeing vaccinated people without masks cause unvaccinated people to let down their guard? Does the slight chance that vaccinated people might still spread the virus justify keeping mask mandates in place, especially

to protect young children and immunocompromised adults who cannot get vaccinated or mount an immune response? Will explaining the nuances of the effectiveness of vaccines lead to more or less hesitancy?

It’s time to think harder about the role of the CDC. If the agency is to continue its integrated mission, then it must be made very clear that it offers independent advice, not commands, and that the final word on public health policy comes from federal, state, and local political leaders. In this capacity, CDC must be given enough clout to hold its own among the forces in Washington, DC. As an alternative, the CDC could stand back and act strictly as a scientific research agency, but that would feel like a loss. Either way, we literally can’t live without the CDC. We just need to sort out our expectations.

—H. Holden Thorp



H. Holden Thorp
Editor-in-Chief,
Science journals.
hthorp@aaas.org;
@hholdenthorp

**“The CDC has
been occupying
a gray zone...
between...
science
and politics.”**

“Truly surrealistic. Hopefully, this all stops soon.”

Anthony Fauci, director of the U.S. National Institute of Allergy and Infectious Diseases, in emails in March and April 2020, as reported by *The Washington Post*, about a surge in Fauci socks, doughnuts, and fan art at the pandemic's start.

IN BRIEF

Edited by **Jeffrey Brainard**

POLICY

Biden requests probe of COVID-19 origin

President Joe Biden last week joined the chorus calling for a fuller, more transparent investigation into whether the virus behind the COVID-19 pandemic escaped from a laboratory in Wuhan, China. In a statement, he said he has “asked the Intelligence Community to redouble their efforts to collect and analyze information that could bring us closer to a definitive conclusion, and to report back to me in 90 days.” Biden added that the inquiry will also involve unspecified work by U.S. national laboratories. Multiple countries, including the United States and United Kingdom, and various groups of scientists have recently renewed calls for China to allow a more thorough investigation of the lab-leak scenario than a World Health Organization (WHO) team conducted earlier this year. At a U.S. Senate hearing last week, top National Institutes of Health officials testified that a lab leak was a credible explanation for the emergence of SARS-CoV-2, although less likely than the virus spilling over from wild or domesticated animals into people. A representative of China told WHO’s annual health assembly last week that the “China part” of the origins investigation “has been completed,” suggesting no further studies there would be considered.

China vaccine validated

PUBLIC HEALTH | CoronaVac, the COVID-19 vaccine made by China’s Sinovac Biotech, got two boosts this week. Despite lingering questions about the protection conferred by the vaccine, which uses inactivated SARS-CoV-2, the World Health Organization (WHO) gave it an emergency use listing, which makes it eligible for distribution by an international consortium—the COVID-19 Vaccines Global Access Facility—to low-income countries. Other countries often embrace WHO’s guidance on vaccines as well. Separately, Brazilian scientists who administered CoronaVac to nearly all adults in Serrana, a town in the state of São Paulo, said it stifled COVID-19 there. Symptomatic cases dropped 80%, related hospitalizations fell 86%, and deaths plummeted 95%.

The researchers speculate the town may have reached “herd immunity,” the point at which the pandemic coronavirus has trouble finding new people to infect, when about 75% of the town’s eligible adult residents were fully vaccinated.

Inflamed hearts tied to vaccine

PUBLIC HEALTH | Pfizer’s COVID-19 vaccine may be linked to rare cases of a heart muscle inflammation called myocarditis, especially in young men, researchers in Israel said this week. In men between 16 and 24 years old, more than one in 6000 recipients were affected, about five to 25 times the background rate in this population, the team said in a report to Israeli health authorities. Most cases appeared days after the second dose of

the messenger RNA (mRNA) vaccine, were mild, and resolved quickly. Israel and many European countries are debating whether younger teenagers should receive COVID-19 inoculations. The United States and other countries continue to investigate myocarditis in people who received mRNA vaccines from Pfizer or a second maker, Moderna, but several researchers say their benefits still exceed the risks, including in young people.

WHO renames virus variants

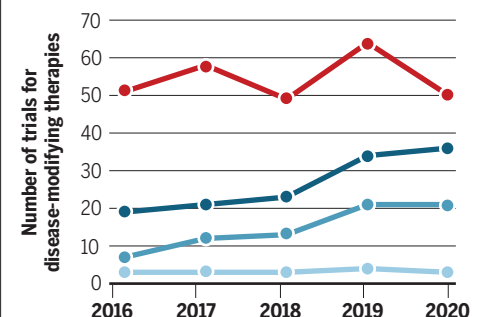
COVID-19 | To avoid stigmatizing nations, the World Health Organization (WHO) on 31 May announced a new naming system for variants of the pandemic coronavirus that have until now been informally identified by the countries in which they were discovered. The proposed naming nomenclature, intended for the public, is based on Greek letters. For example, four “variants of concern” originally found in the United Kingdom, South Africa, Brazil, and India will now be designated, respectively, alpha, beta, gamma, and delta. (Such variants are more transmissible or deadly than original SARS-CoV-2 strains, or evade natural or vaccine-induced immunity.) Technical names and naming systems for variants, already widely used by scientists, will remain in use, WHO said.

Public studies of Alzheimer’s rise

DRUG DEVELOPMENT | A growing proportion of U.S. clinical trials of experimental Alzheimer’s treatments are funded by the

A larger public role

● Corporate ● Academic medical center/NIH
● Public-private partnership ● Other





NATURAL HAZARDS

Risks linger after eruption of Congo volcano

A river of lava from Mount Nyiragongo swallowed up houses near Goma, Democratic Republic of the Congo, causing deaths.

The nearly 400,000 people who evacuated their homes in the Democratic Republic of the Congo in late May, fleeing the eruption of Mount Nyiragongo, were waiting this week for hazard specialists to give them clearance to return.

The volcano's lava and gases killed more than 30 people and spawned small earthquakes that have continued. Scientists remain on alert for a potential, rare, "limnic" discharge of carbon

dioxide from nearby Lake Kivu, where Nyiragongo's eruption might trigger a massive release of the gas sequestered in the lake's depths—a deadly suffocation risk for those onshore. Researchers consider Nyiragongo one of Africa's most dangerous volcanoes, partly because its lava is low in silica, making it fast moving, and because the city of Goma, population 1.5 million, is just 10 kilometers away.

government rather than pharmaceutical companies, researchers reported last week. Data posted on the registry ClinicalTrials.gov revealed that in 2020, more than half of all trials were supported either by academic medical centers—most of which were funded by the National Institutes of Health—or by public-private partnerships, in which companies join government agencies, academic institutes, or foundations to test drugs. (The public-private alliances distribute costs and risks in a field where failure is common.) For disease-modifying treatments, which aim to alter the course of the disease rather than just treat symptoms, support from these two sectors nearly doubled and tripled, respectively (p. 1018), according to the analysis in *Alzheimer's & Dementia: Translational Research & Clinical Interventions*, published by the nonprofit Alzheimer's Association. Public funding plays a smaller role, however, in large, pivotal trials of potential Alzheimer's drugs: All 14 ongoing phase 3 trials in the database had industry support as of 2020, and 11 were sponsored solely by companies.

JAMA head resigns over podcast

RACIAL JUSTICE | Howard Bauchner will step down as editor-in-chief of *JAMA* effective 30 June, the American Medical Association said this week. The announcement comes 4 months after the prestigious medical journal published a controversial podcast and associated tweet questioning the existence of structural racism in health care. After public criticism, then-Deputy Editor Edward Livingston, who hosted the podcast, resigned. Although Bauchner said in a statement that he did not create the podcast or write the tweet, he concluded that as editor-in-chief, "I am ultimately responsible for them." Bauchner had held that title for 10 years.

Drug oversight program revived

REGULATION | The U.S. Food and Drug Administration (FDA) last week reversed a decision by the Trump administration to end a program that requires manufacturers to obtain regulatory approvals for drugs allowed on the U.S. market many years ago under less strict standards. In an unusual statement,

FDA said the Trump action was based on "multiple legal and factual inaccuracies." The move gives a reprieve to the Unapproved Drugs Initiative, started in 2006, which requires updated approvals, although it has been criticized for allowing approvals based only on literature reviews, without new clinical trial data.

Science office head confirmed

POLICY | The U.S. Senate last week confirmed geneticist Eric Lander as director of the White House Office of Science and Technology Policy. Lander will also serve as President Joe Biden's science adviser and hold a seat in his Cabinet. Lander, 64, has long held prominent roles in U.S. science policy and also led the Broad Institute and co-led the public Human Genome Project to the completion of a first draft in 2001. His nomination by the White House pleased many researchers. Others were critical, noting that Lander has a history of conflict with other researchers, and some were disappointed Biden did not make history by nominating a woman or person of color.



Efforts to develop cleaner energy technologies, such as better wind turbines and more efficient trucks, would get major funding increases under a budget proposal.

U.S. SCIENCE POLICY

Applied research gets big role in Biden's budget

2022 spending plan envisions new entities for translating basic research into practical tools

By **Jeffrey Mervis** and **David Malakoff**

Last week, President Joe Biden unveiled a proposed 2022 budget for the U.S. government that would boost federal spending on R&D by 9%, or \$13.5 billion, including what he calls “the biggest increase in non-defense [R&D] spending on record.” The plan puts an unprecedented emphasis on translating scientific discoveries into practical tools for fighting climate change and disease, bolstering the economy, and tackling other issues.

Although Congress is certain to reject or revise parts of the proposal, its support for even a portion of Biden's ambitious vision might lead to numerous new funding entities and alter how the government invests in academic research.

The \$6 trillion spending blueprint released on 28 May adds greater detail to a skeletal plan Biden presented in early April (*Science*, 16 April, p. 221). It asks Congress to boost spending on a wide swath of non-defense science (see table, p. 1021), with increases of 20% or more for research programs at the National Institutes of Health (NIH), the National Science Foundation (NSF), the U.S. Department of Agriculture (USDA), and other agencies. It also includes

a 30% boost for clean energy R&D. At the same time, Biden wants an 11% cut in basic research spending by the military, which is a key funder of academic research in math, computer science, and engineering.

The overall R&D request of \$171 billion would give applied research a greater increase than basic, curiosity-driven research. That preference suggests the Biden administration “is, to some extent, thinking about science as more of a problem-solving enterprise [than] a discovery enterprise,” says David Hart, an R&D policy specialist at George Mason University. Other wealthy countries have already moved in that direction, recognizing that “rebalancing” research funding to emphasize “more applied research is essential to solving national problems,” notes Rebecca Dell of the ClimateWorks Foundation, who leads a program that works with industry to reduce greenhouse gas emissions.

That philosophy is especially visible in proposals for adding entities focused on applied research to several of the government's biggest basic science funders. NSF, for example, would get a technology, innovation, and partnerships (TIP) directorate. Biden also wants to create three agencies modeled on the Defense Advanced Research Projects Agency (DARPA), a Penta-

gon office created during the Cold War to help the country keep up with the Soviet Union and known for its agility in funding risky but potentially high-payoff research.

NIH would add ARPA-Health, getting \$6.5 billion, to be spent over 3 years, to fund “transformational innovation in health research.” Eight agencies would be involved in funding a \$500 million ARPA-Climate, with \$200 million coming from the Department of Energy and \$95 million from USDA. The budget doesn't clarify where ARPA-Climate would be housed or who would be in charge. Even the Department of Transportation would add an ARPA, “to accelerate technology that improves infrastructure performance,” although the budget doesn't specify its funding level. (Ironically, Biden requested less than a 1% increase for DARPA, leaving it at \$3.5 billion.)

Research advocates, including those representing academic institutions, welcomed Biden's backing of research. “The proposed historic increases ... will foster innovation and fuel long-term economic growth,” says M. Peter McPherson of the Association of Public and Land-grant Universities.

But many have questions about how the new funding mechanisms would work. One

sensitive issue is how to ensure that NSF's new TIP directorate and the new ARPAs will be able to operate as intended, and won't duplicate or potentially harm existing programs that enjoy broad political support.

In the case of ARPA-Health, some observers have questioned whether NIH, which has a reputation for being risk averse, is the right home for a new agency designed to think outside the box. ARPA-Health "will need to be audacious, nimble, and have unique authorities," says Ellen Sigal, chair and founder of Friends of Cancer Research, who supports the idea but has concerns about how it will be implemented.

The budget notes that ARPA-Health "will have a distinctive culture and organizational structure" as well as an advisory board. And NIH Director Francis Collins confronted the issue a few days before the budget's release, assuring panels in Congress that NIH can adopt "kind of a DARPA attitude." As proof, he noted NIH had quickly disbursed billions of dollars to develop treatments and vaccines to battle COVID-19.

Still, some research advocates worry ARPA-Health might become simply a larger version of the Common Fund, an existing NIH pot of money that critics say has failed to fund enough innovative research. Many lawmakers and advocates also want to be sure ARPA-Health doesn't end up draining money from NIH's 27 existing institutes, and are lobbying Congress to enlarge the agency's overall budget.

Similar tensions are in play at NSF. The proposed TIP directorate is the result of a yearlong discussion, largely catalyzed by Senate Majority Leader Chuck Schumer (D-NY), on how to re-engineer NSF to help the United States compete with China and other rising global powers. NSF Director Sethuraman Panchanathan says the directorate will be "a cross-cutting platform" that will help NSF advance research in 10 key technologies, take discoveries to market, and train the next generation of scientists and engineers. It will work "in close collaboration with all of NSF's [seven other] directorates and offices" to maximize its effectiveness and avoid duplication, according to NSF budget documents.

The budget envisions TIP starting life with \$865 million, including \$350 million that

will come from absorbing existing NSF programs. Both the White House and the Senate, which is close to approving broader legislation designed to out-innovate China that also includes language creating the new directorate, envision explosive growth for TIP. Biden's budget sets a target of \$10.7 billion by 2026, whereas the Senate bill calls for \$8.4 billion that year.

However, even some senators who support the TIP directorate and a larger NSF budget question whether NSF, with its tradition of supporting basic research, is the best agency to spur U.S. economic growth and bolster national security. Last week, for example, Senator Ben Sasse (R-NE) persuaded his colleagues to add language boosting DARPA's spending to the bill creating TIP, arguing the military agency is a better driver of innovation.

"The NSF is Bill Nye, the Science Guy, and DARPA is a real-life *Mission Impossible*," Sasse asserted in explaining his amendment, which would double DARPA's annual budget. "Both are in the science business, but only one of them [DARPA] scares the crap out of China."

The proposed ARPA-Climate comes with its own complications. It would be an unusual "cross-agency agency," Hart notes, and the involvement of eight different funding sources means multiple appropriations committees in Congress will have a say in setting its annual budget. And, he says, the White House could face "a big burden coordinating a broad range of agencies."

Hiring staff to run the new entities also could present a challenge, observers say. "You'll be asking people to design and build the planes while flying them," says a Senate staffer who was not authorized to speak on the record. But she says it's also a chance "to bring on a new generation of smart, young people dedicated to public service."

Such problems are still a long way off, however. It will take months for Congress to vet Biden's budget request and for the White House and lawmakers to agree on final numbers. If they don't finish the job by 1 October, when the 2022 fiscal year begins, current spending levels would likely be extended for weeks or months. ■

With reporting by Jocelyn Kaiser.

RESEARCH INTEGRITY

Image sleuth faces legal threats

Scientists rally around Elisabeth Bik after accusations of harassment and blackmail

By Cathleen O'Grady

Elisabeth Bik has built a career out of hunting for evidence of errors and misconduct in science. Now, for the first time, scientists she has challenged are threatening legal action. Lawyers representing one or more authors who have published on the benefits of "healing energy" have demanded she retract her critiques of that work and apologize. And a lawyer for Didier Raoult, a controversial microbiologist at the Hospital Institute of Marseille (IHU) Mediterranean Infection in France, has accused her of harassment and blackmail.

More than 1400 researchers have signed an open letter—and more than 3000 others have signed a petition—supporting Bik in the wake of the threats. The letter reflects a concern that "legitimate scientific criticism can be squelched by behaviors that go beyond scholarly debate," says University of Virginia social scientist Brian Nosek, one of its authors.

In March 2020, Bik, who specializes in identifying manipulated images in scientific papers, blogged about her concerns with a widely publicized paper Raoult published on the antimalarial drug hydroxychloroquine, which former President Donald Trump and others promoted as a cure for COVID-19 but which failed to show benefits in large, rigorous clinical trials. She posted her critiques—and concerns about other papers of Raoult's—on PubPeer, an online forum for feedback on scientific papers.

Bik says she then faced months of harassment on Twitter from Raoult's colleague, IHU structural biologist Eric Chabrière, and from anonymous accounts. Most of the tweets question whether Bik is being paid by pharmaceutical companies and whether she profited from alleged securities fraud at microbiome testing startup uBiome, where she worked from 2016 to 2018. Other

Opening bids

Many civilian science programs would see major budget increases under President Joe Biden's 2022 budget plan, but Congress is unlikely to support all of the requests.

	% CHANGE	2022 REQUEST (\$ BILLIONS)
NIH	21%	\$52
NSF	20.2%	\$10.2
NASA science	9.8%	\$7.9
DOE science	5.3%	\$7
Agricultural research	19%	\$4
USGS	24.8%	\$1.6
NIST research	16.5%	\$0.9
EPA science	13.9%	\$0.8
NOAA research	26%	\$0.7
Defense basic science	-10.9%	\$2.4

tweets have attacked Bik's appearance and threatened "justice" in "a real prison" in France. Most frightening, Bik says, has been the doxxing—publication of her home address by both Chabrière and anonymous accounts. Raoult and Chabrière did not respond to requests for comment.

The episode is "bringing to science what has already been brought to lots of other areas—doxxing, threats, and intimidation," says Lisa Rasmussen, a research ethicist at the University of North Carolina, Charlotte.

In a September 2020 French Senate hearing on the country's pandemic policy, including its use of hydroxychloroquine, Raoult denied ever having committed fraud, but admitted there were errors in a small fraction of his work. PubPeer now has comments on 258 papers on which Raoult is an author. Bik says she has flagged image problems, ethical questions, and other concerns in 63 of the papers.



Elisabeth Bik is an independent consultant who specializes in detecting manipulated scientific images.

Raoult's lawyer, Brice Grazzini, told *Science* he filed a complaint against Bik with the French public prosecutor in April, although Bik has not been notified or charged, and it's not clear whether the French legal system will act on the complaint. Grazzini told the tabloid *France-Soir* that an avalanche of notifications from PubPeer—sent automatically when a paper is flagged as problematic—constitutes harassment; responding to these and to questions from publishers has taken IHU researchers "an insane amount of time," he said. Rasmussen, however, sees no evidence of harassment and says Bik was using the appropriate channels to voice

her concerns. "If she was driving past his house and stalking him, or threatening or writing him personal emails, maybe there would be some basis for harassment."

Grazzini also says Bik offered to stop criticizing IHU studies if the institute paid her—a move he says constitutes attempted blackmail. Bik says he is misrepresenting a Twitter exchange she had with Chabrière, who asked her to declare any ties with pharmaceutical companies. She responded with a link to her Patreon account to clarify that pharmaceutical companies do not pay her, but that she does accept fees from universities and scientific publishers to investigate suspicious images. She says she jokingly offered to investigate IHU's papers for a fee.

In April, Chabrière tweeted a screenshot of a document naming Bik and Boris Barbour, a neuroscientist at the Ecole Normale Supérieure's Institute of Biology who helps run PubPeer, as the subjects of the legal complaint. The tweet—now deleted—included Bik's full home address and was the first she heard of the legal threat.

The second threat is from at least one unidentified member of a research team behind a series of papers that reported beneficial effects of the Chinese art of Qi Gong, or cultivating "life energy." Last week, Bik, who has critiqued the papers on PubPeer, Twitter, and her blog, received emails from two lawyers threatening legal action if she doesn't retract her posts and emails to journals about the work and apologize in writing to the authors.

In the open letter, which addresses the legal threat from Raoult, Nosek and his cosignatories call on institutions such as universities and funders to protect whistleblowers. Rasmussen, however, notes that independent contractors like Bik don't have institutions to protect them. "Our system of scientific reliability shouldn't depend on someone who's trying to make a living with her various consulting gigs," she says.

Mike Rossner, a data manipulation consultant, says "people who have the authority to request the source data underlying the published images" should step in to investigate Bik's concerns. That includes institutional research integrity officers and journal editors.

The support expressed for Bik in the open letter does not hinge on whether her concerns prove valid, Nosek says, although he thinks many are credible. "Her work is serious and genuine. That does not mean that her work is infallible," he says. "But it does mean that she should be able to do it without being harassed and maligned beyond normal scholarly debate." ■

COMMUNITY SCIENCE

To study swarming cicadas, it takes a crowd

Cellphone-wielding observers track when and where the insects emerge

By Ian Graber-Stiehl

The billions of periodical cicadas now crawling, fluttering, and singing from trees in the eastern United States have roused a throng of humans as well, who are mapping the insects and timing their emergence in what may be the country's longest public science tradition. Using a free app called Cicada Safari, more than 150,000 people so far have uploaded geotagged photos of cicadas, helping scientists track their emergence after 13 to 17 years underground.

The insects are an ideal target for science-inclined amateurs—unmissable and mysterious at the same time. "We just don't know what's going on in their life" underground, says Douglas Pfeiffer, an entomologist at Virginia Polytechnic Institute and State University. With just a handful of scientists trying to understand a natural event both massive and rare, aid from amateur scientists is invaluable. In recent years, community reports have caught the formation of new populations, helped study the link between emergence and air temperature, and traced how cicada populations respond to stressors.

Periodical cicadas are grouped into 15 broods based on where and in which years they emerge. Eggs laid in tree branches hatch, and the nymphs fall and burrow into the ground. There, they feed on xylem from tree roots, molting four times over the next 13 or 17 years, before emerging when the ground temperature reaches roughly 17.7°C. Then the frenzy of calling and mating begins.

The public can use the Cicada Safari app, released in 2019 by Gene Kritsky, an entomologist at Mount St. Joseph University, to send photos to researchers, who

review the genus, location, and brood identity of paparazzied cicadas. Last year, the abundance of data points revealed something unexpected: The first reports of cicadas in 2020 weren't from the expected Brood IX, which mostly lives in Virginia, West Virginia, and North Carolina. Instead, cicadas were emerging "from Georgia, then South Carolina, then Alabama and Missouri," Kritsky says—areas where an emergence wasn't expected for another 4 years. "We were seeing what turned out to be a 4-year acceleration of a 13-year cicada emerging after 9 years."

Only once, Kritsky says, have scientists observed a large group of stragglers successfully splinter off from its brood. A group of Brood X cicadas (the same enormous brood currently serenading much of the East Coast), known to dominate the area around Cincinnati, emerged there in 2000, 4 years early. The cicadas came out in such force that their numbers overwhelmed predators, leaving them to survive and mate. Then, 17 years later the group emerged for a second time, having spread in geographic range, and likely formed a new brood.

Last year, Cicada Safari data showed that not one, but four broods of periodical cicadas emerged off-cycle. Stragglers, which can emerge years before or after their brood, aren't uncommon. But the scale of their 2020 emergence was. Kritsky says last year's stragglers may have given rise to an entirely new periodical population.

Without the public, the full scope of last year's straggler event would likely have been missed. And it was far from the beginning of cicada citizen science. In 1843, Gideon Smith, a doctor and silkworm cultivator in Baltimore, convinced newspapers to publish his appeals to readers to report emergences of cicadas, which were called locusts at the time. Smith claimed to have ascertained "eighteen districts or families of locusts. If each post master in places where locusts appear will drop me a line ... I shall be able to make out a map of each district." The ensuing mail campaign, arguably the nation's first large-scale community science, "was quite successful," says Kritsky, who wrote about Smith in December 2020 in *American Entomologist*.

"By time [Smith] died, in 1867, he had documented all the known broods of periodical cicadas," Kritsky says.

Another entomologist, U.S. Department of Agriculture (USDA) researcher Charles Marlatt, used a mail-campaign initiative to map periodical cicada distribution in greater detail. In 1902, Marlatt spearheaded a USDA operation to send out more than 15,000 postcards soliciting reports of



Emerging after 17 years, Brood X cicadas have captivated amateur scientists across the eastern United States.

cicadas. The 1000 responses helped him delineate cicada broods by emergence year.

Later, mailed and phoned-in cicada reports went to universities across the country. But the data varied widely in quality and focus, says Chris Simon, an ecologist and biologist at the University of Connecticut, Storrs. She once received a marriage proposal in the mail instead of data.

Kritsky's app took cicada reporting online. And more people than ever are taking part during the pandemic: Between 2019 and 2020, Cicada Safari's user base grew by nearly 50%, to 10,000 contributors. This year, with the emergence of the massive Brood X, the app has leapt to 156,000 users.

In 2020, the team added the ability to upload 11-second videos. Although Kritsky and his colleagues have seen many videos of children chasing cicadas, clips of chorusing cicadas have also allowed the researchers to verify the presence of mating populations rather than one-off sightings.

Last year also marked the first scientific paper based on Cicada Safari data. Published by Michael Raupp, an entomologist at the University of Maryland, College Park, Kritsky, and colleagues in *The Maryland Entomologist* in September 2020, it cross-referenced air temperature with nymph emergences reported through the app. The aim: to improve predictions of cicada emergences using air temperatures, which are far more available than soil temperatures. With a small sample size, the results were inconclusive. Nevertheless, the paper marked another first: using cicada community science to answer nuanced questions, rather than simply reporting distribution and emergence dates.

Raupp thinks data from the public could help address enigmas that still surround cicadas, such as why stragglers break off from broods. One idea: Warm winters may cause cicadas to emerge in the wrong year. Detailed data on weather and emergence patterns might support that idea—or a different hypothesis about why some cicadas miscount the passing years. (In a further mystery, stragglers tend to miscount by specific amounts, either 1 or 4 years.)

Without understanding the factors influencing emergence, it will be hard to protect cicadas from threats that include pesticides, development, and climate change. Raupp says development may have done in Brood XI, a 17-year cicada population in Connecticut last observed in 1954. And this year's group, Brood X, has been in decline on Long Island in New York for nearly 200 years. Cicada Safari reports should help, Raupp says, because researchers can cross-reference them with local records of land use and climate.

Michelle Watson, a retired paralegal who has submitted more photos to Cicada Safari than anyone else, says she has grown addicted to contributing to the community of cicada enthusiasts. Watson, who recently moved to Blue Ridge, Georgia, had never seen periodical cicadas before this year. While looking online for information about whether they were safe for her dogs to eat, she found Cicada Safari.

Even after this year's cicadas disappear once more, Watson says the passion they've sparked for science projects will likely stick around—for her, and tens of thousands of others as well. ■

Ian Graber-Stiehl is a science journalist in Chicago.



WORKFORCE

Mexican funding agency forces out early-career researchers

Conacyt faces at least 145 wrongful termination lawsuits

By **Rodrigo Pérez Ortega** and
Inés Gutiérrez Jaber

When biologist Adriana Gómez Bonilla started her job at the College of Michoacán, Zamora, in September 2014, she never imagined she would become an expert on labor rights. “It would’ve seemed like the farthest thing to me,” she says.

But after 4 years, she was driven out of her job and into activism. Managers at Mexico’s National Council of Science and Technology (Conacyt)—the country’s federal science funding agency—pressured her to resign in March 2018, citing poor evaluations, which she says are inaccurate. She refused; a few months later the agency stopped paying her.

Gómez Bonilla’s dismissal is one of hundreds of similar cases involving researchers employed by the Cátedras Conacyt (Conacyt Professorships) program, launched 7 years ago to alleviate the brain drain of young Mexican researchers. Conacyt has stopped paying researchers, terminated them without reasonable explanation, or coerced them into signing resignations, according to multiple sources who spoke with *Science*. A combination of budget cuts, politics, and a widening

rift between the government and scientists is at work, Mexican researchers say. “I think deep down there is an intention to disappear the Cátedras program,” says a philologist who was terminated from the program.

She and others, including Gómez Bonilla, have filed lawsuits against Conacyt. As of June 2020 the agency faces 145 active lawsuits for wrongful termination amounting to \$8.2 million in damages, according to an internal document reviewed by *Science*, and sources say most are from Cátedras researchers. In February, some 200 Cátedras researchers formed a union, hoping to negotiate a contract that would protect their jobs and improve working conditions.

Conacyt’s director, María Elena Álvarez-Buylla Rocés, denies the agency has unfairly dismissed employees. “No,” she says. “It’s not true.” She did not respond to further requests for comment. Currently the Cátedras program does not have a director, but sources point to Diego Axel López Peláez, deputy director of evaluation and monitoring, as the person making the decisions. López Peláez did not respond to multiple requests for comment.

Conacyt launched the Cátedras program in 2014 to make up for the lack of full-time

Biochemical nutritionist Ana Lucrecia Elías López is one of the researchers Conacyt pushed out.

positions at universities and research institutes in the country. The goal was to hire at least 3000 researchers by 2018. Researchers were matched with institutions that provided work space and infrastructure to do research while Conacyt employed them and paid their salaries for 10 years. The positions were coveted as one of the few opportunities for a science career in Mexico.

As a result of Cátedras, “many Mexican researchers have chosen to stay and do science in the country,” and many came back from abroad to be part of it, says an archaeologist who was dismissed from the program. Between 2015 and 2018, 78% of Cátedras researchers earned membership in Mexico’s prestigious National System of Researchers, says biomedical nutritionist Ana Lucrecia Elías López, a former Cátedras researcher who is fighting to rejoin the program after being coerced into resigning. This “is a sign of productivity,” she says.

Still, the program has struggled. Researchers are not on staff at their host institutions, which creates bureaucratic conflicts that can hinder their work. Finances have also been a challenge: Primarily because of insufficient funding, in 2018 the program was only halfway to its 3000-researcher goal.

But stresses skyrocketed in Álvarez-Buylla Rocés’s term, which began in December 2018 and has been marked by a significant rupture between Conacyt and the scientific community. According to information released in response to a government transparency request and Conacyt documents, at least 425 researchers have left the program since it launched, most beginning in 2019; it now supports 1284 researchers. Sources say government austerity measures may play a role. But in 2020, the program’s budget was up 23% to \$68 million, yet Conacyt hasn’t offered new openings since 2018 and dismissals have soared.

Researchers dismissed by the program report similar experiences. First, they say, Conacyt officials tried to coerce them into resigning with the promise of a severance payment. If they refused, the agency stopped paying them. Aeronautical engineer Oliver Huerta, for example, joined the program in 2014 and worked for 5 years at the Technological Institute of Advanced Studies of Ecatepec. In 2019, he noticed his institutional email had been blocked just when he needed to file a required annual report. Huerta contacted López Peláez, who said they had to meet in person. At Conacyt headquarters in Mexico City, López Peláez and a lawyer invited Huerta to sign his resignation. He refused. A few weeks later, Conacyt stopped paying him

and directors at his host institution told him he had been dropped from the Cátedras program. He filed a lawsuit in December 2019, but there hasn't been much progress. "We're hanging up in a cloud," he says.

For some of those removed from the program, including the archaeologist, being pregnant or having a newborn appears to have been a trigger. There's a "pattern of an absolute ignorance on gender issues," says Claudia Patricia Juan Pineda, a lawyer representing more than 20 former Cátedras researchers. "It seems that getting pregnant is like a crime." In the archaeologist's case, a few months after she notified officials of her high-risk pregnancy, she tried to upload her annual report but the online platform didn't work. She immediately contacted López Peláez, who told her over the phone she was fired. A few days later, Conacyt stopped paying her and disabled her institutional email. "There is a lack of humanity that is completely impregnated in Conacyt," she says.

Geologist María Jazmín Chávez Álvarez, a former Cátedras researcher, says when she was asked to resign in 2018, then-Cátedras Director Lorena Archundia said, "Look, this way you can stop worrying and then you can focus on your daughter." "That really bothered me," she says, because she never brought up her pregnancy and maternity. She refused to sign the form, and Conacyt stopped paying her. Archundia did not respond to multiple requests for comment. Elías López, who was forced to resign in 2019, filed a complaint last year with the National Human Rights Commission accusing Álvarez-Buylla Rocas of wrongfully firing women researchers—including some with small children or experiencing complicated pregnancies—during the COVID-19 pandemic. She plans to file a criminal lawsuit against Conacyt.

Some Cátedras researchers hope the new union, Siintacatedras, can secure greater research support and job security. "We are convinced that once we start a dialogue with Conacyt, we can reach an understanding of the great potential this program has," says Siintacatedras Secretary General Mateo Mier y Terán Giménez Cacho, a political agroecologist at the College of the Southern Border.

Others are less interested in mending bridges. That includes Gómez Bonilla, who now has a full-time position at the Metropolitan Autonomous University. If she wins her suit against Conacyt, the agency would owe her close to \$265,000—double the amount of standard Conacyt grants for basic science projects. "Imagine how much science they could fund with that," she says. "But instead they're spending it on lawsuits that could've been avoided." ■

Inés Gutiérrez Jaber is a journalist in Mexico City.

SCIENTIFIC COMMUNITY

NAS ousts member for first time, for sexual harassment

Academy removes astronomer Geoffrey Marcy

By Jocelyn Kaiser

The U.S. National Academy of Sciences (NAS) last week brought some closure to a long-running saga by rescinding the membership of astronomer Geoffrey Marcy because of sexual harassment. It is the first time the 158-year-old body has expelled a member for any reason.

NAS set the stage for the expulsion in 2019, when it revised its bylaws to allow the removal of members who have been found guilty of misconduct, including sexual harassment, by their employers, journals or funding agencies. No one formally sought such action for sexual harassment transgressions until September 2020, when François-Xavier Coudert, a computational chemist with CNRS, France's national science agency, filed complaints with NAS against Marcy and three other academy members. After a vote that an NAS spokesperson said met the required two-thirds majority, the academy's 17-member council revoked Marcy's membership on 24 May for violating its harassment policy.

"I don't know if there is any justice here for the women Marcy harassed ... but at least the academy is holding him accountable for the damage he did," says Seyda Ipek, a theoretical particle physicist at the University of California (UC), Irvine, who filed her own complaint last fall with NAS against Marcy and evolutionary biologist Francisco Ayala, who was also named in Coudert's complaint.

Marcy, who studies extrasolar planets, was forced out of UC Berkeley in 2015 after BuzzFeed reported that a university investigation had found him guilty of sexual harassment, including kissing and groping students. After his NAS expulsion, Marcy repeated earlier denials of sexual harassment. "My engaging and empathic style could surely be misinterpreted, which is my fault for poor communication," he wrote to *Science*. "I would never intentionally hurt anyone nor cause distress."

Ayala, a second target of Coudert's complaint, resigned from UC Irvine in 2018 after a university investigation found him guilty of sexual harassment, including mak-

ing suggestive comments and inviting a junior professor to sit on his lap. Ayala has "absolutely" denied the allegations. NAS told Coudert in November 2020 it was adjudicating Ayala's case. But its spokesperson said last week the academy does not "have information on [that or] other cases."

Coudert's complaint also included cancer biologist Inder Verma, formerly at the Salk Institute for Biological Studies. In 2018, *Science* published accounts from eight women alleging sexual harassment stretching over decades (*Science*, 4 May 2018, p. 480). Salk investigated but did not release its findings; Verma denied the allegations. NAS told Coudert it could not take action on the basis of media reports alone.

The fourth scientist Coudert named is information theorist Sergio Verdú, who was dismissed by Princeton University after two investigations found he had sexually harassed a graduate student and violated a prohibition on consensual relationships with students. (Verdú has denied both allegations.) NAS told Coudert in November 2020 it was holding off on any action until a lawsuit Verdú has filed against Princeton is resolved.

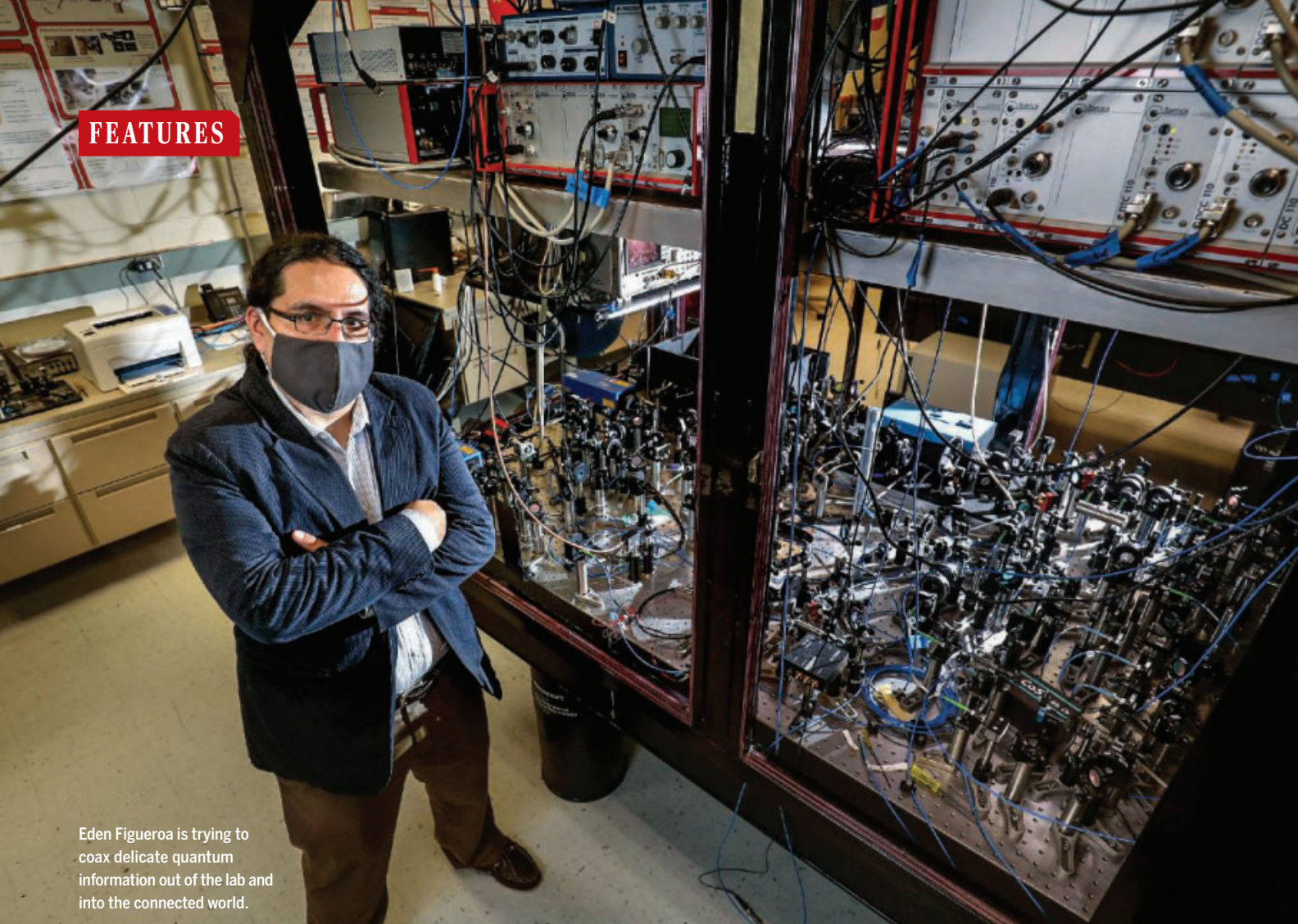
Ipek hopes future NAS cases will be reviewed more quickly, but "given how long Ayala's case is taking ... I am not sure if we can hold our breath." Coudert is also frustrated, arguing that the academy's policy requiring public findings is ineffective. Marcy's expulsion is "a positive step, but a baby step," Coudert says. "They are allowing bad actors to remain members of the academy."

Marcy, now with Space Laser Awareness, a California nonprofit, continues to publish scientific papers and preprints. Some still include a UC Berkeley affiliation; Marcy resigned in 2015, but university policy allows him to claim emeritus status.

A co-author of one paper, graduate student Lee Rosenthal of the California Institute of Technology, tweeted that future papers will recognize any data contributions from Marcy in acknowledgements, not by giving him authorship. "I am so sorry, and heartbroken, that inclusion of Geoff Marcy on this paper has harmed folks that have been sexually harassed," he wrote. ■

"They are allowing bad actors to remain."

François-Xavier Coudert, CNRS



Eden Figueroa is trying to coax delicate quantum information out of the lab and into the connected world.

THE INTERNET GOES QUANTUM

A global network that would use quantum “entanglement” to weave intimate ties between far-flung users is beginning to take shape

A beam of ethereal blue laser light enters a specialized crystal. There it turns red, a sign that each photon has split into a pair with lower energies—and a mysterious connection. The particles are now quantum mechanically “entangled,” linked like identical twins who know each other’s thoughts despite living in distant cities. The photons zip through a tangle of fibers, then ever so gently deposit the information they encode into waiting clouds of atoms.

By **Gabriel Popkin**

The transmogrifications are “a little bit like magic,” exults Eden Figueroa, a physicist at Stony Brook University. He and colleagues have concocted the setup on a few laboratory benches cluttered with lenses and mirrors. But they have a much bigger canvas in mind.

By year’s end, drivers in the largest U.S. metro areas—including, largely thanks to Figueroa, the suburbs of New York City—may unwittingly rumble over the tenuous strands of a new and potentially revolution-

ary network: a “quantum internet” stitched together by entangled photons like those in Figueroa’s lab.

Billions of dollars have poured into research on quantum computers and sensors, but many experts say the devices will flourish only when they are yoked to each other over long distances. The vision parallels the way the web vaulted the personal computer from a glorified typewriter and game console to an indispensable telecommunications portal. Through entanglement, a strange quantum mechanical property once

derided by Albert Einstein as a “spooky distant effect,” researchers aim to create intimate, instantaneous links across long distances. A quantum internet could weld telescopes into arrays with ultrahigh resolution, precisely synchronize clocks, yield hypersecure communication networks for finance and elections, and make it possible to do quantum computing from anywhere. It could also lead to applications nobody’s yet dreamed of.

Putting these fragile links into the warm, buzzing world will not be easy, however. Most strands that exist today can send entangled photons to receivers just tens of kilometers apart. And the quantum links are fleeting, destroyed as the photons are received and measured. Researchers dream of sustaining entanglement indefinitely, using streams of photons to weave lasting quantum connections across the globe.

For that, they will need the quantum equivalent of optical repeaters, the components of today’s telecommunications networks that keep light signals strong across thousands of kilometers of optical fiber. Several teams have already demonstrated key elements of quantum repeaters and say they’re well on their way to building extended networks. “We’ve solved all the scientific problems,” says Mikhail Lukin, a physicist at Harvard University. “I’m extremely optimistic that on the scale of 5 to 10 years ... we’ll have continental-scale network prototypes.”

ON THE NIGHT of 29 October 1969, 2 months after Woodstock and as the Vietnam War raged, Charley Kline, a student at the University of California, Los Angeles, fired off a message to a computer just over 500 kilometers away at the Stanford Research Institute in Menlo Park, California. It was the launch of the Advanced Research Projects Agency Network (ARPANET). From that precarious two-node beginning—Kline’s intended message was “login” but only “lo” made it through before the system crashed—the internet has swelled into today’s globe-encompassing network. About 2 decades ago, physicists began to wonder whether the same infrastructure could shuttle around something more exotic: quantum information.

It was a heady time: A mathematician named Peter Shor had, in 1994, devised a quantum code that could break a leading encryption algorithm, something classical computers could not do. Shor’s algorithm suggested quantum computers, which exploit the ability of very small or cold objects to simultaneously exist in multiple, “superposed” states, might have a killer application—cracking codes—and ignited a decadeslong effort

to build them. Some researchers wondered whether a quantum internet might vastly enhance the power of those machines.

But building a quantum computer was daunting enough. Like entanglement, the superposed states essential to its power are fragile, collapsing when measured or otherwise perturbed by the outside world. As the field focused on general-purpose quantum computers, thoughts about linking those computers were mostly banished to a distant future. The quantum internet,

“On the scale of 5 to 10 years ... we’ll have continental-scale network prototypes.”

Mikhail Lukin, Harvard University

Figueroa quips, became “like the hipster version” of quantum computers.

More recently, with quantum computing starting to become a reality, quantum networking has begun to muscle its way back into the spotlight. To do something useful, a quantum computer will require hundreds of quantum bits, or qubits—still well beyond today’s numbers. But quantum networks can prove their worth as soon as a few distant nodes are reliably entangled. “We don’t need many qubits in order to do something interesting,” says Stephanie Wehner, research lead for the quantum internet division at Delft University of Technology (TU Delft).

The first networks capable of transmitting individual entangled photons have begun to take shape. A 2017 report from China was one of the most spectacular: A quantum satellite named Micius sent entangled particle pairs to ground stations 1200 kilometers apart (*Science*, 16 June 2017, p. 1110). The achievement set off alarms in Washington, D.C., that eventually led to the passage of the 2018 National Quantum Initiative Act, signed into law by then-President Donald Trump and intended to spur U.S. quantum technology. The Department of Energy (DOE), which has led efforts to envision a U.S. quantum internet, added to the momentum in April, announcing \$25 million for R&D on a quantum internet to link up national labs and universities. “Let’s get our science facilities connected, show that this works, and provide a framework for the rest of the country to hop on and scale it up,” says Chris Fall, who until recently led the DOE Office of Science.

The Chinese group, led by Jian-Wei Pan, a physicist at the University of Science and Technology of China, has continued to develop its network. According to a January *Nature* paper, it now spans more than 4600 kilometers, using fibers and non-quantum relays. Shorter quantum links have been demonstrated in other countries.

Industry and government are starting to use those first links for secure communication through a method called quantum key distribution, often abbreviated QKD. QKD enables two parties to share a secret key by making simultaneous measurements on pairs of entangled photons. The quantum connection keeps the key safe from tampering or eavesdropping, because any intervening measurement would destroy the entanglement; information encrypted with the key then travels through ordinary channels. QKD is used to secure some Swiss elections, and banks have tested it. But many experts question its importance, because simpler encryption techniques are also impervious to known attacks, including Shor’s algorithm. Moreover, QKD does not guarantee security at sending and receiving nodes, which remain vulnerable.

A full-fledged quantum network aims higher. It wouldn’t just transmit entangled particles; it “distributes entanglement as a resource,” says Neil Zimmerman, a physicist at the National Institute of Standards and Technology, enabling devices to be entangled for long periods, sharing and exploiting quantum information (*Science*, 19 October 2018, 10.1126/science.aam9288).

Science might be the first to benefit. One possible use is very long baseline interferometry. The method has already linked radio telescopes around the globe, effectively creating a single, giant dish powerful enough to image a black hole at the center of a distant galaxy. Combining light from far-flung optical telescopes is far more challenging. But physicists have proposed schemes to capture light gathered by the telescopes in quantum memories and use entangled photons to extract and merge its phase information, the key to ultrahigh resolution. Entangling distributed quantum sensors could also lead to more sensitive detector networks for dark matter and gravitational waves.

More practical applications include ultra-secure elections and hack-proof communication in which the information itself—and not just a secret key for decoding it, as in QKD—is shared between entangled nodes. Entanglement could synchronize atomic clocks and prevent the delays and errors that accumulate as information is sent between them. And it could offer a way to link up quantum computers, increasing their power. Quantum computers of the near future will likely be limited to a few hundred qubits each, but if entangled together, they may be able to tackle more sophisticated computations.

Taking this idea further, some also envision an analog of cloud computing: so-called blind quantum computing. The thinking is that the most powerful quantum computers will one day be located at national labora-

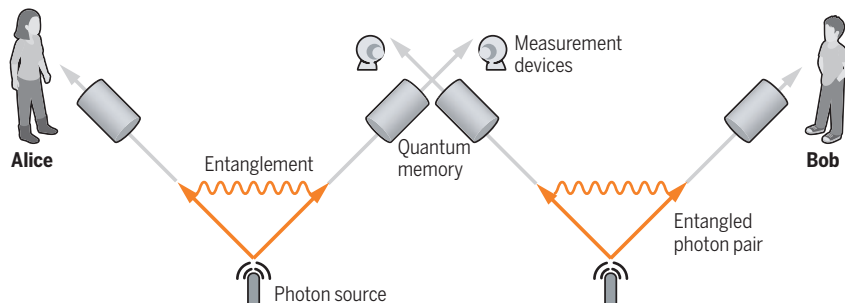
Making connections

A quantum internet would be woven together by photons that are entangled, meaning they share a quantum state. But quantum repeaters would be needed to relay the fragile photons between far-flung users.

A quantum repeater

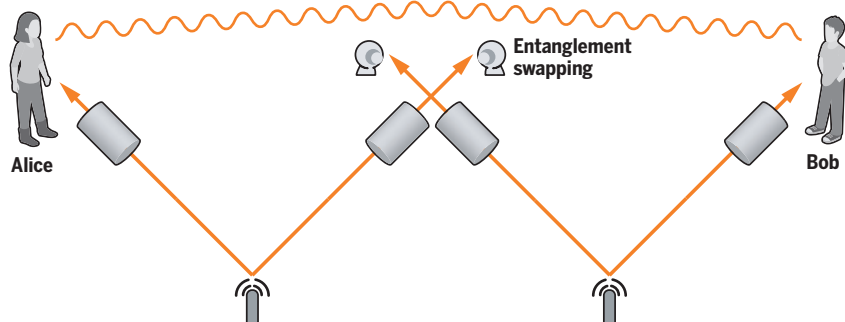
1 Generating photon pairs

One popular protocol begins by creating pairs of entangled photons and sending one member of each pair toward measurement devices while the others fly toward end users, conventionally called Alice and Bob.



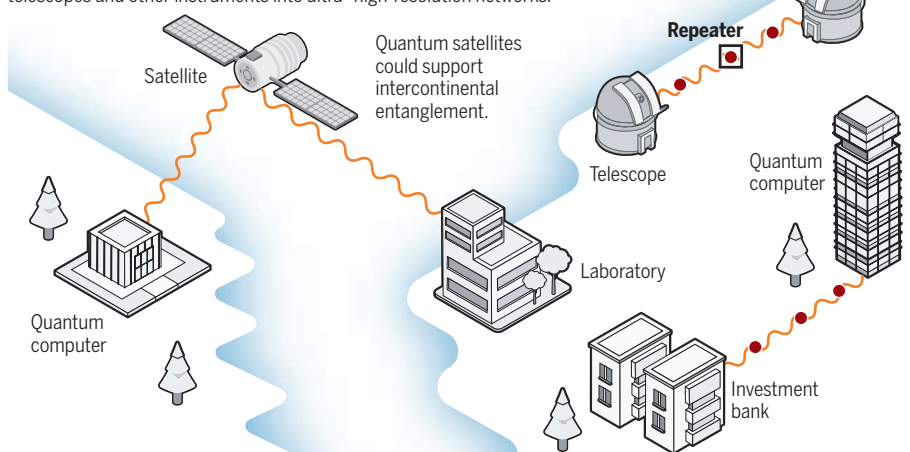
2 Long-range link

The photons are captured in quantum memories that store their quantum states. Processors correct and prepare the states while preserving the entanglements. A specialized measurement on the middle two quantum memories then “swaps” the entanglement to link Alice and Bob.



Versatile network

A quantum internet could establish intimate and secure connections among widely separated users and facilities. It could allow powerful quantum computers to run complicated algorithms for remote users while protecting sensitive information, or merge telescopes and other instruments into ultra-high-resolution networks.



atories, universities, and companies, much as supercomputers are today. Designers of drugs and materials or stock traders might want to run quantum algorithms from distant locations without divulging their programs' contents. In theory, users could encode the problem on a local device that's

entangled with a remote quantum computer—exploiting the distant computer's power while leaving it blind to the problem being solved.

“As a physicist, I think [blind quantum computing] is very beautiful,” says Tracy Northup of the University of Innsbruck.

RESEARCHERS HAVE TAKEN early steps toward fully entangled networks. In 2015, Wehner and colleagues entangled photons with electron spins in nitrogen atoms, encased within two tiny diamonds 1.3 kilometers apart on the TU Delft campus. The photons were then sent to an intermediate station, where they interacted with each other to entangle the diamond nodes. The experiment set a record for the distance of “heralded” entanglement—meaning researchers could confirm and use it—and the link lasted for up to several microseconds.

More expansive networks, however, will likely require quantum repeaters to copy, correct, amplify, and rebroadcast virtually every signal. And although repeaters are a relatively straightforward technology for the classical internet, a quantum repeater has to elude the “no-cloning” theorem—which holds, essentially, that a quantum state cannot be copied.

One popular repeater design starts with two identical, entangled photon pairs at separate sources. One photon from each pair flies toward distant end points, which could be quantum computers, sensors, or other repeaters. Let's call them Alice and Bob, as quantum physicists are wont to do.

The other halves of each pair zip inward, toward the heart of the repeater. That device must trap the photon that arrives first, coax its information into a quantum memory—perhaps a diamond or atom cloud—correct any errors that have accumulated in transit, and coddle it until the other photon arrives. The repeater then needs to mate the two in a way that entangles their far-flung twins. This process, known as entanglement swapping, creates a link between the distant end points, Alice and Bob. Additional repeaters could daisy-chain Alice to a Carol and Bob to a Dave, ultimately spanning big distances.

Figuroa traces his drive to build such a device to his 2008 Ph.D. thesis defense at the University of Calgary. After the young Mexican-born physicist described how he entangled atoms with light, a theorist asked what he was going to do with the setup. “At the time—shame on me—I didn't have an answer. To me, it was a toy I could play with,” Figuroa recalls. “He told me: ‘A quantum repeater is what you're going to do with it.’”

Inspired, Figuroa pursued the system at the Max Planck Institute of Quantum Optics before landing at Stony Brook. He decided early on that commercial quantum repeaters should operate at room temperature—a break from most quantum lab experiments, which are conducted at very cold temperatures to minimize thermal vibrations that could upset fragile quantum states.

Figuroa is counting on rubidium vapor for one component of a repeater, the quantum

memory. Atoms of rubidium, a heavy cousin of the more familiar lithium and sodium, are appealing because their internal quantum states can be set and controlled by light. In Figueroa's lab, entangled photons from the frequency-splitting crystal enter plastic cells containing 1 trillion or so rubidium atoms each. There, each photon's information is encoded as a superposition among the atoms, where it lasts for a fraction of a millisecond—pretty good for a quantum experiment.

Figueroa is still developing the second stage of the repeater: using computer-controlled bursts of laser light to correct errors and sustain the clouds' quantum states. Additional laser pulses will then send photons carrying entanglement from the memories to measurement devices to entangle the end users.

Lukin builds quantum repeaters using a different medium: silicon atoms encased in diamonds. Incoming photons can tweak the quantum spin of a silicon electron, creating a potentially stable memory; in a 2020 *Nature* paper, his team reported catching and storing quantum states for more than one-fifth of a second, far longer than in the rubidium memory. Although the diamonds must be chilled to within a fraction of a degree above absolute zero, Lukin says the fridges needed are fast becoming compact and efficient. "Right now it's the least of my worries."

At TU Delft, Wehner and her colleagues are pushing the diamond approach as well, but with nitrogen atoms instead of silicon. Last month in *Science*, the team reported entangling three diamonds in the lab, creating a miniature quantum network. First, the researchers used photons to entangle two different diamonds, Alice and Bob. At Bob, the entanglement was transferred from nitrogen to a spin in a carbon nucleus: a long-lived quantum memory. The entanglement process was then repeated between Bob's nitrogen atom and one in a third diamond, Charlie. A joint measurement on Bob's nitrogen atom and carbon nucleus then transferred the entanglement to the third leg, Alice to Charlie.

Although the distances were much shorter and the efficiency lower than real-world quantum networks will require, the controllable swapping of entanglement demonstrated "the working principle of a quantum repeater," says TU Delft physicist Ronald Hanson, who led the experiment. It is "something that has never been done."

Pan's team has also demonstrated a partial repeater, with atom clouds serving as the quantum memories. But in a study published in 2019 in *Nature Photonics*, his team demonstrated an early prototype of a radically dif-

ferent scheme: sending such large numbers of entangled photons through parallel fibers that at least one might survive the journey. Although potentially avoiding the need for repeaters, the network would require the ability to entangle at least several hundred photons, Pan says; his current record is 12. Using satellites to generate entanglement, another technology Pan is developing, could also reduce the need for repeaters because photons can survive much longer journeys through space than through fibers.

A true quantum repeater, most experts agree, remains years away, and may ultimately use technologies common in today's quantum computers, such as superconduct-



Impurity atoms in minuscule diamonds like the one at the heart of this chip can store and relay quantum information.

tors or trapped ions, rather than diamonds or atom clouds. Such a device will need to capture nearly every photon that hits it and will probably require quantum computers of at least a few hundred qubits to correct and process signals. In a yin-yang sort of way, better quantum computers could boost the quantum internet—which in turn could supercharge quantum computing.

While physicists labor to perfect repeaters, they are racing to link sites within single metropolitan areas, for which repeaters are not needed. In a study posted to arXiv in February, Figueroa sent photons from two atom-cloud memories in his lab through 79 kilometers of commercial fibers to Brookhaven National Laboratory, where the photons were merged—a step toward end-to-end entanglement of the type demonstrated by the TU Delft group. By next year, he plans to deploy two of his quantum memories—compacted to the size of a minirefrigerator—midway between his university and the New York City office of his startup company, Qunnect, to see if

they boost the odds of photons surviving the journey.

Embryonic quantum networks are also being built in the Boston, Los Angeles, and Washington, D.C., regions, and two networks will link Argonne National Laboratory and Fermi National Accelerator Laboratory in Illinois to several Chicago-area universities. TU Delft researchers hope to soon extend their record-long entanglement to a commercial telecommunications facility in The Hague, Netherlands, and other fledgling networks are growing in Europe and Asia.

The ultimate goal is to use repeaters to link these small networks into an intercontinental internet. But first, researchers face more mundane challenges, including building better photon sources and detectors, minimizing losses at fiber connections, and efficiently converting photons between the native frequency of a particular quantum system—say, an atom cloud or diamond—and the infrared wavelengths that telecom fibers conduct. "Those real-world problems," Zimmerman says, "may actually be bigger than fiber attenuation."

Some doubt the technology will live up to the hype. Entanglement "is a very odd, very special kind of property," says Kurt Jacobs, a physicist at the Army Research Laboratory. "It doesn't necessarily lend itself to all kinds of applications." For clock synchronization, for example, the advantage over classical methods scales only as the square root of the number of entangled devices. A threefold gain requires linking nine clocks—which may be more trouble than it's worth. "It's always going to be harder to have a functional quantum network than a classical one," Jacobs says.

To such doubts, David Awschalom, a physicist at the University of Chicago who is spearheading one of the Midwest networks, counters, "We're at the transistor level of quantum technology." It took a few years after the transistor was invented in 1947 before companies found uses for it in radios, hearing aids, and other devices. Transistors are now etched by the billions into chips in every new computer, smartphone, and car.

Future generations may look back on this moment the way we look nostalgically at ARPANET, a pure infant version of the internet, its vast potential yet to be recognized and commercialized. "You can be sure that we haven't yet thought of some of the most important things this technology will do," Awschalom says. "It would take extraordinary arrogance to believe you've done that." ■

Gabriel Popkin is a journalist in Mount Rainier, Maryland.

INSIGHTS

BOOKS *et al.*

SUMMER BOOKS

Summer reading 2021

A journalist probes the tech companies racing to entice consumers—and investors—with futuristic foods. An outsider documents his ascent in academia. A policy expert proposes a human-centered approach to solving society's problems. From an ode to azure to a deep dive into data, this year's summer reading picks—reviewed by alumni of the AAAS Mass Media Science & Engineering Fellows program—offer readers fresh perspectives on timely scientific topics. Confront the biases that have long imperiled women's health, probe the mysteries of memory, celebrate a prescient economist, and more, with the books reviewed below. —Valerie Thompson

Solving Public Problems

Reviewed by Ming Ivory¹

Governance professor Beth Simone Noveck, who formerly served as the first White House deputy chief technology officer, believes that “public entrepreneur-

ship” can counter the failures that have dominated public policy design in the United States since the 1960s. Her new book, *Solving Public Problems*, revisits the four stages of policy design—identifying problems, identifying solutions, designing for implementation, and evaluation and evolution—while identifying 20 crucial decisions that prioritize “human-centered public policies.”

Experts often expend much effort on program design, but once these programs are created, there is usually little fine-tuning of the implementation and hardly any emphasis on measuring whether the desired outcomes are achieved. The US federal civil service, for example, first celebrated as a defense of the “public interest” for its structural insulation from shortsighted patronage and political corruption, has recently come to be viewed by some as a nonelected “deep state” that frustrates legitimate partisan power and private-sector freedom. Noveck fearlessly defends the existence of “public interests,” arguing that their complexity and ethical significance are distinct from academic theory, electoral politics, and private-sector capitalism.

Noveck describes governance ideas that expand public policy designs in a variety of sectors, such as health care, transportation, housing, employment, justice, information, and education. She emphasizes participatory elements of the process that ensure that the communities most in need and those who will be most directly affected by proposed policies are consulted throughout the process, and she encourages training in quantitative and qualitative scientific

ILLUSTRATION: STEPHANIE SINGLETON



techniques, such as data analysis, research design, artificial intelligence, survey construction, interviewing, crowdsourcing, budgeting, and program evaluation. She discusses what can be learned from administrative records and from the temporary suspension of regulations that encourage private-sector experimentation.

Each chapter ends with exercises that, if conscientiously followed, could launch a community and its institutional partners on the path to practical policies that combat problems such as unemployment, information deficits, and housing discrimination. These exercises include checklists of tasks that must be accomplished to achieve the desired outcome, and they direct readers to an index full of organizations that could be sources of assistance.

If there is a weakness to the guide, it is that there are an almost overwhelming number of examples, replete with management jargon, that must be waded through without a lot of information on their relative quality. A list synthesizing what Noveck considers the best of these programs—organized either by agency type or by the skill set supported—would have been useful. Overall, however, the book offers a

wealth of information necessary to improve human-centered design in public policies.

Solving Public Problems: A Practical Guide to Fix Our Government and Change Our World.

Beth Simone Noveck, Yale University Press, 2021, 448 pp.

Technically Food

Reviewed by Anna Funk²

The latest food tech to hit the mainstream may be plant-based burgers, but countless start-ups and research labs are gearing up to transform the way humans think about what we eat—or at least, so they hope. From giant tanks of protein-rich algae to petri dishes culturing animal cells, researchers are seeking ways to give consumers—and investors—products that will improve food's sustainability, healthiness, or preferably both (bonus points if they are accompanied by new, patentable technologies that will keep the cash coming).

Some groups are trying to turn plants into meat, while others are trying to turn meat into more meat without killing more animals. Others still are trying to revolu-

tionize parts of the production process, building artificial intelligence-laden greenhouses in cities, for example, or salvaging food waste and turning it into more food. In *Technically Food*, journalist Larissa Zimmeroff explores eight of the latest tech trends in the food sector, giving readers an inside look at the progress that has been made in each, a thoughtful look at current shortcomings, and, whenever possible, a taste test.

Zimmeroff walks readers through the latest breakthroughs from groups working to turn algae, fungi, or peas into protein sources; the worlds of upcycling and vertical farming; laboratories culturing cell-based meat; and more-mainstream staples such as nondairy milks, nonchicken eggs, and plant-based burgers. The book wraps up with a surprisingly delightful medley of commentary from 19 experts on what they think will be on our plates in 20 years. (My personal favorite was from author and animal rights activist Paul Shapiro, who asks: What if local establishments could brew their own meat on-site like they would a craft IPA?)

Unfortunately, interspersed throughout Zimmeroff's otherwise detailed reporting



Technology-laden vertical farms, like this one in Sharjah, United Arab Emirates, are one of many ways tech companies hope to disrupt global food systems.

were more than a few technical flubs—mostly harmless in nature but certainly distracting to a careful reader. She mentions, for example, that ocean acidification occurs when pH levels rise (it is the opposite), references COVID-19 when she means SARS-CoV-2, and refers to yeast as bacteria. I also could have done without the occasional implication that science is boring or hard to understand (“Have your eyes glazed over yet?”) and her take on Expo West, a huge natural products show, where she tasted and spat out the free food samples. (The displays, she writes, were “enough to torture anyone’s waistline.”)

Still, the reporting behind this book is masterful. I was constantly pulled along by ideas about the food system that I had never considered, from secondary plant compounds that might be beneficial to human health—and are only produced if you lay off the pesticides and let a plant get nibbled a little—to what the median age of the United States’s traditional farmers (57.5 years in 2017) portends about the future of farming.

Even the title proved to be a wink I did not expect—not just “technically” as in technical, technological, but also “technically” as in “well, technically, it’s food.” The overarching question of whether high-tech food is actually an improvement or not is not answered by Zimmeroff, but she leaves readers with plenty of food for thought.

Technically Food: Inside Silicon Valley’s Mission to Change What We Eat, Larissa Zimmeroff, Abrams Press, 2021, 240 pp.

Unwell Women

Reviewed by **Stephani Sutherland**³

“The history of mankind is a history of repeated injuries and usurpations on the part of man toward woman,” declared abolitionist and suffragist Elizabeth Cady Stanton in 1848 at a convention to address inequities faced by women. Although the sentiment may sound radical to some, cultural historian Elinor Cleghorn’s new book suggests that Stanton’s argument is not far off track. In *Unwell Women*, Cleghorn provides an extensive history of how feminine anatomy, physiology, and psychology have been studied and manipulated—mainly by men—and how they have often been used to oppress the female sex.

The book is populated by meticulously researched and quoted historical figures—some famous, others simply captured in quotidian documentation. The cast of characters includes girls and women who suffered at the hands of men, as well as men who shaped history for pioneering medical techniques and theories under the frequently false guise of protecting, curing, and acting in women’s best interests. Also present are the women who have been driving forces for change, pushing for the right to hold authority over one’s own body and life.

Unwell Women details a history in which women were tortured, burned, and hanged for “witchcraft”; enslaved for the purpose of gynecological experimentation; and clitoridectomized for the crime of masturbation. During Victorian times, we learn, women of

certain social status were often prescribed a forced “rest cure” for hysteria, which entailed utter isolation and inactivity (with the exception of tooth cleaning) and a diet of four quarts of milk per day and raw beef soup. More recently, suffragists were physically assaulted, imprisoned, and force-fed, and many women have been sterilized on the grounds of “feeble-mindedness” and “social inadequacy,” often with racial undercurrents.

Despite the tremendous recent gains made in the rights of women—to vote, to work, to be educated, to control various facets of one’s own life—still, the inequities are massive. Nowhere is that gap more evident and more harshly felt than in the medical realm, where, to this day, women are disbelieved, dismissed, and gaslighted by medical professionals, particularly when their conditions prove difficult to diagnose. One glaring example is the mysterious condition called myalgic encephalomyelitis/chronic fatigue syndrome (ME/CFS). When ME/CFS was “discovered” in the 1980s, it was largely dismissed as a psychosomatic illness in wealthy white women who were perhaps “bored” with their lives—a sentiment not far from those used to explain “hysteria” in years past. Another recent example is the alleged hysterectomies being performed without consent on women at a US Immigration and Customs Enforcement facility in 2020 in Georgia.

Cleghorn brings her message home in the final chapter, aptly titled “Believe us.” She points out that the only path to change is for the medical profession to reckon with how it has used medicalization to control women for centuries and indeed still does.

Although *Unwell Women* may not become required reading for medical professionals and students, Cleghorn's final message should be heard loud and clear: Believe women.

Unwell Women: Misdiagnosis and Myth in a Man-Made World, Elinor Cleghorn, Dutton, 2021, 400 pp.

The Uncommon Knowledge of Elinor Ostrom

Reviewed by Tamar L. Goulet⁴

COVID-19 vaccines are a limited resource. Will some countries hoard them, exhibiting the selfish behavior that ecologist Garrett Hardin anticipated in his 1968 essay “The tragedy of the commons” (1), or will they share their extra doses with others who need them? The answer is currently unfolding, but promising signs suggest the latter, confirming predictions articulated by economist Elinor “Lin” Ostrom in her landmark 1990 book, *Governing the Commons* (2).

Ostrom, who is profiled in Erik Nordman's new book, *The Uncommon Knowledge of Elinor Ostrom*, was the first woman to win the Nobel Prize in Economics, securing the award in 2009 for her work on governing the commons and, according to Nordman, for her integration of theoretical foundations with fieldwork, anchoring economic concepts in real-world research.

At first, the book's chapters do not seem to be connected. Studies about volunteerism are sandwiched between chap-

ters on global climate change and space, and Ostrom's “eight design principles for managing a commons” appear for the first time in chapter four. Several pages into each chapter, however, Nordman presents the links that tie these themes together: Although resource use is key to Ostrom's principles, resources are not really the foci. Rather, managing “any common-pool resource,” as Nordman states, “is really about managing people.”

Ostrom studied a myriad of “commons,” including one that is currently in the societal spotlight: the organization and efficiency of police departments, which are often run through a centralized bureaucracy. Communities with smaller-sized local police departments tend to exert control by engaging in more formal and informal communication with the police, she and her colleagues found, thereby building trust between the two entities. Police forces in larger cities that employ a mixture of centralized and decentralized components may ultimately have better outcomes, they concluded. As Nordman summarizes, “Public safety is a service that is coproduced by police departments and citizens.” Ostrom's observations from the 1970s are worth revisiting half a century later as the United States questions police structure and the role of communities.

The work of managing commons reveals much about the complexities of life, illustrating what happens when these entities fail to fit into neat bins, when consequences are not binary, when outcomes seemingly defy logic, and when interconnectedness is key and collaboration is necessary and a strength. As Nordman asserts, “Ostrom left us with the tools to address

these global challenges, but the work is up to us.”

REFERENCES AND NOTES

1. G. Hardin, *Science* **162**, 1243 (1968).
2. E. Ostrom, *Governing the Commons: The Evolution of Institutions for Collective Action* (Cambridge Univ. Press, 1990).

The Uncommon Knowledge of Elinor Ostrom: Essential Lessons for Collective Action, Erik Nordman, Island Press, 2021, 256 pp.

The Ascent of Information

Reviewed by Max Kozlov⁵

Every cat GIF shared on social media, credit card swiped, video watched on a streaming platform, and website visited add more data to the mind-bending 2.5 quintillion bytes of information that humans produce every single day. All of that information has a cost: Data centers alone consume about 47 billion watts, equivalent to the resting metabolism of more than a tenth of all the humans on the planet.

In *The Ascent of Information: Books, Bits, Genes, Machines, and Life's Unending Algorithm*, astrobiologist Caleb Scharf probes this deluge of data, which he terms the “dataome,” to examine how it is changing us just as quickly as we are changing it. Masterfully weaving together anecdotes and thought experiments from neuroscience, evolutionary biology, theoretical physics, astrobiology, and information theory, Scharf investigates how our relationship with the dataome has fundamentally altered our lives and how it will continue to do so.

Scharf begins by invoking William Shakespeare, whose legacy permeates the public consciousness more than four centuries after his death, to show just how powerful the dataome can be. On the basis of the average physical weight of one of his plays, “it is possible that altogether the simple act of human arms raising and lowering copies of Shakespeare's writings has expended over 4 trillion joules of energy,” he writes. These calculations do not even account for the energy expended as the neurons in our brains fire to make sense of the Bard's language.

Zooming out as the book progresses, Scharf weaves in his own area of expertise—exoplanets—to dissect the argument of whether life exists beyond the confines of our planet. As a result of the same thermodynamic imperatives that gave rise to living systems on this planet,



Managing shared resources effectively is a matter of managing people effectively, argued Elinor Ostrom.

other dataomes, he maintains, are all but an inevitability.

The dataome has been around since long before us, and it will persist long after we are gone, Scharf writes, tracing the flow of information and energy back to the birth of the Universe. He compares the rise of information to the rise of oxygen on Earth; both, he argues, involve the reconfiguration of matter and energy flow in very specific ways.

Unlike atmospheric oxygen, however, humans have contributed to growing the dataome at unparalleled rates. Some estimate that by 2040, the world's computer chips will demand more electricity than is expected to be produced globally. Scharf ends with a sharply worded warning: All of these data represent a vastly different reality than anything biology has equipped us to deal with.

How then, he asks, can we simultaneously preserve and support both our dataome and our planet? We must treat information as a natural resource, Scharf argues, one that cannot be extracted, refined, or used without cost or repercussions. "Information really isn't 'free,' nor has it ever been so," he concludes.

The Ascent of Information: Books, Bits, Genes, Machines, and Life's Unending Algorithm.
Caleb Scharf, Riverhead Books, 2021, 352 pp.

A Quantum Life

Reviewed by **Elizabeth Gamillo**⁶

A Quantum Life: My Unlikely Journey from the Street to the Stars is the autobiography of astrophysicist and science communicator Hakeem Oluseyi, told as a journey from the author's challenging youth to the beginning of his career as a scientist. The book is split into four sections, each documenting pivotal parts of his life, including vivid accounts of his early childhood in an unstable home and his struggles with racism and classism as a Black doctoral student at Stanford University. Oluseyi, born James Plummer Jr., draws readers in with his candid and personable writing style. As I read, it felt as if he was sitting in front of me telling me his life story.

Oluseyi sought refuge in books early on in his life and recounts the transformative moment he learned about Albert Einstein and his theory of relativity as a child. "[R]ight away I felt connected to Einstein," he writes. "I could tell from his photo with that wild hair that he was weird, like me."

As the chapters progress, Oluseyi describes his difficult journey to find acceptance; he is too academically inclined for most of his peers but has trouble fitting in easily in academia. As a graduate student, he is pressured to leave Stanford University after failing his qualifying exam and resents the "privileged snobs" who make up most of the student body, with whom he finds little common ground.

Oluseyi's supervisor, solar physicist Art Walker—the only Black faculty member in the physics department—plays a critical role in helping Oluseyi find his footing, highlighting the critical role of scientific mentorship. "Congratulations, Doctor," Walker tells his young mentee in the book's closing



Astrophysicist Hakeem Oluseyi's candid reflections offer inspiration to aspiring scientists.

pages, acknowledging Oluseyi's successful dissertation defense. "Art's handshake, and the hug that followed, was all the affirmation I could ask for," writes Oluseyi.

In the book's epilogue, Oluseyi describes his efforts to inspire the next generation of research physicists and details the importance of having culturally relevant role models. Here, he reflects on his experience tutoring Black and Latino high school students in the US and the mentoring program he created for Black astronomy students in South Africa, revealing how he uses his own struggles to relate to and motivate them.

I found Oluseyi's perseverance inspiring.

His story serves as a reminder that barriers are meant to be broken and that there is no one right way to be a scientist. We need more such stories if we truly wish to increase diversity within the scientific enterprise.

A Quantum Life: My Unlikely Journey from the Street to the Stars. Hakeem Oluseyi and Joshua Horwitz, Ballantine Books, 2021, 368 pp.

Blue

Reviewed by **Daniel Ackerman**⁷

Pope Julius II spared no expense in commissioning the Sistine Chapel's ceiling frescoes. He fetched Italy's top artistic talent—Michelangelo—for the job and demanded that the artist render the sky a brilliant celestial blue with a particular pigment: ultramarine. Derived from lapis lazuli stone quarried in present-day Afghanistan, ultramarine was worth more than its weight in gold.

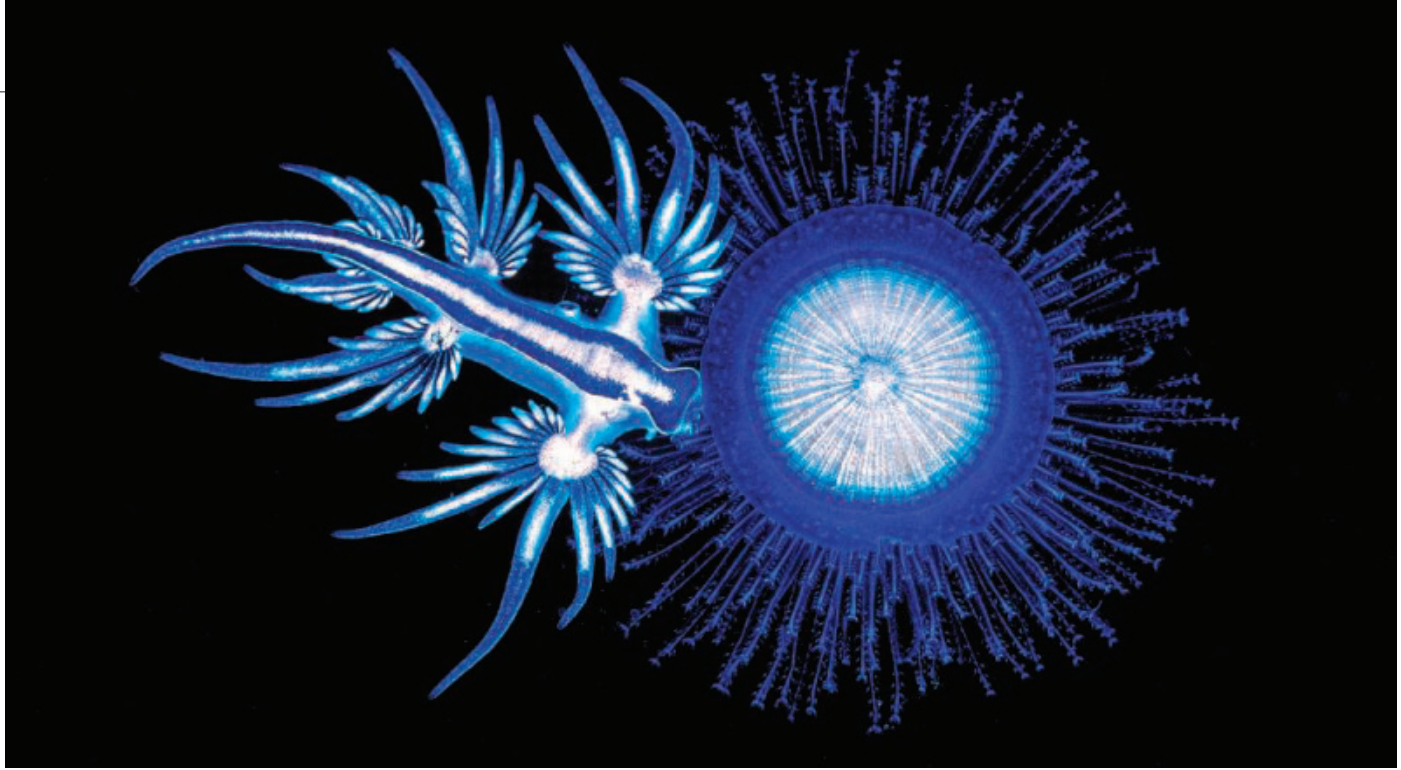
Science journalist Kai Kupferschmidt shares Julius II's obsession with blue, and he indulges it in an ambitious new biography of the color. *Blue: In Search of Nature's Rarest Color* dutifully answers all the expected scientific questions—why is the sky blue?—but it shines brightest when Kupferschmidt blends the physical and the philosophical, asking, for example, is the sky a social phenomenon?

Over 200 pages, Kupferschmidt sketches a comprehensive history of the color blue. He deftly bridges mineralogy, botany, and art history to explore humanity's quest for the perfect blue pigment. With equal ease, he describes Picasso's Blue Period palette and the microstructures that blue jays use to "cheat" their way to a dazzling cerulean.

The book's most fascinating chapters, "Seeing" and "Speaking," dwell on how we perceive and communicate color. "Blue light is not actually blue," writes Kupferschmidt. Light is merely electromagnetic radiation—photons with particular wavelengths. It becomes "blue" only through a dance with the eye, the brain, and our shared understanding of the world.

Here, readers learn about the evolution of the eye and follow along as Kupferschmidt ponders whether the ancient Greek poet Homer, who described both the ocean and oxen as "wine-dark," might have

¹The reviewer is professor emerita at the Department of Integrated Science and Technology, James Madison University, Harrisonburg, VA, USA. Email: ivorymx@jmu.edu ²The reviewer is a freelance writer based in Kansas City, MO, USA. Email: itsdrunk@gmail.com ³The reviewer is a neuroscientist and freelance science journalist based in Southern California, USA. Email: sutherland@nasw.org ⁴The reviewer is at the Department of Biology and the Center for Biodiversity and Conservation Research, University of Mississippi, University, MS, USA, and a AAAS IF/THEN Ambassador. Email: tlouglet@olemiss.edu ⁵The reviewer is a science journalist based in Boston, MA, USA. Twitter: @maxdkozlov ⁶The reviewer is at the Girls' Academy of Science and Mathematics, Alverno College, Milwaukee, WI, USA. Email: elizabeth.gamillo@alverno.edu ⁷The reviewer is a freelance journalist based in Boston, MA, USA. Twitter: @DAckermanNews ⁸The reviewer is at the Department of Veterinary Integrative Biosciences and the Department of Humanities in Medicine, Texas A&M University, College Station, TX, USA. Email: bgastel@cvm.tamu.edu



The blue coloring of the sea swallow (*Glaucus atlanticus*, left; shown feeding on a hydrozoan) helps camouflage the creature in the blue waters in which it lives.

perceived the color blue differently than we do today. Language structures our view of the colorful world, notes Kupferschmidt in this section, revealing that Russian speakers are faster than English speakers in distinguishing shades of blue. (The language splits light and dark blue into different categories, just as English separates green from yellow.)

In his effort to see blue from every possible angle, Kupferschmidt's narrative thread occasionally frays—some sections read more like a collection of essays than a unified whole. Yet his lively writing and ability to wrangle disparate disciplines are more than enough to keep the curious reader aboard. And like the very best science writers, Kupferschmidt paints a radical vision of material that would feel mundane in the hands of a less-capable author.

Blue: In Search of Nature's Rarest Color.
Kai Kupferschmidt, *The Experiment*, 2021, 224 pp.

The Memory Thief and the Secrets Behind How We Remember

Reviewed by **Barbara Gastel**⁸

Mysterious illnesses can serve as starting points for both medical science and popular science writing. They can lead physicians and scientists to identify previously unknown syndromes, better understand the

body's functioning, and ultimately improve the prevention and treatment of diseases. For science writers, such cases supply scaffolding for narrative, allow easy integration of human interest, and offer chances to portray not only the products but also the process of science. Such cases are at the core of *The Memory Thief and the Secrets Behind How We Remember* by science journalist Lauren Aguirre.

Early in the book, a young neurologist named Jed Barash views an MRI scan of the brain of a patient acting strangely after a drug overdose. Barash is taken aback: The patient's hippocampus—crucial to memory—is severely damaged, but the rest of his brain is intact. Upon examination, the patient shows profound memory difficulty, akin to the deficits seen in patients with Alzheimer's disease.

Barash embarks on a search for other such cases, leading to the identification of what is now called opioid-associated amnesic syndrome. Along the way, he enlists other physicians and researchers to try to gain a sense of how common this syndrome might be, how it arises, what it might imply more broadly about the effects of opiate use, and whether it might offer insights into other memory impairments.

Threaded throughout this narrative are accounts of well-known cases in which surgical injury or viral infection ravaged an individual's hippocampus, resulting in permanent memory impairment; descriptions of rodent studies that have helped researchers identify the roles of hippocampal neurons in memory formation; and more information about the

effects of opioids on memory. Aguirre discusses the possible origins of Alzheimer's disease as well as factors that contribute to healthy aging of the human brain.

Aguirre also recounts the story of Owen Rivers, a bright young man who has been all but unable to form new memories since overdosing on fentanyl in 2018. The book's prologue tells Rivers's story from shortly before to shortly after the overdose, and segments interspersed throughout the main text trace his history and follow his experiences and reflections since the incident. The epilogue includes an engaging essay in which Rivers presents his own perspective on his memory loss, offering readers a firsthand account of the experience. "Without Calendar notifications, task organization apps (huge shoutout to Trello), alarms, and meticulous preplanning each day, navigating everyday life on my own would be unfeasible," he writes.

The Memory Thief is extensively researched, and Aguirre writes clearly, concisely, and often cinematically. Some of the book's denser sections might bog down nonscientists, while experts might lose patience with some of the more informal storytelling. However, the book ultimately succeeds in providing an accessible yet substantive look at memory science and offering glimpses of the often-challenging process of biomedical investigation.

The Memory Thief and the Secrets Behind How We Remember: A Medical Mystery, Lauren Aguirre, Pegasus Books, 2021, 336 pp.

10.1126/science.abj2923

PALEONTOLOGY

When sharks nearly disappeared

A previously unidentified extinction event in the open ocean decimated pelagic sharks

By **Catalina Pimiento**^{1,2,3} and
Nicholas D. Pyenson^{4,5}

Each year, the discovery of new shark species underscores how little we know about ocean biodiversity (1). This is alarming not only because human pressures threaten sharks more than other marine lineages (2) but also because their fossil record suggests that they were largely resilient to extinction in the past (3), with some extant species persisting for tens of million years (4). On page 1105 of this issue, Sibert and Rubin (5) report an unexpected finding: a wholesale extinction of shark lineages in the pelagic ocean, the largest ecosystem on Earth, about 19 million years ago. Their discovery suggests that some extinctions in the open sea of the past may have been cryptic. More puzzling is that this event in the early Miocene seems to have been hiding in an interval of geologic time that was previously unremarkable. How did they find it, and what does it mean?

Our view of the ancient oceans is constrained by the environments recorded in the rock record, which are often limited to shallow-water deposits that provide little insight into the ocean-wide history of pelagic faunas. The study of Sibert and Rubin takes advantage of a system that Sibert largely pioneered (6) using ich-

thyoliths—tiny, hard bits of shark skin and bony fish teeth that naturally fall from their bodies to the seafloor. Once retrieved from deep-sea sediment drill cores (about 5700 m deep), these microscopic fossils provide a rich record of ancient oceanic shark (those living in the open ocean) ecomorphotypes and their abundance, all accumulating in fine succession at the scale of thousands of years. Although this proxy record of diversity has weak phylogenetic control because such samples of skin and teeth do not always correspond directly with host lineages, its power derives from the high temporal resolution

for the rate of microfossil accumulation in the seafloor sediment and variation in sedimentation rates as well as the preservation potential of these microfossils. This control of geologic factors, along with the finely resolved cores from two distinct sites (hemispheres apart in the Pacific Ocean), points to a real global event. There is also a strong ecological dimension to this faunal turnover: Nearer-shore taxa appear to survive, whereas migratory, ocean-going ones go extinct. The finding of this study is that shark ecology had undergone a widespread extinction that reorganized their communities, in an apparent global manner, in the early Miocene (about 16 million to 20 million years ago).

Although the early Miocene marine faunas were roughly similar to those of today, the body size distributions of major ocean predators were askew. Whereas whales lacked extreme gigantism at this time (7), the 20-m shark “Megalodon” (8) first appeared (9), persisting as a top predator until the Pliocene (about 2.5 million to 5.3 million years ago) (3, 10, 11). The findings of Sibert and Rubin suggest that there is still much to learn about the ecological roles for these marine predators that likely crossed the interface between the deep ocean and the shallow marine environment (down to 200-m depths, where the continental shelf is located) in the early Miocene. We don’t know whether they migrated to seek seasonal prey, as whales and sharks do today, or what the structure was of their feeding ecology over the course of their life history.

Sibert and Rubin narrowed the disappearance of pelagic sharks to a window of time under 100,000 years around 19 million

Oceanic shark loss, then and now

Pelagic shark communities never recovered from the early Miocene extinction event discovered by Sibert and Rubin. The parallels between that event and today’s crisis driven by human pressures (i.e., overfishing) are striking.

	EARLY MIOCENE (19 MILLION YEARS AGO)	ANTHROPOCENE (13)
Total diversity	81 Morphotypes	31 Species
Abundance decrease	90%	71% (1970–2018)
Diversity decrease	70% (Morphological)	77%* (Species, projected)

*Projection is based on the number of oceanic shark species currently considered threatened by the International Union for Conservation of Nature Red List of Threatened Species.

and broad geographic coverage that comes with sediment cores. By using cores from multiple regions, the diversity patterns from the microfossils of marine fauna can yield major insights into evolution of the open sea that would be otherwise unknown.

Sibert and Rubin quantified the magnitude of a past extinction of sharks, reporting a 90% decline in abundance and >70% drop in morphological diversity. Critically, they make a compelling case for the secular nature of this event by adjusting their counts

¹Paleontological Institute and Museum, University of Zurich, CH-8006 Zurich, Switzerland. ²Department of Biosciences, Swansea University, Swansea, UK. ³Smithsonian Tropical Research Institute, Panama. ⁴Department of Paleobiology, National Museum of Natural History, Smithsonian Institution, Washington, DC, USA. ⁵Department of Paleontology, Burke Museum of Natural History, Seattle, WA, USA. Email: catalina.pimiento@harnandez@pim.uzh.ch; pyenson@si.edu

The scalloped hammerhead shark (*Sphyrna lewini*), as this one seen off the Galapagos Islands, Ecuador, is a critically endangered oceanic shark species.

years ago, but the causes of this event remain obscure. Because the early Miocene does not stand out as a period of major climatic change, the authors do not attribute environmental factors as an extinction driver. Mechanism aside, this extinction resulted in a permanent suppression of pelagic sharks that affected the ecological composition of shark communities through time to the present day.

Despite sharks today being mostly distributed in the continental shelf (2, 12), in less than half a century the global abundance of oceanic sharks has declined by more than 70% (13, 14). This loss of shark diversity is directly linked to overfishing (12, 13), even as the undisputable effects of global heating in the oceans continue to complicate this crisis. The parallels between this ongoing crisis and the extinction of pelagic sharks more than 19 million years ago thus feels like déjà vu, except that this time we know that the decline of sharks is happening at a faster rate than at any other in the history of the planet (see the table).

The loss of sharks from the oceans has profound, complex, and irreversible ecological consequences because their presence reflects the stability of marine ecosystems (15). Yet, one-quarter of the global diversity of sharks is currently threatened with extinction (2), with a substantial risk status increase for all 31 extant oceanic shark species (13). Despite recent improvements in conservation actions, few countries impose restrictions that target oceanic sharks (13). Pelagic shark communities never recovered from a mysterious extinction event 19 million years ago; the ecological fate of what remains is now in our hands. ■

REFERENCES AND NOTES

1. H. S. Randhawa, R. Poulin, M. Krkošek, *Ecography* **38**, 96 (2015).
2. N. K. Dulvy et al., *eLife* **3**, e00590 (2014).
3. C. Pimiento et al., *Nat. Ecol. Evol.* **1**, 1100 (2017).
4. A. Paillard, K. Shimada, C. Pimiento, *J. Fish Biol.* **98**, 445 (2021).
5. E. C. Sibert, L. D. Rubin, *Science* **372**, 1105 (2021).
6. E. C. Sibert, K. L. Cramer, P. A. Hastings, R. D. Norris, *Palaeontol. Electronica* **20**, 1 (2017).
7. G. J. Slater, J. A. Goldbogen, N. D. Pyenson, *Proc. Biol. Sci.* **284**, 20170546 (2017).
8. V. J. Perez, R. M. Leder, T. Badaut, *Palaeontol. Electronica* (2021).
9. C. Pimiento et al., *J. Biogeogr.* **43**, 1645 (2016).
10. C. Pimiento, C. F. Clements, *PLOS ONE* **9**, e111086 (2014).
11. R. W. Boessenecker et al., *PeerJ* **7**, e6088 (2019).
12. R. W. Stein et al., *Nat. Ecol. Evol.* **2**, 288 (2018).
13. N. Pacoureau et al., *Nature* **589**, 567 (2021).
14. N. K. Dulvy et al., *Curr. Biol.* **27**, R565 (2017).
15. R. A. Myers, J. K. Baum, T. D. Shepherd, S. P. Powers, C. H. Peterson, *Science* **315**, 1846 (2007).

10.1126/science.abj2038

METROLOGY

Calibrating experiments at atom-crushing pressures

Shockless compression of platinum and gold provides pressure standards to >1 terapascal

By Raymond Jeanloz

Experimentalists can now generate terapascal pressures in the laboratory, conditions sufficient to alter the structure of atoms and the nature of interatomic bonding (1). These are the pressures of planets' interiors and origins—7 TPa at Jupiter's center, 4 TPa in the middle of Saturn, 0.36 TPa for Earth's inner core—and planet growth involves impacts that generate pressures into the terapascal range (2). Understanding materials and their properties at such conditions provides key insights into how planetary bodies form and then evolve over billions of years. On page 1063 of this issue, Fratanduono *et al.* (3) establish a new calibration for such experiments, and their pressure-volume relations for gold (Au) and platinum (Pt) can now serve as reliable standards to >1 TPa.

This is a notable contribution because the forces that stabilize the atom are of terapascal magnitude. For example, the quantum-mechanical pressure that keeps the negatively charged electron from being pulled into the positively charged nucleus of the Bohr atom is $\hbar/(4\pi m_e a_0^3) = 2.3$ TPa, with \hbar , m_e , and $a_0 = 53$ pm being Planck's constant divided by 2π , the mass of the electron, and the Bohr radius, respectively. Current experiments can thus match or even overwhelm ambient-condition quantum forces and profoundly change the properties of materials.

For comparison, the pressure-volume work associated with compression to million-atmosphere (0.1 TPa) pressures amounts to electron volt changes in a material's energy, affecting the outer bonding electrons and hence the chemical properties of atoms (4). The trends of the periodic table become distorted under these conditions, with xenon, oxygen, and fluid hydrogen all transforming to metals and the "simple metal" sodium becoming a transparent, ionic salt (electride) by 0.2 TPa (5, 6). The more extreme conditions at the atomic unit of pressure, $E_H/a_0^3 = 29$ TPa, alter the in-

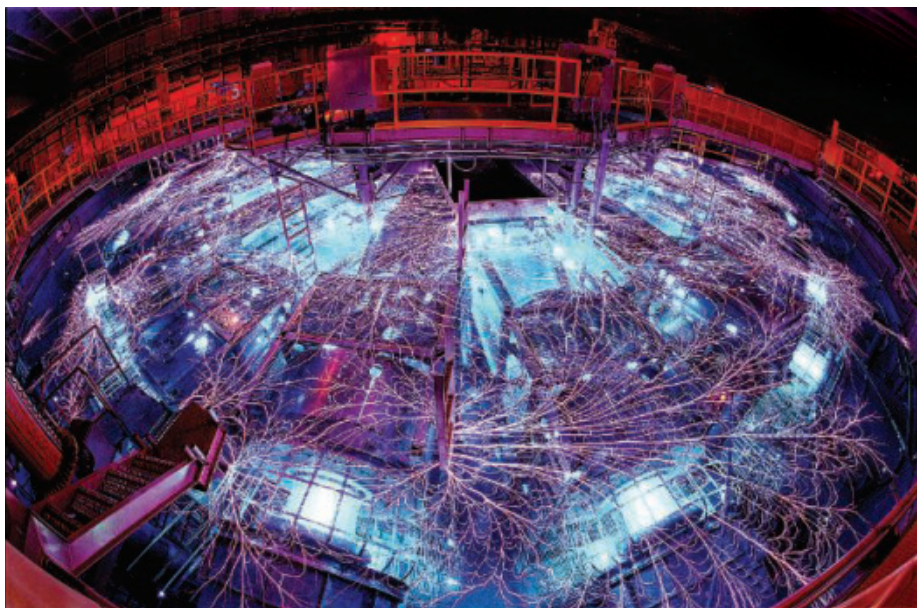
ternal energy of materials by kilo-electron volts (7). These conditions are the gateway to "kilovolt chemistry" in which core electrons—the deeper electron orbitals of the atom—engage in chemical bonding (2, 8).

First-principles quantum mechanical calculations already predict unusual properties at multi-terapascal pressures—for example, with the stabilization of relatively open crystal-structure geometries for elemental iron as well as for a variety of compounds, despite the atoms being under high compression (8–10). Hydrogen is expected to be a metallic quantum-crystal at these conditions, with atomic separations approaching the de Broglie wavelength (atoms becoming quantum indistinct); the liquid state may exhibit exotic combinations of superconductivity and superfluidity (11).

Motivated by these predictions, experimentalists have stretched their capabilities to achieve record high pressures under controlled laboratory conditions. Diamond-anvil cells are now approaching 1 TPa by compressing samples between cleverly sculpted diamond tips, holding the $\sim 1 \mu\text{m}^3$ (1 femtoliter) sample for (as far as we know) arbitrarily long periods of time (12). Room-temperature superconductivity was recently reported in a carbonaceous sulfur hydride compressed inside a diamond cell to 0.3 TPa (13); the impact on technology could be huge, if it leads to the synthesis of ambient-condition superconductors. By contrast, pulsed-power- and laser-driven dynamic compression can characterize much larger (cubic millimeter sized) samples to far higher pressures, but only for tens to hundreds of nanoseconds. For example, laser-driven ramp loading—in principle, a nearly isentropic compression—has taken carbon to 5 TPa, into the Thomas-Fermi-Dirac statistical atom regime; and spherically converging shocks have produced equation-of-state data to nearly 50 TPa, conditions that are relevant to understanding white-dwarf stars (14, 15).

The diversity of techniques is noteworthy, with a variety of static versus dynamic means of generating high pressures and experimental diagnostics ranging from velocity interferometry to x-ray diffraction and spectroscopy. Calibration has thus become

Departments of Earth and Planetary Science and Astronomy, University of California, Berkeley, Berkeley, CA, USA. Email: jeanloz@berkeley.edu



The Z pulsed-power facility used for calibrating terapascal pressures has a diameter of 37 m.

essential for comparing the different laboratory measurements, all the more so because the samples are probed over different temperatures and time scales by the different high-pressure methods. Fratanduono *et al.*'s pressure-volume measurements using both pulsed-power and laser-driven compression show that the two technologies, which can differ by an order of magnitude or more in sample dimensions and compression time, are in good agreement with each other (3). They also find general accord with diamond-cell reports but are able to provide improvements for the necessarily extrapolated calibrations of past experiments.

It is both reassuring and impressive that measurements made over time scales spanning 12 orders of magnitude, from 10^{-8} s for laser-driven compression to 10^4 s or more for static high-pressure experiments, are in such good agreement with each other. Calibration allows completely independent experiments to be compared and even combined, not only validating but also substantially enhancing results because each method has its advantages and drawbacks. Short duration in the dynamic measurements invites nonequilibrium effects, whereas small samples and large stress gradients in the static experiments challenge reproducibility and quantification.

One of the key reasons that robust calibration is essential is that these experiments provide tests of first-principles quantum mechanical calculations of material properties. To be clear, theory and experiment are closely symbiotic, with the laboratory work being guided by quantum calculations, which also help in the interpretation and application of the experimental results. At the same time,

experiments provide important validation for theory, and discrepancies between theory and experiment help guide improvements in both. Working at extreme conditions, the community is moving toward more reliable predictions of material properties and phase stability at ambient conditions, advancing technology as well as fundamental understanding. The work also helps us to better understand planets, the platforms on which life can establish itself and evolve. ■

REFERENCES AND NOTES

1. One terapascal corresponds to 10 million atmospheres pressure.
2. R. Jeanloz *et al.*, *Proc. Natl. Acad. Sci. U.S.A.* **104**, 9172 (2007).
3. D. E. Fratanduono *et al.*, *Science* **372**, 1063 (2021).
4. One electron volt = 96.5 kJ/mol.
5. Y. Ma *et al.*, *Nature* **458**, 182 (2009).
6. The electron-charge density becomes concentrated between the sodium ion cores at high pressure, so that the metal effectively transforms into a "salt" of Na^+ cations bound to e^- "anions" of increased charge density but without a nucleus.
7. Hartree's atomic unit of energy, $E_h = \hbar^2/(m_e a_0^2) = 27$ eV, is the potential energy drawing the electron to the nucleus in the Bohr atom, and the unit of pressure is simply the energy density E_h/a_0^3 derived on dimensional grounds.
8. M. Miao, Y. Sun, E. Zurek, H. Lin, *Nat. Rev. Chem.* **4**, 508 (2020).
9. C. J. Pickard, R. J. Needs, *J. Phys. Condens. Matter* **21**, 452205 (2009).
10. L. Stixrude, *Phys. Rev. Lett.* **108**, 055505 (2012).
11. J. E. McMahon, M. A. Morales, C. Pierleoni, D. M. Ceperley, *Rev. Mod. Phys.* **84**, 1607 (2012).
12. N. Dubrovinskaya *et al.*, *Sci. Adv.* **2**, e1600341 (2016).
13. E. Snider *et al.*, *Nature* **586**, 373 (2020).
14. R. F. Smith *et al.*, *Nature* **511**, 330 (2014).
15. A. L. Kritcher *et al.*, *Nature* **584**, 51 (2020).

ACKNOWLEDGMENTS

I have benefitted from discussions with G. W. Collins, D. E. Fratanduono, N. Y. Yao, and E. Zurek. This work was supported by the National Nuclear Security Administration Center for Matter under Extreme Conditions and the National Science Foundation Physics Frontier Center for Matter at Atomic Pressure.

10.1126/science.abi8015

IMMUNOLOGY

A LoCK at the T cell dock

Topology of T cell receptor–antigen binding constrains T cell activation

By Veronika Horkova and Ondrej Stepanek

The stimulation of T cells with foreign or self-antigens plays a central role in the adaptive immune responses to infection and cancer but also in autoimmunity. T cells use a sophisticated molecular machinery to recognize and respond to cognate antigens. On page 1056 of this issue, Zareie *et al.* (1) examine the productive and unproductive engagement of the T cell receptor (TCR) with antigens by focusing on binding orientation. The polarity of the interaction affects recruitment of key signaling molecules to the TCR. This topology thus constrains T cell immune responses.

Most immune receptors are encoded in the germline DNA. Evolution fine-tuned them to recognize germline-encoded endogenous ligands (such as cytokines, secreted immunoregulatory proteins) or conserved exogenous ligands (such as bacterial products). By contrast, genes encoding the TCR and B cell receptor (BCR) are rearranged in each lymphocyte independently. Clonal selection of lymphocytes during maturation and in the immune response mimics the evolutionary adaptations on a scale of an individual organism.

Whereas the BCR recognizes the antigen directly, a canonical TCR recognizes an antigenic peptide fragment presented by the major histocompatibility complex (MHC) on the surface of a host cell. Therefore, the TCR ligand consists of a germline-encoded component (MHC) and a highly variable antigen (peptide). This bivalent character stirred debate about whether peptide-MHC (pMHC) recognition is determined by inherent properties of the germline-encoded segments of the TCR or by the selection processes during T cell development (2). There is a clear germline bias of the TCR repertoire toward MHC recognition that is manifested by a relatively high percentage of self-pMHC-specific TCRs in the preselection repertoire

Laboratory of Adaptive Immunity, Institute of Molecular Genetics of the Czech Academy of Sciences, 14220 Prague, Czech Republic. Email: ondrej.stepanek@img.cas.cz

(3, 4). Yet the majority of developing T cells do not recognize self-pMHC, indicating a role for T cell selection in shaping the self-MHC-restricted TCR repertoire.

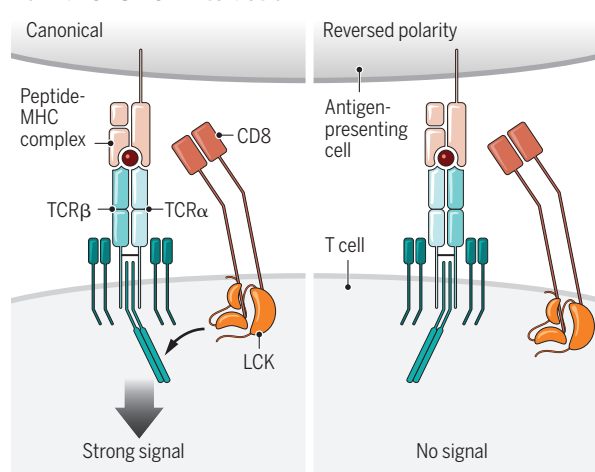
Engagement between a TCR and a cognate pMHC triggers TCR signaling that instructs cell fate decisions. During T cell development in the thymus, self-antigens evoke strong, weak, or negligible TCR signals that lead to T cell death (negative selection), survival (positive selection), or death “by neglect,” respectively. In mature T cells, strong TCR signaling stimulates proliferation and effector immune responses. TCR signaling is initiated by tyrosine phosphorylation of the TCR complex by the intracellular enzyme LCK (lymphocyte-specific protein tyrosine kinase). However, the mechanism of how antigen binding induces the intracellular signaling steps is still unresolved. Although not essential for TCR activation, invariant co-receptors CD4 and CD8 facilitate TCR signaling by binding to MHC class II (MHCII) and class I (MHCI), respectively. The co-receptors deliver LCK to the TCR complex to enhance positive (5) and negative selection (6) of immature T cells and TCR sensitivity in mature T cells (7). The sequestration of LCK by co-receptors shapes the self-MHC-restricted T cell repertoire by preventing maturation of T cells specific for MHCI/II-independent antigens (8).

Various TCRs associated with their cognate pMHC ligands exhibit similar, but not identical, binding orientation (9). High-affinity TCR-pMHCI interactions with deviated (10) or even reversed docking symmetries (11) do not trigger TCR signaling. Zareie *et al.* explored the phenomenon of unproductive antigen engagement by comparing three murine TCRs that interact with an MHCI-restricted influenza antigen (H-2D^b-NP₃₉₆) in the canonical orientation and two TCRs that bind the same antigen in the reversed docking polarity (see the figure). T cells that recognized the reverse orientation did not respond to influenza infection in mice. Only canonical antigen docking recruited CD8 to the proximity of the TCR signaling motifs. Whereas CD8-LCK interaction activated a conventional TCR, it prevented the activation of a TCR recognizing the antigen with reversed docking polarity. The authors concluded that CD8 sequestered LCK and made it inaccessible for TCR-pMHCI pairs with reversed docking polarity.

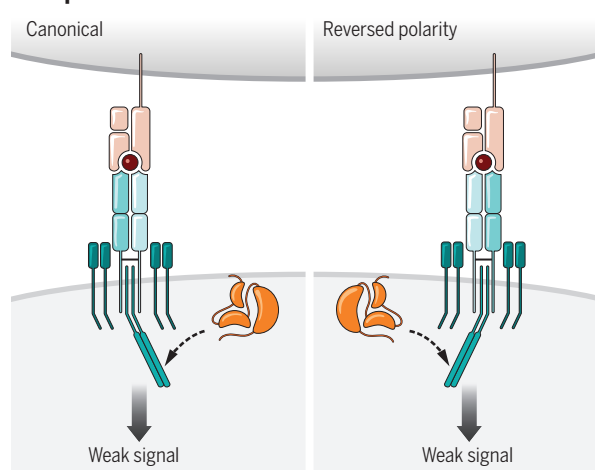
Productive docking

The polarity of T cell receptor (TCR) binding to its cognate peptide ligand [presented by the major histocompatibility complex (MHC)] dictates whether lymphocyte-specific protein tyrosine kinase (LCK) phosphorylates the TCR and initiates signaling. Absence of CD8 alters LCK availability and results in weak signaling regardless of docking polarity.

Normal CD8-LCK interaction



Disrupted CD8-LCK interaction



The major finding of this study is that it provides an explanation for productive versus unproductive TCR-pMHCI interactions by the engagement of CD8-LCK. Overall, CD8-LCK not only increases TCR sensitivity and skews the T cell repertoire toward pMHCI/II recognition (8) but also restricts the orientation of productive TCR-pMHCI docking (11). Two productive TCR-pMHCI interactions with reversed docking orientation have been described in humans (12), suggesting that the mechanism proposed by Zareie *et al.* might not apply to CD4 co-receptor-mediated signaling. However, too few TCR-pMHCI/II pairs with reversed docking polarity have been characterized so far to make any general conclusions.

A previous study characterized three productive and one unproductive human

TCR-pMHCI interaction with conventional docking geometries (13). The most pronounced difference was that only the productive TCR-pMHCI pairs formed catch bonds, which are stabilized by mechanical force. Catch-bond formation also predicted signaling in two pMHCI-restricted TCRs (13). Recruited CD8-LCK stabilizes the TCR-pMHCI interaction, which enables suboptimal antigens to form catch bonds (14). Zareie *et al.* observed that canonical productive TCR-pMHCI interactions formed catch bonds, whereas unproductive interactions with reversed docking polarity did not. Although TCRs with canonical and reversed docking polarity exhibited comparable time of antigen binding at 10-pN force, their differential ability to form catch bonds could be important. The catch bond might not just prolong antigen engagement but might also trigger conformational changes that promote TCR activation (15). However, Zareie *et al.* observed that the exclusion of CD8 resulted in comparable responses of the canonical and reversed docking polarity TCRs without affecting their differential ability to form catch bonds.

The connections between the roles of co-receptors and LCK in initiating TCR signaling, promoting catch-bond formation, and constraining the productive TCR-pMHCI/II orientation are key emerging questions. Although there is no clear physiological role for unproductive TCR binding, such interactions are informative about TCR signaling itself. Understanding of mechanistic details of TCR activation are instrumental for rationalizing the design of antigenic receptors for immunotherapy. ■

REFERENCES AND NOTES

1. P. Zareie *et al.*, *Science* **372**, abe9124 (2021).
2. K. C. Garcia, *Trends Immunol.* **33**, 429 (2012).
3. B. D. McDonald, J. J. Bunker, S. A. Erickson, M. Oh-Hora, A. Bendale, *Immunity* **43**, 859 (2015).
4. S. H. Krovit, J. W. Kappler, P. Marrack, L. Gapin, *Proc. Natl. Acad. Sci. U.S.A.* **116**, 22252 (2019).
5. B. Erman *et al.*, *J. Immunol.* **177**, 6613 (2006).
6. O. Stepanek *et al.*, *Cell* **159**, 333 (2014).
7. A. Drobek *et al.*, *EMBO J.* **37**, 98518 (2018).
8. F. Van Laethem *et al.*, *Cell* **154**, 1326 (2013).
9. J. Rossjohn *et al.*, *Annu. Rev. Immunol.* **33**, 169 (2015).
10. J. J. Adams *et al.*, *Immunity* **35**, 681 (2011).
11. S. Gras *et al.*, *Immunity* **45**, 749 (2016).
12. D. X. Beringer *et al.*, *Nat. Immunol.* **16**, 1153 (2015).
13. L. V. Sibener *et al.*, *Cell* **174**, 672 (2018).
14. J. Hong *et al.*, *Nat. Immunol.* **19**, 1379 (2018).
15. C. Zhu, W. Chen, J. Lou, W. Rittase, K. Li, *Nat. Immunol.* **20**, 1269 (2019).

10.1126/science.abj2937

SYNTHETIC BIOLOGY

Rewriting the genetic code

Making room in the genetic code allows the creation of designer proteins with new building blocks

By **Delilah Jewel** and **Abhishek Chatterjee**

The near-universally conserved genetic code governs the messenger RNA (mRNA)-templated synthesis of proteins in all domains of life, using just 20 amino acid building blocks.

Progress has been made toward artificially expanding the genetic code to enable cotranslational, site-specific incorporation of noncanonical amino acids (ncAAs) into proteins in living cells. (1, 2). Hundreds of different ncAAs have been genetically encoded in various domains of life, enabling powerful new ways to probe and manipulate protein functions. However, this approach has been largely restricted to the incorporation of a single ncAA into a polypeptide. On page 1057 of this issue, Robertson *et al.* (3) report site-specific incorporation of multiple distinct ncAAs into proteins with impressive efficiency and versatility, using liberated sense codons. The ability to generate designer proteins using multiple non-natural building blocks will unlock countless applications, from the development of new classes of biotherapeutics to biomaterials with innovative properties.

Incorporating ncAAs into proteins in living cells involves the use of an engineered transfer RNA (tRNA)-aminoacyl-tRNA synthetase (aaRS) pair, which does not cross-react with its counterparts from the host cell and delivers the desired ncAA in response to a distinct codon—most frequently a reassigned nonsense (stop) codon. The inflexibility of the canonical genetic code, wherein the meaning of the 64 triplet codons is defined, has impeded advances toward simultaneous and unrestricted incorporation of multiple different ncAAs. Only the three nonsense codons are available for reassignment, which inherently limits how

many distinct ncAAs may be simultaneously used. Moreover, the natural function of stop codons—the release factor-mediated termination of translation—competes with ncAA incorporation, compromising the decoding efficiency. Even though it has been possible to site-specifically incorporate up to three different ncAAs by simultaneously reassigning all three stop codons, the low efficiency restricts the incorporation of each ncAA to a single site per polypeptide (4).

Four-base “frameshift” codons have been explored as an alternative to nonsense codons for ncAA incorporation (5). However, competing recognition of the first three bases of such four-base codons, and inefficient processing at the ribosome relative to triplet codons, reduce their decoding efficiency. The recent development of a heritable unnatural base pair, which does not cross-pair with their natural counterparts and can be processed by endogenous tran-

scription and translation machinery, has provided access to fundamentally new triplet codons that can be assigned to ncAAs (6). But, it is unclear whether the current version of this technology is suitable for simultaneous incorporation of multiple ncAAs in an unrestricted number of sites.

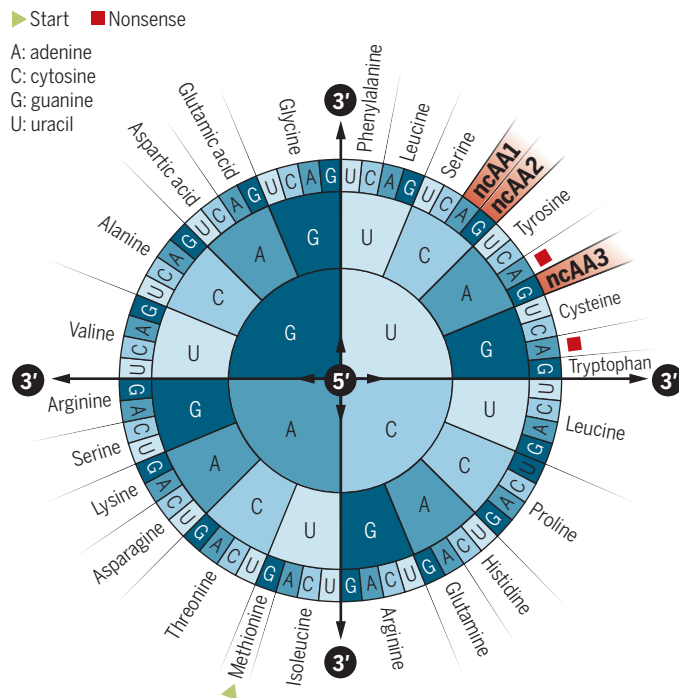
There is a high degree of redundancy within the canonical genetic code. For example, three codons are assigned to translation termination, whereas six codons are assigned to each of the amino acids serine, leucine, and arginine. Reconfiguring the genetic code to partially reduce this redundancy provides an attractive avenue to liberate some of the triplet codons for ncAAs. However, doing so demands global genome engineering to remove all instances of the chosen triplet codon(s), as well as the mechanism of their recognition—a truly daunting task. This was first demonstrated in *Escherichia coli*, in which all UAG nonsense codons were replaced with UAA, using an iterative recombination-mediated site-directed mutagenesis strategy (7). Subsequent deletion of release factor 1 eliminated endogenous recognition of UAG, which significantly enhanced the efficiency of ncAA incorporation at this codon. (8, 9). This work demonstrated the advantage of assigning ncAAs to natural triplet codons

that are truly “blank.” However, extending this approach to liberate sense codons, which are present in far greater numbers relative to UAG, has proved challenging (10).

To overcome this limitation, Fredens *et al.* developed an elegant approach for efficient global engineering of the *E. coli* genome, called REXER (replicon excision for enhanced genome engineering through programmed recombination) (11). This involves precise excision of large segments of the genome using CRISPR-Cas9, followed by their efficient substitution with synthetic counterparts using recombination. With this approach, the authors engineered *E. coli* strain Syn61, in which all instances of serine codons UCG and UCA, and the stop codon UAG, were substituted by their synonyms AGC, AGU, and UAA, respectively. This tour-de-force genome engineering effort, involving >18,000 codon changes, transforms UCG, UCA, and UAG to blank codons, once the corresponding cognate tRNAs, *serT* and *serU*, and release fac-

Encoding designer proteins

The genetic code of *Escherichia coli* was engineered to abolish the use of two sense codons (UCA and UCG) and a nonsense codon (UAG). This freed these codons up for incorporating up to three different noncanonical amino acids (ncAAs) at the same time when these codons appear in messenger RNA.



Department of Chemistry, Boston College,
Chestnut Hill, MA 02467, USA.
Email: abhishek.chatterjee@bc.edu

tor 1 are removed from the genome to create the strain Syn61.Δ3.

Robertson *et al.* used the Syn61.Δ3 strain to demonstrate the advantage of assigning ncAAs to sense codons, enabling multisite ncAA incorporation with improved efficiency and versatility (see the figure). Syn61.Δ3 was evolved to create Syn61.Δ3(ev5), a mutant strain with significantly improved growth kinetics. This strain was resistant to a cocktail of different bacteriophages (viruses that infect bacteria) because of its inability to process UCG, UCA, and UAG. The authors then used archaea-derived tyrosyl and pyrrolysyl pairs—developed previously for expanding the genetic code of *E. coli*—to incorporate ncAAs in response to the liberated sense codons. This enabled efficient incorporation of two distinct ncAAs at up to three different sites each and the simultaneous incorporation of three distinct ncAAs in response to UCG, UCA, and UAG. It has long been hypothesized that liberating a subset of sense codons for reassignment could improve the robustness and versatility of genetic-code expansion technology. This work elegantly transforms that dream into a reality and renders validity to these hypotheses.

Collectively, the development and application of the Syn61.Δ3 strain provides a blueprint for further compression of the genetic code and liberation of additional sense codons. Coupled with the development of mutually orthogonal tRNA-aaRS pairs to efficiently reassign these codons, such efforts will make it possible to incorporate many distinct ncAAs into proteins with unprecedented versatility and efficiency. This will enable countless applications, including the ribosomal synthesis of sequence-defined, genetically encoded non-natural biopolymers. The ability to generate and evolve such non-natural biopolymers with the same versatility as polypeptides could have broad implications for disciplines ranging from medicine to materials science. ■

REFERENCES AND NOTES

1. J. W. Chin, *Nature* **550**, 53 (2017).
2. D. D. Young, P. G. Schultz, *ACS Chem. Biol.* **13**, 854 (2018).
3. W. E. Robertson *et al.*, *Science* **372**, 1057 (2021).
4. J. S. Italia *et al.*, *J. Am. Chem. Soc.* **141**, 6204 (2019).
5. H. Neumann, K. Wang, L. Davis, M. Garcia-Alai, J. W. Chin, *Nature* **464**, 441 (2010).
6. Y. Zhang *et al.*, *Nature* **551**, 644 (2017).
7. M. J. Lajoie *et al.*, *Science* **342**, 357 (2013).
8. M. Amiram *et al.*, *Nat. Biotechnol.* **33**, 1272 (2015).
9. H. Zheng *et al.*, *Mol. Biosyst.* **12**, 1746 (2016).
10. N. Ostrov *et al.*, *Science* **353**, 819 (2016).
11. J. Fredens *et al.*, *Nature* **569**, 514 (2019).

ACKNOWLEDGMENTS

The authors are supported by the National Institute of General Medical Sciences (NIGMS, R35GM136437). A.C. is a senior advisor at BrickBio and owns equity therein.

10.1126/science.abi9892

CORONAVIRUS

Antibody sugars are bittersweet

Antibodies that lack specific sugar modifications can worsen acute viral diseases

By Ruklanthi de Alwis^{1,2} and Eng Eong Ooi^{1,2,3}

Antibodies constitute an integral arm of the adaptive immune system that, in its fight against viruses, can occasionally perform as a double-edged sword. Antibodies are Y-shaped molecules. Historically, research on humoral responses to viral infection have mostly focused on the V end of the Y: the antigen-binding regions, or Fab, which bind and neutralize viral infections. Conversely, the tail of the Y (also called the fragment crystallizable, or Fc, domain) possesses numerous functional properties—namely induction of antibody-dependent complement deposition, cellular phagocytosis and cellular cytotoxicity (1)—but is relatively understudied. On page 1102 of this issue, Bournazos *et al.* (2) and another recent study by Larsen *et al.* (3) demonstrate that modifying the Fc domain with chains of sugar molecules (glycosylation) can trigger cellular immune functions that can either protect against or worsen viral diseases, such as dengue and COVID-19.

Antibodies are produced by B cells, and the most abundant form in humans is immunoglobulin G (IgG). IgG is produced in the endoplasmic reticulum (ER) of B cells and then transported through the Golgi network for secretion. The ER is also where chains of sugar molecules—composed of *N*-acetylglucosamine, mannose, and glucose—are produced in a stepwise manner (see the figure). This sugar chain is then transferred to the Fc domain of IgG molecules and covalently attached to Asp²⁹⁷ (4). The sugar chain is then further modified with the addition of new sugar molecules, such as fucose, and trimmed as the antibodies pass through the Golgi network. The order of addition and trimming of sugar mole-

cules on the glycan chain is highly organized and determined by Golgi-resident enzymes, leading to a total of 36 possible N-linked glycan structures (5).

The N-linked glycosylation of IgG enables proper protein folding and influences the interaction with Fcγ-receptors (FcγRs) on immune cells to shape the specificity of the cellular response. IgG interacts with a total of three types and six subtypes of FcγR. The specificity and strength of this interaction is governed by variability in the sugar chain on the Fc domain. This in turn influences the type and strength of the antiviral killing mechanism triggered by IgG (6). One such variability is the absence of fucose on the gly-

can. More than 90% of serum IgG is fucosylated and has low affinity to FcγRs. However, afucosylation increases the binding affinity of IgG to FcγRIIIa and activates macrophages and natural killer cells (7). Although beneficial for immune-mediated killing of cancer cells, such afucosylated IgGs appear to trigger excessive immune-mediated damage to patients with dengue and COVID-19 (1, 2, 3, 8).

Severe dengue and COVID-19 share a common pathology: excessive inflammation. Inflammation is a part of the immune response to harmful stimuli, such as viral infections. Sensors in cells detect such stimuli and trigger a cascade of signaling events that result in increased blood flow and recruitment of immune cells to the site to contain the harmful stimuli. However, when unchecked, inflammation can result in damage to cells and organs, including the integrity of small blood vessels and lung function, which are the pathological hallmarks of severe dengue and COVID-19, respectively (9, 10).

The findings of Bournazos *et al.* and Larsen *et al.* converged on a possible cause of such excessive inflammation. The investigators found high amounts of virus-specific afucosylated IgGs (specifically of the IgG1 subclass) in the blood of patients with severe dengue or COVID-19. Amounts of these IgGs were also significantly higher in patients with severe disease compared with

**“...afucosylated
antiviral IgG1
[immunoglobulin G1]
may be the trigger
of the excessive
inflammation observed
in severe dengue and
COVID-19 patients...”**

¹Program in Emerging Infectious Diseases, Duke-NUS Medical School, Singapore. ²Viral Research and Experimental Medicine Center, SingHealth Duke-NUS Academic Medical Center, Singapore. ³Saw Swee Hock School of Public Health, National University of Singapore, Singapore. Email: engeong.ooi@duke-nus.edu.sg

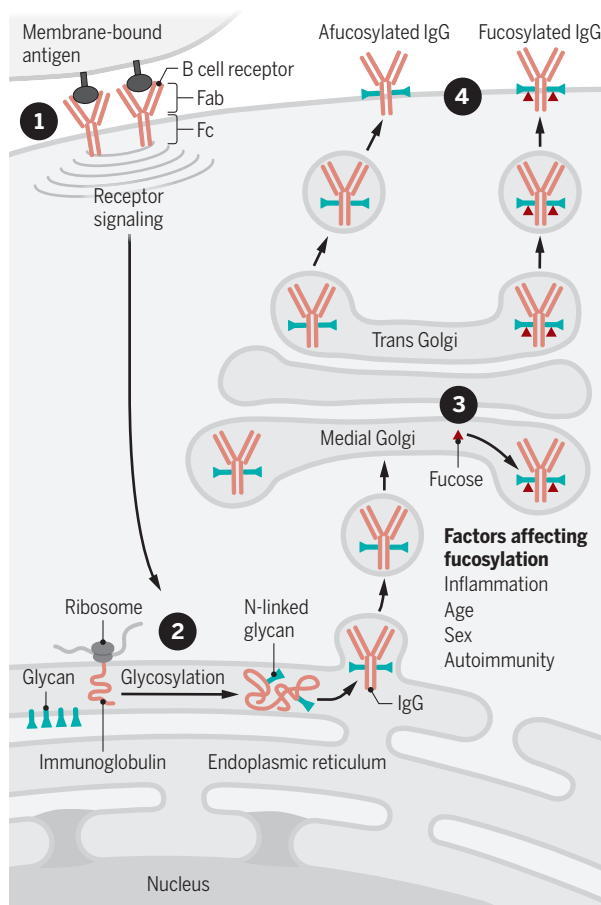
milder disease. Increased amounts of afucosylated IgG1 against dengue virus and severe acute respiratory syndrome coronavirus 2 (SARS-CoV-2) in turn correlated with increased inflammation, as indicated by the expression of proinflammatory cytokines such as interleukin-6 (IL-6) and tumor necrosis factor- α (TNF- α). These afucosylated IgGs were detected in the blood before severe disease manifested, highlighting a possible causal relationship. Collectively, these observations suggest that afucosylated antiviral IgG1 may be the trigger of the excessive inflammation observed in severe dengue and COVID-19 patients and could even potentially serve as a prognostic factor.

Bournazos *et al.* also extend our understanding of antibody-dependent enhancement of dengue virus infection. As of now, there are four known different, but genetically related, dengue viruses (serotypes). Primary infection with one produces not only IgGs that neutralize the infecting serotype but also non-neutralizing IgGs that can bind any of the remaining three dengue serotypes and potentially enhance infection of host cells through Fc γ R-mediated entry. Bournazos *et al.* demonstrate that higher amounts of afucosylated antidengue IgG that develop after primary infection add to antibody-enhanced infection by increasing the susceptibility to severe inflammation and ultimately disease during a subsequent secondary dengue infection. However, the amount of afucosylated IgG is unlikely to be the sole explanation for severe dengue pathogenesis. Others have shown that antibody-enhanced infection is optimal when a particular ratio of virus to antibody is reached (11). Thus, not everyone with secondary dengue infection is at risk of severe dengue. Moreover, differences in host and viral genetics may also shape the development of severe dengue (9).

Fc-mediated antibody functions promoted by afucosylated antibodies are also important for pathogen and infected-cell clearance. For example, afucosylated antibodies have been found to play a protective role (primarily by enabling viral clearance through antibody-dependent cellular cytotoxicity) in individuals who are able to control HIV or latent tuberculosis infections (6, 12). Furthermore, afucosylated monoclonal antibodies against Ebola were found to be protective through multiple Fc-mediated mechanisms and have

N-linked glycosylation of antibodies

1 Membrane-bound antigen of dengue virus or severe acute respiratory syndrome coronavirus 2 (SARS-CoV-2) is recognized by B cell receptors and other coreceptors, which initiates antibody production. **2** Immunoglobulin (Ig) peptides are translated and folded into antibodies at the endoplasmic reticulum membrane, and glycans are attached to Asp²⁹⁷. **3** In the Golgi network, enzymes modify the N-linked glycan, which includes adding fucose, depending on various factors. **4** Either fucosylated or afucosylated IgG is embedded in the plasma membrane or secreted.



high therapeutic value (13). Indeed, Larsen *et al.* observed that several highly efficacious live-attenuated viral vaccines also elicited afucosylated antibodies. However, the role of afucosylation in the context of vaccine responses is unclear and requires better characterization.

Factors that determine the constituents of the glycan chain on the Fc domain of IgG, although not well characterized, are likely to be complex. Demographic factors, such as age and gender, and autoimmune diseases that affect the milieu of inflammatory cytokines during B cell development can affect N-linked Fc glycosylation (1). Larsen *et al.* also observed that only IgGs against viruses with a lipid envelope induced increased amounts of afucosylation. Hence, they hypothesized that afucosylated IgGs are more likely to develop when the immune target is displayed on fluid

lipid membranes because of the co-stimulation of an unidentified host receptor. This postulate is supported by similar findings that increased amounts of afucosylated antibodies against red blood cells and platelets develop after blood transfusion or in mothers who were pregnant with babies with different blood types. Both dengue virus and SARS-CoV-2 are covered by a viral protein-embedded lipid membrane.

The studies of Larsen *et al.* and Bournazos *et al.* raise the question of whether the different types of dengue or COVID-19 vaccines produce varying degrees of IgG fucosylation. Most licensed vaccines or phase 3 candidates for dengue are live-attenuated candidates. However, for SARS-CoV-2, the licensed mRNA and adenoviral-vectored vaccines induce expression of SARS-CoV-2 spike protein on host cell membranes, whereas subunit vaccines (for example, NVX-CoV2373) are soluble antigen proteins. These factors could collectively result in vaccination-induced anti-spike IgGs with varying amounts of Fc N-linked glycosylation and hence influence their potential protective efficacy or inflammation potentiation upon natural infection. This question could be particularly urgent because the possibility of immune enhancement of breakthrough infections in vaccinated people [which has been observed for dengue virus in humans and for related coronaviruses SARS-CoV and Middle East respiratory syndrome coronavirus (MERS-CoV) in animal models (14)] remains to be addressed for COVID-19. ■

REFERENCES AND NOTES

1. M. F. Jennewein, G. Alter, *Trends Immunol.* **38**, 358 (2017).
2. S. Bournazos *et al.*, *Science* **372**, 1102 (2021).
3. M. D. Larsen *et al.*, *Science* **371**, eabc8378 (2021).
4. A. Varki *et al.*, Eds., *Essentials of Glycobiology* (Cold Spring Harbor Laboratory Press, ed. 3, 2015).
5. E. B. Irvine, G. Alter, *Glycobiology* **30**, 241 (2020).
6. M. E. Katzelnick *et al.*, *J. Clin. Invest.* **123**, 2183 (2013).
7. T. Li *et al.*, *Proc. Natl. Acad. Sci. U.S.A.* **114**, 3485 (2017).
8. T. T. Wang *et al.*, *Science* **355**, 395 (2017).
9. C. P. Simmons, J. J. Farrar, V. Nguyen, B. Wills, *N. Engl. J. Med.* **366**, 1423 (2012).
10. W. J. Guan *et al.*, *N. Engl. J. Med.* **382**, 1708 (2020).
11. L. C. Katzelnick *et al.*, *Science* **358**, 929 (2017).
12. L. L. Lu *et al.*, *Cell* **167**, 433 (2016).
13. B. M. Gunn *et al.*, *Cell Host Microbe* **24**, 221 (2018).
14. R. de Alwis, S. Chen, E. S. Gan, E. E. Ooi, *EBioMedicine* **55**, 102768 (2020).

ACKNOWLEDGMENTS

R.d.A. is funded by the Young Investigator Award from the National Medical Research Council (NMRC) Singapore. E.E.O. is funded by the Clinician-Scientist Award from the NMRC.

10.1126/science.abj0435

Uncertain effects of the pandemic on respiratory viruses

Expanded genomic and clinical surveillance are needed to understand the spread of respiratory viruses

By **Gabriela B. Gomez**^{1,2}, **Cedric Mahé**^{1,3},
Sandra S. Chaves^{1,3}

The emergence and spread of severe acute respiratory syndrome coronavirus 2 (SARS-CoV-2) and subsequent mitigation measures have caused widespread social disruption. These disruptions have also affected community transmission of endemic diseases and the seasonal circulation patterns of other respiratory viruses. In both the Northern and Southern hemispheres, within-season influenza activity has been at historically low levels since 2020 (1, 2). Additionally, the circulation of human metapneumovirus, enterovirus, adenovirus, respiratory syncytial virus (RSV), and rhinovirus has been substantially reduced (3). These reductions in respiratory virus infections are linked to changes in health care-seeking behaviors and limited surveillance capacity, but mostly to the widespread implementation of non-pharmacological interventions (NPIs) to control SARS-CoV-2 transmission. How this will affect the transmission patterns of endemic respiratory viruses remains unknown.

NPIs such as face mask use, increased handwashing practices, social distancing, and restrictions of global mobility have been key measures in reducing circulation of other respiratory viruses. As NPIs are relaxed and vaccination programs increase to control SARS-CoV-2 infections, countries have started to report increases in activity and circulation of certain viruses, such as RSV and rhinoviruses, with atypical timing (3–6). It is unclear why similar trends of resurgence (off-seasonal increases) have not been observed so far in other respiratory viruses, such as influenza, following relaxation of NPI measures. Currently, questions remain as to what the downstream impact of the COVID-19 pandemic and our response to it will be on circulation patterns of endemic respiratory viruses.

What can be expected once this pandemic subsides and NPIs are lifted? If there is a reduction of population-level immunity, endemic respiratory viruses could resurge with atypical patterns and/or with high attack rates (higher risk of infection during a specific time period) owing to the large susceptible population. Current disruption in respiratory virus circulation could also lead to changes in their epidemiology—for example, changes in age distribution or disease severity. Moreover, it is unclear how many years it would take to reestablish regular seasonal patterns and whether new pandemic threats can be expected, especially considering the unpredictability of influenza virus evolution and the role of animal reservoirs (see the figure).

Modeling studies have started to explore the impact of an increase in population susceptibility due to minimal RSV and influenza virus infections in 2020–2021 on the magnitude of subsequent seasons (7). RSV is a common respiratory virus that often circulates during cold months in temperate countries, causing mostly mild disease in the general population but with a risk for severe disease in infants and the elderly. Contrary to influenza viruses, RSV has no known animal reservoir. Two main antigenic groups (A and B) present variability that may contribute to the ability of RSV to establish reinfections throughout a life span. Data from surveillance systems have recently identified off-season circulation of RSV in both Northern and Southern hemispheres, albeit of lower magnitude than in previously documented RSV seasons and despite some NPIs still in use. This increased circulation could have been driven by an increased susceptibility in the very young and waning of immunity among adults (5). Periodic circulation of RSV, even if limited, may minimize the pool of susceptible population in the long term and prevent large outbreaks in the future (6).

For influenza viruses, the overall modeling conclusions are less robust than for RSV (7). The rapid evolution and the dynamics of host immunity associated with influenza virus infections add further uncertainty and complexity to the modeling forecast. Although initial modeling analyses (7) help

illustrate broad scenarios of the possible impact of the COVID-19 pandemic on endemic respiratory diseases, they also highlight the gaps in data and knowledge on viral interference theories (which explain how an individual infected by a virus becomes resistant to infection by a second virus), environmental and temperature effects on virus seasonality, and the role of immunity in transmission at the population level.

Theoretically, in the case of influenza virus, limited community transmission, as documented in the last seasons, could present less opportunity for viral mutations (8) through antigenic drift (a process of gradual accumulation of mutations in the surface glycoproteins, or antigens, of the influenza virus). Overall, the lack of new mutation opportunities could limit the variability of circulating influenza viruses (9, 10). In turn, those viruses accumulating mutations could face limited antigenic selection due to a lower immunological pressure because there is a reduction in population-wide immunity, despite the increased influenza vaccination coverage observed in 2020 in various countries (11).

The pool of susceptible individuals could also change qualitatively, with children becoming especially vulnerable during future influenza epidemics if the rest of the population maintains cross-protection from infection with previous seasonal strains. The implication of this scenario is the possibility of future (larger) influenza seasonal outbreaks affecting clinically different subpopulations. Nonetheless, if more homogeneous populations of viruses are observed, disease could be controlled through well-matched vaccines. Conversely, reduced population-wide immunity could allow for the emergence of variant strains with pandemic potential, including those possibly introduced from other species. This is observed, for example, with H3N2v viruses, which are often detected during summertime in the US from exposure to swine in agricultural fairs (12). These variant strains mostly affect children because population immunity from other H3N2 circulating viruses may be controlling their spread among the adult population (13). Further research into the underlying mechanisms determining the epidemiological features of specific respiratory viruses that considers viral evolution, interactions among viruses, and between virus and host immunity is needed. This will help identify emerging pandemic threats as well as better prepare for the long-term management of future outbreaks and epidemics.

The evolution of SARS-CoV-2 and the appearance of variants threatening the effectiveness of newly authorized vaccines have underlined the importance and limitations of genomic surveillance networks globally.

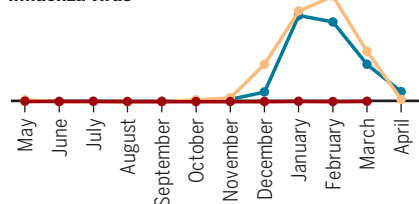
¹Department of Modelling, Epidemiology and Data Science, Sanofi Pasteur, Lyon, France. ²Department of Global Health and Development, London School of Hygiene and Tropical Medicine, London, UK. ³Foundation for Influenza Epidemiology, Fondation de France, Paris, France.
Email: gabriela.gomez@sanofi.com

Patterns of respiratory virus infections

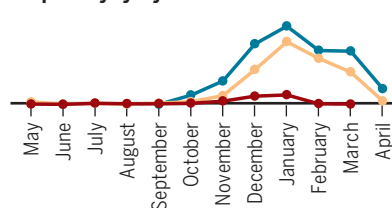
During the pandemic, circulation patterns of respiratory viruses other than severe acute respiratory syndrome coronavirus 2 (SARS-CoV-2) have been disrupted. This could mean a future shift in the epidemiology of respiratory diseases, potential for new epidemic threats, or larger outbreaks than previously observed. It is also unknown how long it will take for seasonal circulation patterns to return to prepandemic levels. Graphs illustrate trends in detection of respiratory viruses. Data are from respiratory illness surveillance in participating sites of the Global Influenza Hospital Surveillance Network (14).

— 2018–2019 — 2019–2020 — 2020–2021

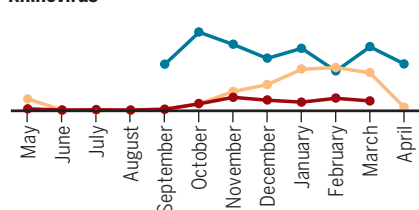
Influenza virus



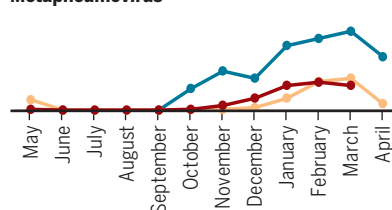
Respiratory syncytial virus



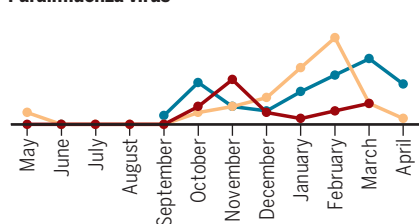
Rhinovirus



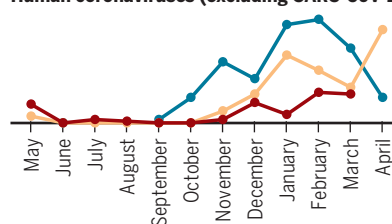
Metapneumovirus



Parainfluenza virus



Human coronaviruses (excluding SARS-CoV-2)



The uncertainty in future scenarios for other respiratory viruses in the post-COVID-19 period, including possible surges off-season and changes in clinical burden distribution, raises the need for an improved and comprehensive approach to respiratory disease and viral genomic surveillance. Widespread virus genomic surveillance embedded as part of national disease surveillance efforts and with links to clinical and epidemiological data could not only help monitor evolution but also identify those changes in strains associated with increased disease severity or vaccine breakthrough. It could improve current and new vaccine targets by refining vaccine strain selection against COVID-19 and influenza.

The COVID-19 pandemic has exposed the extent to which countries are still ill-prepared to monitor the emergence of new viruses, to assess their potential public health risk and the effectiveness of public health responses. The World Health Organization's Global Influenza Surveillance and Response

System (GISRS) network, though providing much needed surveillance coverage, has limited linkages to clinical data, and global hospital-based surveillance networks once heavily supported by the US Centers for Disease Control and Prevention have suffered from disinvestments in recent years. Ensuring effective and real-time data sharing, expanding geographical coverage, and integrating genomic data of identified viruses with clinical data will require dedicated financing mechanisms and a stronger scientific collaboration between diagnostic and pharmaceutical companies, public health authorities, and academic institutions.

The Global Influenza Hospital Surveillance Network (GIHSN) has provided a proof of concept for the expansion of current systems (14). This public-private partnership initiative was built 8 years ago to improve surveillance of influenza viruses and covers more than 100 hospitals across over 20 countries. Centers are asked to identify episodes of severe acute respiratory illness among hospital-

ized patients, testing primarily for influenza virus but covering other selected respiratory viruses, such as SARS-CoV-2, as resources allow. The network then ensures that virus whole-genome sequencing data are linked to epidemiologic and clinical data. The genomic sequences are uploaded into GISAID, a global data-sharing platform that has become the largest database of SARS-CoV-2 genomic data (15). These initiatives aim to provide flexibility to collaborating stakeholders, creating a solid infrastructure for expanded respiratory disease surveillance.

The vision of a global surveillance network for respiratory viruses, bringing together key players (multilateral and bilateral organizations, local governments, foundations, civil society, academia, and industry) with a common mission and roadmap, could ground an efficient global pandemic preparedness framework. Public and private resources could empower initiatives such as GISRS or the Coalition for Epidemic Preparedness Innovations (CEPI) in supporting governments and academic centers to maintain a sustainable surveillance and research platform to respond to public health agendas and promote preparedness. Currently, the emergency response to COVID-19 is a global priority, but preparation for future threats by building on existent global networks, fostering synergies, and expanding collaborations among a more inclusive stakeholder population should not be overlooked. ■

REFERENCES AND NOTES

1. World Health Organization, Influenza surveillance and monitoring: Updates (WHO, 2020); www.who.int/influenza/surveillance_monitoring/updates/latest_update_GIP_surveillance/en.
2. S. J. Olsen et al., *MMWR Morb. Mortal. Wkly. Rep.* **69**, 1305 (2020).
3. Q. S. Huang et al., *Nat. Commun.* **12**, 1001 (2021).
4. S. Poole, N. J. Brendish, A. R. Tanner, T. W. Clark, *Lancet Respir. Med.* **8**, e92 (2020).
5. P. N. Britton et al., *Lancet Child Adolesc. Health* **4**, e42 (2020).
6. J.-S. Casalegno et al., *medRxiv* 10.1101/2021.03.12.21253446 (2021).
7. R. E. Baker et al., *Proc. Natl. Acad. Sci. U.S.A.* **117**, 30547 (2020).
8. T. Bedford et al., *Nature* **523**, 217 (2015).
9. V. N. Petrova, C. A. Russell, *Nat. Rev. Microbiol.* **16**, 47 (2018).
10. N. M. Ferguson, A. P. Galvani, R. M. Bush, *Nature* **422**, 428 (2003).
11. Public Health England, Official Statistics: Seasonal flu vaccine uptake in GP patients: monthly data, 2020 to 2021 (2020); www.gov.uk/government/statistics/seasonal-flu-vaccine-uptake-in-gp-patients-monthly-data-2020-to-2021.
12. M. I. Nelson et al., *J. Virol.* **90**, 10963 (2016).
13. F. Liu et al., *J. Infect. Dis.* **216** (suppl_4), S539 (2017).
14. Global Influenza Hospital Surveillance Network (GIHSN), www.gihsn.org/.
15. GISAID Initiative, www.gisaid.org/about-us/mission/.

ACKNOWLEDGMENTS

All authors are Sanofi Pasteur employees and may hold shares in the company. S.S.C. and C.M. dedicate part of their time to the Foundation for Influenza Epidemiology, a public-private partnership initiative to scale up multidisciplinary surveillance of respiratory viruses.

10.1126/science.abh3986

AGRICULTURE AND DEVELOPMENT

Agricultural productivity must improve in sub-Saharan Africa

The region must pivot from area expansion to increasing crop yields on existing farmland

By **Thomas S. Jayne¹** and **Pedro A. Sanchez²**

In the first two decades of the 21st century, sub-Saharan Africa (SSA) has changed rapidly for the better in many ways, counter to many outdated narratives. Many of these improvements—including those in gross domestic product (GDP) per capita, poverty rates, health, life expectancy, education, and agriculture—have been mutually reinforcing (1, 2). SSA achieved the highest rate of growth in agricultural production value (crops and livestock) of any region in the world since 2000, expanding by 4.3% per year in real [inflation-adjusted US dollars (USD)] between 2000 and 2018, roughly double that of the prior three decades. The world average over the same period was 2.7% per year (1). Agricultural value added per worker in real 2010 USD rose from \$846 in 2000 to \$1563 in 2019, a 3.2% annual rate of growth. But to assert that Africa is rapidly developing does not mean that all livelihood indicators are improving, though most are in most countries (1, 3). SSA faces many major challenges. We focus below on one such challenge, which we see as a precondition for sustaining livelihood improvements in the region: transitioning from area expansion to productivity growth as the source of Africa's agricultural development.

GROWTH, EXTENSIFICATION, INTENSIFICATION

Most African countries show a strong correlation between agricultural growth and GDP. Even for the region as a whole, the degree of correlation is notable (see the figure, top), confirming the reinforcing synergies between agriculture and African economies. When agriculture grows, its extensive linkages with off-farm stages of the agrifood system and nonfarm sec-

tors expand employment and livelihoods in the rest of the economy (2, 4). Rapid agricultural growth since 2000 encouraged new private investment and employment in agricultural value chains and nonfarm sectors of African economies, pulling labor from farming into off-farm jobs that provide considerably higher returns to labor than semisubsistence farming (5). More than 40% of SSA's labor force, mainly young people, is now engaged in off-farm jobs (2, 5). The bottom line is that high farm production growth in SSA has contributed to high overall economic growth and improvements in the welfare of most Africans (2, 4).

Notwithstanding the region's impressive agricultural growth since 2000, roughly 75% of its crop production growth came from the expansion of area under cultivation and only 25% from improvements in crop yield (metric tons per harvested hectare) (see the figure, middle). Cereal yields in SSA rose by 38% in the 38 years between 1980 and 2018, roughly half that of South Asia and Southeast Asia (3). There remains great unmet potential for crop yield improvement—or, more appropriately, increases over time in the ratio of agricultural output to inputs, hereafter “productivity.”

WHY IS INTENSIFICATION NECESSARY?

Pivoting from area expansion to sustained productivity growth on existing farmland is becoming increasingly urgent for several reasons.

Mounting land pressures

Most smallholder households' farm sizes have been gradually shrinking for decades because of rural population growth and limited potential for continued area expansion in relatively densely populated areas where most rural Africans live. At the continental level, estimates show that 52% of the world's remaining arable land is in SSA (6). Yet, most of this land is concentrated in just eight countries, whereas many of the region's remaining 41 countries contain large rural populations clustered in notably small

areas (6). Of SSA's arable rural lands that receive more than 400 mm average rainfall per year, 20% contains 74% of its rural people (6). Many young rural Africans today cannot obtain additional land through inheritance or customary land institutions as they used to. Hence, even though most of SSA might be considered “land abundant,” a relatively large proportion of rural Africans face land scarcity. Land prices in the region are also rising rapidly, even in areas once considered remote (2). For these reasons, improving livelihoods for African farmers increasingly depends on raising the productivity of existing farmland.

Environmental costs of area expansion

Continued reliance on area expansion as the main source of agricultural growth is not a viable option on environmental grounds, including biodiversity conservation and destruction of natural vegetation. The goals of feeding Africa's growing population and conserving the planet's natural resources, diverse ecosystems, and the services they provide will be more effectively achieved through productivity improvements on existing farmland instead of area expansion (7, 8).

DOING THINGS DIFFERENTLY

Achieving higher rates of agricultural productivity growth will require technical innovation, that is, doing things differently and doing existing things more efficiently. Greater and more efficient use of improved seed, mineral fertilizers, and organic inputs are widely recognized as preconditions for achieving productivity growth on African farms (4, 7–9).

Plant breeders tended to test their improved materials in Africa using state-of-the-art agronomic practices, including mineral fertilizers. These tests produced greater yields than could be obtained on most smallholder fields in SSA, which tended to have nutrient-depleted soils. Farmers generally did not return the nutrients removed by crop harvests as fertilizers and manures, creating a vicious cycle of soil fertility depletion that prevented the yield potential of improved varieties when used in most farmer fields. This contrasts with what happened during the Green Revolution in Asia where farmers found that the improved varieties doubled or tripled yields when nitrogen fertilizers were added (9). Soil fertility replenishment in SSA was finally recognized as the key entry point for increasing crop yields in Africa in the late 1990s. In 2006, farmers in SSA used 8 kg of mineral fertilizers per hectare, whereas Asian farmers used 15 times more (3). Though fertilizer use per hectare in SSA has since doubled to

¹Department of Agricultural, Food, and Resource Economics, Michigan State University, East Lansing, MI, USA. ²Soil and Water Sciences Department, Food Systems Institute, University of Florida, Gainesville, FL, USA. Email: jayne@msu.edu; pedrosanchez@ufl.edu

17.9 kg per hectare in 2018 (3), this is still far short of what is needed to compensate for the harvested nutrients (8, 9).

Raising fertilizer use efficiency

There is growing recognition that many African farmers obtain widely varying and generally low crop response to the fertilizers that are applied (8, 10). The agronomic efficiency of nitrogen (AEN) (i.e., the additional kilograms of crop output per kilogram of nitrogen nutrient applied to the field) in Africa averages 14.2 (8), with considerable variability across seed and soil type, rainfall, and management. With appropriate mineral fertilizers, organic inputs, fertilizer-responsive seeds, and improved soil management, crop response to fertilizers can be doubled or tripled, reaching the global average AEN of 37 (8). Raising crop response to mineral fertilizer is one of the most important steps toward achieving agricultural productivity growth in SSA because it will raise the profitability of using fertilizers, organic inputs, and fertilizer-responsive high-yielding seed varieties. This would in turn promote greater demand for these inputs and greater investment in the supply chains for all manner of agricultural inputs and support services, which in turn would support virtuous cycles of farm productivity improvements, greater competitiveness of African food and agricultural export crops, higher smallholder incomes, and increased private investment in agrifood systems. Policy environments conducive to private investment and competition in agrifood systems are also necessary to ensure that these virtuous cycles can materialize (2, 4).

Promoting the use of blending facilities

Most fertilizers used in SSA are imported. In the past decade, many small fertilizer blending facilities that can produce appropriate nutrient compositions for specific areas, based on recommendations from soil tests along with digital soil maps, have sprouted in the region. Some recommendations often include sulfur, a nutrient that is commonly deficient in large areas of SSA (8). Improved blending to suit specific soil needs has contributed to the doubling of fertilizer use in SSA over the past decade (8). Still, much greater intensity of fertilizer use is needed for SSA to achieve strong agricultural growth led by productivity gains on existing cropland (2, 4, 8).

Greater use of organic inputs

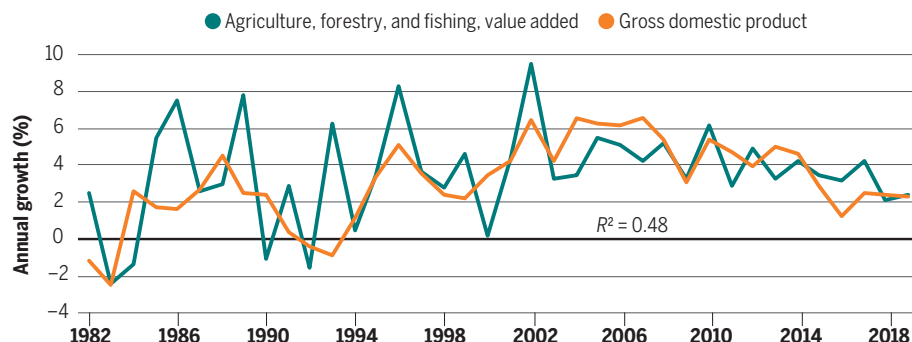
African smallholder farmers use little cattle manures, crop residues, and cover crops (planted to cover soil, rather than for harvesting), partly because such inputs are dif-

Crop yield must increase in sub-Saharan Africa (SSA)

Strong correlation between agricultural growth and economic growth

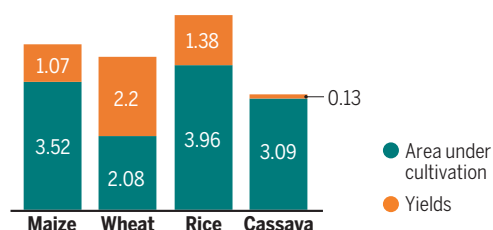
Data reflect averages across 46 countries in SSA (excluding high-income countries).

Data are from the World Bank's World Development Indicators (1).

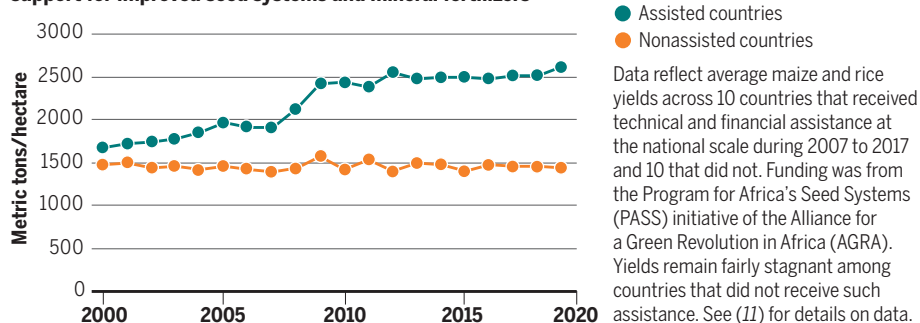


Agricultural growth relies mainly on cropland expansion, not productivity growth

Data reflect average annual percent increases across 49 countries in SSA between 2000 and 2018. Data are from the FAOSTAT West Africa, Middle Africa, East Africa, and Southern Africa country groups (3).



Cereal yields increased in countries that received international support for improved seed systems and mineral fertilizers



ficult to grow in fertility-depleted soils (9). Though cattle manures are used all over Africa as organic inputs, with those produced from dairy farms generally of high nutrient quality, most manures used by smallholder farmers often are of low nutrient quality, because cattle graze on low-quality grasses grown on nutrient-depleted soils and the manures are often mixed with soil (8). Crop residues such as cereal stover (leaves and stalks remaining after harvest) are mainly fed to cattle, but when cereal crop yields more than double, as commonly happens with mineral fertilizers and improved seeds (8), crop residues also increase. This provides an opportunity to satisfy feeding cattle while returning substantial quantities of crop residues containing 45% carbon to the soil. Because mineral fertilizers contain no carbon, organic inputs must be part of the equation to achieve soil health (8).

Increasing the use of improved, high-yielding seeds

There are now more than 100 African-owned seed companies that sell improved seeds that can attain high yields when fertilized. Regulatory reforms that remove barriers on seed trade and allow for greater private investment in seed development and distribution are, in many cases, needed to make improved seed more accessible to African farmers (4, 11). For example, early generation seed production (breeder seed and foundation seed) has been a frequent bottleneck in the production and supply of certified seed, delaying farmers' access to improved seed. Most African governments formerly held a monopoly on seed production, but now many have allowed private companies to begin producing it, including in Ghana, Mali, Nigeria, Ethiopia, and Uganda (11). Improving soil health without improved seeds is a nonstarter (4, 8).

There is also a need to expand the coverage of SSA countries benefiting from national and international seed research. Huge increases in maize and rice yields have occurred in 10 countries that received technical and financial assistance from international and national research and development institutions on seed systems and fertilizers, in contrast to 10 other African countries that received relatively little (17) (see the figure, bottom). Although this bivariate comparison does not control for other confounding factors, the two sets of countries had very similar yield levels at the beginning of the 2000s. Today, the countries benefiting from sustained support achieve 80% higher yields.

OVERDUE FOR IMPLEMENTATION

Investment in agricultural research and development has been consistently demonstrated to be one of the most effective ways to promote agricultural productivity growth (4, 12). Especially because SSA is highly vulnerable to climate change and is experiencing greater prevalence of extreme weather, plant diseases, and pests, greater investment in adaptive and site-specific agricultural research and development and extension (R&D&E) is a precondition for productivity-led agricultural growth in SSA.

Agricultural R&D&E is especially needed to respond to the growing challenges caused by climate change; leaching and runoff of nitrogen and phosphorus that result in eutrophication of water bodies; and detrimental effects on pollinators when soils, crops, livestock, fertilizers, manures, or pesticides are misused. Effective communications to farmers and the general public, such as Digital Green and Kenya's farm-focused "Shamba Shape Up" television program, can also raise public awareness of the societal benefits of agricultural R&D&E and hence bolster support for such expenditures.

Most African governments devote less than 10% of their agricultural expenditures to R&D and spend much less on agricultural R&D than governments in other regions (4). Most Asian governments spend at least four times more per farmer and per hectare cultivated than African governments (4). Cereal yields more than doubled over the past 40 years in South and Southeast Asia but rose by only 38% in Africa (3).

The Asian efforts focused first on the most obvious agricultural concern: low-yielding, tall-statured varieties of rice and wheat that, when fertilized, fell on the ground to rot. Although varieties overcoming this constraint have been bred in Africa, research institutions did not confront, until the past two decades, the first and most obvious agricultural limiting factor: the depletion of soil fertility in smallholder farmer fields (4). Now

that fertilizer and organic inputs are being addressed together with higher yielding varieties, the potential for sustained crop yield increases has become realistic (8).

These are not new ideas, but they are long overdue for implementation and sustained support. Most international development organizations and foundations dedicated to promoting agricultural development in Africa have shied away from addressing the issue of adaptive local agricultural R&D. Donors and policy-makers tend to prefer low-hanging fruit that offers quick wins that are highly visible, avoiding investments that require dedicated long-term support and have long gestation periods before impacts are felt (13). But if left unaddressed, the constraints posed by the slow pace of technical innovation on African farms will retard the achievement of almost all rural development goals, including those pertaining to reducing inequalities and improving the livelihoods of rural women and youth. Sooner or later, local agricultural R&D&E will need to be addressed head-on if the region is to pivot decisively to a productivity-led agricultural growth path.

The main ingredients are sustained strengthening of adaptive R&D&E to support farm technical innovation and adaptation, supportive agricultural marketing and trade policies—including implementation of the African Continental Free Trade Agreement—and infrastructural investments that reduce costs and risks in the food system, promote investment and competition in agricultural value chains, and enable farmers to adopt these technical innovations (2, 4, 12).

Bidirectional extension and learning

Although the importance of agricultural extension as a means for bidirectional learning between farmers and scientists is well known, these systems in Africa have suffered from chronic underfunding and variable management. Because agriculture in SSA spans a tremendous range of agroecological and economic conditions and resources and capacities of farmers, the benefits of strong agricultural science and technical innovation often cannot translate into farmer adoption and improved productivity unless the innovations can be tailored appropriately to farmers' specific conditions. Local adaptation of agricultural research to the diverse farming conditions of SSA will require bidirectional learning between farmers and agricultural scientists to identify how farmers can adapt improved management practices that fit within their resource constraints (14). Bidirectional learning is especially important when farming systems are changing, for example, because of climate change. Ethiopia is one of

the few African countries to substantially increase its spending on public agricultural research, which has more than tripled in real terms since 2000 (15). Ethiopia also has half of SSA's agricultural extension workers (4). Not surprisingly, Ethiopia has enjoyed the highest rate of agricultural growth of any country in SSA since 2000 (1, 3). Each additional \$1 of agricultural value-added in the Ethiopian economy generated an additional \$0.29 in nonfarm GDP and hence contributed powerfully to the country's rapid economic transformation (15).

Ethiopia's successes provide a powerful example for other SSA countries: By committing greater investment to national and international agricultural R&D and focusing on improving the operational performance of these organizations, SSA governments will be taking one of the single most important steps to sustain Africa's economic transformation. ■

REFERENCES AND NOTES

1. The World Bank, World Development Indicators; <https://data.worldbank.org/region/sub-saharan-africa>.
2. T. S. Jayne, L. Fox, K. Fuglie, S. Adelaja, "Agricultural productivity growth, resilience, and economic transformation in sub-Saharan Africa: Implications for USAID" (Bureau for International Food and Agricultural Development, 2020); www.usaid.gov/sites/default/files/documents/BIFAD_Agricultural_Productivity_Growth_Resilience_and_Economic_Transformation_in_SSA_Final_Report_4.20.21_2_2.pdf.
3. Food and Agriculture Organization of the United Nations, FAOSTAT database; www.fao.org/faostat/en/#data/QC.
4. K. Fuglie, M. Gautam, A. Goyal, W. Maloney, *Harvesting Prosperity: Technology and Productivity Growth in Agriculture* (World Bank, 2020).
5. M. McMillan, D. Rodrik, I. Verduzco-Gallo, *World Dev.* **63**, 11 (2014).
6. T. S. Jayne, J. Chamberlin, D. Headey, *Food Policy* **48**, 1 (2014).
7. M. K. van Ittersum *et al.*, *Proc. Natl. Acad. Sci. U.S.A.* **113**, 14964 (2016).
8. P. A. Sanchez, *Properties and Management of Soils in the Tropics* (Cambridge Univ. Press, ed. 2, 2019).
9. P. A. Sanchez, *Science* **295**, 2019 (2002).
10. R. Laajaj *et al.*, *Nat. Resour.* **10**, 14286 (2020).
11. J. DeVries, "Extending the benefits of improved seed and other farming practices to farmers in countries left behind in Africa's green revolution" (The Seed Systems Group, Nairobi, 2019).
12. P. G. Pardey *et al.*, in *Encyclopedia of Agriculture and Food Systems*, N. K. Van Alfen, Ed. (Academic Press, 2014), pp. 78–97.
13. D. Resnick, S. Haggblade, S. Babu, S. Hendriks, D. Mather, *World Dev.* **109**, 101 (2018).
14. S. Snapp, G. Kanyama-Phiri, B. Kamanga, R. Gilbert, K. Wellard, *Exp. Agric.* **38**, 411 (2002).
15. P. A. Dorosh, B. Minten, Eds., *Ethiopia's Agrifood System: Past Trends, Present Challenges, and Future Scenarios* (International Food Policy Research Institute, 2020).

ACKNOWLEDGMENTS

The authors are grateful for research support provided by the Consultative Group on International Agricultural Research (CGIAR) Research Program on Policies, Institutions, and Markets (PIM); the Feed the Future Innovation Lab for Food Security Policy Research, Capacity and Influence; and the University of Florida's Food Systems Institute.

10.1126/science.abf5143



A treaty under negotiation can help protect marine biodiversity and ensure sustainable use of the high seas.

Edited by Jennifer Sills

Protect high seas biodiversity

The high seas—marine areas beyond national jurisdiction (1)—cover nearly half of Earth's surface (2). The high seas support our planet in countless ways, from regulating the climate, to feeding millions of people, to supporting industries that contribute billions of dollars to the global economy (3). Even so, less than 1% of the high seas are fully protected (4), and the current patchwork of management and lack of oversight leaves them vulnerable to abuse. In 2017, the United Nations resolved to develop an international treaty for the conservation and sustainable use of the high seas. Negotiations are set to end this year. We must ensure that the forthcoming framework conserves high-seas biodiversity and promotes sustainable and equitable use.

To maximize biodiversity protection beyond national jurisdiction, the high seas treaty should incorporate the timely establishment of a network of fully protected marine protected areas for diverse habitats in strategic locations. Fully protected marine reserves in the open ocean preserve fish populations, protect fragile and valuable ecosystems, and increase

ecosystem resilience (5, 6). Implementing effective marine protected areas will require a coordinated approach across existing regional and sectoral bodies and the scientific community (6, 7).

The treaty should also provide a robust framework to assess the environmental impacts of activities on the high seas. Such evaluations should use comprehensive and rigorous global standards and transparent monitoring. Where necessary, existing assessment processes should be reimagined to better measure cumulative impacts. Because the high seas are dynamic and poorly understood, strategic environmental assessments will be required to design effective policies in the future (7).

Finally, the treaty should establish a robust institutional framework that will enable the successful implementation of these safeguards. At a minimum, the changes will require an administrative body, a decision-making body, a scientific committee with influence over decision-making, and a compliance committee. All activities, decisions, and plans should be open and transparent.

Every year, vulnerable and under-studied marine ecosystems are substantially, and in some cases permanently, altered by human activities (8, 9). The proposed treaty provides an opportunity to conserve the high seas for generations to

come and create a more equitable ocean for all humankind (10, 11). We call on all nations to construct an ambitious treaty and conclude these negotiations as soon as possible, to finally put legal protection in place for the unprotected half of our planet (12).

Rebecca R. Helm^{1,2*}, Nichola Clark^{3,4}, Harriet Harden-Davies^{3,5}, Diva Amon^{6,7}, Peter Girguis^{8,5}, Cesar Bordehore⁹, Sylvia Earle¹⁰, Mark J Gibbons¹¹, Yimnang Golbuu¹², Steven H. D. Haddock¹³, Jonathan D. R. Houghton¹⁴, Jamileh Javidpour¹⁵, Douglas J. McCauley¹⁶, Lance Morgan¹⁷, David Obura¹⁸, Evgeny A. Pakhomov¹⁹, Kylie A. Pitt²⁰, Jorge Jimenez Ramon²¹, Rashid Sumaila²², Jean-Baptiste Thiebot²³

¹University of North Carolina Asheville, Asheville, NC 28804, USA. ²Smithsonian Institution National Museum of Natural History, Washington, DC 20560, USA. ³Australian National Centre for Ocean Resources and Security, University of Wollongong, Wollongong NSW 2522, Australia. ⁴The Pew Charitable Trusts, Washington, DC 20004, USA. ⁵Woods Hole Oceanographic Institution, Woods Hole, MA 02543, USA. ⁶SpeSeas, D'Abadie, Trinidad and Tobago. ⁷Natural History Museum, London, UK. ⁸Harvard University, Cambridge, MA 02138, USA. ⁹Multidisciplinary Institute for Environmental Studies "Ramon Margalef" and Department of Ecology, University of Alicante, 03690 Alicante, Spain. ¹⁰Mission Blue, Napa, CA 94581 USA. ¹¹University of the Western Cape, Bellville 7535, Republic of South Africa. ¹²Palau International Coral Reef Center, Koror, Palau. ¹³Monterey Bay Aquarium Research Institute, Moss Landing, CA 95039, USA. ¹⁴School of Biological Sciences, Queen's University Belfast, BT9 7DL, Northern Ireland. ¹⁵Department of Biology, University of Southern Denmark, 5230 Odense-M, Denmark. ¹⁶Marine Science Institute,

University of California Santa Barbara, Santa Barbara, CA 93106, USA. ¹⁷Marine Conservation Institute, Seattle, WA 98103, USA. ¹⁸CORDIO East Africa, Mombasa, Kenya. ¹⁹Earth, Ocean and Atmospheric Sciences Department and the Institute for the Oceans and Fisheries, University of British Columbia, Vancouver, BC, V6T 1Z4, Canada. ²⁰School of Environment and Science, Griffith University, Southport, QLD 4222, Australia. ²¹MarViva, San José, Costa Rica. ²²University of British Columbia, Vancouver, BC V6T 1Z4, Canada. ²³National Institute of Polar Research, Tachikawa, Tokyo, 190-8518, Japan.
*Corresponding author. Email: rrhelm@gmail.com

REFERENCES AND NOTES

1. United Nations, Intergovernmental Conference on Marine Biodiversity of Areas Beyond National Jurisdiction, Fourth Session of the Intergovernmental Conference (www.un.org/bbnj/).
2. G. Wright, J. Rochette, K. M. Gjerde, L. A. Levin, *Nature* **554**, 163 (2018).
3. E. Sala et al., *Nature* **592**, 397 (2021).
4. Marine Conservation Institute, Marine Protection Atlas (2021); <https://mpatlas.org/countries/HS>.
5. E. Sala, S. Giakoumi, *J. Mar. Sci.* **75**, 1166 (2017).
6. M. E. Visalli et al., *Mar. Pol.* **122**, 103927 (2020).
7. N. C. Ban et al., *Conserv. Lett.* **7**, 41 (2014).
8. B. S. Halpern et al., *Nat. Commun.* **6**, 1 (2015).
9. E. Ramirez-Llodra et al., *PLoS One* **6**, e22588 (2011).
10. D. J. McCauley et al., *Sci. Adv.* **4**, eaau2161 (2018).
11. U. R. Sumaila et al., *Sci. Rep.* **5**, 1 (2015).
12. Scientists who wish to support this Letter can add their signature here: <http://protectthehighseas.com/>.

COMPETING INTERESTS

H.H.-D. has received honoraria and fees for consulting related to the Internationally Legally Binding Instrument on the Conservation and Sustainable Use of Marine Biological Diversity of Areas Beyond National Jurisdiction (BBNJ treaty) from the Deep-Ocean Stewardship Initiative, High Seas Alliance, Intergovernmental Oceanographic Commission of UN Educational, Scientific and Cultural Organization.

10.1126/science.abj0581

Trophy hunting undermines public trust

In March, one of the largest brown bears in Europe was shot in the Eastern Carpathians, Romania. A member of one of Europe's royal families allegedly paid at least EUR7000 for the hunt (1), even though the brown bear is strictly protected in Romania and bear trophy hunting is banned (2). The government's tolerance of trophy hunts and inadequate oversight of hunting permits threaten protected species and undermine public trust.

Under provisions of Article 16(1) of the EU Habitats Directive, the national wildlife authority can grant permission for lethal removal of brown bears if a bear is deemed a repeated threat to livestock, crops, or human life (3). However, the local wildlife administrators allowed trophy hunting by issuing a permit, approved by the Ministry of Environment and the local Environmental Protection Agency, that was intended for a nuisance animal. The event

is under investigation as wildlife crime (4).

In Romania, wildlife authorities are mandated by law to protect people's lives and livelihoods through lethal and nonlethal management of problem bears (1). In this case, the authorities breached public trust by not enforcing current legislation and giving game managers, often private entities, complete control over which animal is removed and when. Thus, wildlife authorities failed to protect people's livelihoods and enabled an illegal trophy hunt of a nonoffending bear. This event shows that wildlife species in Romania are still at the mercy of the rich and powerful (5) despite being protected by European legislation (3).

To regain the trust of local communities and society at large, the Romanian government must deliver and enforce effective legislation that allows for accountable management of nuisance animals. Transparent large carnivore management should be rooted in social realities and the best available science and capitalize on the opportunities afforded by the trophy hunt ban to facilitate positive change (6). The European Commission can actively assist member states to manage the increasingly abundant and conflictual large carnivore populations.

Viorel D. Popescu^{1,2*}, Mihai I. Pop^{2,3}, Laurentiu Rozyłowicz²

¹Department of Biological Sciences, Ohio University, Athens, OH 45701, USA. ²Center for Environmental Research, University of Bucharest, Bucharest, Romania. ³Association for Biodiversity Conservation, Focsani, Romania.

*Corresponding author. Email: popescu@ohio.edu

REFERENCES AND NOTES

1. A. Alexander, "Liechtenstein prince accused of shooting Romania's largest bear," *The Guardian* (2021).
2. V. Popescu, M. Pop, S. Chiriac, L. Rozyłowicz, *Science* **364**, 1041 (2019).
3. Y. Epstein, A. Christiernsson, J. V. López-Bao, G. Chapron, *Conserv. Sci. Pract.* **1**, e18 (2019).
4. Government of Romania, Ministerul Mediului, Apelor și Pădurilor, "Comunicat de presă" (2021); www.mmediu.ro/app/webroot/uploads/files/11.05.2021 COMUNICAT DE PRESA.pdf [in Romanian].
5. C. T. Darimont, P. C. Paquet, A. Treves, K. A. Artelle, G. Chapron, *Conserv. Biol.* **32**, 747 (2018).
6. K. Nowak et al., *Science* **366**, 434 (2019).

10.1126/science.abj4014

Brazil's doomed environmental licensing

On 13 May 2021, Brazil's Chamber of Deputies approved bill 3729/2004 (1, 2), which essentially abolishes environmental licensing. The procedural changes outlined by the bill will have catastrophic effects on Brazil's environment. The February 2021 takeover of both houses of

Congress by a coalition of parties supporting President Jair Bolsonaro's positions on the environment (3) practically guarantees that the bill will soon be approved by the Federal Senate and then signed by Bolsonaro. Nevertheless, efforts to influence the Senate vote, in addition to legal challenges, can and must continue.

The bill creates a new "general law for environmental licensing" that allows any project, including highways, ports, railways, and large dams, to be built under a kind of self-licensing by means of a mere "declaration of adhesion and commitment" by the proponent affirming intention to abide by requirements established by the licensing authority. This means that licenses will be issued automatically without any analysis by technical staff in the environmental agencies. For some types of projects, even this token declaration will be unnecessary, including projects for agriculture (and biofuels), cattle ranching, low-voltage electricity distribution, and water and sewage treatment systems. The bill essentially eliminates public participation in the process, as well as the roles of agencies such as the Chico Mendes Institute of Biodiversity Conservation and the National Foundation of the Indian, which are responsible, respectively, for conservation units (protected areas for biodiversity) and for guaranteeing rights of Indigenous peoples.

One of the first Amazonian infrastructure projects likely to benefit from the new licensing procedures is the planned reconstruction of the environmentally disastrous Highway BR-319, which, together with its planned side roads, would open a vast area of Amazonia to deforestation (4). Amazon deforestation contributes to climate change and loss of ecosystem services with consequences for Brazil and for the entire world. The effective end to environmental licensing will make it much more difficult for countries importing Brazilian commodities to identify imports whose production and transport are not tied to deforestation and associated land grabbing and violation of the rights of traditional peoples (5, 6).

The vice-president of Brazil's Senate has announced the intention to hold public hearings before the vote on the bill (7). The Federal Public Ministry (a public prosecutor's office for defending the rights of the people) has analyzed the bill and considers it unconstitutional (8). This is important in both the legislative and the legal battles but is no guarantee of the bill's defeat in either the legislature or the courts. In addition to discussion in

Optical Beam Combining System

Easy to change the spectral output of the light source

Any LED cube can be placed in any of 7 positions without concern for the order

Wavelength selection and beam reflection using Semrock® STR Filters

LAMBDA 721



SUTTER INSTRUMENT

PHONE: +1.415.883.0128
FAX: +1.415.883.0572
EMAIL: INFO@SUTTER.COM
WWW.SUTTER.COM

the Senate, it is important that the bill be discussed transparently with the citizens of Brazil, who should be aware of the impacts of approval.

Bills such as this one, which has been pending in congressional committees since 2004, can suddenly surge forth for a plenary vote when the political climate is favorable, as it is now. Almost all bills presented for a plenary vote are passed, and the key decision is in the hands of the president of the chamber in bringing a bill to the floor. This presents an opportunity for influence from abroad, given that the presidencies of both houses are controlled by the “ruralist” voting block that represents agribusiness. Brazil’s agribusiness leaders are sensitive to reputational risks that can cause countries, companies, and consumers to boycott or impose conditions on Brazilian commodities.

Renata Ruaro^{1*}, Lucas Ferrante², Philip M. Fearnside³

¹Programa de Pós-graduação em Ciência e Tecnologia Ambiental, Federal Technological University of Paraná, 81280-340, Curitiba, PR, Brazil. ²Programa de Pós-graduação em Ecologia, National Institute for Research in Amazonia (INPA), 69067-375 Manaus, AM, Brazil. ³National Institute for Research in Amazonia (INPA), 69067-375 Manaus, AM, Brazil.
*Corresponding author.
Email: renataruaro@utfpr.edu.br

REFERENCES AND NOTES

1. Câmara dos Deputados, PL3729/2004 (2021); www.camara.leg.br/propostas-legislativas/257161 [in Portuguese].
2. O. B. de Souza, “Câmara aprova texto principal de projeto que praticamente acaba com licenciamento ambiental,” Instituto Socioambiental (2021); www.socioambiental.org/pt-br/noticias-socioambientais/camara-aprova-texto-principal-de-projeto-que-praticamente-acaba-com-licenciamento-ambiental [in Portuguese].
3. L. Ferrante, P. M. Fearnside, *Science* **371**, 898 (2021).
4. L. Ferrante, P. M. Fearnside, *Science* **369**, 634 (2020).
5. L. Kehoe *et al.*, *One Earth* **3**, 268 (2020).
6. S. L. Bager *et al.*, *One Earth* **4**, 289 (2021).
7. Senado Federal, “Senado vai analisar projeto com novas regras para o licenciamento ambiental,” Agência Senado (2021); <https://www12.senado.leg.br/noticias/materias/2021/05/15/senado-vai-analisar-projeto-com-novas-regras-para-o-licenciamento-ambiental> [in Portuguese].
8. M. J. Gisi, F. A. B. Leite, “Nota Técnica 4ª CCR Nº 6/2017” (Ministério Público Federal 4ª Câmara de Coordenação e Revisão Meio Ambiente e Patrimônio Cultural, Rio de Janeiro, 2017); www.mpf.mp.br/pgr/documentos/NT620174CCRGTEPL3729.pdf [in Portuguese].

10.1126/science.abj4924

TECHNICAL COMMENT ABSTRACTS

Comment on “Individual heterozygosity predicts translocation success in threatened desert tortoises”

Philip W. Hedrick

Scott *et al.* (Reports, 27 November 2020, p. 1086) suggest, on the basis of conclusions obtained from a desert tortoise

reintroduction program, that higher genomic heterozygosity should be used to identify individuals for successful translocation. I contend that this recommendation is questionable given these relocated tortoises’ unknown origin, their high mortality, insufficient data on resident tortoises and other components of fitness, and potential allelic dropout.

Full text: [dx.doi.org/10.1126/science.abg2673](https://doi.org/10.1126/science.abg2673)

Response to Comment on “Individual heterozygosity predicts translocation success in threatened desert tortoises”

Peter A. Scott, Linda J. Allison, Kimberleigh J. Field, Roy C. Averill-Murray, H. Bradley Shaffer Hedrick brings up several potential concerns that he feels challenge or limit our main finding. Hedrick does not comment on our empirical results, but rather argues that several factors may confound or invalidate our conclusion. Many of these concerns focus on unknown ecological aspects of the translocated tortoises, but we believe there is no reason to conclude that they bias the results or interpretation as presented in our original paper.
Full text: [dx.doi.org/10.1126/science.abg3199](https://doi.org/10.1126/science.abg3199)

Comment on “Individual heterozygosity predicts translocation success in threatened desert tortoises”

Bengt Hansson, Hernán E. Morales, Cock van Oosterhout

Scott *et al.* (Reports, 27 November 2020, p. 1086) bring much-needed attention to species conservation by demonstrating heterozygote superiority among translocated tortoises. However, we believe that their recommended heterozygosity decision rule risks taking conservation genomics backward. We argue that their advice could misguide conservation management aimed at establishing viable populations, and that it can be improved by also assessing the genetic load.

Full text: [dx.doi.org/10.1126/science.abh1105](https://doi.org/10.1126/science.abh1105)

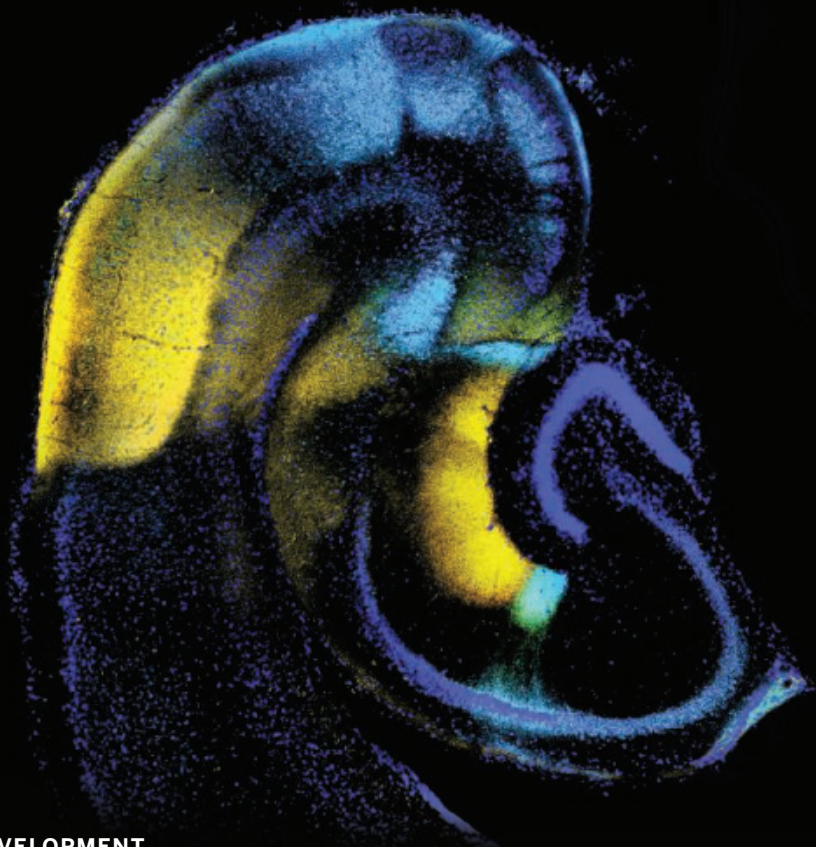
Response to Comment on “Individual heterozygosity predicts translocation success in threatened desert tortoises”

Peter A. Scott, Linda J. Allison, Kimberleigh J. Field, Roy C. Averill-Murray, H. Bradley Shaffer Hansson *et al.* argue that our main finding could provide an overly simplistic metric for maximizing genetic rescue. They agree that translocating the most genetically diverse individuals led to a large increase in translocated tortoise survival, but recommend instead moving individuals that have a low genetic load and the greatest representation of metapopulation diversity. Their recommendation is based on specific model assumptions and fitness effects that are often unknown and are not generalizable to many endangered species applications.
Full text: [dx.doi.org/10.1126/science.abh2633](https://doi.org/10.1126/science.abh2633)

RESEARCH

IN SCIENCE JOURNALS

Edited by
Michael Funk



NEURODEVELOPMENT

Keeping brain development untangled

Brain circuits established during development can be overlapping or parallel as needed. Pederick *et al.* analyzed how parallel circuits in the mouse medial and lateral hippocampus develop without getting tangled up. Regulated expression of the cell surface molecules teneurin-3 (Ten3) and latrophilin-2 (Lphn2) keeps confusion at bay. Together, these factors act as a membrane-bound ligand-receptor pair with repulsive outcomes, and they are able to destabilize a nascent but incorrect axon-target interaction. Individually, they each mediate homophilic attraction as axons search for their favored targets. —PJH *Science*, abg1774, this issue p. 1068

Fluorescence microscopy image of a mouse brain section showing the expression pattern of two cell surface proteins involved in parallel hippocampal network formation

ELECTROCHEMISTRY

Potassium helps CO₂ compete in acid

Electrochemical reduction of carbon dioxide (CO₂) is a promising means of converting this greenhouse gas into

valuable fuels and chemicals. However, two competing reactions restrict the efficiency of this process. In base, much of the CO₂ is trapped as carbonate before reduction; in acid, protons outpace CO₂ at catching electrons from the cathode.

Huang *et al.* report that a high dose of potassium ions can help to solve the latter problem. By concentrating potassium ions at the electrode, high selectivity toward CO₂ reduction at high current in acid is possible, which the authors attribute to

electrostatic stabilization of the desired adsorbates. —JSY

Science, abg6582, this issue p. 1074

GENETICS OF OBESITY

Obesity genes working together

The biological causes of obesity are not well understood. Sobreira *et al.* examined the chromatin interactions between key genes in a locus known for its associations with obesity in human patients. In addition to directly interrogating the connections between these genes and examining the mechanisms that regulate their activity, the authors used mouse models to study the target genes' effects on both adipose tissue and brain cells that play a role in regulating dietary preferences. —YN

Science, abf1008, this issue p. 1085

HYDROGELS

Tougher when stressed

Hydrogels are typically weak materials because they contain only a small fraction of polymeric material highly swollen with water. Strength can be increased by adding extra cross-linking or interpenetrating networks with some sacrificial bonds to enhance toughness; however, these properties deteriorate upon stretching and may be slow to recover after relaxation. Liu *et al.* developed polyethylene glycol hydrogels cross-linked with moderate fractions of polymers that form sliding rings. These allow the chain to orient in parallel when stretched, leading to rapid and reversible strain-induced crystallization and thus much tougher hydrogels. —MSL

Science, aaz6694, this issue p. 1078

GAMMA-RAY BURSTS

An intrinsic gamma-ray burst afterglow

Long gamma-ray bursts (GRBs) are emitted by relativistic jets generated during the collapse of a massive star in a

distant galaxy. The GRB itself lasts only a few seconds but is followed by an afterglow that can persist for hours or days. The H.E.S.S. Collaboration observed the afterglow of GRB 190829A, a nearby long GRB. The proximity of this burst allowed it to be detected at tera-electron volt energies that would otherwise be absorbed in the intergalactic medium. By analyzing the spectrum and light curve at x-ray and gamma-ray wavelengths, the authors show that the afterglow cannot be explained by standard models. —KTS

Science, abe8560, this issue p. 1081

PALEOCLIMATE

Antarctic paleotemperatures

It has been widely thought that East Antarctica was ~9°C cooler during the Last Glacial Maximum, close to the ~10°C difference between then and now determined independently for West Antarctica. Buizert *et al.* used borehole thermometry, firn density reconstructions, and climate modeling to show that the temperature in East Antarctica was actually only ~4° to 7°C cooler during the Last Glacial Maximum. This result has important consequences for our understanding of Antarctic climate, polar amplification, and global climate change. —HJS

Science, abd2897, this issue p. 1097

CORONAVIRUS

Back to school—safely

Severe COVID-19 in children is rare, but many schools remain closed because the transmission risk that school contact poses to adults and the wider community is unknown. Observing the heterogeneity of approaches taken among U.S. school districts, Lessler *et al.* investigated how different strategies influence COVID-19 transmission rates in the wider community using COVID-19 Symptom Survey data from Carnegie Mellon and Facebook. The authors found that when mitigation measures

are in place, transmission within schools is limited and infection rates mirror that of the surrounding community. —CA

Science, abh2939, this issue p. 1092

HOST SIGNALING

Virus beats bronchodilators in airways

Agonists of the β_2 -adrenergic receptor (β_2 AR) are used as bronchodilators to relieve airway obstruction in asthmatic patients, but they are less effective in patients infected with respiratory syncytial virus (RSV). Harford *et al.* found that RSV infection of human airway smooth muscle cells resulted in the loss of the β_2 AR from the plasma membrane and in its proteasomal cleavage, and enhanced the contractility of these cells in vitro. Drugs that do not act on the β_2 AR may be needed to relieve airway obstruction in patients infected with RSV. —JFF

Sci. Signal. **14**, eabc1983 (2021).

T CELLS

Reconstructing T_{FR} cell development

Antibody responses, including those against self-antigens, are tightly controlled within germinal centers by balancing the activity of T follicular regulatory (T_{FR}) and T follicular helper (T_{FH}) cells. Kumar *et al.* reconstructed the developmental trajectory of T_{FR} cells using flow cytometry-indexed single-cell transcriptomics of follicular T cells isolated from human peripheral blood, lymph nodes, and tonsils. They used transcriptomics to support a model in which mature germinal center T_{FR} cells arise from regulatory T cells, with circulating T_{FR} cells representing a separate developmental pathway. These results suggest that mature T_{FR} cells primarily arise independently from their less mature counterparts in peripheral blood, providing further insight into how human T_{FR} cells develop. —CO

Sci. Immunol. **6**, eabd8411 (2021).

IN OTHER JOURNALS

Edited by Caroline Ash
and Jesse Smith



CARDIOLOGY

Taking machine learning to heart

Both children and adults can have cardiac problems. Congenital problems predominate in childhood, whereas adults are more likely to suffer from conditions associated with age. In both cases, however, accurate diagnosis depends on access to health care and the availability of trained specialists. In two recent studies, Arnaout *et al.* and Yao *et al.* showed how machine learning can supplement specialist care in both pediatric and adult cardiology settings. Arnaout *et al.* analyzed fetal ultrasound images to detect congenital heart disease. Yao *et al.* used machine learning in conjunction with electrocardiogram imaging to detect adults with low ejection fraction (a measure of the amount of blood that the heart succeeds in pumping), which is a risk factor for subsequent heart failure. In each case, the technology should help to improve diagnostic accuracy and access to appropriate treatment. —YN

Nat. Med. **27**, 815, 882 (2021).

MECHANOCHEMISTRY

N-heterocyclic carbenes by compression

Mechanochemistry, the application of mechanical force to drive chemical reactions, is widely used in industry to activate force-sensitive inorganic materials (mechanophores). In recent years, there has been considerable interest in developing organic and polymeric mechanophores that could offer new opportunities for the development of catalytic systems, drug-release technologies, sensors, and other advanced functional materials. Shen *et al.* report that some flex-activated polymeric mechanophores can release an N-heterocyclic carbene under mechanical load without degradation of the polymer main chain and over multiple compression-activation cycles. The proposed mechanophores could be used as a platform to release various classes of N-heterocyclic carbenes, widely used organocatalysts, which could trigger practically useful secondary reactions upon activation. —YS

Angew. Chem. Int. Ed. **10.1002/anie.202100576** (2021).



AGRICULTURE

Intervention beans

Agricultural interventions to improve human nutrition do not always recognize ecological and social processes. To explore how multiple aspects of farming can be integrated, Santoso *et al.* designed an agricultural intervention study among Tanzanian smallholder farmers. Mentor farmers were asked to share agricultural information, and legume seeds were supplied to participating villages for two growing seasons between 2016 and 2019. Although the effect depended on local context, by comparison with similar programs using more expensive livestock interventions, this study achieved results at the upper end of the range. Although little change was observed in anthropometric measures, children's diet was diversified, household food insecurity improved, men became more involved in household tasks, and women's well-being improved. —CA *J. Nutr.* 10.1093/jn/nxab052 (2021).

Providing legume seeds for agricultural intervention results in a wide range of nutritional and social benefits.

HUMAN EVOLUTION

Origins of the sweaty ape

Humans are unique mammals that lack hair in many parts of their body and have an increased capacity for sweating, which assists in thermoregulation, through eccrine sweat glands. Using a comparative genomics approach to study the regulation of genes involved in the development of eccrine sweat glands, Aldea *et al.* investigated noncoding genomic elements to determine the differences underlying the increased eccrine sweat gland density of humans relative to other primates and mice. They found that human-specific evolution in a noncoding enhancer, hECE18, likely increases gene expression of the *Engrailed1* gene, which is required for the development of eccrine sweat glands. Furthermore, humanized hECE18 knock-in mice have an increased number of these glands, supporting the idea that this human-specific adaptation is a result of changes in the noncoding regulatory regions of proteins. —LMZ

Proc. Natl. Acad. Sci. U.S.A. **118**, e2021722118 (2021).

GEOLOGY

Hydrogen coal storage

Hydrogen is a zero-carbon fuel that is particularly difficult to store because of its high diffusivity in many materials. Iglaue *et al.* found that hydrogen adsorbs onto sub-bituminous coal and suggest using coal seams for large-scale hydrogen storage. The authors

made these measurements in the laboratory under various pressure and temperature conditions. The gas adsorption substantially increased with pressure, suggesting that deeper coal seams might be the best candidates for storage if this adsorption behavior is validated in the field. —BG

Geophys. Res. Lett. 10.1029/2021GL092976 (2021).



Large-scale hydrogen storage may be possible underground in sub-bituminous seams (black, pictured).

QUANTUM OPTICS

Harnessing the dark to store light

An excited atom will naturally decay to the ground state, with the exciting and emitted photons forming the basis for the optical protocols in quantum communication and computation. Within an ensemble of atoms, this emission process can proceed constructively, resulting in faster ensemble decay in an effect known as superradiance. In contrast to the superradiant process, Ferioli *et al.* report subradiance in an ensemble of excited rubidium atoms, where collective behavior between the decaying atoms proceeds destructively, thereby extending the lifetime of the excited atom ensemble in what can be described as a dark state. Engineering such dark states could provide a route to storing light. The reduced linewidth could also be useful in metrology applications. —ISO

Phys. Rev. X **11**, 021031 (2021).

CELL BIOLOGY

Cells feel the strain

Cells respond to mechanical strain by stiffening their actin cytoskeleton, a process that is energetically costly. Salvi *et al.* show that cells anticipate this cost by increasing glucose transport when subjected to mechanical strain. In canine or human epithelial cells in culture, exposure to strain caused accumulation of the glucose transporter GLUT1 at cell-cell junctions. The increase in transporters increased the uptake of glucose required for cytoskeletal stiffening. The transporters were tethered by the ankyrin G protein to E-cadherin-containing adhesion complexes at the cell junctions. Cells expressing a mutant form of E-cadherin that did not interact with ankyrin G failed to accumulate GLUT1 and were unable to form an effective epithelial barrier. —LBR

Nat Cell Biol. **23**, 457 (2021).

REVIEW SUMMARY

GRAVITATIONAL WAVES

The first 5 years of gravitational-wave astrophysics

Salvatore Vitale

BACKGROUND: Gravitational waves are ripples in spacetime produced by accelerating masses, as predicted by the general theory of relativity. They have been directly detected by the Laser Interferometer Gravitational-Wave Observatory (LIGO) and the Virgo detector.

Gravitational waves encode several physical properties of their sources, such as the masses, spins, equation of state of nuclear matter, and distances. Because they are emitted in regions where gravity is extremely strong, gravitational waves also enable tests of the general theory of relativity.

Some astrophysical phenomena are expected to emit both gravitational and electromagnetic waves, including the mergers of binary neutron stars, a neutron star merger with a black hole, or core-collapse supernovae within the Milky Way. This potentially enables multimessenger studies of these objects.

ADVANCES: More than 50 gravitational-wave events have been detected, emitted by the inspiral and merger of compact objects (i.e.,

neutron stars and black holes) in binary systems. The gravitational-wave event GW170817 was emitted by a binary neutron star merger 40 million parsecs from Earth. The collision also generated a highly energetic flash of gamma rays, which yielded the first multimessenger observation of a gravitational-wave source. These measurements showed that binary neutron star mergers are the progenitors of at least some gamma-ray bursts, confirming a hypothesis made decades earlier. The discovery of electromagnetic emission at lower energies—from x-ray to radio frequencies—has enabled an extensive study of the source and has shown that binary neutron stars can produce many of the elements heavier than iron.

Analysis of GW170817 and its electromagnetic counterparts has constrained the equation of state of nuclear matter, the relation between density and pressure in the core of neutron stars; has measured the Hubble constant, which quantifies the local expansion rate of the Universe; and has confirmed that the speed of gravitational waves is equal to the

speed of light, within one part in $\sim 10^{15}$. A second binary neutron star gravitational-wave signal, GW190525, has neutron star masses outside the range measured in the Milky Way using x-ray observations.

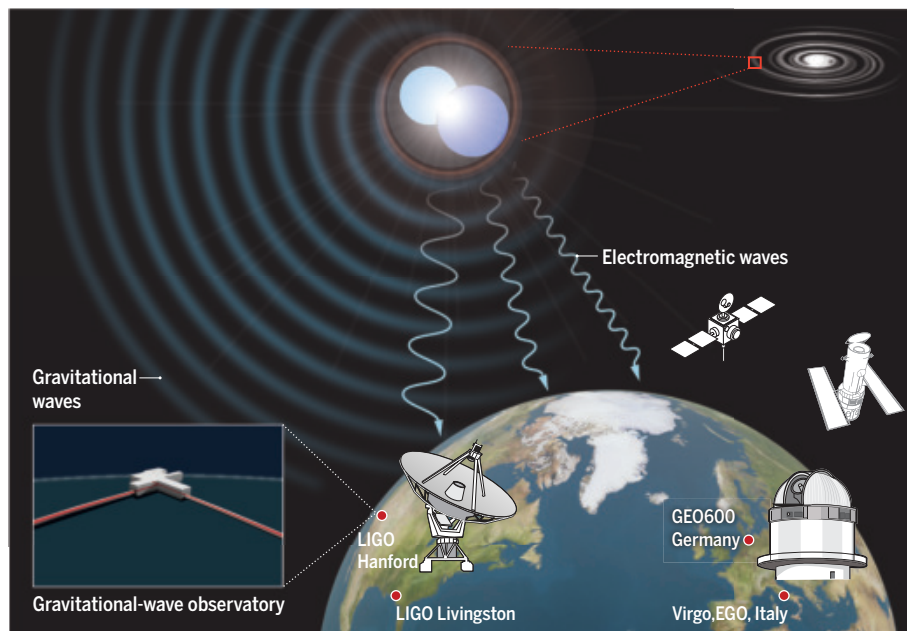
Dozens of gravitational-wave events have been detected from binary black hole mergers. These have shown that the mass distributions of black holes cannot be a single power law, like the mass distribution of the parent stars. Instead, the preferred model has both a power law component and a Gaussian component, centered at $33.5^{+4.5}_{-5.5}$ solar masses. This could indicate that gravitational-wave events arise from more than one astrophysical population. This two-component distribution might be a result of the physical processes involved in the explosions of stars of more than ~ 100 solar masses, which predict a maximum mass for black holes formed in supernovae.

The highest mass source detected, GW190521, has component black holes that are more massive than expected from stellar evolution theory. This could indicate that one or both component black holes were formed in a previous merger event. Meanwhile, the binary system GW190814 hosts an ~ 2.6 -solar masses compact object, which makes it either the least massive black hole or the most massive neutron star yet observed.

The spins of black holes in all of these mergers are consistent with being preferentially small, unlike Galactic black holes observed in x-ray binaries. This could indicate that most black holes are born with small spin and are later spun-up by accretion.

Tests of the general theory of relativity using gravitational-wave data have found no departure from its predictions. Within the current precision, general relativity correctly describes the behavior of compact astrophysical objects moving in extreme gravitational fields.

OUTLOOK: Existing gravitational-wave detectors are undergoing upgrades to their sensitivities, and additional detectors are under construction. These are expected to detect multiple neutron star binary mergers and ~ 100 binary black hole mergers every year. The growing dataset should provide a better understanding of the astrophysical formation pathways of compact objects over the mass range between ~ 1 and a few hundred solar masses. Independent measurements using pulsar timing arrays could detect the lower-frequency gravitational waves produced by supermassive black hole binaries, which are expected to form when galaxies merge. ■



Multimessenger observations of a binary neutron star merger. Two merging neutron stars produce gravitational waves, observed by gravitational-wave detectors in the minutes preceding the collision. When the neutron stars collide, they emit a flash of gamma rays, observed as a short gamma-ray burst. Electromagnetic radiation at lower frequencies (from x-ray to radio frequencies) can be observed for hours to years following the merger. The combination of gravitational and electromagnetic waves provides complementary information about the source. The Japanese gravitational-wave detector KAGRA (Kamioka Gravitational Wave Detector) is not shown in this figure. EGO, European Gravitational Observatory.

The list of author affiliations is available in the full article online.
Email: salvatore.vitale@ligo.org
Cite this article as S. Vitale, *Science* 372, eabc7397 (2021).
DOI: 10.1126/science.abc7397

S READ THE FULL ARTICLE AT
<https://doi.org/10.1126/science.abc7397>

RESEARCH ARTICLE SUMMARY

TRANSCRIPTION

Structures of the human Mediator and Mediator-bound preinitiation complex

Xizi Chen[†], Xiaotong Yin[†], Jiabei Li[†], Zihan Wu[†], Yilun Qi[†], Xinxin Wang[†], Weida Liu, Yanhui Xu^{*}

INTRODUCTION: The multisubunit Mediator binds RNA polymerase II (Pol II), transduces regulatory signals from transcription factors to Pol II, facilitates preinitiation complex (PIC) assembly, and stimulates cyclin-dependent kinase 7 (CDK7)-mediated Pol II C-terminal domain (CTD) phosphorylation. The 14-subunit transcription factor IID (TFIID) is globally required for almost all Pol II-mediated transcription initiation and cannot be replaced by TATA box-binding protein (TBP), a TFIID subunit. Previous structural studies focused on the TBP-based system. However, the mechanism by which Mediator is assembled into TFIID-based PIC and regulates Pol II CTD phosphorylation remains elusive.

RATIONALE: We reconstituted and determined the cryo-electron microscopy structures of human 26-subunit Mediator and its complex with TFIID-based PIC (76 polypeptides, ~4.1 megadaltons). Structural analyses were performed using the

structures of Mediator and PIC-Mediator in distinct conformations, as well as the previously reported TBP-based PIC-Mediator structure.

RESULTS: Mediator in the Tail-extended (MED^E) and Tail-bent (MED^B) conformations reveals similar separation of the Head and Middle modules. The structure of MED^E at 3.5-Å resolution reveals the mechanism of Mediator assembly. Binding of PIC induces concerted modular reorganization (Head-tilting and Middle-down) of Mediator through two connected molecular levers. The α -helix bundle HB1 of the Head and the Knob of the Middle form a Head-Middle sandwich, which stabilizes two CTD segments with the longer segment extending toward the CDK7 active site. The CTD-Mediator-CDK7 binding pattern suggests a CTD-gating mechanism, by which Mediator binds and brings Pol II CTD to CDK7 for efficient and persistent phosphorylation. Structures of PIC-Mediator in distinct

conformations indicate that PIC's architecture modulates Mediator organization. Mediator and TFIID together position TFIIF, stabilize xeroderma pigmentosum type B (XPB)-promoter-Pol II contacts, and may facilitate XPB-mediated promoter melting and DNA translocation toward Pol II. Structural comparison with TBP-based PIC-Mediator reveals considerable differences in Mediator conformation, CTD-Mediator interaction, and XPB stabilization, underscoring the critical role of TFIID in organizing PIC-Mediator.

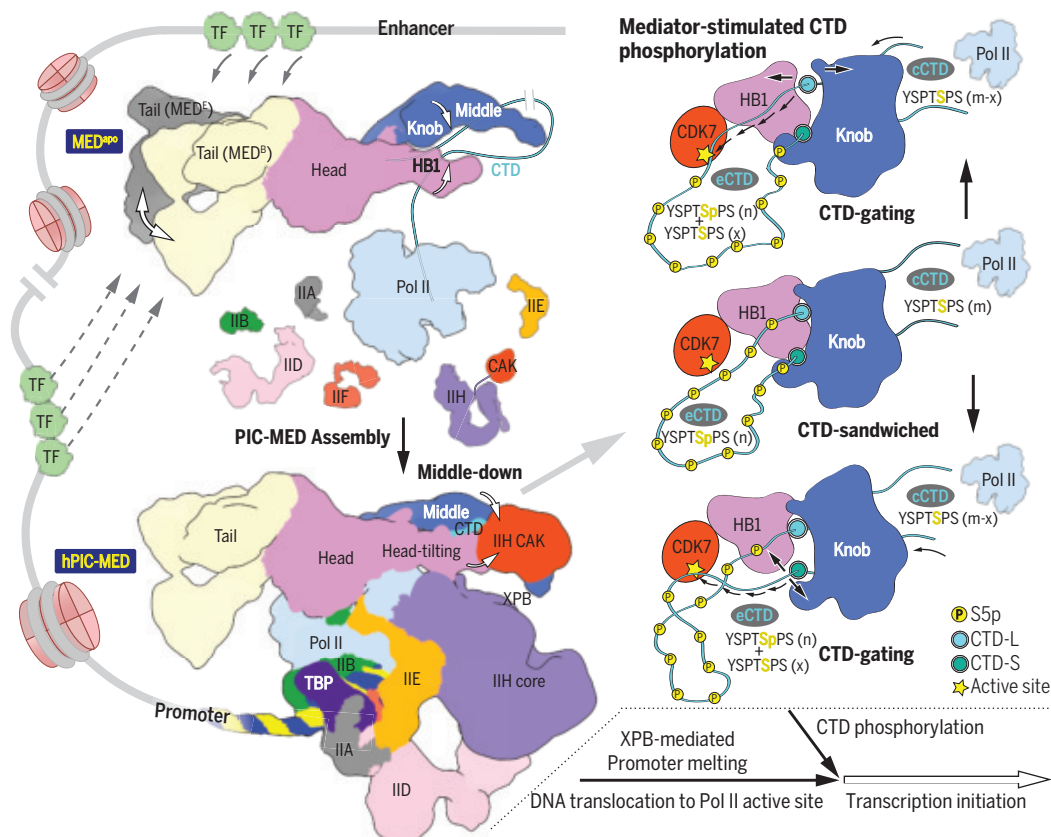
CONCLUSION: Our study provides the structure of the human Mediator at near-atomic resolution as well as the structure of the complete PIC-Mediator holocomplex. These structures provide insights into PIC-Mediator assembly and Mediator-stimulated CTD phosphorylation. TFIID may confer considerable complexity and dynamics of PIC-Mediator organization to accommodate highly dynamic processes of transcription initiation. The structures also provide a framework for further studies of Mediator-stimulated transcription activation by transcription factors. ■

†These authors contributed equally to this work.

*Corresponding author. Email: xuyh@fudan.edu.cn

Cite this article as X. Chen et al., *Science* **372**, eabg0635 (2021). DOI: 10.1126/science.abg0635

S **READ THE FULL ARTICLE AT**
<https://doi.org/10.1126/science.abg0635>



Schematic model of PIC-Mediator assembly and Mediator-stimulated CTD phosphorylation. The enhancer- or promoter-bound transcription factors recruit and bring Mediator to the core promoter, on which Mediator, Pol II, and general transcription factors TFIID/IIA/IIB/IE/IF/IIH are assembled into PIC-Mediator, during which Mediator undergoes concerted modular reorganization. The Head-Middle sandwich provides two CTD-anchoring sites, which facilitate phosphorylation of the exposed CTD (eCTD) and may allow for gating of the cradled CTD (cCTD) for phosphorylation. Mediator and TFIID stabilize TFIIF, in which XPB mediates promoter melting and DNA translocation to Pol II and CDK7 phosphorylates Pol II CTD; both processes are required for transcription initiation.

RESEARCH ARTICLE SUMMARY

IMMUNOLOGY

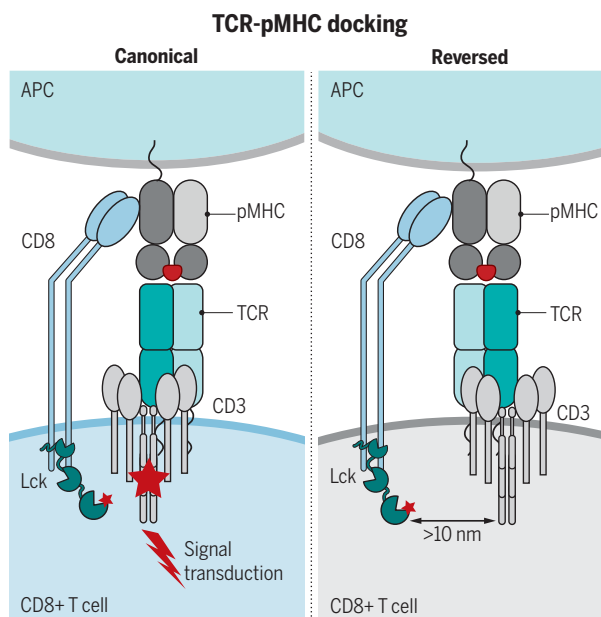
Canonical T cell receptor docking on peptide–MHC is essential for T cell signaling

Piروز Zareie, Christopher Szeto[†], Carine Farenc, Sachith D. Gunasinghe, Elizabeth M. Kolawole, Angela Nguyen, Chantelle Blyth, Xavier Y. X. Sng, Jasmine Li, Claerwen M. Jones, Alex J. Fulcher, Jessica R. Jacobs, Qianru Wei, Lukasz Wojciech, Jan Petersen, Nicholas R.J. Gascoigne, Brian D. Evavold, Katharina Gaus, Stephanie Gras^{†‡*}, Jamie Rossjohn^{†*}, Nicole L. La Gruta^{†*}

INTRODUCTION: T cell receptor (TCR) recognition of peptide–major histocompatibility complexes (pMHCs) is one of the most diverse receptor–ligand interactions in biology. Nevertheless, these interactions exhibit a highly conserved, or canonical, TCR–pMHC docking polarity in both mice and humans. Whether this canonical docking polarity is driven by evolutionarily conserved, germline-encoded complementarity between the TCR and MHC or by signaling constraints imposed by coreceptors has been a question of enduring debate. Here, we demonstrate that although reversed-polarity TCR–pMHC recognition is prevalent within a naïve, viral epitope-specific T cell repertoire and may exhibit relatively high pMHC affinity, such TCRs are unable to support TCR signaling in the presence of CD8 coreceptor because of mislocalization of Lck. These data support a paradigm in which the highly conserved TCR–pMHC docking polarity is driven by structural constraints on TCR signaling.

RATIONALE: Evidence suggests that the canonical TCR–pMHC docking polarity is driven by evolutionary hardwiring of complementary germline-encoded motifs at the TCR and MHC interface. An alternate model suggests that TCR recognition of pMHC is driven during thymic selection by the need for the CD4 or CD8 coreceptors to bind MHC and deliver coreceptor-associated Lck to the CD3 signaling complex. We previously identified reversed-polarity TRBV17⁺ TCRs from the preimmune influenza A virus (IAV)-specific repertoire that bound pMHC I (H-2D^bNP₃₆₆) with a moderate affinity but were unable to support robust T cell recruitment. Here, using a range of canonical and reversed TCRs specific for the same cognate pMHC, we tested the hypothesis that the TCR–pMHC docking polarity precedes binding strength as a key determinant of T cell activation. We

hypothesized that the underlying driver of the canonical docking polarity is the colocalization of signaling molecules central to the TCR signal transduction pathway.



The canonical polarity of TCR–pMHC docking is essential for colocalization of CD3 and coreceptor-associated Lck and for productive TCR signaling. Schematic shows how canonical TCR–pMHC recognition colocalizes Lck and CD3, driving TCR-mediated signaling. By contrast, a reversed TCR–pMHC recognition polarity mislocalizes Lck and CD3, impeding signaling.

RESULTS: In this study, we demonstrate that reversed TCRs are prevalent in a naïve virus-specific repertoire but are poorly represented in the immune response after virus challenge. We identified antigen-specific TCRαβ clonotypes that were either poorly recruited or clonally expanded and found an overriding association between immune prevalence and canonical TCR–pMHC docking. This was irrespective of pMHC affinity, catch or slip bond formation, or TCR clustering, demonstrating that a canonical docking polarity is required for T cell activation. This finding was verified after viral challenge of adoptively

transferred retrogenic T cells expressing reversed or canonical docking TCRs of varying affinities. The inability of T cells expressing reversed-docking TCRs to be recruited into the antiviral immune response demonstrates that TCR–pMHC docking topology supersedes TCR–pMHC affinity as the primary determinant for effective in vivo immune recruitment. Using fluorescence lifetime imaging microscopy (FLIM)–Förster resonance energy transfer (FRET) analyses, we show that canonical TCR–pMHC docking is essential for the colocalization of CD8–Lck with CD3ζ, which is impaired when the TCR engages pMHC with reversed polarity. The requirement for canonical TCR–pMHC docking can be circumvented by the removal of the CD8 coreceptor or by dissociation of Lck from CD8, suggesting that sequestration of Lck by the CD8 coreceptor has a dual role: potentiating signaling arising from canonical TCR–pMHC interactions and impeding reversed-polarity TCR–pMHC signaling.

CONCLUSION: The inability of reversed-polarity TCRs to participate in the immune response occurs independently of TCR–pMHC binding affinity and instead is a direct consequence of reversed TCR–pMHC engagement. Most TCR–pMHC complexes that have been solved to date, upon which the canonical TCR–pMHC docking paradigm has been established, were derived from expanded immune repertoires. Thus, we conclude that the highly conserved docking polarity is driven predominantly by the structural constraints imposed on TCR signaling and recruitment into an immune response. In addition to the well-recognized augmentation of signaling resulting from canonical TCR–pMHC engagement, our findings suggest a role for coreceptor–Lck association in preventing signaling by noncanonical TCR–pMHC recognition. Such negative regulation would serve to limit the extent of functional TCR cross-reactivity and constrain the number of signaling-competent TCR-binding modalities. ■

The list of author affiliations is available in the full article online.
*Corresponding author. Email: nicole.la.gruta@monash.edu (N.L.G.); jamie.rossjohn@monash.edu (J.R.); s.gras@latrobe.edu.au (S.G.)

[†]Present address: Department of Biochemistry and Genetics, La Trobe Institute for Molecular Science, La Trobe University, Melbourne, Victoria, Australia.

[‡]Joint senior authors.

Cite this article as P. Zareie *et al.*, *Science* 372, eabe9124 (2021). DOI: 10.1126/science.abe9124

READ THE FULL ARTICLE AT
<https://doi.org/10.1126/science.abe9124>

RESEARCH ARTICLES

SYNTHETIC BIOLOGY

Sense codon reassignment enables viral resistance and encoded polymer synthesis

Wesley E. Robertson^{1†}, Louise F. H. Funke^{1†}, Daniel de la Torre^{1†}, Julius Fredens^{1†}, Thomas S. Elliott¹, Martin Spinck¹, Yonka Christova¹, Daniele Cervettini¹, Franz L. Böge¹, Kim C. Liu¹, Salvador Buse¹, Sarah Maslen¹, George P. C. Salmond², Jason W. Chin^{1*}

It is widely hypothesized that removing cellular transfer RNAs (tRNAs)—making their cognate codons unreadable—might create a genetic firewall to viral infection and enable sense codon reassignment. However, it has been impossible to test these hypotheses. In this work, following synonymous codon compression and laboratory evolution in *Escherichia coli*, we deleted the tRNAs and release factor 1, which normally decode two sense codons and a stop codon; the resulting cells could not read the canonical genetic code and were completely resistant to a cocktail of viruses. We reassigned these codons to enable the efficient synthesis of proteins containing three distinct noncanonical amino acids. Notably, we demonstrate the facile reprogramming of our cells for the encoded translation of diverse noncanonical heteropolymers and macrocycles.

Nature uses 64 triplet codons to encode the synthesis of proteins composed of the 20 canonical amino acids, and most amino acids are encoded by more than one synonymous codon (1). It is widely hypothesized that removing sense codons and

the tRNAs that read them from the genome may enable the creation of cells with several properties not found in natural biology, including new modes of viral resistance (2) and the ability to encode the biosynthesis of noncanonical heteropolymers (3–6). However, these hypotheses have not been experimentally tested. Removing release factor 1 (RF1) (and therefore the ability to efficiently terminate translation on the TAG stop codon) from *Escherichia coli* provides some resistance to a limited subset of phage (7, 8). However,

this resistance is not general, and phage are often propagated in the absence of RF1 (8), because the TAG stop codon is rarely used for the termination of translation (9), and—even when viral genes do terminate in an amber codon—the inability to read a stop codon does not limit the synthesis of full-length viral proteins. In contrast, sense codons are commonly at least 10 times more abundant than amber codons in viral genomes and occur over the length of viral genes; thus, we predicted that a cell that does not read sense codons would not make full-length viral proteins and would therefore be completely resistant to viruses.

Current strategies for encoding new monomers in cells are limited to encoding a single type of monomer (commonly in response to the amber stop codon) (3, 10, 11), directing the inefficient incorporation of monomers or potentially incompatible with encoding sequential monomers (12–17); these limitations preclude the synthesis of noncanonical heteropolymer sequences composed entirely of noncanonical monomers. We hypothesized that reassigning sense codons to noncanonical monomers may enable the efficient and sequential polymerization of distinct noncanonical monomers to produce noncanonical heteropolymers.

Recently, a strain of *E. coli*, Syn61, was created with a synthetic recoded genome in which all annotated occurrences of two sense codons (serine codons TCG and TCA) and a stop codon (TAG) were replaced with synonymous codons (18). In this study, we evolved Syn61 and deleted the tRNAs and release

¹Medical Research Council Laboratory of Molecular Biology, Cambridge, UK. ²Department of Biochemistry, University of Cambridge, Cambridge, UK.

*Corresponding author. Email: chin@mrc-lmb.cam.ac.uk

†These authors contributed equally to this work.

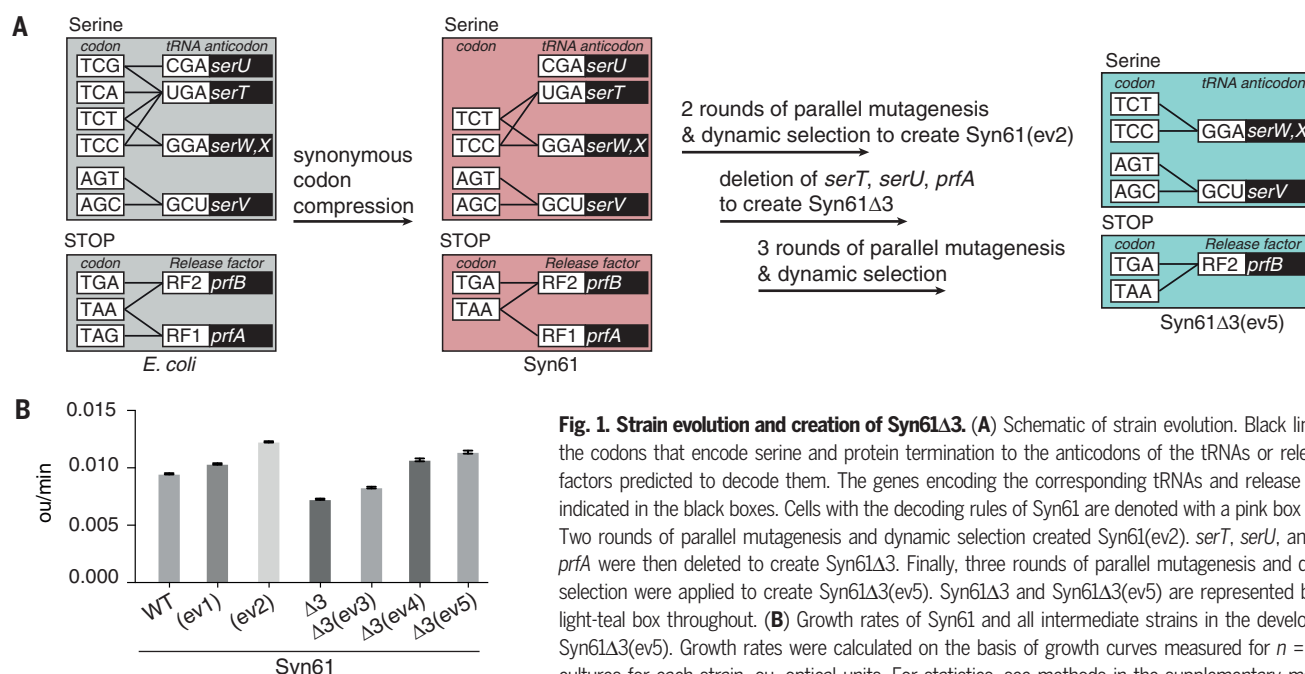
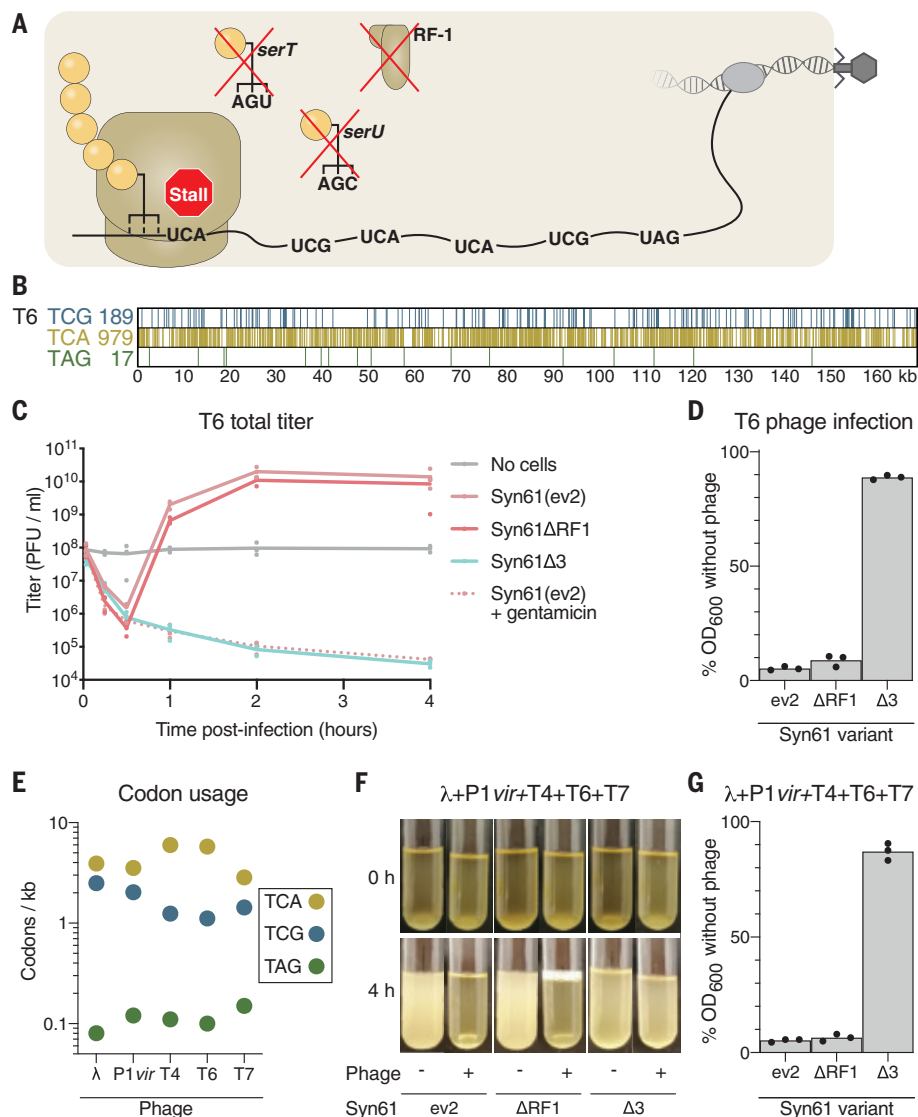


Fig. 1. Strain evolution and creation of Syn61Δ3. (A) Schematic of strain evolution. Black lines connect the codons that encode serine and protein termination to the anticodons of the tRNAs or release factors predicted to decode them. The genes encoding the corresponding tRNAs and release factors are indicated in the black boxes. Cells with the decoding rules of Syn61 are denoted with a pink box throughout. Two rounds of parallel mutagenesis and dynamic selection created Syn61(ev2). *serT*, *serU*, and *prfA* were then deleted to create Syn61Δ3. Finally, three rounds of parallel mutagenesis and dynamic selection were applied to create Syn61Δ3(ev5). Syn61Δ3 and Syn61Δ3(ev5) are represented by the light-teal box throughout. (B) Growth rates of Syn61 and all intermediate strains in the development of Syn61Δ3(ev5). Growth rates were calculated on the basis of growth curves measured for $n = 8$ replicate cultures for each strain. ou, optical units. For statistics, see methods in the supplementary materials.

Fig. 2. Lytic phage propagation and cell lysis are obstructed in Syn61Δ3.

(A) Schematic of viral infection of Syn61Δ3. Deletion of *serU* (encoding tRNA^{Ser}_{CGA}), *serT* (encoding tRNA^{Ser}_{UGA}), and *prfA* (encoding RF1) makes the UCG, UCA, and UAG codons unreadable, and the ribosome will stall at these codons within an mRNA that contains them, as shown here for a viral mRNA. **(B)** Schematic of the number of TCG, TCA, and TAG codons and their positions in the genome of T6 phage. **(C)** Cultures were infected with T6 phage at a multiplicity of infection (MOI) of 5×10^{-2} , and the total titer (intracellular phage plus free phage) was monitored over 4 hours. PFU, plaque-forming units. Treatment with gentamicin was used to ablate protein synthesis, providing a control for cells that cannot synthesize viral proteins or produce new viral particles. **(D)** T6 efficiently lyses Syn61 variants but not Syn61Δ3. Cultures were infected as in panel (C), and OD₆₀₀ was measured after 4 hours. **(E)** Number of the indicated codons per kilobase in each indicated phage. **(F and G)** Syn61Δ3 survives simultaneous infection of multiple phage. **(F)** Photos of the culture at the indicated time points after infection (+) or in the absence of infection (−). Cultures were infected with phage λ, P1, T4, T6, and T7, each with an MOI of 1×10^{-2} . **(G)** OD₆₀₀ of the cultures was measured after 4 hours. All experiments were performed in three independent replicates; the dots represent the independent replicates, and the line (C) or bar [(D) and (G)] represents the mean. The photo (F) is a representative of data from three independent replicates.



factor that decode TCG, TCA, and TAG codons. We show that the resulting strain provides complete resistance to a cocktail of viruses. Moreover, we demonstrate the encoded incorporation of noncanonical amino acids (ncAAs) in response to all three codons and the encoded, programmable cellular synthesis of entirely noncanonical heteropolymers and macrocycles.

Creating Syn61Δ3

We predicted that replacing the annotated TCA, TCG, and TAG codons in the genome would enable deletion of *serT* and *serU* (encoding tRNA^{Ser}_{UGA} and tRNA^{Ser}_{CGA}, respectively) and *prfA* (encoding RF1), which decode these codons, in a single strain (Fig. 1A). We previously showed that *serT*, *serU*, and *prfA* could be deleted in separate strains derived from Syn61 (18); however, this does not capture the potential epistasis between these genes. We sought to determine whether *serT*,

serU, and *prfA* could be deleted in a single strain derived from Syn61.

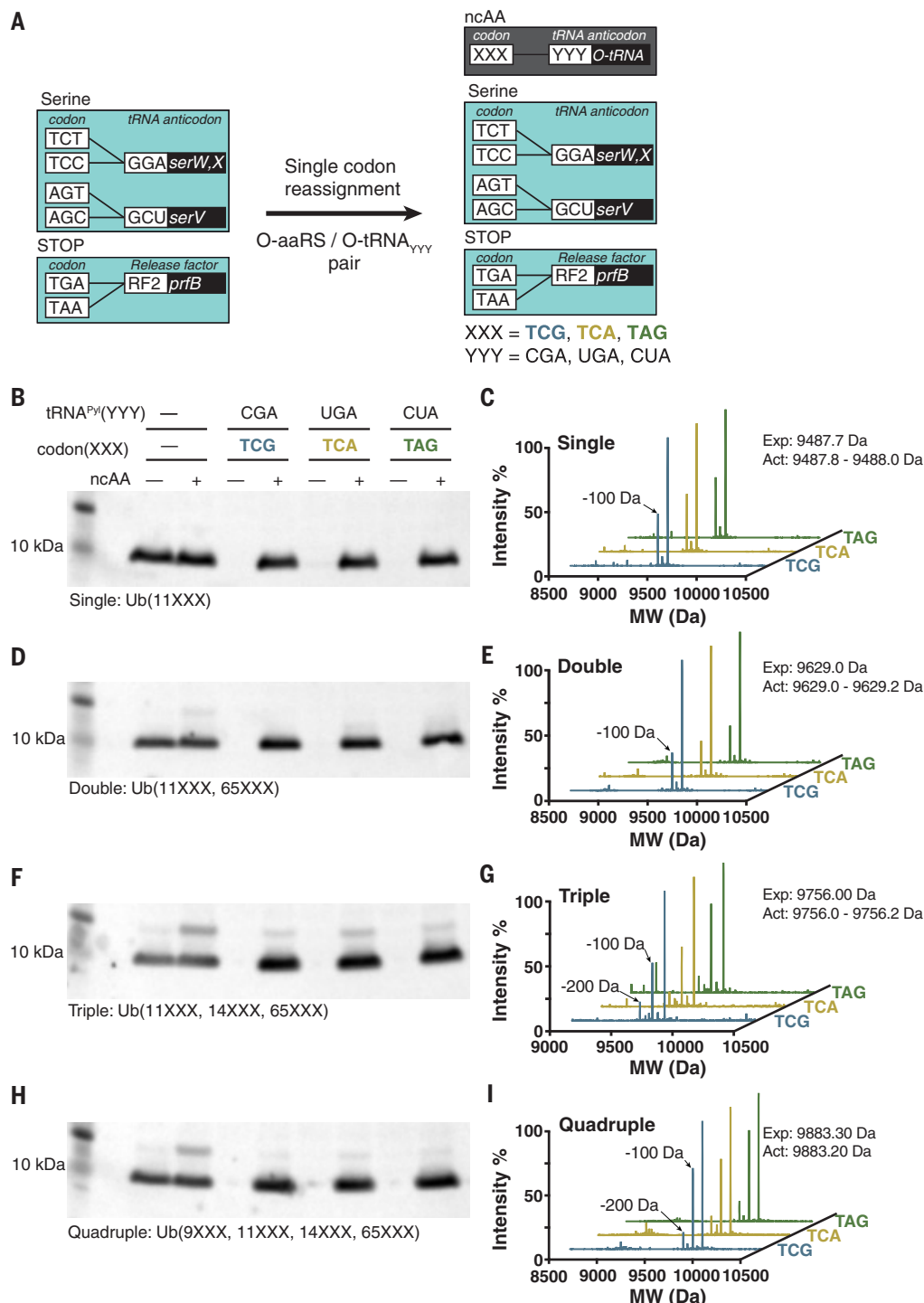
Syn61 grows 1.6 times slower than the strain from which it was derived (18). To increase the growth rate of the strain before *serT*, *serU*, and *prfA* deletion, we applied a previously described random parallel mutagenesis and automated dynamic parallel selection strategy (19); this approach uses feedback control to dynamically dilute mutated cultures on the basis of growth rate and thereby selects fast-growing strains from within mutated populations (fig. S1A). Through two consecutive rounds of mutagenesis and selection, we created a strain, Syn61(ev2), which grew 1.3-fold faster (Fig. 1B; fig. S1, B to E; and data S1 and S2).

Next, we removed *serU*, *serT*, and *prfA* from Syn61(ev2) to create Syn61Δ3 (Fig. 1A, fig. S1C, and data S1 and S2). This demonstrated that removing the target codons in Syn61 was sufficient to enable the deletion of all decoders of the target codons in the same

strain. However, Syn61Δ3 grew 1.7 times slower than Syn61(ev2) (Fig. 1B). This growth decrease may result from the presence of target codons in the genome of Syn61 that were not annotated and targeted (20, 21), and it may also result from the other noncanonical roles that tRNAs may play (22, 23).

We performed three sequential rounds of random parallel mutagenesis and automated dynamic parallel selection to evolve Syn61Δ3 to Syn61Δ3(ev5), which grew 1.6-fold faster than Syn61Δ3 (Fig. 1, A and B; fig. S1, B, C, and F to H; and data S1). When grown in lysogeny broth (LB) media in shake flasks, the doubling time of Syn61Δ3(ev5) was 38.72 ± 1.02 min (fig. S1I). Syn61Δ3(ev5) contains 482 additional mutations with respect to Syn61—420 substitutions and 62 indels—of which 72 are in intergenic regions (data S1 and S3 and fig. S2). No target codons were reverted, further demonstrating the stability of our recoding scheme. Sixteen sense codons in nonessential genes were converted

Fig. 3. Reassigning two sense codons and a stop codon to noncanonical amino acid in Syn61Δ3. (A) Schematic of each codon reassignment. Introduction of an orthogonal aaRS/tRNA_{YYY} pair—where YYY is the sequence of the anticodon of the orthogonal tRNA (encoded by *O*-tRNA)—to Syn61Δ3 (light-teal box, as described in Fig. 1A) enables decoding of the cognate codon (XXX) introduced into a gene of interest. The orthogonal pair directs the incorporation of a noncanonical amino acid (ncAA) in response to the XXX codon. These codon reassignments are indicated in the dark gray box. (B) TCG, TCA, and TAG codons are not read by the translational machinery in Syn61Δ3, and codon reassignment enables ncAA incorporation into Ub_{11XXX}. Plasmids encoding the orthogonal *Mm*PylRS/*Mmt*tRNA^{Pyl}_{YYY} pair and a C-terminally His₆-tagged ubiquitin, with a single TCG, TCA, or TAG codon at position 11 (*Ub*_{11XXX}), or no target codons (wild type, wt) were introduced into Syn61Δ3. “XXX” denotes a target codon, and “YYY” denotes a cognate anticodon. Expression of ubiquitin-His₆ was performed in the absence (–) or presence (+) of a ncAA substrate for *Mm*PylRS, Bock. Full-length ubiquitin-His₆ was detected in cell lysate from an equal number of cells with an anti-His₆ antibody. (C) Production of ubiquitin-His₆ incorporating Bock, Ub_{11Bock}-His₆, from a *Ub*_{11XXX} gene bearing the indicated target codon was confirmed by ESI-MS. MW, molecular weight. Theoretical mass: 9487.7 Da; measured mass: 9487.8 Da (TCG), 9487.8 Da (TCA), and 9488.0 Da (TAG). The smaller peak of –100 Da results from the loss of *tert*-butoxycarbonyl from Bock. (D) As in (B), but using *Ub*_{11XXX,65XXX}, which contains target codons at positions 11 and 65 of the *Ub* gene. (E) Production of ubiquitin-His₆ incorporating Bock at positions 11 and 65, from a *Ub*_{11XXX,65XXX} gene bearing the indicated target codons was confirmed by ESI-MS. Theoretical mass: 9629.0 Da; measured mass: 9629.2 Da (TCG), 9629.0 Da (TCA), and 9629.0 Da (TAG). The smaller peak of –100 Da corresponds to loss of *tert*-butoxycarbonyl from Bock. (F) As in (B), but using *Ub*_{11XXX,14XXX,65XXX}, which contains target codons at positions 11, 14, and 65 of the *Ub* gene. (G) Production of ubiquitin-His₆ incorporating Bock at positions 11, 14, and 65, from *Ub*_{11XXX,14XXX,65XXX} bearing the indicated target codons was confirmed by ESI-MS. Theoretical mass: 9756.0 Da; measured mass: 9756.2 Da (TCG), 9756.0 Da (TCA), and 9756.0 Da (TAG). The smaller peaks of –100



or –200 Da correspond to loss of *tert*-butoxycarbonyl from one or two Bock residues, respectively. (H) As in (B), but using *Ub*_{9XXX,11XXX,14XXX,65XXX}, which contains target codons at positions 9, 11, 14, and 65 of the *Ub* gene. (I) Production of ubiquitin-His₆ incorporating Bock at positions 9, 11, 14, and 65, from *Ub*_{9XXX,11XXX,14XXX,65XXX} bearing the indicated target codons was confirmed by ESI-MS. Theoretical mass: 9883.3 Da; measured mass: 9883.2 Da (TCG), 9883.2 Da (TCA), and 9883.2 Da (TAG). The smaller peaks of –100 or –200 Da correspond to loss of *tert*-butoxycarbonyl from one or two Bock residues, respectively. All experiments were performed in biological replicates three times with similar results.

to target codons (5×TCG, 3×TCA, 8×TAG); these frequencies are comparable to those observed for other codons (data S1). Subsequent experiments used Syn61Δ3 or, once available, its evolved derivatives to investigate the new properties of these strains.

tRNA deletion ablates virus production in Syn61Δ3

We investigated the effects of deleting the genes encoding tRNA^{Ser}_{CGA}, tRNA^{Ser}_{UGA}, and RF1 on phage propagation by Syn61Δ3 (Fig. 2A) in a modified one-step growth experiment (24). For Syn61(ev2), the total titer of phage T6 [a representative of the lytic, T-even family (Fig. 2B)] briefly dropped (as phage infected cells) before rising to two orders of magnitude above the input titer, as infected cells produced new phage particles (Fig. 2C and fig. S3A). As expected, the optical density at 600-nm wavelength (OD₆₀₀) of Syn61(ev2) was decreased by infection with T6 phage, which is lytic (Fig. 2D). Syn61ΔRF1 (data S1) and Syn61(ev2) produced

a comparable amount of phage on a comparable time scale and showed similar changes in OD₆₀₀ upon infection. We conclude that deletion of RF1 alone has little, if any, effect on T6 phage production or cell lysis.

Infection of Syn61Δ3 with T6 phage led to a steady decrease in total phage titer. Notably, this decrease was comparable to that observed when protein synthesis, and therefore phage production in cells, was completely inhibited by addition of gentamicin (Fig. 2C and fig. S3B). Moreover, T6 infection had a minimal effect on the growth of Syn61Δ3 (Fig. 2D). We conclude that Syn61Δ3 does not produce new phage particles upon infection with T6 phage and that T6 phage does not lyse these cells. Similar results were obtained with T7 phage, which has 57 TCG codons, 114 TCA codons, and 6 TAG codons in its 40-kb genome (fig. S3, A, C, and D). We treated cells with a cocktail of phage containing lambda, P1vir, T4, T6, and T7, which have TCA or TCG sense codons that are 10 to 58 times more abundant

than the amber stop codon in their genomes (Fig. 2E and fig. S3E), and found that the treatment with this phage cocktail led to lysis of Syn61(ev2) and Syn61ΔRF1 but had little effect on the growth of Syn61Δ3 (Fig. 2, F and G), suggesting that the deletion of tRNAs in Syn61Δ3 provides resistance to a broad range of phage.

Reassigning target codons for ncAA incorporation

We expressed *Ub_{11XXX}* genes (*ubiquitin-His₆* bearing TCG, TCA, or TAG at position 11) and genes encoding the cognate orthogonal *MmtRNA^{Pyl}/MmtRNA^{Pyl}* pair (25) (in which the anticodon is complementary to the codon at position 11 in the *Ub* gene) in Syn61Δ3(ev5) (Fig. 3A and data S2).

In the absence of added ncAA, little to no ubiquitin was detected from *Ub* genes bearing a target codon at position 11, while control experiments demonstrated that ubiquitin is produced from a “wild-type” gene that does

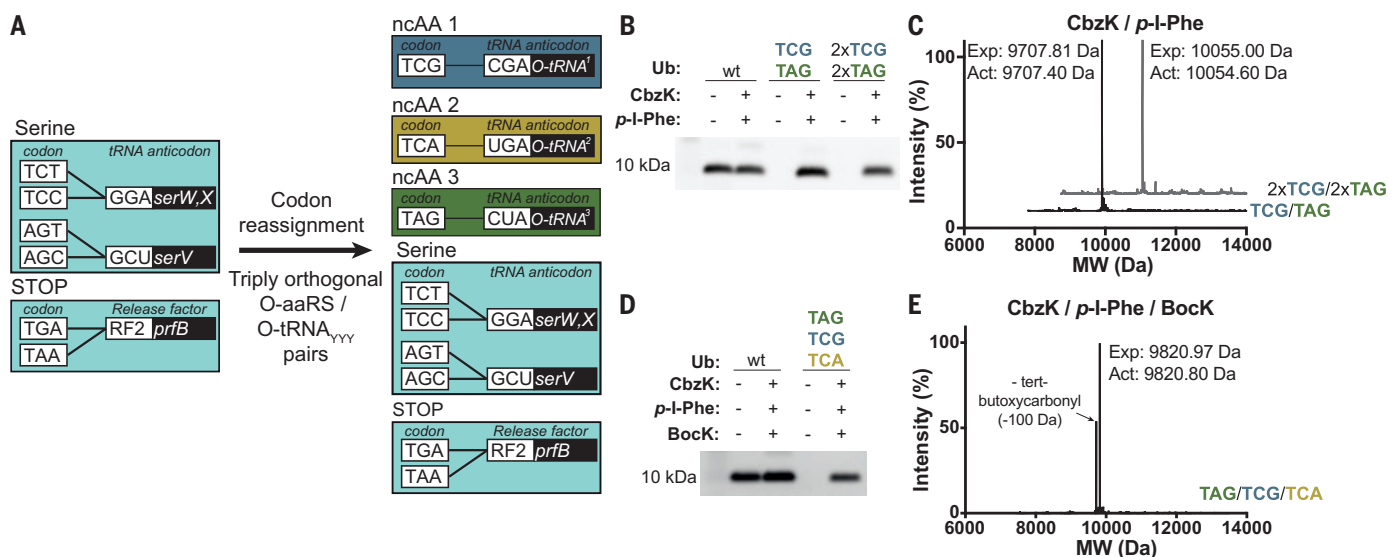


Fig. 4. Double and triple incorporation of distinct noncanonical amino acids into TCG, TCA, and TAG codons in Syn61Δ3 cells. (A) Reassignment of TCG (blue box), TCA (gold box), and TAG (green box) codons to distinct ncAAs in Syn61Δ3. Reassigning all three codons to distinct ncAAs in a single cell requires three engineered triply orthogonal aaRS/tRNA pairs. Each pair must recognize a distinct ncAA and decode a distinct codon. The tRNAs from these triply orthogonal pairs are labeled O-tRNA¹⁻³. (B) The incorporation of two distinct noncanonical amino acids in response to TCG and TAG codons in a single gene. Syn61Δ3(ev4)—containing the *IR26PylRS*(CbzK)/*AlvtRNA^{ANPyl(8)}*_{CGA} pair (16) and the *AfTyrRS*(p-I-Phe)/*AfRNA^{Tyr(A01)}*_{CUA} pair (29), which direct the incorporation of CbzK into TCG and p-I-Phe into TAG, respectively—were provided with CbzK and p-I-Phe. Cells also contained *Ub_{11TCG,65TAG}* (TCG/TAG), *Ub_{9TCG,11TCG,14TAG,65TAG}* (2×TCG/2×TAG), or wt *Ub*, which contains no target codons. Expression of ubiquitin-His₆ was performed in the absence (–) or presence (+) of the ncAAs. Full-length ubiquitin-His₆ was detected in cell lysate from an equal number of cells with an anti-His₆ antibody. (C) ESI-MS analyses of purified Ub-(11CbzK, 65p-I-Phe) (black trace) and Ub-(11CbzK, 14CbzK, 57p-I-Phe, 65p-I-Phe) (gray trace),

expressed in the presence of CbzK and p-I-Phe, as described in (E) and purified by nickel–nitrilotriacetic acid chromatography. These data confirm the quantitative incorporation of CbzK and p-I-Phe in response to TCG and TAG codons, respectively. Ub-(11CbzK, 65p-I-Phe), theoretical mass: 9707.81 Da; measured mass: 9707.40 Da. Ub-(11CbzK, 14CbzK, 57p-I-Phe, 65p-I-Phe), theoretical mass: 10,055.00 Da; measured mass: 10,054.60 Da. (D) The incorporation of three distinct noncanonical amino acids into TCG, TCA, and TAG codons in a single gene. Syn61Δ3(ev4)—containing the *IR26PylRS*(CbzK)/*AlvtRNA^{ANPyl(8)}*_{CGA} pair, the *MmtRNA^{Pyl}*_{UGA} pair, and the *AfTyrRS*(p-I-Phe)/*AfRNA^{Tyr(A01)}*_{CUA} pair—were provided with CbzK, Bock, and p-I-Phe. Cells also contained *Ub_{9TAG,11TCG,14TCA}* (TCG/TCA/TAG). Expression of this gene was performed in the absence (–) or presence (+) of the ncAAs. Full-length Ub-(9p-I-Phe, 11CbzK, 14BocK)-His₆ was detected in cell lysate from an equal number of cells with an anti-His₆ antibody. (E) ESI-MS of purified Ub-(9p-I-Phe, 11CbzK, 14BocK)-His₆, theoretical mass: 9820.97 Da; measured mass: 9820.80 Da. Western blot experiments [(B) and (D)] were performed in five biological replicates with similar results. The ESI-MS data [(C) and (E)] were collected once.

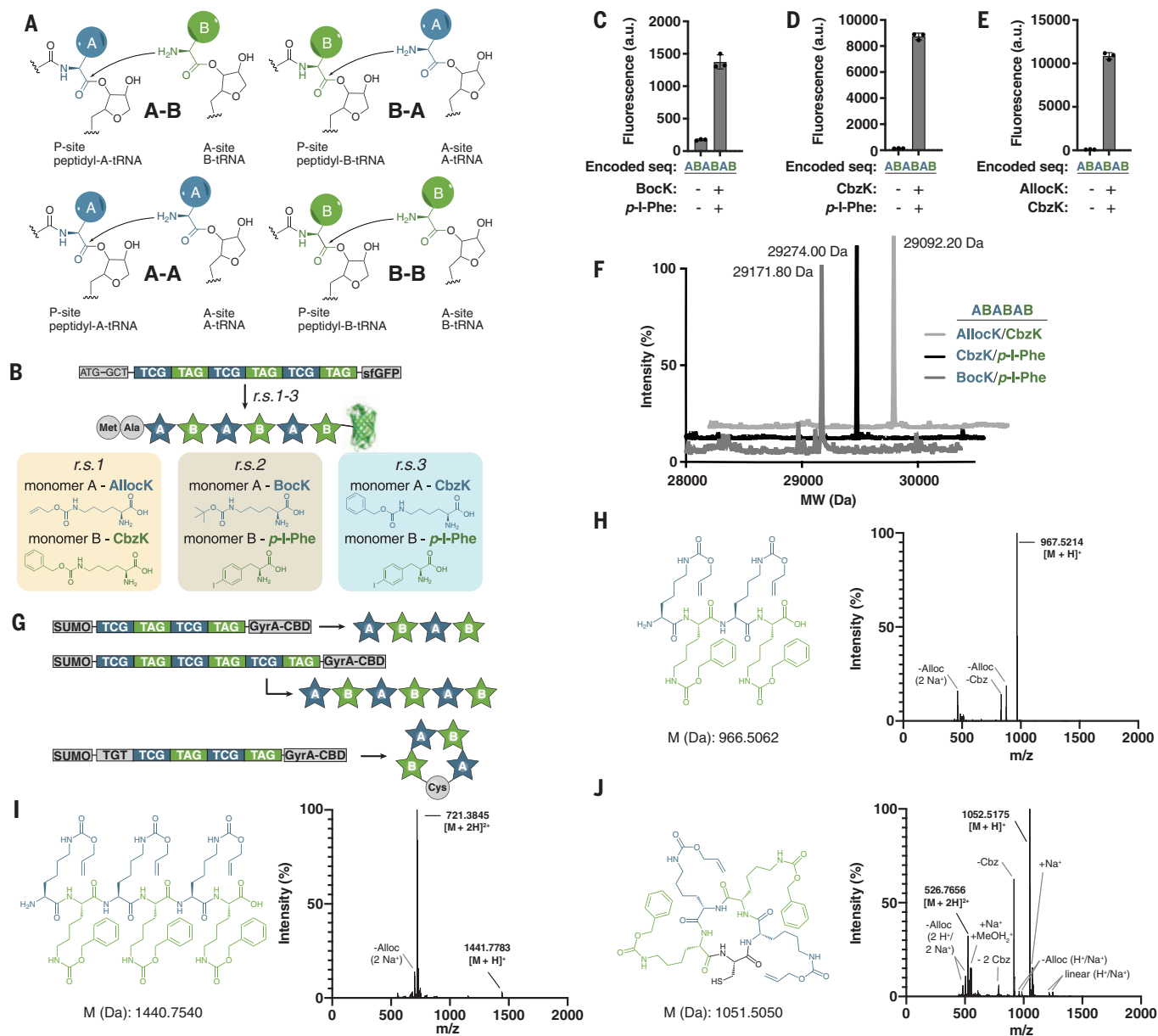


Fig. 5. Programmable, encoded synthesis of noncanonical heteropolymers and macrocycles. (A) Elementary steps in the ribosomal polymerization of two distinct ncAA monomers [labeled A (dark blue) and B (green)]. All linear heteropolymer sequences composed of A and B can be encoded from these four elementary steps. (B) Encoding heteropolymer sequences (noncanonical monomers are shown as stars). The sequence of monomers in the heteropolymer is programmed by the sequence of codons written by the user. The identity of monomers (A and B) is defined by the aaRS/tRNA pairs added to the cell. Cells can be reprogrammed to encode different heteropolymer sequences from a single DNA sequence. Sequences were encoded as insertions at position 3 of *sfGFP-His6*. Reassignment scheme 1 (r.s.1) uses the *MmPylRS/MmtRNA^{Pyl}_{CGA}* pair to assign AllocK as monomer A and the *IR26PylRS(CbzK)/AlfRNA^{ANPyl(8)}_{CUA}* pair to assign CbzK as monomer B (fig. S7, D and E). r.s.2 uses the *MmPylRS/MmtRNA^{Pyl}_{CGA}* pair to assign BockK as monomer A and an *AfTyrRS(p-I-Phe)/AftRNA^{Tyr(A01)}_{CUA}* pair to assign p-I-Phe as monomer B. r.s.3 uses the *IR26PylRS(CbzK)/AlfRNA^{ANPyl(8)}_{CGA}* pair to assign CbzK as monomer A and the *AfTyrRS(p-I-Phe)/AftRNA^{Tyr(A01)}_{CUA}* pair to assign p-I-Phe as monomer B. (C to E) Polymerization of the encoded sequence composed of the indicated ncAAs and the resulting *sfGFP-His6* expression in Syn61Δ3(ev5) were dependent on the

addition of both ncAAs to the medium. a.u., arbitrary units. (F) ESI-MS of purified *sfGFP-His6* variants containing the indicated ncAA hexamers. BockK/p-I-Phe (expected mass after loss of N-terminal methionine: 29,172.07 Da; observed: 29,171.8 Da), CbzK/p-I-Phe (expected mass after loss of N-terminal methionine: 29,274.13 Da; observed: 29,274.0 Da), and AllocK/CbzK (expected mass after loss of N-terminal methionine: 29,091.64 Da; observed: 29,092.2 Da). The ESI-MS data was collected once. (G) Encoded synthesis of free noncanonical polymers. DNA sequences encoding a tetramer and a hexamer were inserted between SUMO and a GyrA intein coupled to a CBD, in Syn61Δ3(ev5) cells containing the same pairs as in r.s.1 (B). Expression of the constructs, followed by ubiquitin-like-specific protease 1 (Ulp1) cleavage and GyrA transthiostereification cleavage, results in the isolation of free noncanonical tetramer and hexamer polymers. Adding an additional cysteine immediately upstream of the polymer sequence results in self-cleavage and release of a macrocyclic noncanonical polymer. (H to J) Chemical structures and ESI-MS spectra of the purified linear and cyclic AllocK/CbzK heteropolymers. The raw ESI-MS spectra show the relative intensity and observed mass/charge ratios for the different noncanonical peptides. The observed masses corresponding to the expected $[M + H]^+$ or $[M + 2H]^{2+}$ ions are highlighted in bold. Other adducts and fragment ions are labeled relative to these.

not contain any target codons (Fig. 3B). Thus, none of the target codons are read by the endogenous translational machinery in Syn61Δ3. This further demonstrates that all of the target codons are orthogonal in this strain.

Upon addition of a ncAA substrate for the *MmPylRS/MmtRNA^{Pyl}* pair [*N*^ε-(*tert*-butoxycarbonyl)-L-lysine (BocK)] (25), ubiquitin was produced at levels comparable to wild-type controls (Fig. 3B and data S4). Electrospray ionization mass spectrometry (ESI-MS) and tandem mass spectrometry demonstrated the genetically directed incorporation of BocK at position 11 of Ub in response to each target codon using the complementary *MmPylRS/MmtRNA^{Pyl}* pair (Fig. 3C and fig. S4A). Additional experiments demonstrated efficient incorporation of ncAAs in response to sense and stop codons in glutathione *S*-transferase-maltose binding protein fusions (fig. S5 and data S4). We demonstrated good yields of Ub-His₆ incorporating two, three, or four ncAAs into a single polypeptide in response to each of the target codons (data S4; Fig. 3, D to I; and fig. S4, B to G), and we further demonstrated the incorporation of nine ncAAs in response to nine TCG codons in a single repeat protein (fig. S6). Together, these results demonstrate that the sense codons TCG and TCA and the stop codon TAG can be efficiently reassigned to ncAAs in Syn61Δ3 derivatives.

Encoding distinct ncAAs in response to distinct target codons

Next, we assigned TCG, TCA, and TAG codons to distinct ncAAs in Syn61Δ3(ev4) using engineered mutually orthogonal aminoacyl-tRNA synthetase (aaRS)/tRNA pairs that recognize distinct ncAAs and decode distinct codons (Fig. 4A and fig. S7). We incorporated two distinct ncAAs into ubiquitin in response to TCG and TAG codons (Fig. 4B; fig. S8, A and B; and data S4) and demonstrated the incorporation of two distinct ncAAs at four sites in ubiquitin, with each ncAA incorporated at two different sites in the protein (Fig. 4, B and C; fig. S8, C to E; and data S4). We incorporated three distinct ncAAs into ubiquitin, in response to TCG, TCA, and TAG codons (Fig. 4, D and E; fig. S8F; and data S4). We demonstrated the generality of our approach by synthesizing seven distinct versions of ubiquitin, each of which incorporated three distinct ncAAs (figs. S9 and S10 and data S4).

Encoded noncanonical polymers and macrocycles

For a linear polymer composed of two distinct monomers (A and B), there are four elementary polymerization steps (A+B→AB, B+A→BA, A+A→AA, B+B→BB) from which any sequence can be composed (Fig. 5A). For ribosome-mediated polymerization, these four elementary steps correspond to each monomer acting

as an aminoacyl-site (A-site) or peptidyl-site (P-site) substrate to form a bond with another copy of the same type of monomer or with a different type of monomer (Fig. 5A). We encoded each elementary step by inserting TCG-TCG (encoding AA; we arbitrarily assign monomer A to the TCG codon in this nomenclature), TAG-TAG (encoding BB; we assign monomer B to the TAG codon), TCG-TAG (encoding AB), and TAG-TCG (encoding BA) at codon 3 of a superfolder green fluorescent protein (sfGFP) gene. We demonstrated the elementary steps for three pairs of monomers: A = BocK, B = (*S*)-2-amino-3-(4-iodophenyl)propanoic acid (*p*-I-Phe); A = *N*^ε-(carbobenzoyloxy)-L-lysine (CbzK), B = *p*-I-Phe; and A = *N*^ε-allyloxycarbonyl-L-lysine (AllocK), B = CbzK (Fig. 5B and fig. S11). We genetically encoded six entirely non-natural tetrameric sequences and a hexameric sequence for each pair of monomers, as well as an octameric sequence for the AllocK/CbzK pair (22 synthetic polymer sequences in total) (figs. S11 and S12 and Fig. 5, C to E). All encoded polymerizations were ncAA-dependent (figs. S11 and S12B and Fig. 5, C to E), and ESI-MS confirmed that we had synthesized the noncanonical hexamers and octamers as sfGFP fusions (Fig. 5F and fig. S12C). We encoded tetramer and hexamer sequences composed of AllocK and CbzK between SUMO (small ubiquitin-like modifier) and GyrA-CBD (DNA gyrase subunit A intein-chitin-binding domain) and purified the free polymers (Fig. 5, G to I; fig. S13; and data S4). Finally, we encoded the synthesis of a non-natural macrocycle reminiscent of the products of nonribosomal peptide synthetases (Fig. 5, G and J).

Discussion

We have synthetically uncoupled our strain from the ability to read the canonical code, and this advance provides a potential basis for bioproduction without the catastrophic risks associated with viral contamination and lysis (26, 27). We note that the synthetic codon compression and codon reassignment strategy we have implemented is analogous to models proposed for codon capture in the course of natural evolution (28).

Future work will expand the principles we have exemplified herein to further compress and reassign the genetic code. We anticipate that, in combination with ongoing advances in engineering the translational machinery of cells (4), this work will enable the programmable and encoded cellular synthesis of an expanded set of noncanonical heteropolymers with emergent, and potentially useful, properties.

REFERENCES AND NOTES

1. F. H. C. Crick, L. Barnett, S. Brenner, R. J. Watts-Tobin, *Nature* **192**, 1227–1232 (1961).
2. P. Marliere, *Syst. Synth. Biol.* **3**, 77–84 (2009).
3. J. W. Chin, *Nature* **550**, 53–60 (2017).

4. D. de la Torre, J. W. Chin, *Nat. Rev. Genet.* **22**, 169–184 (2021).
5. T. Passioura, H. Suga, *Trends Biochem. Sci.* **39**, 400–408 (2014).
6. A. C. Forster et al., *Proc. Natl. Acad. Sci. U.S.A.* **100**, 6353–6357 (2003).
7. M. J. Lajoie et al., *Science* **342**, 357–360 (2013).
8. N. J. Ma, F. J. Isaacs, *Cell Syst.* **3**, 199–207 (2016).
9. G. Korkmaz, M. Holm, T. Wiens, S. Sanyal, *J. Biol. Chem.* **289**, 30334–30342 (2014).
10. D. D. Young, P. G. Schultz, *ACS Chem. Biol.* **13**, 854–870 (2018).
11. C. C. Liu, P. G. Schultz, *Annu. Rev. Biochem.* **79**, 413–444 (2010).
12. Y. Zhang et al., *Nature* **551**, 644–647 (2017).
13. E. C. Fischer et al., *Nat. Chem. Biol.* **16**, 570–576 (2020).
14. H. Neumann, K. Wang, L. Davis, M. Garcia-Alai, J. W. Chin, *Nature* **464**, 441–444 (2010).
15. K. Wang et al., *Nat. Chem.* **6**, 393–403 (2014).
16. D. L. Dunkelmann, J. C. W. Willis, A. T. Beattie, J. W. Chin, *Nat. Chem.* **12**, 535–544 (2020).
17. J. S. Italia et al., *J. Am. Chem. Soc.* **141**, 6204–6212 (2019).
18. J. Fredens et al., *Nature* **569**, 514–518 (2019).
19. W. H. Schmied et al., *Nature* **564**, 444–448 (2018).
20. M. R. Hemm et al., *J. Bacteriol.* **192**, 46–58 (2010).
21. S. Meydan et al., *Mol. Cell* **74**, 481–493.e6 (2019).
22. A. Katz, S. Elgamil, A. Rajkovic, M. Ibba, *Mol. Microbiol.* **101**, 545–558 (2016).
23. Z. Su, B. Wilson, P. Kumar, A. Dutta, *Annu. Rev. Genet.* **54**, 47–69 (2020).
24. L. You, P. F. Suthers, J. Yin, *J. Bacteriol.* **184**, 1888–1894 (2002).
25. T. Yanagisawa et al., *Chem. Biol.* **15**, 1187–1197 (2008).
26. V. Bethencourt, *Nat. Biotechnol.* **27**, 681 (2009).
27. J. A. Zahn, M. C. Halter, in *Bacteriophages: Perspectives and Future*, R. Savva, Ed. (IntechOpen, 2018).
28. S. Osawa, T. H. Jukes, *J. Mol. Evol.* **28**, 271–278 (1989).
29. D. Cervettini et al., *Nat. Biotechnol.* **38**, 989–999 (2020).
30. D. Cervettini, K. C. Liu, J. W. Chin, Scripts for Sense Codon Reassignment Enables Viral Resistance and Encoded Polymer Synthesis, Version 1.0, Zenodo (2021); <https://doi.org/10.5281/zenodo.4666529>.

ACKNOWLEDGMENTS

We thank Z. Zeng and R. Monson (Department of Biochemistry, University of Cambridge) for helping with phage assays. **Funding:** This work was supported by the Medical Research Council (MRC), UK (MC_U105181009, MC_UP_A024_1008, and Development Gap Fund Award P2019-0003) and an ERC Advanced Grant SCCR, all to J.W.C. **Author contributions:** L.F.H.F. and K.C.L. performed strain evolution experiments. L.F.H.F., W.E.R., and S.B. performed experiments to knock out *serT*, *serU*, and *prfA*. L.F.H.F. analyzed genome sequences. J.F. performed phage experiments, with advice and supervision from G.P.C.S. W.E.R., D.d.I.T., T.S.E., Y.C., D.C., F.L.B., M.S., and S.M. performed experiments and analysis to demonstrate codon reassignment and ncAA incorporation in response to target codons. D.C. wrote scripts to analyze codon usage in bacteriophage genomes. J.W.C. supervised the project and wrote the manuscript, together with the other authors. **Competing interests:** The authors declare no competing interests. **Data and materials availability:** The GenBank accession numbers for all the strains and plasmids described in the text are provided in data S1 and S2, and the authors agree to provide any data or materials and strains used in this study upon request. Scripts for analyzing codon usage, next-generation sequencing sample preparation, and automated strain evolution are available in Zenodo (30).

SUPPLEMENTARY MATERIALS

science.sciencemag.org/content/372/6546/1057/suppl/DC1
Materials and Methods
Figs. S1 to S13
References (31–41)
MDAR Reproducibility Checklist
Data S1 to S4

23 December 2020; accepted 8 April 2021
10.1126/science.abg3029

HIGH PRESSURE

Establishing gold and platinum standards to 1 terapascal using shockless compression

D. E. Fratanduono^{1*}, M. Millot¹, D. G. Braun¹, S. J. Ali¹, A. Fernandez-Pañella¹, C. T. Seagle², J.-P. Davis², J. L. Brown², Y. Akahama³, R. G. Kraus¹, M. C. Marshall¹, R. F. Smith¹, E. F. O'Bannon III¹, J. M. McNaney¹, J. H. Eggert¹

New techniques are advancing the frontier of high-pressure physics beyond 1 terapascal, leading to new discoveries and offering stringent tests for condensed-matter theory and advanced numerical methods. However, the ability to absolutely determine the pressure state remains challenging, and well-calibrated pressure-density reference materials are required. We conducted shockless dynamic compression experiments at the National Ignition Facility and the Z machine to obtain quasi-absolute, high-precision, pressure-density equation-of-state data for gold and platinum. We derived two experimentally constrained pressure standards to terapascal conditions. Establishing accurate experimental determinations of extreme pressure will facilitate better connections between experiments and theory, paving the way toward improving our understanding of material response to these extreme conditions.

Extreme pressure conditions are known to fundamentally change bonding, crystal structures, and transport properties. In the terapascal range (1 TPa = 10 Mbar = 10 million atmospheres), these changes give rise to exotic physical properties, including pressure-induced insulator-to-metal phase transitions [metallic hydrogen (1, 2)], electride structures (3, 4) [insulating sodium (5)], superionicity [proton conductivity in water (6)], and room-temperature superconductivity (7, 8). Recent improvements in experimental capabilities in static compression (9–16) and dynamic compression (1, 2, 6, 17) have made these extreme pressures more readily accessible, opening up the exploration of material properties under these conditions. These exciting discoveries (1, 2, 4, 6–8) and new theoretical predictions (3, 18, 19) of material behavior at extreme conditions motivate access to these ultrahigh pressures and beyond.

Characterizing materials at extreme pressures is often accomplished through x-ray diffraction (10–16), neutron scattering (20, 21), or optical techniques (1, 2, 6, 17). However, accurately determining the pressure in static experiments at high pressure (22) is demanding because of the small sample sizes, potential pressure gradients, and substantial anvil-gasket friction that results in a deviation between the external load on the anvil and the internal pressure of the cell. These studies instead rely on reference materials to act as pressure gauges (standards) (23). Equation-of-state (EOS) standards are calibrated by means of direct pressure-density measurements using several types of experiments and have been limited to pressures below ~0.450 TPa. At terapascal

conditions, the material response of these standards have been determined through extrapolation of the low-pressure behavior, and these extrapolations have errors of >10% near 1 TPa at room temperature (298 K) (24, 25). Discrepancies are very apparent when different standards are compared with each other (26) and when those standards are used at elevated temperatures. Therefore, reliable pressure standards at terapascal conditions are needed for comparing data from different experimental approaches and to better connect experi-

ments to theoretical models and advanced numerical simulations.

Ultrafast shockless dynamic compression

The shock compression of dense materials has a long history of providing high-precision, absolute pressure-density measurements (27). Symmetric impacts allow the measurement of pressure, density, and internal energy of the shocked state independent of a reference material. The most common high-pressure standards are derived from these shock-wave experiments. (28, 29). The early development of the ruby luminescence pressure scale up to 20 GPa was benchmarked to the sodium chloride (NaCl) EOS by using shock data to validate its accuracy (28, 30). Similarly, the first-order Raman spectra of diamond anvils (31) were investigated at high pressures to develop an optical method for pressure determination. The widely used diamond Raman scale (31) is anchored to the platinum (Pt) shock EOS (27).

In practice, most static compression experiments, theoretical models, and numerical simulations correspond to an isothermal compression path, usually at 298 K for experiments and 0 K in quantum simulations, whereas shock compression realizes an irreversible, adiabatic compression path. The Rankine-Hugoniot equations (27) show that shock compression to a given pressure (P_H) achieves a change in density (ρ_H) but also an increase in internal energy greater than the isentropic compression work

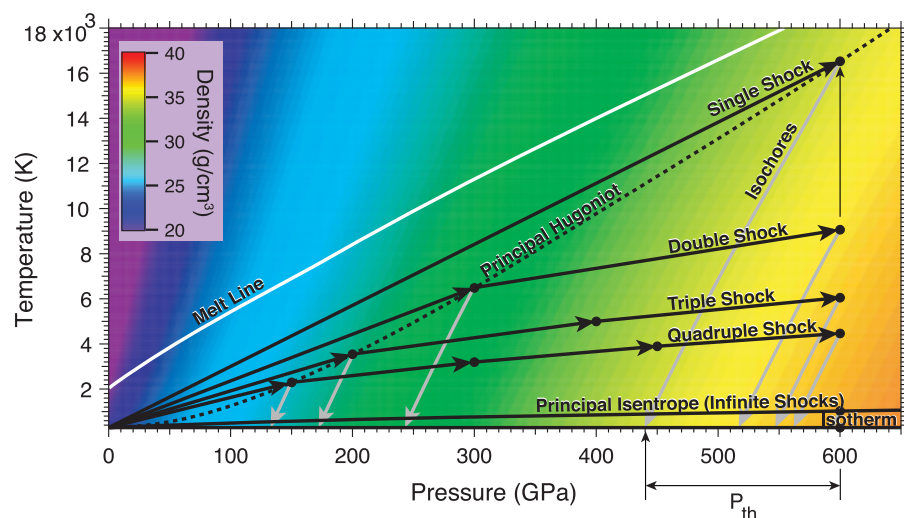


Fig. 1. The phase diagram of platinum. Five different dynamic compression pathways, each achieving a peak pressure state of 600 GPa, are shown. The room-temperature isotherm (the fundamental thermodynamic path used in the development of wide-ranging EOS models) is also shown. Under single-shock compression, a single end state along the principal Hugoniot is achieved. As more intermediate dynamic shock states are added, a higher-density and lower-temperature end state is achieved (more work is put into compression and less into waste heat). In the limit of an infinite number of weak shocks, the dynamic compression pathway approximates the principal isentrope. Because of thermal effects in dynamic compression experiments, a single shock to 600 GPa can be used to constrain the isotherm to only 440 GPa. This is observed by following lines of constant density (isochores) from the shock state to the isotherm. In ramp-compression experiments, the systematic correction to reduce the dynamic compression measurements to the isotherm are less than shock compression, making ramp compression a better technique to constrain the isotherm.

¹Lawrence Livermore National Laboratory, Livermore, CA 94550, USA. ²Sandia National Laboratories, Albuquerque, NM 87185-1195, USA. ³Graduate School of Material Science, University of Hyogo, 3-2-1 Kouto, Kamigohri 678-1297, Japan.

*Corresponding author. Email: fratanduono1@llnl.gov

to the same density. This additional energy raises the temperature of the shock-compressed material to a given shock temperature (T_H). Shock compression and heating are therefore inseparable, and the locus of possible shock states is a curve in the pressure-density-temperature space called the Hugoniot (Fig. 1, dotted line). As a consequence of shock heating, the pressure required to reach a certain density ρ by using shock compression will be greater than the pressure needed using isothermal compression by an amount called the thermal pressure (P_{th}). For example, following the isochore (Fig. 1, gray line of constant density) from the single shock state at 600 GPa and 16,000 K to $P_T = 440$ GPa where it intersects the 298 K isotherm, the thermal pressure contribution from shock compression results in a $\sim 25\%$ pressure difference between the Hugoniot and the isotherm. The amount of shock-induced heating depends on material-specific properties and on the initial state of the system (P_0 , ρ_0 , T_0). Fundamentally, dense and stiff materials stay much colder than light and compressible materials for a given shock pressure. For example, at 200 GPa, the single shock temperature of Pt is less than 4000 K, but water reaches almost 15,000 K (32).

To define a high-pressure standard, shock $P - \rho$ data are often used to estimate the room-temperature isotherm. This requires thermodynamics modeling and additional, experimentally or numerically determined, values such as the specific heat or the Grüneisen parameter. As long as the heating is moderate and the thermal pressure remains much smaller than the shock pressure (a few percent of the shock pressure), the uncertainty of the systematic correction between the Hugoniot and the 298 K isotherm is less than the experimental uncertainty, yielding a high-accuracy isotherm. Shock compression of dense metals were therefore suitable to define high-pressure standards up to a few hundred gigapascals, but this becomes inadequate at higher pressure as the thermal pressure corrections diverge, and the latent heat of melting adds additional uncertainties.

For a fixed peak pressure, dividing the shock compression into multiple intermediate shock states is an effective way to reduce the shock-induced heating. We illustrate this with the compression paths to 600 GPa when using single-, double-, triple-, and quadruple-shock compression (Fig. 1). As the number of intermediate shocks increases, a greater portion of the internal energy is partitioned into pressure-volume work, and less energy is partitioned into waste heat, resulting in a higher-density, lower-temperature end state. In the limit of an infinite number of shocks, the amplitude of each shock approaches zero, and the multishock compression path becomes equivalent to shockless, isentropic compression. When compared with the 298 K isotherm, the pressure along the

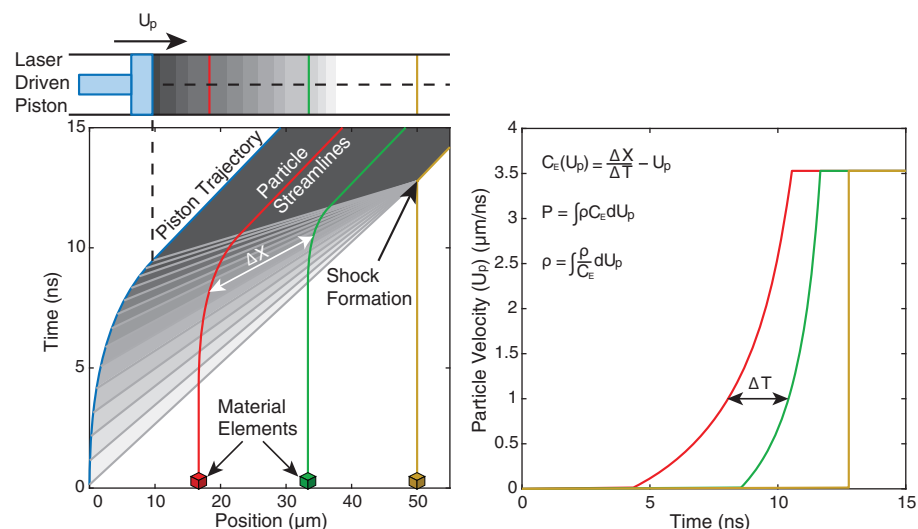


Fig. 2. The ramp-compression technique. In shockless compression experiments, a series of wavelets (gray lines) are carefully generated by a laser-driven piston. Increasing the applied piston pressure results in a steepening of these wavelets (called “characteristics”). The piston drive is carefully tailored so that the characteristics do not intersect over the duration of the experiment. In these experiments, we measured the speed of multiple material elements (shown as red, green, and yellow cubes). By measuring the element or particle velocity as a function of time [$U_p(t)$], and knowing the relative initial positions, we are able to determine the Eulerian speed of these characteristics (C_E). Using the measured $C_E(U_p)$ relationship and the known identities (Riemann invariants), we can determine the material pressure (P) and density (ρ) states accessed throughout the experiment.

isentrope at 600 GPa differs by only 6 GPa, providing a thermodynamic pathway that is far closer to the room-temperature isotherm than single-shock-wave experiments. In this work, we describe how the technique of shockless ramp compression eliminates the fundamental limitation of the shock heating and offers an alternative method to establish high-pressure standards to terapascal conditions. To minimize the thermal pressure corrections required to reduce the experimentally measured pressure to the isothermal pressure, dense and stiff materials are desirable. We chose gold (Au) and Pt, which are widely used reference materials because of their simple crystal structure, good x-ray scattering efficiencies, malleability, and phase stability along the room-temperature isotherm.

Using lasers and pulsed power to ramp compress Au and Pt

The culmination of multiple decades of technological developments (17, 33–35) allowed us to perform high-precision, shockless ramp-compression experiments, which represent a close approximation to isentropic compression up to terapascal pressures. We describe how these experiments yield quasi-absolute $P - \rho$ data suitable for a terapascal pressure standard and establish a new isothermal compression reference for Au and Pt to 1 TPa.

Shockless compression requires precise control over the applied loading pressure (Fig. 2). Driven in a precisely controlled way by a laser or pulsed-power source, a gradually accelerat-

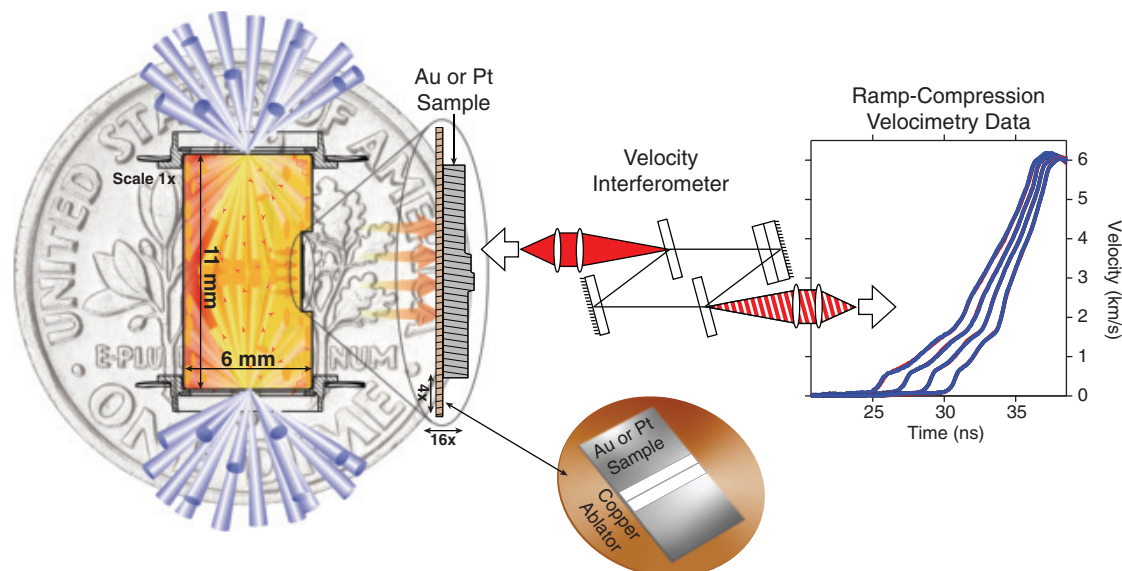
ing piston applies an increasing pressure and sends into the sample a series of compression (acoustic) waves of increasing amplitude. These wavelets propagate through the material at the speed of sound, along straight lines (called characteristics) in the Eulerian (laboratory) position-time diagram. Characteristics emerging from states of increasing compression become shallower because the slope is proportional to the summation of the particle speed and the Eulerian sound speed. Because the speed of sound usually increases with compression, ramp-compression loading is inherently unstable and leads to shock formation. If the piston accelerates too rapidly, characteristics could potentially cross, leading to the undesirable formation of a shock wave. However, using an educated guess for the pressure dependence of the sample's sound speed, we can precisely tune the rate of piston acceleration (that is, the temporal shape of the compression pulse) to delay the shock formation until after the experiment is over. We were able to compress Au and Pt samples to terapascal pressure in less than 30 ns using laser drivers (Fig. 2) or in hundreds of nanoseconds using pulsed-power drivers.

To extract the compressibility of the material, the particle velocity must be measured as a function of time [$U_p(t)$, where t is time and U_p is the particle velocity] for at least two material elements separated by an initially known distance (Δx) (Fig. 2). The speed of the “sound waves” (slope of the characteristics, $\Delta x/\Delta t$) is extracted through simple geometric means. Once we determined the slope of

Fig. 3. Schematic of the NIF experimental design.

The NIF facility accesses high-pressure conditions by generating high-energy-density states within a small volume. Using the NIF, we shine 172 beams into a gold hohlraum (a gold can), whose cross section is smaller than that of a U.S. dime. The optical 351-nm light ablates the interior of the hohlraum, generating an x-ray bath that ablates the physics package mounted on the equator. We carefully tune the laser pulse energy as a function of time to generate a smooth increasing ablation pressure

on our physics package (a 20- μm copper ablator with a diamond-turned multisteped Au or Pt sample). The ablation pressure generates a compression wave that propagates through the sample. Using a spatially resolving velocimeter, we measured the arrival of time of the compression waves and the corresponding acceleration of each step of the sample.



the characteristics, we then extracted the material sound speed as a function of particle velocity. We then integrated the sound speed as a function of particle velocity to extract the absolute pressure-density EOS information along the ramp-compression path. In our experiments, wave interactions at material interfaces further complicate the characteristics analysis and require a more detailed analysis (17, 33–35). This overall strategy is similar to the principles used in absolute Hugoniot flyer-plate measurements in that the particle velocity is determined from a measurement of the flyer-plate speed, and the shock velocity (akin to the sound speed) is determined from a transit time measurement through a known thickness (27).

We used the National Ignition Facility (NIF) to ramp compress Au and Pt (17). Using 172 laser beams, we coupled up to 500 kJ of laser energy over 30 ns into a 11- by 6-mm Au cylinder (hohlraum) to create a temporally controlled pressure source. Laser ablation of the Au cylinder walls converts the 351-nm laser light into an x-ray bath with a radiative temperature $T_r \sim 200$ eV. X-ray ablation of a copper (Cu) layer mounted on the equator of the hohlraum drives compression waves, with ablation pressure scaling approximately as T_r to the 3.5 power. The Cu compression waves propagate into the Au or Pt samples (Fig. 3), compressing them to high pressure. High precision in the delivery of a tailored laser-power pulse shape is essential to finely control the time-dependence of T_r and successfully achieve shockless ramp compression of the sample. Beam smoothing, power balance, and power accuracy among the 172 beams are essential to create a uniform pressure source across the 3.2-mm-diameter ablator.

On the NIF, we conducted three experiments on Au and four experiments on Pt (26).

We also used the Z pulsed-power accelerator at Sandia National Laboratories (33, 35) to magnetically drive uniaxial compression waves to compress Au and Pt samples (26). The Z accelerator produces a ~ 700 -ns temporally shaped ~ 20 MA current pulse that flows along the surface of Cu electrodes. The current pulse creates a time-varying magnetic field, and the interaction of the magnetic field with the current flux produces a time-varying force on the Cu electrodes that is propagated to the sample. On the Z machine, we conducted one experiment on Au and three experiments on Pt (26).

The NIF and the Z machine each provide specific benefits to constraining the EOS. The large sample sizes and longer time scales allows the Z machine to produce higher-accuracy measurements to ~ 400 GPa (35). The smaller sample size and higher available energy for compression enables the NIF to achieve pressure states of up to 5 TPa (34). Because the precision at the highest-pressure states is dependent on lower-pressure measurements (uncertainties integrate), combining the individual advantages of these two high-energy-density facilities enabled us to tightly constrain the material response of Au and Pt to terapascal conditions (26).

Measuring the velocity history of multiple material elements is key to determining the evolution of the sound speed in the sample and obtaining absolute pressure-density information along the ramp-compression path. Both the NIF and the Z machine used a velocity interferometer system for any reflector (VISAR) diagnostic to determine the interface velocities. Our NIF samples were precisely machined into

four-step profiles, and we recorded the free-surface velocity history $U_{FS}^i(t)$ for each step of thickness d^i (Fig. 3) with line-imaging VISAR. On the Z machine, the rectangular samples of thickness ranging from ~ 0.60 to ~ 1.6 mm were mounted onto a solid Cu electrode. A stripline geometry was used in which the free-surface velocity histories of step pairs were measured with multiple-point VISAR probes. Combining the velocity histories and the known thicknesses of the steps, we established the speed of the successive compression waves as a function of their amplitude. Achieving the level of accuracy on the sound speed measurements needed to establish a high-pressure standard requires great care for the machining and metrology of the steps, for the velocimetry measurements, and for the data analysis process. For the NIF samples, the steps are diamond-turned to achieve a ~ 10 -nm root-mean-square surface roughness, and their step heights (ranging from 60 to 90 μm) were measured to better than 50 nm (~ 500 atomic spacings) by means of optical interferometry. For the Z machine, each sample was diamond milled, and the thicknesses were measured to an accuracy of ~ 3 μm . Typical accuracy for the velocimetry measurements for each facility are better than ~ 30 m/s in velocity and ~ 30 ps in timing (~ 200 ps for the Z machine).

In our work, the velocity interferometer tracks the individual motion of material at the rear surface of the target, obtaining measurements in the Lagrangian reference frame. A more natural and simpler analysis approach is to transform the wave equations from the Eulerian (laboratory) frame of reference (Fig. 2) to a Lagrangian (material) frame through the transformation $\rho C_E = \rho_0 C_L$ and $\rho dx = \rho_0 dh$,

where C_E is the Eulerian sound speed, C_L is the Lagrangian sound speed, h is the Lagrangian coordinate, and ρ_0 is the ambient density. In this frame of reference, we used a non-iterative characteristics-based method (36) to correct for the compression wave reflection off the free surface of the target while applying a Lagrangian analysis to determine the sound speed as a function of particle velocity [$C_L(U_p)$]. Because of material strength and plastic work heating, we actually measured the longitudinal stress-density response. We obtained the longitudinal stress from the Riemann invariant $\sigma_x = \rho_0 [C_L dU_p]$ and the density $\rho = \rho_0 / (1 - \int dU_p / C_L)$.

Determination of Au and Pt isotherms

We iteratively applied a series of corrections to reduce the longitudinal stress-density measurements to the hydrostatic pressure-density principal isentrope from which we derived the 298 K (principal) isotherm (26). We used thermodynamic modeling to estimate the am-

plitude of deviatoric stress offsets, contributions to thermal pressure owing to the initial weak shock (~20 GPa) present in our NIF experiments, and plastic work heating owing to the material strength to determine an equivalent isentropic pressure-density response (17, 35). Further modeling of the isentropic thermal contribution allows us to obtain the absolute pressure-density response along the 298 K isotherm (26). For materials that exhibit complex physical properties, it has been shown that compression rates and time-dependent material response (such as strength and phase transition effects) can modify the isentrope. In these experiments, we saw no difference in the material response despite the 10× differences in strain-rate between the Z machine and the NIF, which is similar to previous observations on other simple metals (35, 36). The consistency between NIF and Z is likely due to the fact that Au and Pt are closely packed, high-density metals with low strength and no low-temperature

phase transitions. A reduced isotherm for materials that show no strain-rate response is increasingly important as techniques with different strain rates continue to evolve and result in different observations due to complex behavior (1, 2, 37). We performed a weighted average of the reduced isentrope for the NIF and Z data. At 800 GPa, the pressure correction at a fixed volume between the ramp-compression curve and the reduced isotherm amounts to a 15.7-GPa correction for Au (1.9% of the total pressure) and a 28.4-GPa correction for Pt (3.5% of the total pressure). The uncertainty associated with these corrections, when added in quadrature with the experimental uncertainties, contribute negligibly to the total (26). We found that for Au and Pt at 800 GPa, the relative standard deviations are 5.0 and 3.9%, respectively, which is a notable accuracy given the extreme condition of the measurement (pressure approximately two to three times greater than that in the center of the Earth).

We compared our averaged stress measurements, reduced isentrope, and 298 K isotherm for both Au (Fig. 4, left) and Pt (Fig. 4, right) with static compression experiments, including diamond anvil cell (DAC) data. Discrepancies between DAC data and our measurements were attributed to the pressure standard used in the DAC work. The lower plots in Fig. 4 illustrate the improvements in precision when using ramp compression to constrain the isotherm compared with shock measurements. We compared the magnitudes of the thermodynamic corrections applied to reduce Hugoniot (Fig. 4, black dashed line) and isentropic measurements (Fig. 4, cyan line) to the room-temperature isotherm. In our ramp experiments, the magnitude of the theoretical corrections is less than or comparable with the uncertainty in the experimental measurements for Au and Pt, respectively. For shock-wave measurements, above ~200 GPa the theoretical corrections and associated systematic errors dominate the uncertainties.

DACs with double-stage anvils (9, 10, 14, 16) and toroidal anvils (12, 13, 15) have accessed pressure states two to three times higher than states obtained in conventional DACs, which is a large advance in the accessible pressure range for static compression. Double-stage anvil experiments reported pressures in excess of 1.0 TPa in Au (9) on the basis of isotherm extrapolations of about two times in pressure beyond the shock experimental constraint (38). Using our experimentally constrained Au isotherm to 1.1 TPa and the highest measured Au volume in static compression experiments (9), we determined a peak pressure of 0.937 TPa, which is 12% lower than estimates based on previous isotherm extrapolations (1.065 TPa) (38). Such disagreement between model extrapolations and experimental measurements to terapascal conditions exemplifies the need

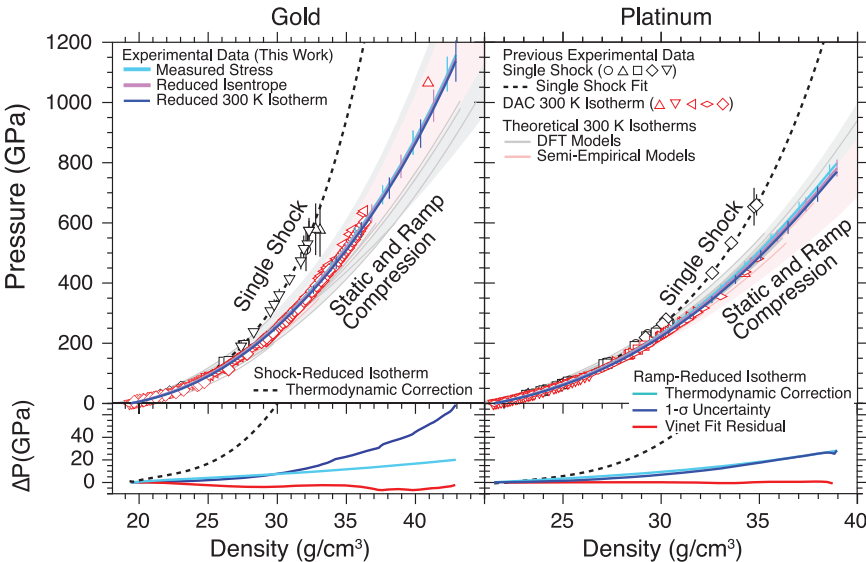
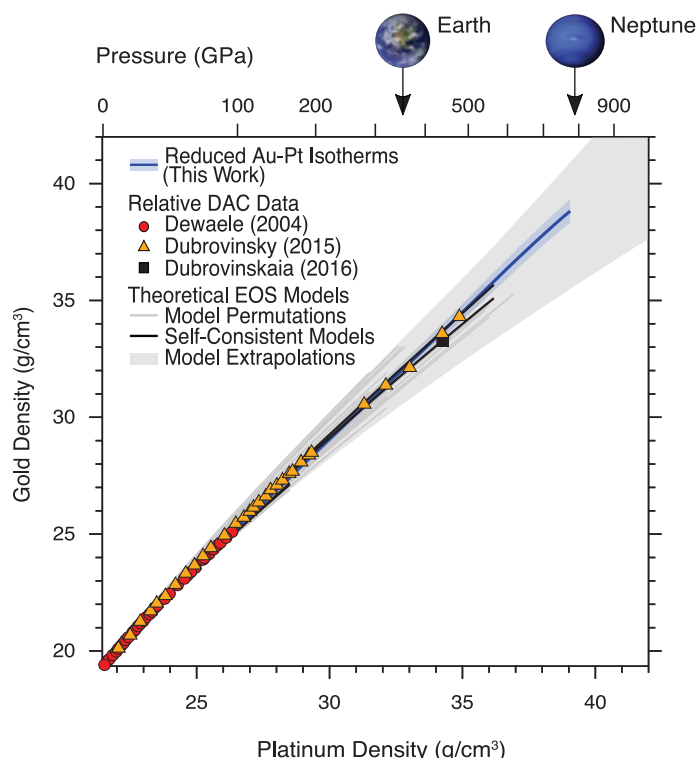


Fig. 4. The EOS of Au and Pt. The pressure-density response of Au and Pt to pressures in excess of 800 GPa are shown. **(Top)** The measured stress (cyan), reduced isentrope (purple), and the 298 K reduced isotherms (blue) are shown. The error bars represent 1σ standard deviation of multiple measurements collected and averaged into a single result. Existing density function theory (DFT) and semi-empirical models are shown as gray and red lines, respectively, with shaded regions indicating the extrapolation bounds of those models. Shock-wave data (black symbols) (27, 38, 40) and static data (red symbols) (39, 41–46) are shown. **(Bottom)** Illustration of the uncertainty in our reduced isotherm (blue), the magnitude of our corrections to reduce the stress measurements to the isotherm (cyan), the magnitude of shock-wave-reduced isotherm corrections (black dashed line), and the residual from our Vinet fit (solid red line).

Table 1. Vinet parameters. The Vinet fit parameters for the 298 K isotherm of Au and Pt.		
	Au	Pt
$\rho_0(\text{g}/\text{cm}^3)$	19.32	21.45
$V_0(\text{\AA}^3/\text{at})$	16.929	15.102
$K_{0,T}$	170.9 (±0.24)	259.7 (±0.16)
$K'_{0,T}$	5.880 (±0.005)	5.839 (±0.003)

Fig. 5. The high-pressure behavior of Au relative to Pt. Comparison of Au and Pt isothermal density with the isothermal pressure plotted along the top axis (planetary interior pressures are shown for pressure scale reference). This work (blue line, with shading representing the Au and Pt 1σ uncertainty) is compared with permutations of various Au and Pt EOS isotherm models (gray lines). Self-consistent models are shown as the black lines. The existing relative Pt-Au DAC data are shown as red circles (39), and double DAC measurements are shown as orange triangles (10) and black squares (11).



for more robust high-pressure scales, especially because the pressure-density conditions for the onset of complex physics behaviors are used to test theoretical predictions (15).

Our determinations of the isothermal compressibility of Au and Pt allowed us to compare the density of Au and Pt at a given pressure (Fig. 5). This allows comparison with high-pressure DAC experiments that simultaneously measured Au and Pt densities (Fig. 5) (11, 39). The agreement between our isotherms reduced from dynamic measurements with static measurements demonstrates the viability of our reference isotherms to 800 GPa. The remaining differences between the static and dynamic measurements may be attributed to nonhydrostatic conditions, pressure gradients (16), or differences in material response at high strain rates (36). The excellent agreement between results at different time scales (static DAC, $\sim 10^{-5}$ s; the Z machine, $\sim 10^{-7}$ s; and NIF, $\sim 10^{-8}$ s) give us some confidence in assuming that laboratory-based experiments are relevant for the much slower rates characteristic of planetary interior evolution ($\sim 10^4$ to 10^{16} s).

We propose our quasi-absolute isothermal data as a robust basis for pressure determination from volume measurements in DAC experiments. To this end, we fitted our data to the Vinet EOS and provide fit parameters for the Au and Pt 298 K isotherms in Table 1. The Vinet fitting form is $P(X) = 3K_{0,T}(1-X)X^{-2}e^{[1.5(K'_{0,T}-1)(1-X)]}$, where $X = (\frac{\rho_0}{\rho})^{1/3}$, ρ_0 is the ambient density, $K_{0,T}$ is the

isothermal bulk modulus, and $K'_{0,T}$ is the isothermal bulk modulus pressure derivative. Free parameters in the fit to the data are $K_{0,T}$ and $K'_{0,T}$ (Table 1). Fits to the Vinet equation provide a convenient way of tabulating and interpolating the reduced isotherms, but this form of the EOS should not be used to extrapolate beyond the region of the data. Fits to different functional forms and their covariance matrices are provided in the supplementary materials (26). We recommend using our isotherm over the entire pressure range measured in these experiments.

We provide an update to the first-order Raman spectra of diamond anvils benchmarked to our Pt isotherm (26). As suggested by Akahama and Kawamura (31), we performed a weighted fit to the corrected Raman frequency change as a function of pressure data below 300 GPa to the functional form $P(\text{GPa}) = 530.77(\pm 17)\frac{\Delta\omega}{\omega_0} + 753.83(\pm 56.9)\left(\frac{\Delta\omega}{\omega_0}\right)^2$, where $\frac{\Delta\omega}{\omega_0}$ is the relative Raman frequency change and ω_0 is the edge frequency at ambient pressure (1334 cm^{-1}). For the high-pressure data ($P > 200$ GPa), our weighted fit to the corrected Pt EOS data are $P(\text{GPa}) = 199.49(\pm 89.4) - 852.78(\pm 529)\frac{\Delta\omega}{\omega_0} + 3103.8(\pm 776)\left(\frac{\Delta\omega}{\omega_0}\right)^2$.

The application of extreme pressures to materials has been shown to give rise to exotic physical properties (insulator to metal phase transition, electrified structures, superionicity, and superconductivity). In planetary science and high-pressure mineral physics, scientists aim to accurately link the composition and temperature of the planetary cores to fun-

damental high-pressure laboratory measurements. As new experimental techniques enable even higher-pressure conditions to be achieved within the laboratory, more accurate links between experimental measurements, theory, and simulations are required. Absolute, experimentally benchmarked extreme-pressure scales are critical for comparing high-pressure experiments with theoretical models, as well as comparing measurements produced in different laboratories or by different means. We present the first high-accuracy, high-pressure calibrations of Au and Pt isotherms to terapascal pressures. We provide Vinet fits to terapascal conditions and an update to the first-order Raman spectra of diamond. Altogether, our measurements provide high-accuracy standards anchored to quasi-absolute measurements, without the need to rely on a particular theoretical framework or simulation method. We hope that this will enable new exciting discoveries at the science frontier and will contribute to a better understanding of material properties.

REFERENCES AND NOTES

1. M. D. Knudson et al., *Science* **348**, 1455–1460 (2015).
2. P. M. Celliers et al., *Science* **361**, 677–682 (2018).
3. C. J. Pickard, R. J. Needs, *Nat. Mater.* **9**, 624–627 (2010).
4. X. Dong et al., *Nat. Chem.* **9**, 440–445 (2017).
5. Y. Ma et al., *Nature* **458**, 182–185 (2009).
6. M. Millot et al., *Nat. Phys.* **14**, 297–302 (2018).
7. M. Somayazulu et al., *Phys. Rev. Lett.* **122**, 027001 (2019).
8. E. Snider et al., *Nature* **586**, 373–377 (2020).
9. L. Dubrovinsky, N. Dubrovinskaia, V. B. Prakapenka, A. M. Abakumov, *Nat. Commun.* **3**, 1163 (2012).
10. L. Dubrovinsky et al., *Nature* **525**, 226–229 (2015).
11. N. Dubrovinskaia et al., *Sci. Adv.* **2**, e1600341 (2016).
12. A. Dewaele, P. Loubeyre, F. Occelli, O. Marie, M. Mezouar, *Nat. Commun.* **9**, 2913 (2018).
13. Z. Jenei et al., *Nat. Commun.* **9**, 3563 (2018).
14. T. Sakai et al., *High Press. Res.* **38**, 107–119 (2018).
15. P. Loubeyre, F. Occelli, P. Dumas, *Nature* **577**, 631–635 (2020).
16. T. Yagi, T. Sakai, H. Kadobayashi, T. Irfune, *High Press. Res.* **40**, 148–161 (2020).
17. R. F. Smith et al., *Nat. Astron.* **2**, 452–458 (2018).
18. F. Peng et al., *Phys. Rev. Lett.* **119**, 107001 (2017).
19. L. Moncali, I. Errea, M. Calandra, F. Mauri, *Nat. Phys.* **17**, 63–67 (2021).
20. R. Boehler et al., *High Press. Res.* **33**, 546–554 (2013).
21. B. Haberli et al., *High Press. Res.* **37**, 495–506 (2017).
22. C.-S. Zha, H. Mao, R. J. Hemley, *Proc. Natl. Acad. Sci. U.S.A.* **97**, 13494–13499 (2000).
23. G. Shen et al., *High Press. Res.* **40**, 299–314 (2020).
24. A. Dewaele, M. Torrent, P. Loubeyre, M. Mezouar, *Phys. Rev. B Condens. Matter Mater. Phys.* **78**, 104102 (2008).
25. K. Jin et al., *High Press. Res.* **31**, 560–580 (2011).
26. Materials and methods are available as supplementary materials.
27. N. C. Holmes, J. A. Moriarty, G. R. Gathers, W. J. Nellis, *J. Appl. Phys.* **66**, 2962–2967 (1989).
28. H. K. Mao, P. M. Bell, J. W. Shaner, D. J. Steinberg, *J. Appl. Phys.* **49**, 3276–3283 (1978).
29. H. K. Mao, J. Xu, P. M. Bell, *J. Geophys. Res.* **91** (B5), 4673–4676 (1986).
30. V. E. Bean et al., *Physica B+C* **139–140**, 52–54 (1986).
31. Y. Akahama, H. Kawamura, *J. Phys. Conf. Ser.* **215**, 012195 (2010).
32. T. Kimura et al., *J. Chem. Phys.* **142**, 164504 (2015).
33. J.-P. Davis, J. L. Brown, M. D. Knudson, R. W. Lemke, *J. Appl. Phys.* **116**, 204903 (2014).
34. R. F. Smith et al., *Nature* **511**, 330–333 (2014).
35. R. G. Kraus et al., *Phys. Rev. B* **93**, 134105 (2016).
36. D. E. Fratanduono et al., *Phys. Rev. Lett.* **124**, 015701 (2020).
37. R. P. Dias, I. F. Silvera, *Science* **355**, 715–718 (2017).
38. M. Yokoo et al., *Phys. Rev. B Condens. Matter Mater. Phys.* **80**, 104114 (2009).
39. A. Dewaele, P. Loubeyre, M. Mezouar, *Phys. Rev. B Condens. Matter Mater. Phys.* **70**, 094112 (2004).

40. S. Marsh, *LASL Shock Hugoniot Data* (Univ. California Press, 1980).
41. K. Takemura, A. Dewaele, *Phys. Rev. B Condens. Matter Mater. Phys.* **78**, 104119 (2008).
42. S.-H. Shim, T. S. Duffy, K. Takemura, *Earth Planet. Sci. Lett.* **203**, 729–739 (2002).
43. Y. Fei *et al.*, *Proc. Natl. Acad. Sci. U.S.A.* **104**, 9182–9186 (2007).
44. S. M. Dorfman, V. B. Prakapenka, Y. Meng, T. S. Duffy, *J. Geophys. Res. Solid Earth* **117** (B8), n/a (2012).
45. C.-S. Zha *et al.*, *J. Appl. Phys.* **103**, 054908 (2008).
46. Y. Ye, V. Prakapenka, Y. Meng, S. H. Shim, *J. Geophys. Res. Solid Earth* **122**, 3450–3464 (2017).

ACKNOWLEDGMENTS

We thank C. Castro, A. Nikroo, the NIF target fabrication team, and the NIF Operations and Management teams for their contributions

to this research and NIF director M. Herrmann for the allocation of director's reserve experimental time. **Funding:** This work was performed under the auspices of the U.S. Department of Energy by Lawrence Livermore National Laboratory under contract DE-AC52-07NA27344. Sandia National Laboratories is a multimission laboratory managed and operated by National Technology & Engineering Solutions of Sandia, a wholly owned subsidiary of Honeywell International, for the U.S. Department of Energy's National Nuclear Security Administration under contract DE-NA0003525. **Author contributions:** D.E.F., M.M., D.G.B., S.J.A., A.F.-P., M.C.M., R.F.S., J.M.M., and J.H.E. designed the NIF experiments; D.E.F., S.J.A., A.F.-P., M.C.M., and R.F.S. executed the NIF experiments; D.E.F., C.T.S., J.-P.D., J.L.B., and R.G.K. designed the Z experiments; C.T.S., J.-P.D., and J.L.B. executed the Z experiments; D.E.F., S.J.A., A.F.-P., M.C.M., R.F.S., M.M., E.F.O., C.T.S., J.-P.D., R.G.K., Y.A., and J.L.B. analyzed the data; D.E.F.

and M.M. wrote the manuscript; and all authors reviewed and discussed the manuscript during preparation. **Competing interests:** All authors declare no competing interests. **Data and materials availability:** All data are available in the manuscript or the supplementary materials.

SUPPLEMENTARY MATERIALS

science.sciencemag.org/content/372/6546/1063/suppl/DC1
Materials and Methods
Supplementary Text
Figs. S1 to S10
Tables S1 to S10
References (47–77)

11 February 2021; accepted 14 April 2021
10.1126/science.abh0364

NEURODEVELOPMENT

Reciprocal repulsions instruct the precise assembly of parallel hippocampal networks

Daniel T. Pederick¹, Jan H. Lui¹, Ellen C. Gingrich^{1,2}, Chuanyun Xu¹, Mark J. Wagner¹, Yuanyuan Liu^{3†}, Zhigang He³, Stephen R. Quake^{4,5}, Liqun Luo^{1*}

Mammalian medial and lateral hippocampal networks preferentially process spatial- and object-related information, respectively. However, the mechanisms underlying the assembly of such parallel networks during development remain largely unknown. Our study shows that, in mice, complementary expression of cell surface molecules teneurin-3 (Ten3) and latrophilin-2 (Lphn2) in the medial and lateral hippocampal networks, respectively, guides the precise assembly of CA1-to-subiculum connections in both networks. In the medial network, Ten3-expressing (Ten3+) CA1 axons are repelled by target-derived Lphn2, revealing that Lphn2- and Ten3-mediated heterophilic repulsion and Ten3-mediated homophilic attraction cooperate to control precise target selection of CA1 axons. In the lateral network, Lphn2-expressing (Lphn2+) CA1 axons are confined to Lphn2+ targets via repulsion from Ten3+ targets. Our findings demonstrate that assembly of parallel hippocampal networks follows a “Ten3→Ten3, Lphn2→Lphn2” rule instructed by reciprocal repulsions.

Parallel information processing is a salient feature of complex nervous systems. One example is the mammalian hippocampal-entorhinal network, which is essential for explicit memory formation and spatial representation (1–4). Spatial- and object-related information are preferentially processed by the medial and lateral hippocampal networks, respectively (5, 6). In the medial network, proximal CA1 axons project to the distal subiculum (Fig. 1A, cyan), and both proximal CA1 and the distal subiculum also form reciprocal connections with the medial entorhinal cortex. In the lateral network, distal CA1 axons project to the proximal subiculum (Fig. 1A, yellow), and both distal CA1 and the proximal subiculum form

reciprocal connections with the lateral entorhinal cortex (7, 8) (fig. S1A).

We previously showed that the type II transmembrane protein teneurin-3 (Ten3) has matching expression in all interconnected regions of the medial hippocampal network (9). Ten3 is required in both proximal CA1 and the distal subiculum for target selection of the proximal CA1→distal subiculum axons, and it promotes aggregation of nonadhesive cells (9). These data support a homophilic attraction mechanism by which Ten3 regulates target selection in the medial hippocampal network. It remains unclear whether matching gene expression exists in the lateral hippocampal network and how this contributes to parallel hippocampal network assembly.

Complementary Lphn2/Ten3 expression across parallel hippocampal networks

We hypothesized that cell surface molecules with expression patterns inverse to those of *Ten3*, and therefore enriched in the lateral hippocampal network, may play a role in the precise assembly of parallel hippocampal networks. To identify such genes, we performed fluorescence-activated cell sorting–based single-cell RNA sequencing of postnatal day 8 (P8)

excitatory neurons that express vesicular glutamate transporter 1 in subregions of the medial or lateral networks (figs. S1 and S2). Among cell surface molecules that are differentially expressed in CA1 and the subiculum (fig. S3A), we identified *latrophilin-2* (*Lphn2*), an adhesion G protein–coupled receptor known to bind teneurins (10–15), which showed expression inverse to that of *Ten3*, not only in CA1 and the subiculum but also in the entorhinal cortex (Fig. 1B, fig. S4A, and table S1). Other *teneurin* and *latrophilin* family members did not display such differential expression (fig. S3, B and C).

Double in situ hybridization for *Lphn2* and *Ten3* mRNA in the P8 mouse brain revealed preferential expression of *Lphn2* in distal CA1, the proximal subiculum, and the lateral entorhinal cortex, complementary to *Ten3* enrichment in proximal CA1, the distal subiculum, and the medial entorhinal cortex (Fig. 1, C and D, and fig. S4, B and C). We also examined protein expression by using an anti-Ten3 antibody (9) and an anti-green fluorescent protein (GFP) antibody in *Lphn2-mVenus* knock-in mice (16). In all regions, Lphn2 and Ten3 proteins were expressed in the synaptic layers corresponding to their mRNA expression, including the molecular layer of CA1, the cell body and molecular layers of the subiculum, and layer III of the entorhinal cortex (Fig. 1, E and F, and fig. S4, D and E). Thus, *Lphn2* and *Ten3* mRNA, as well as Lphn2 and Ten3 proteins, exhibit complementary expression in multiple regions of the developing hippocampal networks, including CA1, the subiculum, and the entorhinal cortex (fig. S4F). In all cases, the connection specificity follows a “Ten3→Ten3, Lphn2→Lphn2” rule that correlates cell surface molecule expression with connectivity.

In the rest of this study, we focused on the target selection of CA1→subiculum axons to investigate the developmental mechanisms by which the “Ten3→Ten3, Lphn2→Lphn2” rule is established. Ten3+ and Lphn2+ CA1 axons extend along a tract above the subiculum cell body layer until they reach the Ten3+ distal subiculum and Lphn2+ proximal subiculum, respectively, where they invade the cell

¹Department of Biology, Howard Hughes Medical Institute, Stanford University, Stanford, CA, USA. ²Neurosciences Graduate Program, Stanford University, Stanford, CA, USA. ³F.M. Kirby Neurobiology Center, Department of Neurology, Boston Children's Hospital, Harvard Medical School, Boston, MA, USA. ⁴Departments of Bioengineering and Applied Physics, Stanford University, Stanford, CA, USA. ⁵Chan Zuckerberg Biohub, Stanford, CA, USA.

*Corresponding author. Email: lluo@stanford.edu

†Present address: Somatosensation and Pain Unit, National Institute of Dental and Craniofacial Research (NIDCR), National Center for Complementary and Integrative Health (NCCIH), National Institutes of Health, Bethesda, MD, USA.

body layer of the subiculum to form synapses (9) (fig. S5). Lphn2 and Ten3 proteins were first detected in subiculum targets (by P2) and displayed increasing expression in CA1 in subsequent days. By P8, the highest levels of Lphn2 and Ten3 in CA1 and the subiculum are comparable (fig. S6). This increase in expression coincides with the timing of target selection of CA1 axons in the subiculum (9).

Subiculum Lphn2 repels Ten3+ CA1 axons

Ten3 directs axon targeting in the medial hippocampal network through matching expression and homophilic attraction (9). Does Lphn2 also mediate homophilic attraction to assemble the lateral hippocampal network? To test this, we performed an *in vitro* cell aggregation assay using nonadhesive K562 cells. We confirmed that Ten3-expressing K562 cells formed aggregates, as previously reported (9), but found that Lphn2-expressing cells did not (fig. S7, A and B). However, Ten3-expressing cells aggregated with Lphn2-expressing cells (fig. S7, A and B), consistent with the previously reported heterophilic interaction between teneurins and latrophilins (10–15). The heterophilic interaction of Ten3 and Lphn2, combined with their complementary expression in the medial versus lateral hippocampal network, suggests that the interaction between Lphn2 and Ten3 may result in repulsion, which could allow distinct target selection of axons in the medial and lateral hippocampal networks.

The CA1→subiculum projection develops postnatally (9), so we injected lentivirus expressing GFP (control) or GFP-P2A-Lphn2 into the Lphn2-low distal subiculum of mice at P0 to create a region of the subiculum expressing Lphn2 across the entire proximal-distal axis. We then injected adeno-associated virus expressing membrane-bound mCherry (44V-mCh) into proximal CA1 in these same mice as adults to label and trace Ten3+ CA1 axons (Fig. 2, A and B). The portion of the subiculum transduced by lentivirus was only a subset of the total proximal CA1 axon targeting region along the orthogonal medial-lateral axis, allowing us to determine whether proximal CA1 axons target lentivirus-transduced subiculum regions differently compared with neighboring non-lentivirus-transduced subiculum regions.

To visualize the relationship between Ten3+ axon projections and ectopically expressed GFP-Lphn2 in the subiculum, we plotted signal intensity from proximal CA1 axons (mCh) and the lentivirus injection site (GFP) on the same subiculum graph as color and height, respectively. Expression of GFP alone did not affect the intensity of proximal CA1 axons in the subiculum target (Fig. 2C and fig. S8, A to C). However, proximal CA1 axon intensity was reduced in distal subiculum regions ectopically expressing Lphn2 (Fig. 2D and fig. S8, D to F; quantified in Fig. 2G). These data suggest that Ten3+ axons are repelled by ecto-

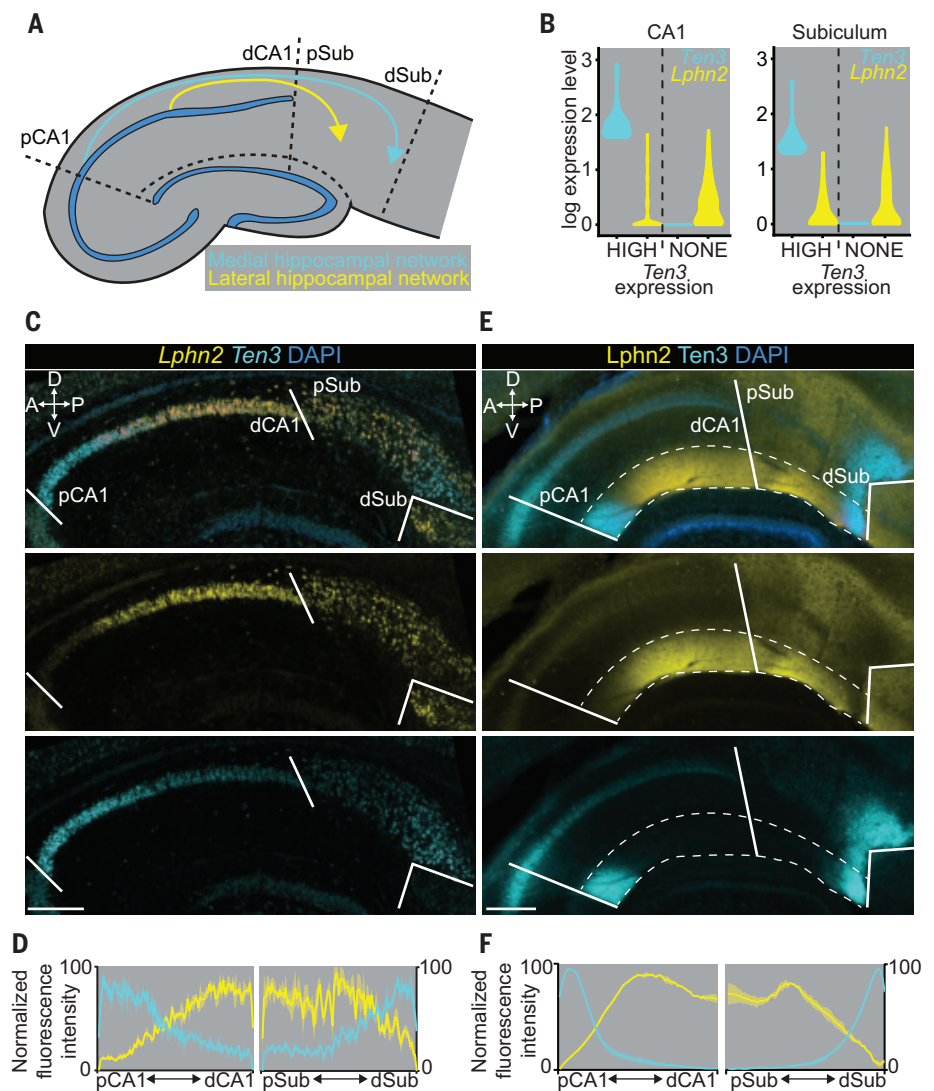


Fig. 1. Complementary expression patterns of Lphn2 and Ten3 in the hippocampal network. (A) Summary of connection patterns of medial (cyan) and lateral (yellow) hippocampal networks. pCA1 and dCA1, proximal and distal CA1; pSub and dSub, proximal and distal subiculum. (B) Violin plots highlighting Lphn2 and Ten3 expression in Ten3-HIGH and Ten3-NONE cells in CA1 and the subiculum. The unit of expression level is $\ln[1 + (\text{reads per 10,000 transcripts})]$. (C) Double in situ hybridization for Lphn2 (middle) and Ten3 (bottom) mRNA on a sagittal section of P8 mouse brain. Solid lines represent boundaries between CA1 and the subiculum, as labeled in the overlay (top). DAPI, 4',6-diamidino-2-phenylindole. (D) Quantification of Lphn2 and Ten3 mRNA across the proximal-distal axis of CA1 and subiculum cell body layers ($n = 3$ mice). Means \pm SEMs are shown. (E) Double immunostaining for Lphn2 (middle; anti-GFP antibody) and Ten3 (bottom) on a sagittal section of P8 Lphn2-mVenus knock-in mouse (16) brain. Solid lines represent boundaries between CA1 and the subiculum, as labeled in the overlay (top). The region between the dashed lines is the molecular layer. (F) Quantification of Lphn2 and Ten3 protein across the proximal-distal axis of molecular layers of CA1 and the subiculum ($n = 3$ mice). Means \pm SEMs are shown. Scale bars in (C) and (E), 200 μm . Axis labels in this and all subsequent figures: A, anterior; P, posterior; D, dorsal; V, ventral.

pically expressed Lphn2 at the distal subiculum target.

Repulsion requires Lphn2/teneurin but not Lphn2/FLRT interaction

To test whether Lphn2-mediated repulsion requires Lphn2 and Ten3 (Lphn2/Ten3) interaction, we used a deletion of the lectin binding

domain in latrophilins, which has been shown to abolish teneurin binding without affecting cell surface expression or interactions with other known partners (12–15). In our K562 cell aggregation assay, we validated that Lphn2 ΔLec disrupted Ten3 interaction without affecting interaction with FLRT2 (fig. S7, C and D), a member of the fibronectin leucine-rich

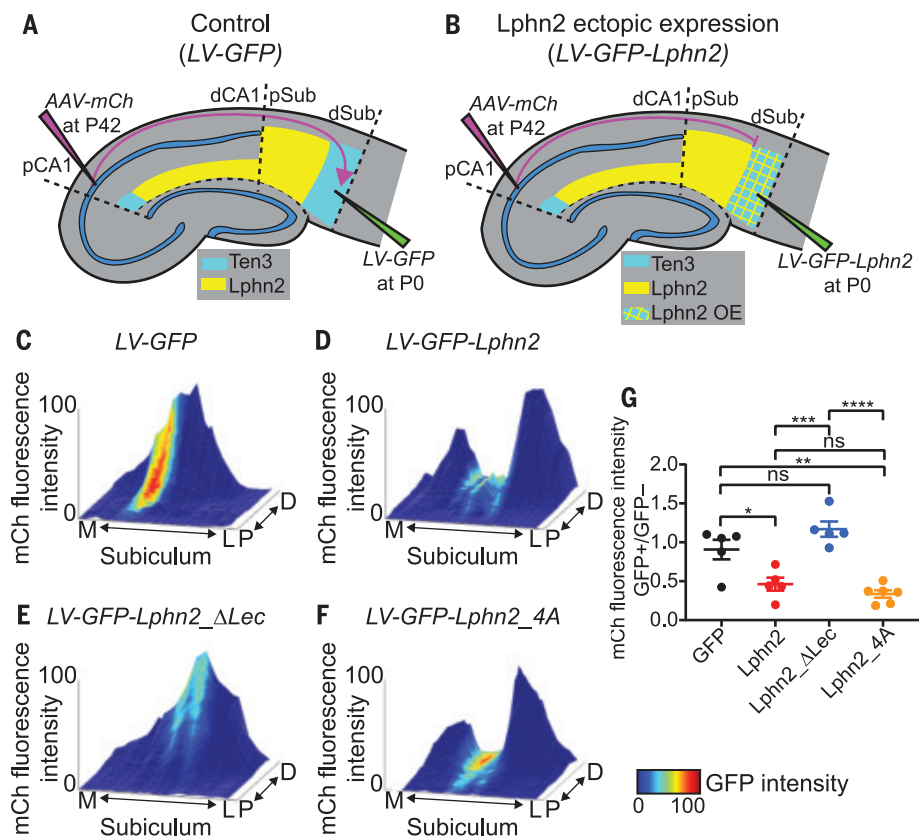


Fig. 2. Ten3+ proximal CA1 axons avoid the distal subiculum ectopically expressing Lphn2 in a Lphn2/teneurin interaction-dependent and Lphn2/FLRT interaction-independent manner. (A and B) Experimental design and summary of results. LV, lentivirus; AAV-mCh, adeno-associated virus expressing membrane-bound mCherry as an anterograde tracer. (C to F) Representative mountain plots showing normalized GFP fluorescence intensity as color (LV expression) and normalized mCh fluorescence intensity as height (proximal CA1 axon projections) in the subiculum. P, proximal; D, distal; M, medial; L, lateral. (G) Ratio of mCh fluorescence intensity of GFP+ versus GFP- regions. LV-GFP, $n = 5$ mice; LV-GFP-P2A-Lphn2 (wild-type Lphn2), $n = 5$ mice; LV-GFP-P2A-Lphn2_ΔLec (Lphn2 that does not bind teneurins), $n = 5$ mice; and LV-GFP-P2A-Lphn2_4A (Lphn2 that does not bind FLRTs), $n = 6$ mice. Means \pm SEMs are shown; one-way analysis of variance (ANOVA) with Tukey's multiple comparisons test was performed. **** $P \leq 0.0001$; *** $P \leq 0.001$; ** $P \leq 0.01$; * $P \leq 0.05$; ns, not significant.

transmembrane protein family known to bind latrophilins (11, 17). We then ectopically expressed Lphn2_ΔLec in the subiculum to determine whether proximal CA1 axon avoidance depends on a Lphn2/teneurin interaction. We found that in brains ectopically expressing GFP-P2A-Lphn2_ΔLec, Ten3+ proximal CA1 axons no longer avoided Lphn2_ΔLec-expressing regions in the distal subiculum (Fig. 2E and fig. S9, A to C; quantified in Fig. 2G).

FLRTs interact with teneurin and latrophilin to direct synapse specificity and repulsive guidance for migrating neurons (14, 15). Expression of *Flrt2* was enriched in Ten3-high CA1 cells (fig. S3D), suggesting that it may play a role in the repulsion of proximal CA1 axons by target-derived Lphn2. Mutation of four residues in the olfactomedin domain of latrophilin to alanines abolishes FLRT-Lphn binding while maintaining cell surface expression and teneurin binding (18). We confirmed that in K562 cells, Lphn2_4A disrupted

FLRT2 binding without affecting Ten3 binding (fig. S7, E and F). Yet ectopic expression of Lphn2_4A in the subiculum caused a decrease of Ten3+ proximal CA1 axon intensity in GFP+ distal subiculum regions compared with adjacent GFP- regions (Fig. 2F and fig. S9, D to F; quantified in Fig. 2G), to the same extent as wild-type Lphn2 (Fig. 2G). These gain-of-function experiments suggest that repulsion of Ten3+ proximal CA1 axons by target-derived Lphn2 requires Lphn2/teneurin but not Lphn2/FLRT interaction.

Ten3+ CA1 axons invade Lphn2-null subiculum targets

To determine whether endogenous Lphn2 in the subiculum is necessary for correct proximal CA1→distal subiculum targeting, we performed a loss-of-function experiment by injecting lentivirus expressing GFP-Cre into the subiculum of control and Lphn2^{fl/fl} mice (16) at P0, followed by AAV-mCh in proximal CA1 of the same mice as adults

to assess Ten3+ axon targeting (Fig. 3, A and C). In Lphn2^{+/+} control mice, proximal CA1 axons targeted the distal subiculum and were not disrupted when projecting into GFP-Cre+ regions (Fig. 3B). By contrast, proximal CA1 axons targeted more broadly in GFP-Cre+ regions in Lphn2^{fl/fl} mice (Fig. 3D). Quantification of proximal CA1 axon intensity in GFP-Cre+ sections revealed that proximal CA1 axons in Lphn2^{fl/fl} mice had increased intensity in the more proximal regions and decreased intensity in the most distal region of the subiculum compared with Lphn2^{+/+} mice (Fig. 3, G and H; red versus black). These data suggest that Lphn2 in the proximal subiculum normally repels Ten3+ proximal CA1 axons, enabling them to specifically target the distal subiculum.

To rule out the possibility that the ectopic invasion of proximal CA1 axons into the Lphn2^{fl/fl} proximal subiculum results from loss of Lphn2 interaction with a molecule other than Ten3 [e.g., another teneurin that is expressed in CA1 (fig. S3B)], we performed the same Lphn2 loss-of-function experiment in Ten3^{-/-} mice. Anterograde tracing from proximal CA1 in Lphn2^{+/+};Ten3^{-/-} mice showed that proximal CA1 axons spread more along the proximal-distal axis of the subiculum (fig. S10, A and B). In Lphn2^{fl/fl};Ten3^{-/-} mice, proximal CA1 axons also showed similar spreading (fig. S10, C and D; quantified in fig. S10, E and F). The lack of an additional axon mistargeting phenotype in Lphn2^{fl/fl};Ten3^{-/-} mice compared with Lphn2^{+/+};Ten3^{-/-} mice suggests that Ten3 is required for the effect of loss of subiculum Lphn2 on proximal CA1 axon targeting and that Lphn2/Ten3-mediated repulsion instructs proximal CA1→distal subiculum target selection.

Lphn2/Ten3-mediated repulsion and Ten3/Ten3-mediated attraction cooperate

Loss of Lphn2/Ten3 heterophilic repulsion (above) or Ten3 homophilic attraction (9) alone both disrupt precise proximal CA1→distal subiculum axon targeting. What is the relative contribution of each? To address this, we simultaneously conditionally deleted both Lphn2 and Ten3 in the subiculum and assessed the targeting of Ten3+ proximal CA1 axons (Fig. 3E). We found that proximal CA1 axons projecting into GFP-Cre+ regions of Lphn2^{fl/fl};Ten3^{fl/fl} mice targeted more proximal regions of the subiculum and also had decreased fluorescence intensity in the distal subiculum (Fig. 3F).

Quantification of proximal CA1 axons in GFP-Cre+ subiculum sections of Lphn2^{fl/fl};Ten3^{fl/fl} mice showed a significant increase in axon intensity into the Lphn2^{fl/fl} proximal subiculum compared with axons in Lphn2^{+/+};Ten3^{+/+} mice (Fig. 3, G and H; blue versus black), confirming a loss of repulsion of Ten3+ proximal CA1 axons from the proximal subiculum that normally expresses Lphn2. Additionally, proximal CA1 axons in Lphn2^{fl/fl};

Ten3^{fl/fl} mice had decreased fluorescence intensity in the distal subiculum compared with axons in *Lphn2^{fl/fl};Ten3^{+/+}* mice (Fig. 3, G and H; blue versus red), indicating a loss of attraction of *Ten3*+ proximal CA1 axons to the distal subiculum that normally expresses *Ten3*. Thus, *Lphn2*/*Ten3*-mediated heterophilic repulsion and *Ten3*/*Ten3*-mediated homophilic attraction cooperate in orchestrating the precise targeting of proximal CA1 axons to the distal subiculum.

Subiculum *Ten3* repels *Lphn2*+ CA1 axons

In addition to serving as a repulsive ligand for target selection of *Ten3*+ medial hippocampal network neurons, could *Lphn2* also act as a receptor to regulate target selection of lateral hippocampal network neurons? Could *Lphn2*+ axons be repelled from *Ten3*+ targets to regulate the precision of lateral hippocampal network connections? To test these ideas, we injected lentivirus expressing *GFP-Cre* into the subiculum of *Ten3^{+/+}* (control) and *Ten3^{fl/fl}* mice at P0, followed by *AAV-mCh* in mid-CA1 of the same mice as adults to assess *Lphn2*+ mid-CA1 axon targeting (Fig. 4, A and C). In *Ten3^{+/+}* mice, mid-CA1 axons predominantly targeted the mid-subiculum (Fig. 4B). However, in *Ten3^{fl/fl}* mice, mid-CA1 axons spread into the *Ten3*-null distal subiculum (Fig. 4D). Quantification of axons in the subiculum showed a significant increase in axon intensity in the distal subiculum of *Ten3^{fl/fl}* mice compared with *Ten3^{+/+}* mice (Fig. 4, E and F). Thus, *Ten3* in the distal subiculum prevents *Lphn2*+ mid-CA1 axon invasion into the distal subiculum.

To test whether *Lphn2* in mid-CA1 axons is required for their target precision, we deleted *Lphn2* from CA1 and then traced *Lphn2*-null mid-CA1 axons (Fig. 4, G and I). Control mid-CA1 axons targeted the mid-subiculum (Fig. 4H), whereas *Lphn2*-null mid-CA1 axons spread into the most distal subiculum (Fig. 4J; quantified in Fig. 4, K and L). Thus, *Lphn2* is cell-autonomously required in mid-CA1 neurons to prevent their axons from invading the *Ten3*+ distal subiculum. Taken together with the *Ten3* conditional deletion in the subiculum above, these data indicate that *Lphn2*+ mid-CA1 axons are repelled by target-derived *Ten3*.

Discussion

In this study, we used CA1→subiculum axon targeting as a model to investigate how parallel networks are assembled during development. Our results demonstrate that *Lphn2* and *Ten3* instruct the precise assembly of both medial and lateral hippocampal networks (Fig. 5A). In the medial network, *Lphn2*/*Ten3*-mediated heterophilic repulsion and *Ten3*/*Ten3*-mediated homophilic attraction cooperate to instruct proximal CA1→distal subiculum axon targeting. In the lateral network, *Ten3*/*Lphn2*-mediated heterophilic repulsion

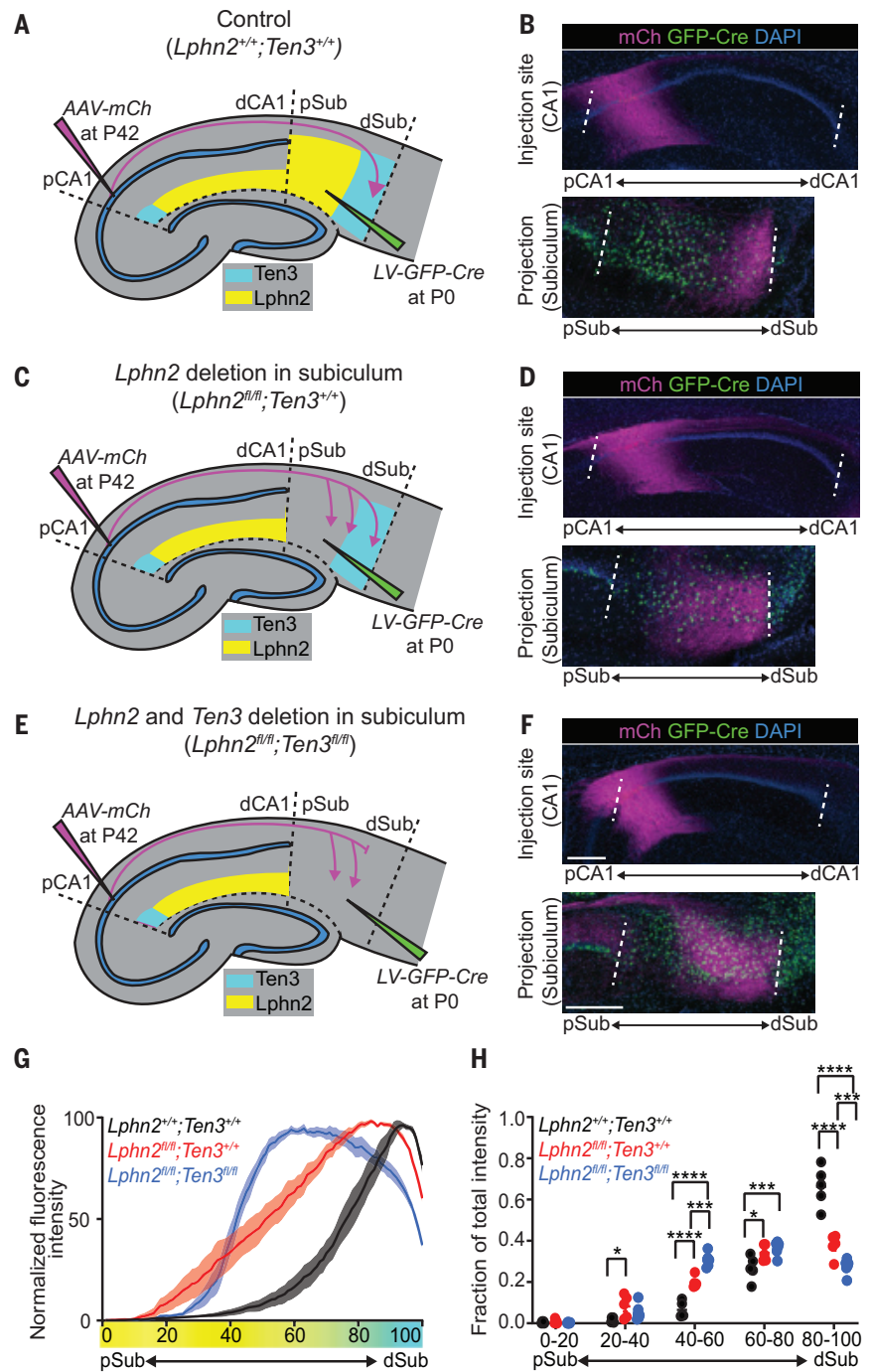


Fig. 3. *Lphn2*/*Ten3*-mediated repulsion and *Ten3*/*Ten3*-mediated attraction cooperate to guide proximal CA1→distal subiculum target selection. (A, C, and E) Experimental design and summary of results for control (A), *Lphn2* conditional knockout in the subiculum (C), and *Lphn2* and *Ten3* double conditional knockout in the subiculum (E). (B, D, and F) Representative images of *AAV-mCh* (magenta) injections in proximal CA1 (top) and corresponding projections of proximal CA1 axons overlapping with *LV-GFP-Cre* (green) injection sites in the subiculum (bottom). Data in (B), (D), and (F) correspond to experimental conditions in (A), (C), and (E), respectively. (G) Normalized mean fluorescence intensity traces of subiculum projections from proximal CA1 in *GFP-Cre*+ sections for *Lphn2^{+/+};Ten3^{+/+}* mice ($n = 5$), *Lphn2^{fl/fl};Ten3^{+/+}* mice ($n = 5$), and *Lphn2^{fl/fl};Ten3^{fl/fl}* mice ($n = 6$). Means \pm SEMs are shown. The color bar under the x axis represents *Lphn2* (yellow) and *Ten3* (cyan) expression in the subiculum, as quantified in Fig. 1F. (H) Fraction of total axon intensity for the same data as in (G) across 20% intervals. Means \pm SEMs are shown; two-way ANOVA with Sidak's multiple comparisons test was performed. **** $P \leq 0.0001$; *** $P \leq 0.001$; * $P \leq 0.05$. Scale bars in (F), 200 μ m. Injection site locations in CA1 are shown in fig. S11.

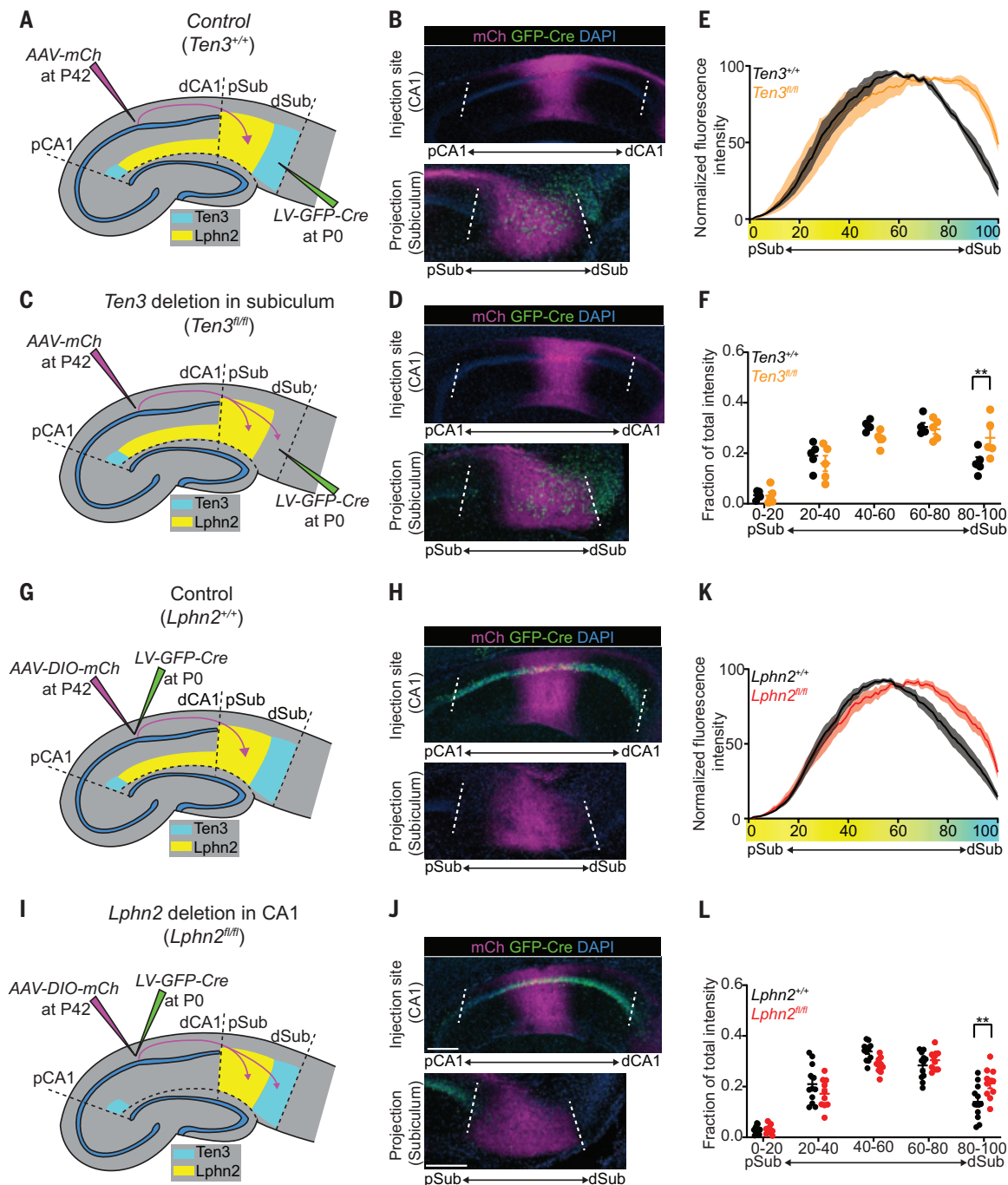
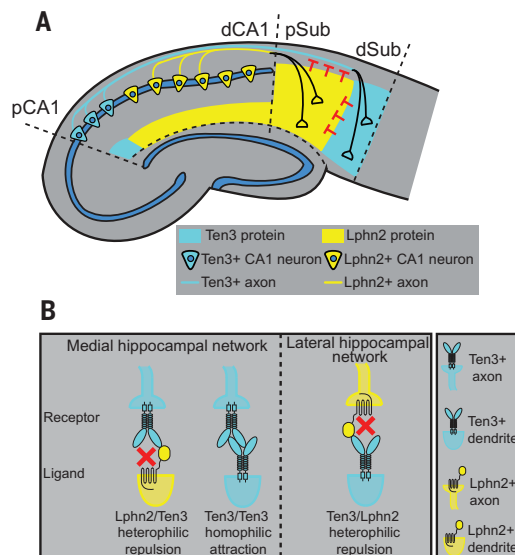


Fig. 4. $Lphn2^{+}$ mid-CA1 axons avoid the $Ten3^{+}$ distal subiculum. (A and C) Experimental design and summary of results for tracing mid-CA1 axons in control (A) and $Ten3$ conditional knockout in the subiculum (C). (B and D) Representative images of AAV-mCh (magenta) injections in mid-CA1 (top) and corresponding projections overlapping with LV-GFP-Cre (green) injection sites in the subiculum (bottom). Data in (B) and (D) correspond to experimental conditions in (A) and (C), respectively. (E) Normalized mean fluorescence intensity traces of subiculum projections from mid-CA1 in GFP-Cre+ sections for $Ten3^{+/+}$ mice ($n = 5$) and $Ten3^{fl/fl}$ mice ($n = 5$). Means \pm SEMs are shown. The color bar under the x axis represents $Lphn2$ (yellow) and $Ten3$ (cyan) expression in the subiculum, as quantified in Fig. 1F. (F) Fraction of total axon intensity [same data as in (E)] across 20% intervals. Means \pm SEMs are shown; two-way ANOVA with Sidak's multiple comparisons test was performed. $^{**}P \leq 0.01$.

(G and I) Experimental design and summary of results for tracing control (G) and $Lphn2$ -null (I) mid-CA1 axon projections to the subiculum. (H and J) Representative images of AAV-DIO-mCh (magenta; mCh expression in a Cre-dependent manner) injections in mid-CA1 (top) and corresponding projections in the subiculum (bottom). Data in (H) and (J) correspond to experimental conditions in (G) and (I), respectively. (K) Normalized mean fluorescence intensity traces of subiculum projections from $Lphn2^{+/+}$ ($n = 12$ mice) and $Lphn2^{fl/fl}$ ($n = 10$ mice) mid-CA1 axons. Means \pm SEMs are shown. The color bar under the x axis represents $Lphn2$ (yellow) and $Ten3$ (cyan) expression in the subiculum, as quantified in Fig. 1F. (L) Fraction of total axon intensity [same data as in (K)] across 20% intervals. Means \pm SEMs are shown; two-way ANOVA with Sidak's multiple comparisons test was performed. $^{**}P \leq 0.01$. Scale bars in (J), 200 μ m. Injection site locations in CA1 are shown in fig. S11.

Fig. 5. Lphn2 and Ten3 instruct target selection of hippocampal axons through reciprocal repulsions. (A) Ten3+ CA1 axons target the Ten3+ subiculum via repulsion from Lphn2 and attraction to Ten3 in the subiculum. Lphn2+ CA1 axons target the Lphn2+ subiculum via repulsion from Ten3 in the subiculum. (B) Cartoon representation of ligand-receptor interactions that instruct target selection of Ten3+ (left) and Lphn2+ (right) axons. Red crosses symbolize repulsion.



confines Lphn2+ axons to the Lphn2+ target region (Fig. 5B). Additional cell surface molecules may further subdivide the Lphn2+ region to determine targeting specificity between mid-CA1→mid-subiculum and distal CA1→proximal subiculum. Together, these data indicate that the mechanisms required for parallel network assembly in the hippocampus are intertwined, using multiple interactions of two cell surface molecules and reciprocal repulsions to ensure the precise segregation of connections.

Our results reveal that Lphn2 acts both cell nonautonomously in targets and cell autonomously in axons during the target selection stage of hippocampal circuit assembly, preceding synapse formation. This is in contrast to previous studies suggesting that latrophilins act strictly as postsynaptic adhesion molecules to establish or maintain synaptic connections (14, 16, 19). Although defects in axon targeting may contribute to synaptic deficits in *latrophilin* early postnatal loss-of-function experiments (14, 16, 20), our study is compatible with latrophilin/teneurin interactions playing additional roles in synaptic adhesion if the repulsive mechanism is switched off after target selection is complete. While the most parsimonious interpretation is that the interactions between Lphn2 and Ten3 mediate repulsion directly, our study does not rule out the possibility that Lphn2/Ten3 interactions initiate signaling cascades that activate repulsive interactions mediated by additional molecules. Latrophilins bind both teneurins and FLRTs, and the cooperative binding of these three proteins has been implicated in directing synapse specificity and repulsion-mediated neuronal migration (14, 15). However, ectopic expression of a mutant Lphn2 that cannot bind FLRT (fig. S7, E and F) still repelled Ten3+ proximal CA1 axons to the same extent (Fig. 2G), suggesting that

FLRT binding is not required for Lphn2/Ten3-mediated repulsion during target selection of axons.

Cooperation of attraction and repulsion has been described in neuronal circuit assembly (21, 22). For example, the PlexB receptor interacts with *Sema2a* and *Sema2b* through repulsion and attraction, respectively, to mediate axon guidance during *Drosophila* sensory circuit assembly (23). We found that target selection of proximal CA1 axons is determined by Lphn2/Ten3-mediated repulsion from the proximal subiculum and Ten3/Ten3-mediated attraction to the distal subiculum (Fig. 3). Thus, Ten3 acts as a receptor for both repulsive and attractive ligands in the same axon during target selection. Conversely, as a ligand, Ten3 acts as an attractant for Ten3+ axons but a repellent for Lphn2+ axons (Fig. 5).

We show the complementary expression of Ten3 and Lphn2 across all interconnected regions of the hippocampal network. This is reminiscent of Ephrin-A/EphA countergradients found across interconnected regions of the developing visual system (24) that use bidirectional Ephrin-A/EphA interactions for the formation of topographic projections (25, 26). The patterns of Ten3 and Lphn2 expression across the hippocampal network follow a “Ten3→Ten3, Lphn2→Lphn2” rule (fig. S4F). The reciprocal repulsions we demonstrated in the CA1→subiculum projection may guide target selection across additional projections to and from the entorhinal cortex. With repeated use in various connections combined with multifunctionality, in which a single protein serves as both receptor and ligand, a limited number of cell surface molecules can specify a diversity of connections in the mammalian brain.

REFERENCES AND NOTES

1. O'Keefe, J. Dostrovsky, *Brain Res.* **34**, 171–175 (1971).

2. W. B. Scoville, B. Milner, *J. Neuropsychiatry Clin. Neurosci.* **12**, 103–113 (2000).
3. L. R. Squire, C. E. L. Stark, R. E. Clark, *Annu. Rev. Neurosci.* **27**, 279–306 (2004).
4. T. Hafting, M. Fyhn, S. Molden, M.-B. Moser, E. I. Moser, *Nature* **436**, 801–806 (2005).
5. K. M. Igarashi, H. T. Ito, E. I. Moser, M.-B. Moser, *FEBS Lett.* **588**, 2470–2476 (2014).
6. M. S. Cembrowski et al., *Cell* **173**, 1280–1292.e18 (2018).
7. P. A. Nabers, F. H. Lopes da Silva, M. P. Witter, *Hippocampus* **11**, 99–104 (2001).
8. N. Tamamaki, Y. Nojyo, *J. Comp. Neurol.* **353**, 379–390 (1995).
9. D. S. Berns, L. A. DeNardo, D. T. Pederick, L. Luo, *Nature* **554**, 328–333 (2018).
10. J.-P. Silva et al., *Proc. Natl. Acad. Sci. U.S.A.* **108**, 12113–12118 (2011).
11. M. L. O'Sullivan et al., *Neuron* **73**, 903–910 (2012).
12. A. A. Boucard, S. Maxeiner, T. C. Südhof, *J. Biol. Chem.* **289**, 387–402 (2014).
13. J. Li et al., *Cell* **173**, 735–748.e15 (2018).
14. R. Sando, X. Jiang, T. C. Südhof, *Science* **363**, eaav7969 (2019).
15. D. del Toro et al., *Cell* **180**, 323–339.e19 (2020).
16. G. R. Anderson et al., *J. Cell Biol.* **216**, 3831–3846 (2017).
17. V. A. Jackson et al., *Structure* **23**, 774–781 (2015).
18. Y. C. Lu et al., *Structure* **23**, 1678–1691 (2015).
19. T. C. Südhof, *Neuron* **100**, 276–293 (2018).
20. R. Sando, T. C. Südhof, *eLife* **10**, e65717 (2021).
21. A. L. Kolodkin, M. Tessier-Lavigne, *Cold Spring Harb. Perspect. Biol.* **3**, a001727 (2011).
22. J. R. Sanes, S. L. Zipursky, *Cell* **181**, 536–556 (2020).
23. Z. Wu et al., *Neuron* **70**, 281–298 (2011).
24. M.-A. Lambot, F. Depasse, J.-C. Noel, P. Vanderhaeghen, *J. Neurosci.* **25**, 7232–7237 (2005).
25. J. Cang, D. A. Feldheim, *Annu. Rev. Neurosci.* **36**, 51–77 (2013).
26. J. Egea, R. Klein, *Trends Cell Biol.* **17**, 230–238 (2007).
27. D. T. Pederick et al., Reciprocal-repulsions-instruct-the-precise-assembly-of-parallel-hippocampal-networks, version 1, Zenodo (2021), <https://doi.org/10.5281/zenodo.4716610>.

ACKNOWLEDGMENTS

We thank T. Südhof for the *Lphn2^{tmVenus}* and *Lphn2^{fl}* mice; the Neuroscience Gene Vector and Virus Core at Stanford University for producing viruses; D. Berns for advice, inspiration, and artwork; J. Ferguson for artwork; J. Keschull for MATLAB code; H. Meng for virus preparation; members of the Luo laboratory for advice and support; and D. Berns, J. Keschull, A. Khalaj, H. Li, J. Li, T. Li, C. McLaughlin, K. Shen, and A. Shuster for critiques of the manuscript. **Funding:** D.T.P. was supported by an American Australian Association Education Fund Scholarship. J.H.L. is supported by a National Institutes of Health grant (K01-MH14022). L.L. is an investigator of Howard Hughes Medical Institute. This work was supported by National Institutes of Health grant (R01-NS050580 to L.L.). **Author contributions:** D.T.P. performed all of the experiments and analyzed the data, except for single-cell sequencing sample collection and data processing, which were performed by J.H.L., with support from S.R.Q. E.C.G. and C.X. assisted in tissue processing. M.J.W. generated MATLAB code and analyzed data. Y.L. and Z.H. produced custom lentiviruses. L.L. supervised the study. D.T.P., J.H.L., and L.L. wrote the paper. **Competing interests:** The authors declare no competing interests. **Data and materials availability:** The sequencing datasets generated in this study are available in the NCBI Gene Expression Omnibus under accession number GSE162552. Custom analysis codes are available at <https://github.com/dpedrick/Reciprocal-repulsions-instruct-the-precise-assembly-of-parallel-hippocampal-networks> or Zenodo (27). All other data are available in the main paper and the supplementary materials. All materials are available through requests to the corresponding author.

SUPPLEMENTARY MATERIALS

science.sciencemag.org/content/372/6546/1068/suppl/DC1
Materials and Methods
Figs. S1 to S11
Table S1
References (28–41)
MDAR Reproducibility Checklist

15 December 2020; accepted 27 April 2021
10.1126/science.abg1774

REPORTS

ELECTROCHEMISTRY

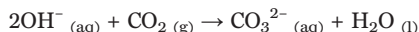
CO₂ electrolysis to multicarbon products in strong acid

Jianan Erick Huang^{1†}, Fengwang Li^{1,2,*†}, Adnan Ozden^{3†}, Armin Sedighian Rasouli¹, F. Pelayo García de Arquer^{1†}, Shijie Liu³, Shuzhen Zhang², Mingchuan Luo¹, Xue Wang¹, Yanwei Lum¹, Yi Xu³, Koen Bertens¹, Rui Kai Miao³, Cao-Thang Dinh¹, David Sinton^{3*}, Edward H. Sargent^{1*}

Carbon dioxide electroreduction (CO₂R) is being actively studied as a promising route to convert carbon emissions to valuable chemicals and fuels. However, the fraction of input CO₂ that is productively reduced has typically been very low, <2% for multicarbon products; the balance reacts with hydroxide to form carbonate in both alkaline and neutral reactors. Acidic electrolytes would overcome this limitation, but hydrogen evolution has hitherto dominated under those conditions. We report that concentrating potassium cations in the vicinity of electrochemically active sites accelerates CO₂ activation to enable efficient CO₂R in acid. We achieve CO₂R on copper at pH <1 with a single-pass CO₂ utilization of 77%, including a conversion efficiency of 50% toward multicarbon products (ethylene, ethanol, and 1-propanol) at a current density of 1.2 amperes per square centimeter and a full-cell voltage of 4.2 volts.

Electrochemical reduction of CO₂ (CO₂R) using renewable electricity offers an attractive approach to produce widely needed chemicals and feedstocks while mitigating greenhouse gas emissions (1, 2). Effort has been dedicated to developing catalysts that achieve high faradaic efficiency (FE) toward carbon monoxide and formate and to promoting C–C coupling toward multicarbon (C₂₊) products such as ethylene and ethanol (3–6). Lowering overpotentials of these reactions and increasing their productivity (current density) have been priorities for the field (7, 8).

Despite many recent advances, CO₂R remains far from practical viability because strong local alkaline conditions are present (Fig. 1A). Rather than being reduced, a major fraction of the input CO₂ is instead consumed in the electrolyte through reaction with OH[–] to produce CO₃^{2–}



Carbonate formation imposes a limit of carbon utilization efficiency (fraction of CO₂ in the input feed converted to CO₂R products) that is prohibitively low (9). For every H₂O–

electron pair transferred during CO₂R, one hydroxide is produced at the cathode, reacting with ½ CO₂ to form carbonate. As a result, the maximum carbon efficiency is 50% for two-electron-transfer processes such as CO₂ to CO.

For CO₂R to more valuable C₂₊ products, the effect is even more acute: The carbon efficiency of CO₂R to ethylene or ethanol is limited to 25%, as six electrons are needed per CO₂ reacted. In practice, due in part to nonunity selectivity and use of alkaline electrolyte, the carbon efficiency is even lower than these best-case theoretical limits (Fig. 1B) (7, 10–15).

Dealing with CO₂ loss in alkaline and neutral environments leads to a severe energy penalty if one seeks to recycle the emitter CO₂ from carbonate or cathodic and anodic streams (16). Technoeconomic analysis of alkaline CO₂ electrolyzers shows that >50% of input energy is used to regenerate CO₂ lost to carbonate (Fig. 1C and tables S1 and S2; details in supplementary materials). CO₂ electrolyzers using neutral electrolyte produce a local alkaline environment under operating conditions and thus also suffer from carbonate formation and crossover (17, 18). The problem of inefficient CO₂ utilization in CO₂R is central to the field and severely limits its prospects (9). While advances in FE and current density have been steady, the utilization challenge demands a new approach.

CO₂R in acidic media offers an avenue to reduce carbonate formation to near zero and thus also eliminate CO₂ crossover (Fig. 1, D and E). Specifically, when H₃O⁺ is the proton source for CO₂R, no OH[–] is generated, and CO₂ conversion can proceed without carbon-

ate formation; when H₂O is the proton source, any carbonate generated locally will lie within the diffusion layer and be converted back to CO₂ by protons in the bulk electrolyte (19). Initial tests using phosphate buffer electrolytes (pH 1 to 4; see supplementary materials for detailed preparation methods) showed no measurable loss of CO₂ to the anode at 400 mA/cm² over 6 hours compared with a loss of ~70% of input CO₂ in the reference case with bicarbonate electrolyte (Fig. 1F and fig. S1). However, under acidic conditions, the kinetically more favorable hydrogen evolution reaction (HER) outcompetes the reduction of CO₂, with CO₂R FE close to zero in strong acids (pH <1). These results are in agreement with past work on acidic CO₂R, in which only single-carbon products, such as CO and methane, were observed in electrolytes of elevated pH in the range 3 to 5 (19–25); one of these works achieved near 100% FE to CO in pH 3 electrolyte (19).

In this study, we pursued a cation augmenting strategy to improve CO₂ activation kinetics in strong acid (pH <1). We used high-concentration phosphate buffer (total phosphorus species kept to 1 M) as electrolyte to keep pH locally at the cathode as close as possible to that at the bulk (26). Modeling of reaction and diffusion of species within a typical diffusion layer of 50 μm indicates that, in the phosphoric acid (H₃PO₄, 1 M, pH 1.05) electrolyte, the surface (distance to cathode of 0 μm) pH is similar to the bulk at current densities <200 mA/cm² while becoming neutral and alkaline when current densities increase further (Fig. 2A, fig. S2, and tables S3 to S5; details in supplementary materials). The locally alkaline conditions result from a consumption rate of local protons that exceeds mass transport of protons from the bulk (27). Despite elevated pH at the surface, pH decreases to an acidic range within a short distance of the cathode. Even at a current density as high as 1 A/cm², the pH decreases to 6.3 [first acid dissociation constant (pK_{a1}) of carbonic acid] within 33 μm of the electrode. This confinement assures that any locally generated carbonate would be converted back to CO₂ for ensuing reduction, avoiding carbonate crossover and the associated loss of reactant CO₂. In comparison, similar conditions (pH 6.3 at a distance to cathode of 30 μm) are reached at much lower current densities (<200 mA/cm²) in electrolytes of pH 2 to 4 (fig. S2). In the interest of realizing economic CO₂ electrolyzers (28), we focus this study on high-rate CO₂ electrolysis in strong acid (pH <1).

To circumvent the kinetically more favorable HER in acid, we sought to operate CO₂R at current densities where the H₃O⁺ mass-transport limitation occurs and H₂O becomes the main proton donor at the cathode surface (19, 22). Modeling shows that the surface pH

¹Department of Electrical and Computer Engineering, University of Toronto, Toronto, ON M5S 1A4, Canada.

²School of Chemical and Biomolecular Engineering and University of Sydney Nano Institute, University of Sydney, Sydney, NSW 2006, Australia. ³Department of Mechanical and Industrial Engineering, University of Toronto, Toronto, ON M5S 3G8, Canada.

*Corresponding author. Email: ted.sargent@utoronto.ca (E.H.S.); sinton@mie.utoronto.ca (D.S.); fengwang.li@sydney.edu.au (F.L.)

†These authors contributed equally to this work.

‡Present address: ICFO – Institut de Ciències Fotòniques, Barcelona Institute of Science and Technology, Barcelona 08860, Spain.

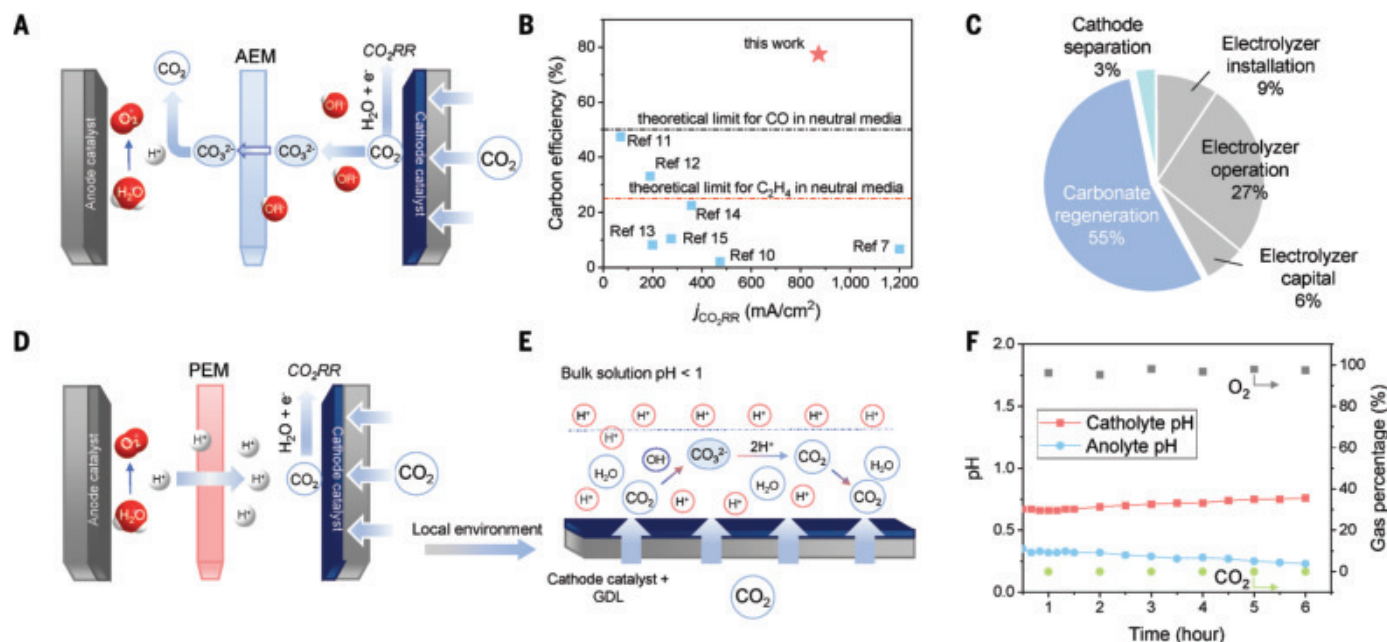


Fig. 1. Acidic CO₂ reduction versus alkaline and neutral CO₂ reduction.

(A) Schematic of carbonate formation and crossover phenomenon observed in neutral electrolyte-based reactor using anion exchange membrane (AEM). CO₂RR, CO₂ reduction reaction. (B) Comparison of carbon efficiency and current density in the benchmark alkaline and neutral CO₂R electrolyzers (7, 10–15). The dashed lines indicate theoretical carbon efficiency for CO (black) and C₂H₄ (red), respectively, in neutral media. Carbon efficiency in alkaline media is lower than in neutral media owing to additional consumption of CO₂ by bulk OH[−]. (C) Cost

breakdown of an alkaline CO₂R flow cell based on technoeconomic analysis (see supplementary materials for details; see also tables S1 and S2). (D and E) Schematics of ion transport and reactions in acidic CO₂R reactors. PEM, proton exchange membrane; GDL, gas diffusion layer. (F) Product analysis of the outlet gases at the anode side and monitoring of pH of catholyte and anolyte in a flow cell comprising 1 M H₃PO₄ and 3 M KCl as the catholyte, 0.5 M H₂SO₄ as the anolyte, and Nafion as the membrane. The cell was operated at a constant current density of 400 mA/cm².

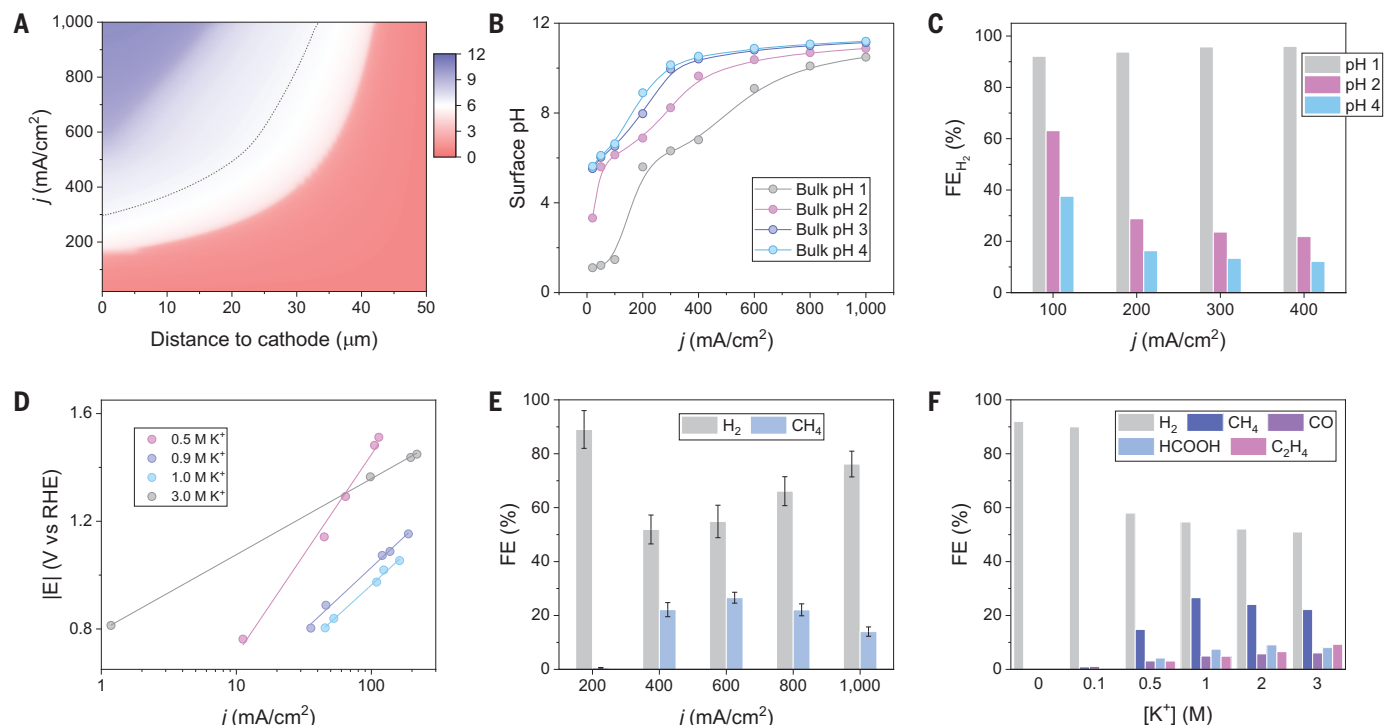


Fig. 2. Cation-enabled CO₂ reduction in acidic electrolyte. (A) Modeling of pH at different distances to cathode and current density in 1 M H₃PO₄ and 3 M KCl. The pH was adjusted to 1 by KOH. See supplementary materials for modeling details. (B) Surface (distance to cathode of 0 μm) pH at various pH and current density values. (C) FE toward hydrogen at current densities from 100 to 400 mA/cm² in phosphate

electrolytes with different pH values. (D) Tafel slopes obtained in electrolyte with different K⁺ concentrations. (E) FE toward H₂ and CH₄ on sputtered Cu catalyst at different current densities in 1 M H₃PO₄ and 3 M KCl. Values are means, and error bars indicate SD (*n* = 3 replicates). (F) FE toward all products on sputtered Cu catalyst in 1 M H₃PO₄ with different KCl concentrations at 400 mA/cm².

approaches neutrality when the current density reaches 100 mA/cm² for electrolytes with pH 2 to 4, or above 200 mA/cm² for electrolyte with pH 1 (Fig. 2B). Indeed, we observed experimentally a marked decrease of HER selectivity in electrolytes with pH 2 and 4 at a current density range of 100 to 400 mA/cm²; however, no measurable CO₂R products were detected in electrolyte with pH 1, even at a current density of 400 mA/cm² (Fig. 2C and fig. S3), at which the surface pH was modeled to be 7.

When we added 0.5 M KCl into the H₃PO₄ electrolyte (pH 1) in the middle of the reaction, however, we observed a slight decrease in FE toward hydrogen and detected CH₄ (FE 2.1 ± 0.3%) at a current density of 200 mA/cm² (fig. S4). Noting that the phosphate buffer electrolytes with different pH were prepared by mixing H₃PO₄ and KH₂PO₄ at different ratios, we posited that ion species, particularly cations (29–31), might steer kinetics of CO₂R catalysis at bulk pH <1.

To test this hypothesis, we carried out Tafel analysis at different pH and found that the Tafel slope decreased along with an increase in K⁺ concentration in the electrolytes (Fig. 2D). The slope reaches a minimum of 0.28 volts per decade at an electrolyte composition of 1 M H₃PO₄ with 3 M KCl (pH 0.67). This result suggests that the change in Tafel slope is not attributable to pH and that the rate-determining step is the adsorption of CO₂ (25). The presence of cations is key to CO₂ activation on the catalyst surface. Previous studies attributed the enhanced activation achieved with cations to their electrostatic interactions with the electric dipole of adsorbates or changes of surface charge density (30, 31). We assessed this activation enhancement on silver catalysts; in 1 M H₃PO₄ electrolyte, no CO₂R reactivity was observed, whereas ~50% CO₂R selectivity was achieved in the presence of 3 M K⁺ in the same electrolyte (fig. S5). The CO₂R selectivity on Cu catalysts was dependent on current density, and the FE of the main CO₂R product, CH₄, reached a maximum of 27% at 600 mA/cm² (Fig. 2E).

We studied the impact of local pH (equivalent to concentration of protons accessible to CO₂R and HER) on the activation of CO₂ and suppression of HER. At current densities <200 mA/cm², in which the local pH in 1 M H₃PO₄ electrolyte exhibits pH ≪7, the addition of K⁺ into the electrolyte did not affect voltametric properties of the Cu electrode, regardless of the concentration of K⁺ and the atmosphere (N₂ versus CO₂) (fig. S6), suggesting that K⁺ does not play a role in the activation of CO₂ nor does it suppress HER (from proton reduction) in a locally acidic environment. However, when operating at a higher current density of 400 mA/cm² to deplete local protons (local pH >7), while adding

K⁺ did not affect applied potentials, it did tune selectivity from HER (from water reduction) to CO₂R. The change of gas flow from N₂ to CO₂ increased the CO₂R partial current density from 0 to nearly 200 mA/cm² and decreased HER partial current density by about the same amount, but we did not observe any CO₂R activity in the electrolyte without K⁺ (fig. S7). These observations indicate a full mechanistic picture for CO₂R in bulk acidic electrolyte: Under a proton-depletion local environment, the cation triggers CO₂ activation, which suppresses the HER from water reduction, consistent with prior reports (19, 32).

The effect of anions on CO₂R reactivity is not significant; substitution of SO₄²⁻ or I⁻ for Cl⁻ showed product distribution similar to that of the Cl⁻ case (fig. S8). It is unlikely that K⁺ affects the oxidation state of Cu catalysts. Only metallic Cu was observed by operando x-ray absorption spectroscopy (fig. S9).

We examined CO₂R product distribution in 1 M H₃PO₄ with different concentrations of K⁺, and current density remained constant at 400 mA/cm² (Fig. 2F). The HER selectivity decreased with an increase in K⁺ concentration, and CO₂R selectivity increased. Selectivity for CH₄ was the highest, at ~28%, for 1 M K⁺. The FE toward C₂H₄, although not dominant, increased steadily from 3.1% with 0.5 M K⁺ to 9.3% with 3 M K⁺.

We sought to selectively steer further toward C₂H₄, in light of its high value and broad application in chemical manufacturing (33). However, the solubility of K⁺ in aqueous electrolytes is limited while maintaining a low pH. We turned to the enrichment of K⁺ at the Cu surface by a cation-augmenting layer (CAL). We used a cationic perfluorosulfonic acid (PFSA) ionomer composed of tetrafluoroethylene and sulfonyl fluoride vinyl ether. The acidic -SO₃H group is expected to exchange its protons with K⁺ from the bulk electrolyte in a nonacidic local environment, sustaining a high K⁺ concentration at the catalyst surface (Fig. 3A). In addition, the CAL allows cation (e.g., H⁺ and K⁺) transport in the direction from electrolyte to catalyst surface while slowing OH⁻ diffusion out, leading to higher surface pH, which was reported to facilitate C–C coupling (10, 15, 34). The ionomer was loaded onto the sputtered Cu surface as a blend with carbon nanoparticles (NPs) to increase its adhesion to the catalyst (fig. S10; details in supplementary materials).

The CAL-modified Cu showed a further increase of FE toward C₂H₄ to 13% and a much lower FE toward CH₄ of <1% compared with the bare Cu catalyst, while the remaining CO₂R gaseous product was CO at a current density of 400 mA/cm² in 1 M H₃PO₄ with 3 M KCl (Fig. 3B). The product selectivity shift was attributed to electrostatic interactions of cation species (e.g., K⁺) with the electric dipole of specific adsorbates that favor C₂⁺ reaction

pathways (31, 35). The FE toward C₂H₄ was ~10% for current densities in the range 300 to 800 mA/cm² (fig. S11). X-ray photoelectron spectroscopy (XPS) showed a marked increase of potassium on the CAL-modified Cu surface compared with the bare Cu after CO₂R operation (fig. S12), confirming the preservation of K⁺ by the ionomer layer.

To improve CO₂R productivity still further, we increased the electrochemically active surface area of the electrode by forming a Cu-NPs/PFSA composite material (fig. S13; details in supplementary materials) (7, 36). Similar to the case of bare Cu, the CO₂R selectivity was dependent on the bulk concentration of K⁺ in 1 M H₃PO₄; the FE toward C₂H₄ increased from ~10% with 1 M K⁺ to 26% with 3 M K⁺ at a current density of 1.2 A/cm² (Fig. 3C and fig. S14). The overall CO₂R selectivity reached 61%, including a total C₂⁺ FE of 40%.

Using a slim, low-resistance flow cell (fig. S15), we operated the high-surface-area CAL-modified Cu electrode at a current density of 1.2 A/cm² stably for an initial 12-hour test (details in supplementary materials). The full-cell voltage was 4.2 V (without compensation of voltage drop due to solution resistance, *i*R) and the FE toward C₂H₄ was constantly ~25% (Fig. 3D and fig. S16). In-depth XPS analyses indicate that K distributed evenly across the top layer of the composite electrode after CO₂R reaction (fig. S17). The percentages of Cl and P were five times lower than that of K, suggesting that the observed K concentration was sustained by the ionomer rather than caused by residual electrolyte salts.

CO₂R in acid enables CO₂ electrolysis without carbonate formation and crossover in bulk electrolytes, circumventing the CO₂ utilization limit that is fundamental to neutral and alkaline systems and permitting a carbon efficiency that is capable of increasing further in the direction of unity. To reduce energy demand of product separation from dilute streams (37), we pursued single-pass carbon efficiency (SPCE) toward the new theoretical limit.

By gradually reducing the flow rate of CO₂ from 50 to 5 standard cubic centimeters per minute (sccm), the C₂⁺ FE was improved to 48% (31% toward C₂H₄, 12% toward C₂H₅OH, 4% toward C₃H₇OH, and 1% toward CH₃COOH) (fig. S18). This combination of current density and selectivity results in a high overall C₂⁺ productivity of 600 mA/cm² (Fig. 3E).

By further lowering the flow rate of CO₂ to 3 sccm, we achieved, at a current density of 1.2 A/cm², an SPCE of ~77% for all the CO₂R products, including ~50% for C₂⁺ products (Fig. 3F). This outperforms previously reported alkaline and neutral CO₂R electrolyzers (Fig. 1B and table S6).

The cation augmentation takes CO₂ electrolysis from high-pH neutral and alkaline electrolytes to a pH <1 acidic environment. The

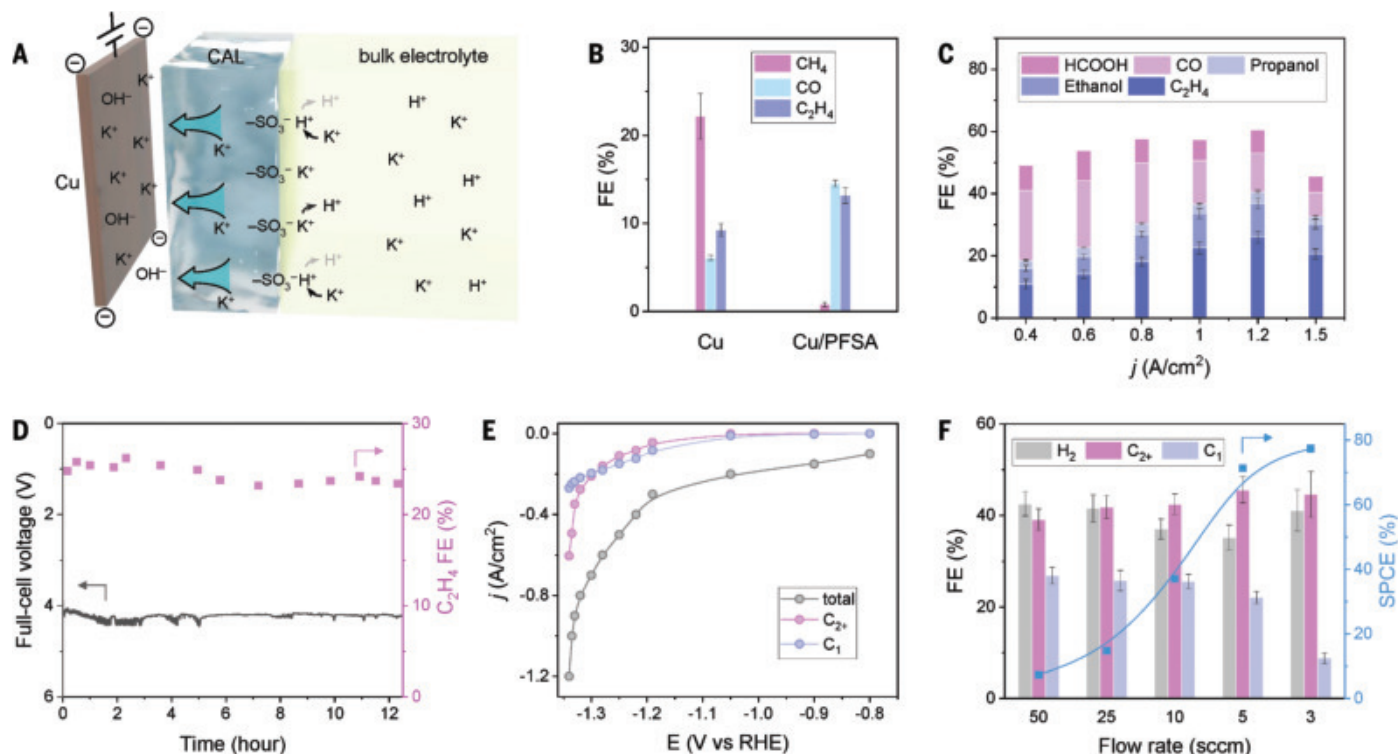


Fig. 3. Cation-augmenting layer (CAL) for multicarbon product formation and high carbon efficiency in acidic electrolyte. (A) Schematic illustration of ionic environment and transport near the catalyst surface functionalized by the PFSA ionomer. (B) FEs toward gaseous CO₂R products on bare Cu and PFSA-modified Cu (Cu/PFSA) at 400 mA/cm² in 1 M H₃PO₄ with 3 M KCl. Values are means, and error bars indicate SD (*n* = 3 replicates). (C) FEs toward CO₂R products at 400 to 1500 mA/cm² on CAL-modified Cu electrode. The flow rate of CO₂ inlet was 50 sccm. Values are means, and error bars indicate SD (*n* = 3 replicates). (D) The

extended CO₂R performance of the CAL-modified Cu-NP electrode in a slim flow cell at a constant current density of 1.2 A/cm². Nafion 117 membrane was used as the cation exchange membrane and high-surface-area IrO_x-Ti catalyst was used as the anode electrode. (E) Current density toward CO₂R products on CAL-modified Cu electrode. The flow rate of CO₂ inlet was 5 sccm. (F) FEs toward H₂ and CO₂R products as well as SPCE on CAL-modified Cu electrode at 1.2 A/cm² with different CO₂ flow rates. All experiments were performed using 1 M H₃PO₄ + 3 M KCl catholyte. Values are means, and error bars indicate SD (*n* = 3 replicates).

approach overcomes the problems of carbonate formation and CO₂ crossover. A voltage breakdown analysis shows that the full-cell voltage required to operate in this acidic system is comparable to that in the state-of-art neutral membrane electrode assembly cells (fig. S19) (7). We note that further improvement in selectivity and a decrease in operating voltage will be required on the path to energy-efficient electrochemical CO₂ conversion.

REFERENCES AND NOTES

- S. Chu, A. Majumdar, *Nature* **488**, 294–303 (2012).
- P. De Luna et al., *Science* **364**, eaav3506 (2019).
- S. Ren et al., *Science* **365**, 367–369 (2019).
- Y. Wu, Z. Jiang, X. Lu, Y. Liang, H. Wang, *Nature* **575**, 639–642 (2019).
- B. A. Rosen et al., *Science* **334**, 643–644 (2011).
- H. Xu et al., *Nat. Energy* **5**, 623–632 (2020).
- F. P. García de Arquer et al., *Science* **367**, 661–666 (2020).
- W. Ma et al., *Nat. Catal.* **3**, 478–487 (2020).
- J. A. Rabinowitz, M. W. Kanan, *Nat. Commun.* **11**, 5231 (2020).
- C.-T. Dinh et al., *Science* **360**, 783–787 (2018).
- T. Haas, R. Krause, R. Weber, M. Demler, G. Schmid, *Nat. Catal.* **1**, 32–39 (2018).
- R. B. Kutz et al., *Energy Technol.* **5**, 929–936 (2017).
- S. Verma et al., *ACS Energy Lett.* **3**, 193–198 (2018).
- T. T. H. Hoang et al., *J. Am. Chem. Soc.* **140**, 5791–5797 (2018).
- S. Ma et al., *J. Power Sources* **301**, 219–228 (2016).
- D. W. Keith, G. Holmes, D. St. Angelo, K. Heidel, *Joule* **2**, 1573–1594 (2018).
- M. Ma et al., *Energy Environ. Sci.* **13**, 977–985 (2020).
- F. Li et al., *Nature* **577**, 509–513 (2020).
- C. J. Bondue, M. Graf, A. Goyal, M. T. M. Koper, *J. Am. Chem. Soc.* **143**, 279–285 (2021).
- Z. Wang, P. Hou, Y. Wang, X. Xiang, P. Kang, *ACS Sustain. Chem. Eng.* **7**, 6106–6112 (2019).
- R. Kortlever, C. Balemans, Y. Kwon, M. T. M. Koper, *Catal. Today* **244**, 58–62 (2015).
- H. Ooka, M. C. Figueiredo, M. T. M. Koper, *Langmuir* **33**, 9307–9313 (2017).
- Y. Liu, C. C. L. McCrory, *Nat. Commun.* **10**, 1683 (2019).
- Y. Yu et al., *Electrochemistry* **88**, 359–364 (2020).
- J. Shen et al., *Nat. Commun.* **6**, 8177 (2015).
- I. Katsounaros et al., *Electrochem. Commun.* **13**, 634–637 (2011).
- N. Gupta, M. Gattrell, B. MacDougall, *J. Appl. Electrochem.* **36**, 161–172 (2006).
- M. Jouny, W. W. Luc, F. Jiao, *Ind. Eng. Chem. Res.* **57**, 2165–2177 (2018).
- A. Murata, Y. Hori, *Bull. Chem. Soc. Jpn.* **64**, 123–127 (1991).
- S. Ringe et al., *Energy Environ. Sci.* **12**, 3001–3014 (2019).
- J. Resasco et al., *J. Am. Chem. Soc.* **139**, 11277–11287 (2017).
- S. Ringe et al., *Nat. Commun.* **11**, 33 (2020).
- H. Zimmermann, R. Walzl, in *Ullmann's Encyclopedia of Industrial Chemistry* (Wiley-VCH, 2009).
- J. H. Montoya, C. Shi, K. Chan, J. K. Nørskov, *J. Phys. Chem. Lett.* **6**, 2032–2037 (2015).
- R. B. Sandberg, J. H. Montoya, K. Chan, J. K. Nørskov, *Surf. Sci.* **654**, 56–62 (2016).
- A. Özden et al., *ACS Energy Lett.* **5**, 2811–2818 (2020).
- D. S. Ripatti, T. R. Veltman, M. W. Kanan, *Joule* **3**, 240–256 (2019).

ACKNOWLEDGMENTS

We thank T. Wu and G. Sterbinsky for technical support at 9BM beamline of Advanced Photon Source (APS). **Funding:** This work was financially supported by the Ontario Research Foundation: Research Excellence Program, the Natural Sciences and Engineering Research Council (NSERC) of Canada, TOTAL SE, and Australian Research Council (project number DE200100477). This research used synchrotron resources of the APS, an Office of Science User Facility operated for the U.S. Department of Energy (DOE) Office of Science by Argonne National Laboratory, and was supported by the U.S. DOE under contract no. DE-AC02-06CH11357, and the Canadian Light Source and its funding partners. **Author contributions:** E.H.S., F.L., and D.S. supervised the project. F.L. and C.-T.D. conceived of the idea. J.E.H. and F.L. designed and carried out all the electrochemical experiments. A.O. fabricated nanoparticle electrodes and carried out slim flow cell measurement. S.Z. and A.O. assisted with electrochemical experiments. A.S.R. and S.L. performed pH simulation with the assistance of Y.X. K.B. performed XPS measurements. A.O., F.L., F.P.G.d.A., M.L., X.W., Y.L., and D.S. contributed to data analysis and manuscript editing. J.E.H. and E.H.S. co-wrote the manuscript.

All authors discussed the results and assisted with the manuscript preparation. **Competing interests:** A provisional patent application US 63/200,393 titled “CO₂ electroreduction to multi-carbon products in strong acid” was filed on 4 March 2021 by the University of Toronto in the joint names of Total SE and the Governing Council of the University of Toronto. **Data and**

materials availability: All experimental data are available in the main text or the supplementary materials.

SUPPLEMENTARY MATERIALS

science.sciencemag.org/content/372/6546/1074/suppl/DC1
Materials and Methods

Figs. S1 to S19
Tables S1 to S6
References (38–45)

20 January 2021; accepted 28 April 2021
10.1126/science.abg6582

HYDROGELS

Tough hydrogels with rapid self-reinforcement

Chang Liu¹, Naoya Morimoto¹, Lan Jiang¹, Sohei Kawahara¹, Takako Noritomi¹, Hideaki Yokoyama¹, Koichi Mayumi^{1,2,3,*}, Kohzo Ito^{1,*}

Most tough hydrogels are reinforced by introducing sacrificial structures that can dissipate input energy. However, because the sacrificial damage cannot rapidly recover, the toughness of these gels drops substantially during consecutive cyclic loadings. We propose a damageless reinforcement strategy for hydrogels using strain-induced crystallization. For slide-ring gels in which polyethylene glycol chains are highly oriented and mutually exposed under large deformation, crystallinity forms and melts with elongation and retraction, resulting both in almost 100% rapid recovery of extension energy and excellent toughness of 6.6 to 22 megajoules per square meter, which is one order of magnitude larger than the toughness of covalently cross-linked homogeneous gels of polyethylene glycol.

Hydrogels, polymer networks containing water as a solvent, generally have low mechanical strength because of their low polymer concentration and inhomogeneous network structure (1). Reinforcement of hydrogels has broadened their application as wearable sensors, actuators, and soft robots (2). Commonly, sacrificial bonds (1, 3–7), nanoparticles (8, 9), and crystalline structures (10–12) are incorporated into hydrogels for energy dissipation to achieve high toughness. Under large deformations, the “sub-

tractive” damage of these structures dissipates energy and raises the apparent work required to rupture the material. By using reversible interactions as the energy dissipation mechanism, tough gels with a high extent of structural and mechanical recovery can be realized (1, 3–6, 9, 11). Moreover, more than 100% mechanical recovery against repetitive loading was achieved by the initiation of polymerization by mechanoradicals generated from sacrificially damaged structures (7). However, the reconstruction of damaged structures usually takes minutes or hours; the greater the energy dissipated, the longer the time required for reconstruction. This leads to a deterioration in mechanical strength when tough hydrogels undergo multiple loading–unloading cycles with no waiting time (13).

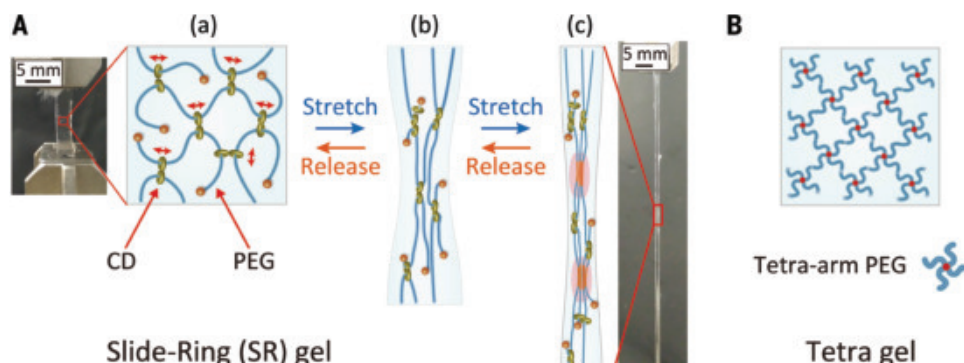
Herein, we propose a damageless reinforcement strategy by fabricating slide-ring (SR) hydrogels in which polyethylene glycol (PEG) chains are connected by slidable cross-links composed of hydroxypropyl- α -cyclodextrin

(CD) rings [Fig. 1A, (a)] (14, 15). The CDs are covalently cross-linked by divinyl sulfone (DVS). An excess amount of DVS (0.27 mol/liter) was added to CDs (0.051 to 0.11 mol/liter) (table S1). Unlike covalent cross-links fixed on polymer chains in conventional chemical gels, the cross-links in SR gels can slide on the PEG chains to release stress in the network. Under uniaxial stretching, the cross-links slide along the chains to approach each other, and polymer strands between the cross-linking points become longer and are uniformly stretched in the tensile direction [Fig. 1A, (b)] (16, 17). At extremely large strains, the exposed, highly oriented PEG chains repetitively form and destroy a close-packed structure with stretching and releasing [Fig. 1A, (c)]. For SR gels, optimizing two important parameters allows the attainment of the strain-induced aggregated structure of the PEG chains. One is the coverage of the CDs on the PEG chains. According to our previous work, reducing the number of CDs on one PEG chain increases the slidable range of the cross-links and thus the extensibility of SR gels (15). In this work, the average molecular weight of PEG was 35,000 g/mol and the CD coverage was 2%, corresponding to ~8 CDs on one PEG chain because gelation did not occur when CD coverage was 1%. The other important parameter is the polymer concentration. Increasing the PEG concentration in SR gels enhances the PEG-PEG interactions. The prepared SR gels with different PEG volume fractions (ϕ_{PEG}) were named SR- ϕ_{PEG} (ϕ_{PEG} = 0.18, 0.30, and 0.38). The CD coverage was fixed as 2% (CD/PEG molar ratio = 8) for all gels. The sample compositions of the SR gels are presented in table S1. For verifying the effect of the SR cross-links on the strain-induced structural

¹Material Innovation Research Center (MIRC) and Department of Advanced Materials Science, Graduate School of Frontier Sciences, The University of Tokyo, 5-1-5 Kashiwanoha, Kashiwa, Chiba 277-8561, Japan. ²AIST-UTokyo Advanced Operando-Measurement Technology Open Innovation Laboratory (OPERANDO-OIL), National Institute of Advanced Industrial Science and Technology (AIST), 5-1-5 Kashiwanoha, Kashiwa, Chiba 277-8561, Japan. ³The Institute for Solid State Physics (ISSP), The University of Tokyo, 5-1-5 Kashiwanoha, Kashiwa, Chiba 277-8581 Japan.

*Corresponding author. Email: kmayumi@g.ecc.u-tokyo.ac.jp (K.M.); kohzo@edu.k.u-tokyo.ac.jp (K.I.)

Fig. 1. Schematic of samples and reinforcement strategy. (A) SR gel with movable cross-links composed of CDs. The close-packed structure of PEG is formed and destroyed during stretching and releasing. **(B)** Tetra gel with fixed cross-links.



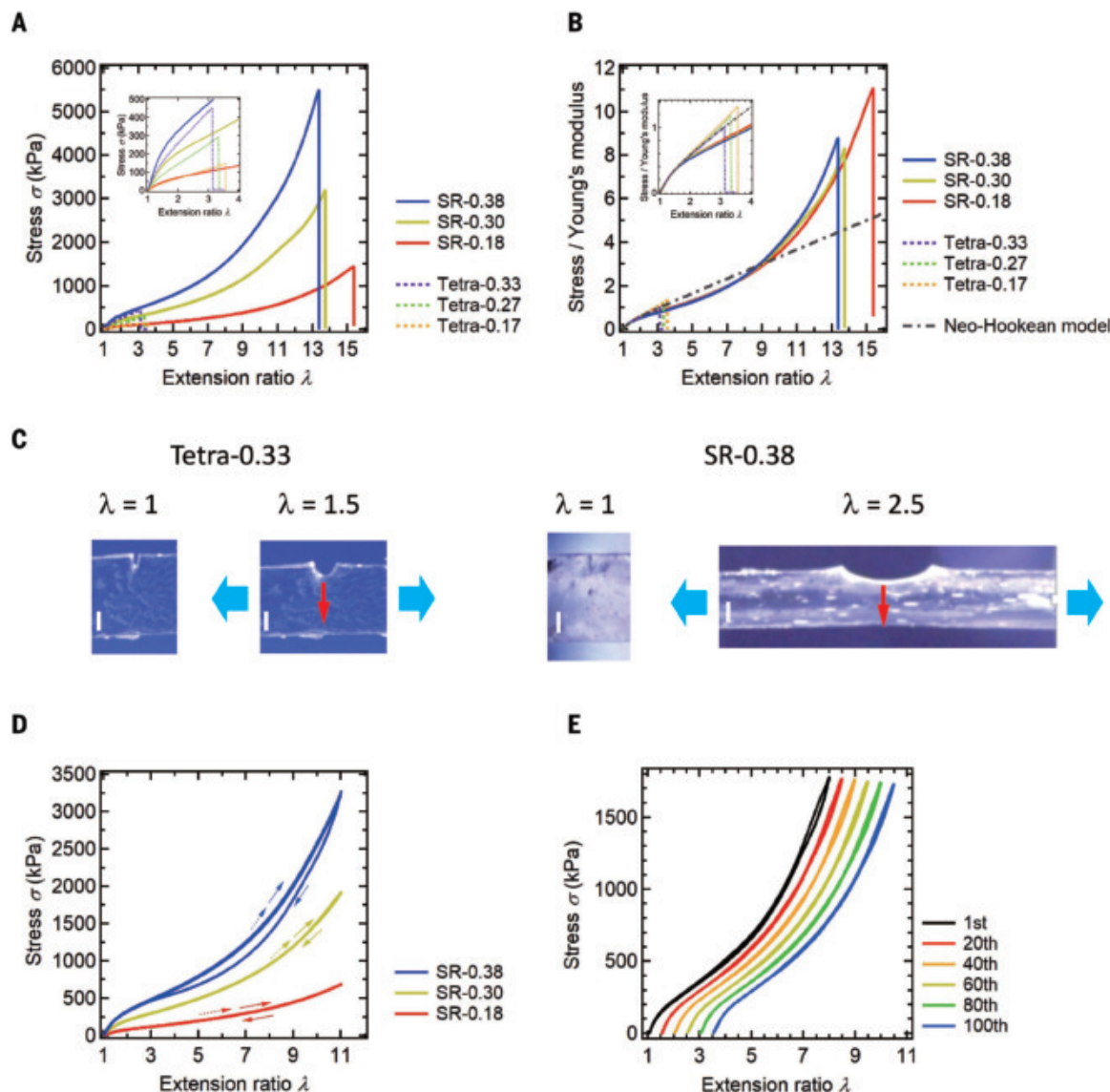


Fig. 2. Reversible reinforcement under extreme extension. (A) σ - λ curves of SR and Tetra gels. (B) σ - λ curves of SR and Tetra gels normalized by Young's moduli. (C) Photographs of single-edge notched specimens of Tetra-0.33 and SR-0.38 before stretching (left) and just after the cracks started to propagate under stretching (right). The blue and red arrows denote the direction of the

stretching and crack propagation, respectively. The white scale bars represent 1 mm. (D) Loading-unloading curves of SR gels. The solid (dotted) arrows denote the first (second) loading cycle. (E) One hundred consecutive cycles of eightfold loading and unloading for SR-0.38 gel. Horizontal shifts are applied to the 20th, 40th, 60th, 80th, and 100th cycle curves.

transformation, fixed cross-link PEG gels were prepared by end cross-linking of Tetra-armed PEG prepolymers (Fig. 1B) (18). The molecular weight of polymer strands between cross-linking points in the Tetra gels was 5000 g/mol, which is close to the average PEG molecular weight between neighboring CDs in the SR gels (4400 g/mol). The PEG volume fractions in the Tetra gels were varied in a range from 0.17 to 0.33 and named Tetra- ϕ_{PEG} ($\phi_{\text{PEG}} = 0.17, 0.27, \text{ and } 0.33$). The initial network structure was similar for the SR and Tetra gels, with the only difference being the slidability of the cross-linking points.

Figure 2A shows the tensile stress (σ)-extension ratio (λ) curves until rupture for

the SR and Tetra gels. SR-0.18 and Tetra-0.17 show similar Young's moduli of 130 and 110 kPa, respectively. According to the phantom network model, which is a classical rubber elasticity theory applicable to the mechanical responses of polymer gels (19), the Young's modulus E of polymer networks is given by $E = 3\rho RT/(2M)$, where ρ is the polymer mass concentration, R is the gas constant, T is the absolute temperature, and M is the average molecular weight of polymer strands between cross-linking points. From the Young's moduli, M is estimated to be 5,600 g/mol for SR-0.18 and 5,700 g/mol for Tetra-0.17; these values are close to the average PEG molecular weights of network strands calculated from their chem-

ical structures. As shown in Fig. 2B, the σ - λ curves of the Tetra gels with different PEG concentrations can be normalized by the Young's moduli and follow the classical rubber elasticity theory, the neo-Hookean model: $\sigma/E = (\lambda - \lambda^{-2})/3$ (19). The normalized σ - λ curves of the SR gels, which are independent of the strain rate (fig. S2), show softening compared with the neo-Hookean model in the moderate strain range $2 < \lambda < 8$, which can be attributed to the stress relaxation caused by the sliding of the cross-links [Fig. 1A, (b)] (16, 20).

The mechanical toughness of the SR and Tetra gels was evaluated quantitatively by the work of rupture U (area under the σ - λ

Table 1. Reversibility (U_2/U_1) and toughness (U and Γ) of SR gels compared with existing fixed cross-link and “subtractive” tough gels.				
Sample	ϕ_{polymer}	U_2/U_1 (%), λ_{cycle}	U (kJ/m ³)	Γ (J/m ²)
Tough and reversible gels				
SR-0.18	0.18 (ϕ_{PEG})	100 (11)	6600	2900
SR-0.30	0.30 (ϕ_{PEG})	100 (11)	14,000	2200
SR-0.38	0.38 (ϕ_{PEG})	98 (11)	22,000	3600
Fixed cross-link gels				
Tetra-0.17	0.17	100 (2)	160	47
Tetra-0.27	0.27	100 (2.8)	370	130
Tetra-0.33	0.33	100 (3)	550	240
“Subtractive” tough gels				
DFT-10-7 (12)	0.12	49 (3)	1300	280
Crystallized PVA-PAAm (11)	0.30	45 (2.5)	1800	2900
PAM-CS-A (4)	0.21	36 (4)	10,000	13,000
s-gel (AA/AM = 0.2) (5)	0.49	34 (2)	17,000	4800
Hybrid (1)	0.14	29 (7)	2400	8700
MM-0.2-6 (6)	0.53	21 (2)	31,000	19,000

ϕ_{polymer} , polymer volume fraction; ϕ_{PEG} , volume fraction of PEG in the SR gels; λ_{cycle} , largest extension during loading-unloading tests

curves in Fig. 2A) and fracture energy Γ obtained from tensile measurements of single-edge notched specimens. As shown in Table 1, U and Γ of the SR gels are one order of magnitude larger than those of the Tetra gels and similar to those of the existing “subtractive” tough hydrogels (1, 4–6, 11, 12) (experimental conditions are shown in table S2). The marked toughening by the slidability of the cross-links is confirmed by the crack blunting of the SR gels as shown in Fig. 2C and fig. S3. The toughness of SR gels is reduced by decreasing the PEG molecular weight (fig. S4), suggesting more network defects and smaller sliding distance of the cross-links (17).

An important feature of the SR gels compared with the “subtractive” tough gels is the high recoverability comparable to that of the fixed cross-link gels (Fig. 2D, fig. S5, and Table 1). Although mechanical hysteresis was observed especially for SR-0.38, the SR gels exhibited almost no residual strain and similar mechanical responses during the first and second loadings (Fig. 2D), implying a robust network

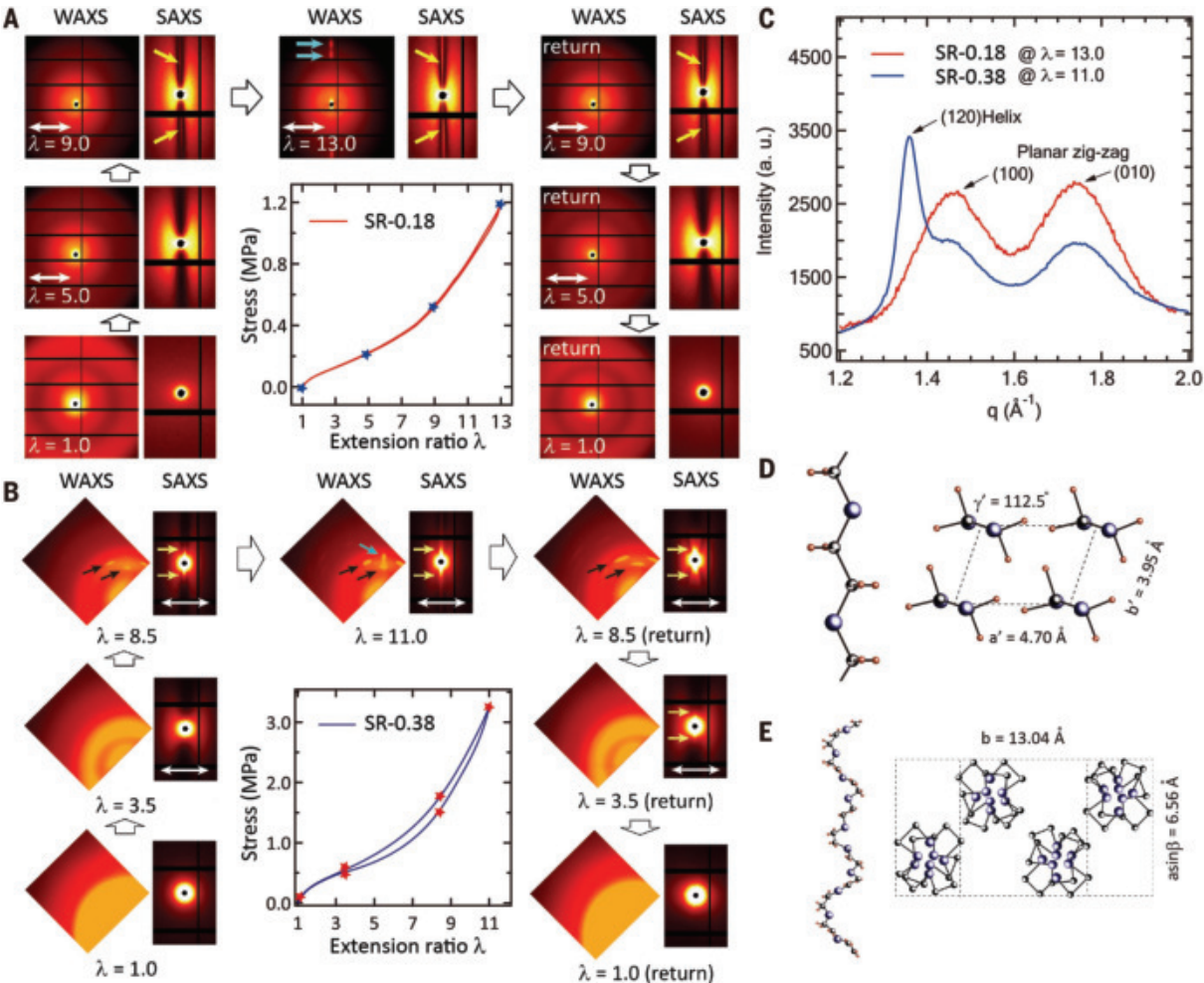


Fig. 3. Structural transition under cyclic loading. (A and B) WAXS and SAXS patterns of SR-0.18 (A) and SR-0.38 (B) during a loading-unloading cycle. The white double arrows denote the stretching direction. (C) WAXS profiles of SR-0.18 and SR-0.38 gels in the direction perpendicular to stretching. (D) Structure of planar zigzag PEG and its triclinic crystal. (E) Structure of 7/2 helix PEG and its monoclinic crystal.

structure against consecutive cyclic deformation. The reversibility of hydrogels is defined as the ratio of the area covered by the second cycle loading curve to that covered by the first one, U_2/U_1 (fig. S6). For “subtractive” gels, reversibility in consecutive loading cycles is sacrificed for gaining high toughness in the first loading (Table 1). By contrast, the SR gels simultaneously show a reversibility of 98 to 100% and high toughness comparable to the “subtractive” tough gels (Table 1). The high reversibility of the SR gels was observed during 100 cycles of consecutive loading–unloading in liquid paraffin (Fig. 2E and figs. S7 and S8).

The high toughness of the SR gels originates from strain-induced crystallization (SIC), which is a well-known toughening mechanism for rubbers (21–23). At large strains, the stretched SR gels show diffraction spots in the wide-angle x-ray scattering (WAXS) patterns of Fig. 3, A and B, indicating the occurrence of SIC of the PEG chains [Fig. 1A, (c)]. No diffraction spots were observed for the Tetra gels or the SR gel with the shorter PEG under stretching (figs. S9 and S10). The SR network with a sufficiently long chain length promotes the SIC of the main chains. The two diffraction peaks in the profile of SR-0.18 gel (Fig. 3C) denote the (100) and (010) reflections of planar zigzag PEG crystalline with triclinic unit cells (Fig. 3D) (24), and the additional peak in that of SR-0.38 gel (Fig. 3C) denotes the (120) reflection of 7/2 helix PEG crystalline with monoclinic unit cells (Fig. 3E) (25). On the basis of the Scherrer equation, the sizes of planar zigzag and helix PEG crystallines were estimated to be 6 and 28 nm, respectively (fig. S11). Sharp streaks were observed in the small-angle X-ray scattering (SAXS) patterns of the SR gels before the formation of planar zigzag crystals (yellow arrows in Fig. 3, A and B), suggesting the formation of a crystalline precursor composed of highly extended chains (figs. S12 and S13). In the large strain regime, the SR gels show the upturn of the stress extension ratio curves (Fig. 2A). During the unloading process, the strain-induced crystalline phase disappeared (Fig. 3, A and B, and figs. S14 and S15). The reversible formation and destruction of the PEG crystals under loading and unloading cycles is the origin of the high mechanical reversibility of the SR gels.

Although a similar phenomenon has been reported in rubbers (21–23), we achieved reversible SIC in hydrogel systems with much lower polymer concentrations. This rapid self-reinforcement concept should also be applicable to gels composed of other semicrystalline polymers and provides insights into the practical applications of tough hydrogels.

REFERENCES AND NOTES

1. J. Y. Sun *et al.*, *Nature* **489**, 133–136 (2012).

2. C. Yang, Z. Suo, *Nat. Rev. Mater.* **3**, 125–142 (2018).
3. T. L. Sun *et al.*, *Nat. Mater.* **12**, 932–937 (2013).
4. Y. Yang, X. Wang, F. Yang, H. Shen, D. Wu, *Adv. Mater.* **28**, 7178–7184 (2016).
5. Y. Liang, J. Xue, B. Du, J. Nie, *ACS Appl. Mater. Interfaces* **11**, 5441–5454 (2019).
6. Y. J. Wang *et al.*, *Chem. Mater.* **31**, 1430–1440 (2019).
7. T. Matsuda, R. Kawakami, R. Namba, T. Nakajima, J. P. Gong, *Science* **363**, 504–508 (2019).
8. H. J. Li, H. Jiang, K. Haraguchi, *Macromolecules* **51**, 529–539 (2018).
9. G. Gao, G. Du, Y. Sun, J. Fu, *ACS Appl. Mater. Interfaces* **7**, 5029–5037 (2015).
10. S. Lin *et al.*, *Sci. Adv.* **5**, eaau8528 (2019).
11. J. Li, Z. Suo, J. J. Vlassak, *J. Mater. Chem. B Mater. Biol. Med.* **2**, 6708–6713 (2014).
12. L. Zhang, J. Zhao, J. Zhu, C. He, H. Wang, *Soft Matter* **8**, 10439–10447 (2012).
13. R. Bai *et al.*, *Extreme Mech. Lett.* **15**, 91–96 (2017).
14. Y. Okumura, K. Ito, *Adv. Mater.* **13**, 485–487 (2001).
15. L. Jiang *et al.*, *Chem. Mater.* **30**, 5013–5019 (2018).
16. A. A. Gavrilov, I. I. Potemkin, *Soft Matter* **14**, 5098–5105 (2018).
17. C. Liu *et al.*, *ACS Macro Lett.* **6**, 1409–1413 (2017).
18. T. Sakai *et al.*, *Macromolecules* **41**, 5379–5384 (2008).
19. Y. Akagi *et al.*, *Macromolecules* **44**, 5817–5821 (2011).
20. C. Liu *et al.*, Direct observation of large deformation and fracture behavior at the crack tip of slide-ring gel. *J. Electrochem. Soc.* **166**, B3143–B3147 (2019).
21. J. C. Mitchell, D. J. Meier, *J. Polym. Sci. Pol. Phys.* **6**, 1689–1703 (1968).
22. S. Toki, T. Fujimaki, M. Okuyama, *Polymer* **41**, 5423–5429 (2000).
23. H. P. Zhang, J. Niemczura, G. Dennis, K. Ravi-Chandar, M. Marder, *Phys. Rev. Lett.* **102**, 245503 (2009).
24. Y. Takahashi, I. Sumita, H. Tadokoro, *J. Polym. Sci., B, Polym. Phys.* **11**, 2113–2122 (1973).

25. H. Tadokoro, Y. Chatani, T. Yoshihara, S. Tahara, S. Murahashi, *Makromol. Chem.* **73**, 109–127 (1964).

ACKNOWLEDGMENTS

We thank T. Sakai and T. Fujiyabu for valuable discussions and T. Hoshino, S. Fujinami, and T. Nakatani (RIKEN Spring-8 Center) for their generous efforts in the beamline setup. **Funding:** This work was partially supported by the ImPACT Program of the Council for Science, Technology, and Innovation (Cabinet Office, Government of Japan), JSPS KAKENHI (grants JP15K17905, JP 18J13038, and JP20K05627), JST-Mirai Program (grant JPMJMI18A2), JST CREST (grant JPMJCR1992), and AIST-UTokyo Advanced Operando-Measurement Technology Open Innovation Laboratory (OPERANDO-OIL). **Author contributions:** C.L., K.M., and K.I. conceived the concept and designed the experiments. C.L., N.M., S.K., and T.N. performed the experiments. L.J. and H.Y. assisted with material fabrication and characterization. C.L., K.M., and K.I. wrote the manuscript. All authors discussed the results and commented on the manuscript. **Competing interests:** The authors declare no competing interests. **Data and materials availability:** All data are available in the main text or supplementary materials.

SUPPLEMENTARY MATERIALS

science.sciencemag.org/content/372/6546/1078/suppl/DC1
Materials and Methods
Figs. S1 to S15
Tables S1 and S2
References (26–30)

29 September 2019; resubmitted 28 February 2020

Accepted 23 April 2021

10.1126/science.aaz6694

GAMMA-RAY BURSTS

Revealing x-ray and gamma ray temporal and spectral similarities in the GRB 190829A afterglow

H.E.S.S. Collaboration†*

Gamma-ray bursts (GRBs), which are bright flashes of gamma rays from extragalactic sources followed by fading afterglow emission, are associated with stellar core collapse events. We report the detection of very-high-energy (VHE) gamma rays from the afterglow of GRB 190829A, between 4 and 56 hours after the trigger, using the High Energy Stereoscopic System (H.E.S.S.). The low luminosity and redshift of GRB 190829A reduce both internal and external absorption, allowing determination of its intrinsic energy spectrum. Between energies of 0.18 and 3.3 tera-electron volts, this spectrum is described by a power law with photon index of 2.07 ± 0.09 , similar to the x-ray spectrum. The x-ray and VHE gamma-ray light curves also show similar decay profiles. These similar characteristics in the x-ray and gamma-ray bands challenge GRB afterglow emission scenarios.

The core collapse of a rapidly rotating massive star produces a supernova explosion, accompanied by a fast jet-like outflow propagating close to the speed of light (a relativistic outflow). These outflows produce long gamma-ray bursts (GRBs), observed as prompt gamma-ray emission

episodes lasting for several seconds. This is followed by an afterglow of slowly fading emission, caused by the interaction of the relativistic ejecta with surrounding gas, lasting hours or days. The first radiative signature of GRB afterglows is nonthermal synchrotron emission from electrons accelerated at the forward shock of the relativistic outflow (1). The same electrons up-scatter the synchrotron photons through the inverse Compton mechanism, producing a synchrotron self-Compton (SSC) emission component extending into the very-high-energy (VHE) (>100 GeV) regime. This emission has been proposed as a second radiative signature of GRB afterglows (2, 3). Two VHE GRB detections (4–6) have separately

*Corresponding authors: contact.hess@hess-experiment.eu; Andrew M. Taylor (andrew.taylor@desy.de); Felix Aharonian (felix.aharonian@mpi-hd.mpg.de); Carlo Romoli (cromoli@mpi-hd.mpg.de); Dmitry Khangulyan (d.khangulyan@rikkyo.ac.jp); Edna Ruiz-Velasco (edna.ruiz@mpi-hd.mpg.de); Fabian Schüssler (fabian.schussler@cea.fr); Sylvia J. Zhu (sylvia.zhu@desy.de)

†H.E.S.S. Collaboration authors and affiliations are listed in the supplementary materials.

probed the early and late-time afterglow phases.

We observed the afterglow of GRB 190829A using the High Energy Stereoscopic System (H.E.S.S.) on three consecutive nights, from 4.3 to 55.9 hours after the GRB began. GRB 190829A was initially detected by the Gamma-ray Burst Monitor (GBM) on the *Fermi* space telescope on 29 August 2019 at 19:55:53 universal time (UT) (hereafter T_0) (7). The Burst Alert Telescope (BAT) on the *Neil Gehrels Swift Observatory* spacecraft triggered on this burst 51 s later, and observations with the X-Ray Telescope (XRT) on *Swift* began 97.3 s after the BAT trigger (8). The *Swift* Ultraviolet/Optical Telescope began observing the GRB

afterglow at $T_0 + 158$ s. The afterglow was also detected by ground-based telescopes in the optical, the near-infrared (NIR), and the radio bands, starting 1318 s after the GBM trigger and continuing for several days. The afterglow brightened in the optical-to-NIR bands starting about 4 days after T_0 , owing to the supernova associated with this GRB (9–13). The host galaxy has a redshift of $z = 0.0785 \pm 0.0005$ (14).

The first hour of the x-ray light curve contained three flares or rebrightening events. The prompt emission comprised a short peak at 0 to 4 s after T_0 and a second broader peak at 50 to 60 s after T_0 , both detected with *Swift*-BAT. A third rebrightening at 1000 to 3000 s after T_0 was detected with *Swift*-XRT. After

this final rebrightening, the x-ray light curve followed a smooth power-law decay, typical of the onset of a GRB afterglow (15). Our H.E.S.S. observations were performed during this power-law decay afterglow phase, beginning at $T_0 + 10^4$ s.

The H.E.S.S. observations were performed on three consecutive nights: the first night starting at $T_0 + 4.3$ hours for an observing time of 3.6 hours, the second night at $T_0 + 27.2$ hours for 4.7 hours, and the third night at $T_0 + 51.2$ hours for 4.7 hours (16). Our analysis detected a VHE gamma-ray signal on each of the three nights, spatially coincident with the GRB position (fig. S1), with statistical significances of 21.7σ , 5.5σ , and 2.4σ (16).

We performed a spectral analysis of the first two nights; the signal on the third night was too weak to determine the spectrum. We fitted a power-law model to the photon spectrum

of the form $dN/dE = N_0(E/E_0)^{-\gamma_{\text{VHE}}^{\text{obs}}}$, where N_0 is the spectrum normalization at photon energy E_0 , and $\gamma_{\text{VHE}}^{\text{obs}}$ is the observed spectral index. We find $\gamma_{\text{VHE}}^{\text{obs}} = 2.59 \pm 0.09$ (stat.) ± 0.23 (syst.) (0.18 to 3.3 TeV) on the first night and 2.46 ± 0.23 (stat.) ± 0.14 (syst.) (0.18 to 1.4 TeV) on the second night (Fig. 1).

Gamma rays from distant astronomical sources are attenuated by photon interactions with radiation fields both within the source (“internal” absorption) and with the extragalactic background light (EBL) (17). Extragalactic absorption depends on the redshift z , and internal absorption depends on the source compactness (the ratio of the intrinsic source luminosity to its radius). The modest luminosity of GRB 190829A (18) and the late observation epochs reduce the internal absorption, so we expect attenuation by the EBL to dominate in the H.E.S.S. observation period (16). The gamma-ray attenuation by the EBL increases with source distance; the Universe is optically thick to multi-TeV gamma rays beyond a redshift of $z \approx 0.1$ (17). Nearby GRBs experience less attenuation, requiring a smaller correction due to EBL absorption and allowing the intrinsic spectrum to be determined. Figure 2 shows the model EBL absorption levels for GRB 190829A and the two GRBs previously detected at VHEs (4, 6).

To characterize the intrinsic GRB spectrum (corrected for EBL absorption), we fitted an attenuated power-law model of the form $dN/dE = N_0(E/E_0)^{-\gamma_{\text{VHE}}^{\text{int}}} e^{-\tau(E,z)}$ to the data.

The exponential term corresponds to the absorption of photons through their interaction with the EBL, τ is the energy-dependent optical depth for a source at redshift z , and $\gamma_{\text{VHE}}^{\text{int}}$ is the intrinsic spectral index (16).

For the first two observation nights, we determined VHE intrinsic photon indices of $\gamma_{\text{VHE}}^{\text{int}} = 2.06 \pm 0.10$ (stat.) ± 0.26 (syst.) (first night) and

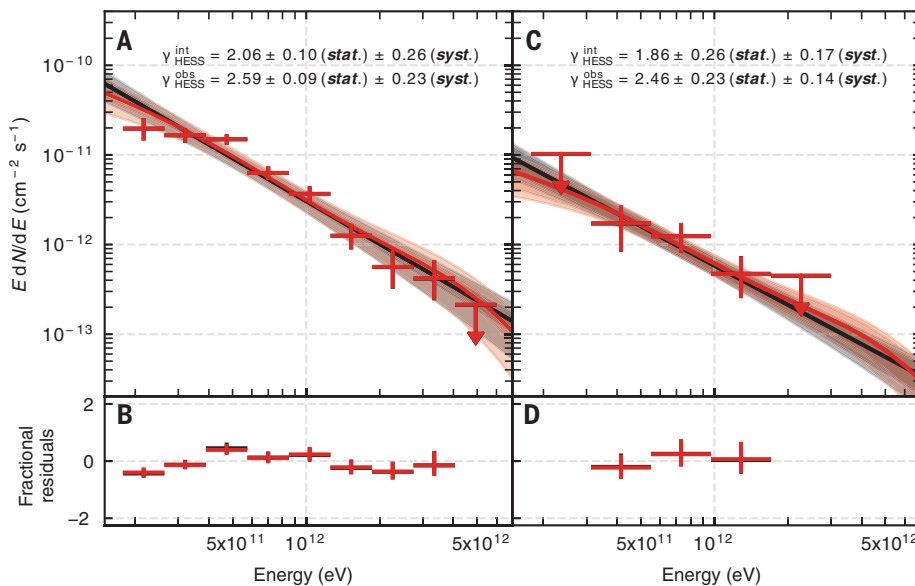


Fig. 1. H.E.S.S. VHE spectra of GRB 190829A on the first and second nights. (A) The power-law (black) and EBL attenuated power-law (red) models (lines) fitted to the observational data (red crosses), with shaded regions indicating the 1σ statistical and systematic uncertainty on the first night. (C) The same as in (A) but for the second night of observations. (B and D) the fractional residuals, (data – model)/model, between the data and the power-law (black) and EBL attenuated power-law (red) models. Error bars in all panels are 1σ statistical uncertainty, and upper limits are the 95% confidence level.

Fig. 2. Model extragalactic background light absorption for three GRBs detected in the VHE band. Models of

EBL absorption in the energy range 0.1 to 3 TeV are shown for GRB 190829A [$z = 0.0785$, blue (14)], GRB 190114C [$z = 0.4245$ (4), green], and GRB 180720B [$z = 0.653$ (6), orange]. The solid lines indicate the EBL absorption from our preferred model (17), the darker shaded areas indicate the spread when adopting EBL models (25–28), and the lighter shaded areas indicate the additional uncertainty from a shift of 10% in the energy scale.

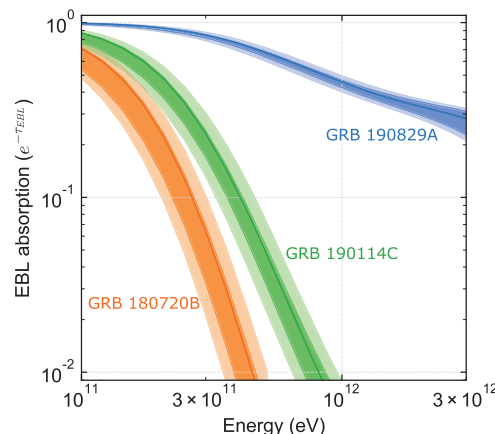
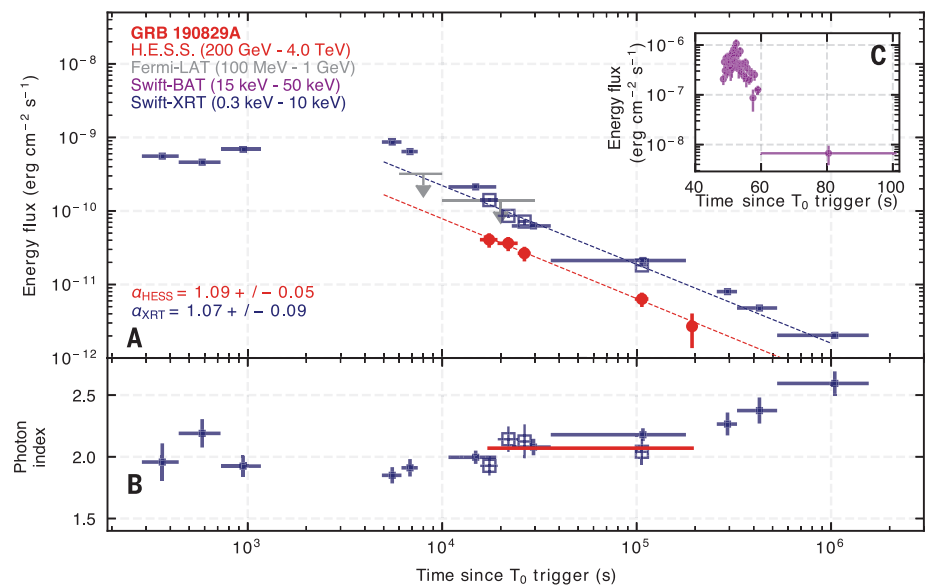


Fig. 3. Logarithmic x-ray and gamma-ray multiwavelength energy-flux light curves of the GRB 190829A afterglow. (A) The temporal evolution of the energy flux detected in x-rays with *Swift*-XRT (blue closed squares), upper limits on MeV gamma rays from *Fermi*-LAT (gray arrows), and VHE gamma rays from H.E.S.S. (red circles). The XRT temporal decay index (α_{XRT}) was determined by fitting a model to only the XRT data that were simultaneous with the H.E.S.S. observations (blue open squares). (B) The corresponding intrinsic photon indices. The H.E.S.S. intrinsic spectral index, indicated by the continuous red line, is assumed to be constant at the mean value of 2.07 ± 0.09 determined from nights 1 to 3. (C) The energy-flux evolution of the prompt emission observed by *Swift*-BAT, obtained from the *Swift* Burst Analyser (22). All error bars correspond to 1σ uncertainty, and the *Fermi*-LAT upper limits are at the 95% confidence level.



1.86 ± 0.26 (stat.) ± 0.17 (syst.) (second night). These values indicate that within the uncertainties, the spectral shape remains unchanged, so we performed a joint spectral analysis (16). Combining the three nights of observation data, the photon index found is $\gamma_{\text{VHE}}^{\text{int}} = 2.07 \pm 0.09$ (stat.) ± 0.23 (syst.), in the energy range (0.18 to 3.3 TeV). These per-night VHE photon indices are consistent, within the statistical uncertainties, with the photon indices of the x-ray emission (γ_{XRT}) we measured from the *Swift*-XRT data taken during the same observational periods: $\gamma_{\text{XRT}} = 2.03 \pm 0.06$ (first night), and $\gamma_{\text{XRT}} = 2.04 \pm 0.10$ (second night) (16).

We extracted a light curve of the H.E.S.S. observations in the energy range 0.2 to 4.0 TeV for the entire temporal coverage up to $T_0 + 56$ hours. We split the first observation night into three subintervals (Fig. 3). The gamma-ray energy flux, F_{VHE} , depends on how much time t has passed after T_0 , and the time evolution is characterized by a power-law model $F_{\text{VHE}}(t) \propto t^{-\alpha_{\text{VHE}}}$, with $\alpha_{\text{VHE}} = 1.09 \pm 0.05$ (16). This VHE gamma-ray flux behavior is similar to the x-ray light curve derived for the same time period. The flux measured by *Swift*-XRT can also be described as a power law, with index α_{XRT} ; using the *Swift*-XRT data in the energy interval 0.3 to 10 keV, we find that $\alpha_{\text{XRT}} = 1.07 \pm 0.09$.

The photon index of the GRB 190829A afterglow in the x-ray band is typical for GRB afterglows, which have a mean value of $\bar{\gamma}_{\text{XRT}} \approx 2$ (19). However, the afterglow decayed more slowly than is typical over this time interval. The average decay index for all GRB afterglows measured by *Swift*-XRT up to 56 hours after the T_0 time period (observer frame) is $\bar{\alpha}_{\text{XRT}} \sim 1.4$, based on the best-fitting broken power-law light-curve models, with less than 30% of the XRT-detected GRBs having smaller

temporal decay indices than GRB 190829A during the same time period (16).

Figure 3 shows the x-ray and gamma-ray afterglow temporal evolutions between 20 s and 11 days after T_0 . The afterglow phase, $t \geq 10^3$ s, shows the H.E.S.S.- and *Swift*-XRT-detected fluxes and upper limits on the gamma-ray flux at 0.1 to 1 GeV, derived from the *Fermi*-Large Area Telescope (LAT) observations (20). During this afterglow period, the temporal profiles in the x-ray band show no short-time scale variability. The VHE light curve closely matches the x-ray light curve (16).

During the prompt phase ($t < 100$ s), the total isotropic energy in the GBM energy band (10 to 1000 keV) was $E_{\text{GBM}}^{\text{iso}} \approx 2 \times 10^{50}$ erg with 1% uncertainty (18) and in the *Swift*-BAT energy range (15 to 150 keV) was $E_{\text{BAT}}^{\text{iso}} \approx 1 \times 10^{50}$ erg with 10% uncertainty ($t < 60$ s). With the energy flux in the afterglow decaying at approximately t^{-1} , the energy output per logarithmic time interval is approximately constant. Consequently, no single logarithmic temporal bin dominates the total fluence of the outburst (fig. S2). The isotropic energy output measured by *Swift*-XRT during the afterglow phase was $E_{\text{XRT}}^{\text{iso}} \approx 5 \times 10^{50}$ erg ($t < 10^6$ s) with 10% uncertainty (16). This is larger than it was during the prompt phase, a feature that has rarely been observed (21).

We investigated whether the VHE light curve and spectrum of GRB 190829A are compatible with the standard GRB afterglow emission model. This model assumes particle acceleration at the forward shock (16), where the outflow propagates outward through the circumburst material (22). As a result, a non-negligible fraction of the shock energy is transferred into magnetic field enhancement and particle acceleration, leading to the production of broadband non-thermal emission.

Although both hadrons and leptons are accelerated, typical values of the circumburst density at the forward shock suggest that the time for hadrons to cool is substantially longer than the dynamical shock time, resulting in low radiative efficiencies. Unlike hadrons, VHE electrons promptly lose their energy through synchrotron and inverse Compton radiation.

The observed energy flux decays as approximately t^{-1} in both x-ray and gamma-ray bands. Decay of this form suggests that the shocked plasma magnetization level, the fraction of energy transferred to nonthermal electrons, and radiative efficiency of the forward shock effectively remain constant during the afterglow (16).

We performed multiwavelength modeling of the *Swift*-XRT, *Fermi*-LAT, and H.E.S.S. data. We averaged these spectral results on a per-night basis because this time period is similar to the evolution time scale of the outflow Lorentz factor, dictated by GRB kinematics (23). We find that the emission region has a Lorentz factor $\Gamma = 4.7$ and 2.6 for the first and second nights, respectively.

For Lorentz factors < 10 , which we expect during the H.E.S.S. observation window (16), the accelerated electrons producing the VHE emission experience recoil when up-scattering the synchrotron photons, referred to as the onset of the Klein-Nishina regime (16), resulting in a steepening of the inverse Compton spectrum. This steepening makes it challenging for SSC models to reproduce simultaneously the observed x-ray and VHE spectra. We therefore introduced an alternative leptonic scenario with no limitation placed on the electron maximum energy (which would otherwise be set by energy losses). This assumption implies that the synchrotron spectrum can extend up into the VHE regime.

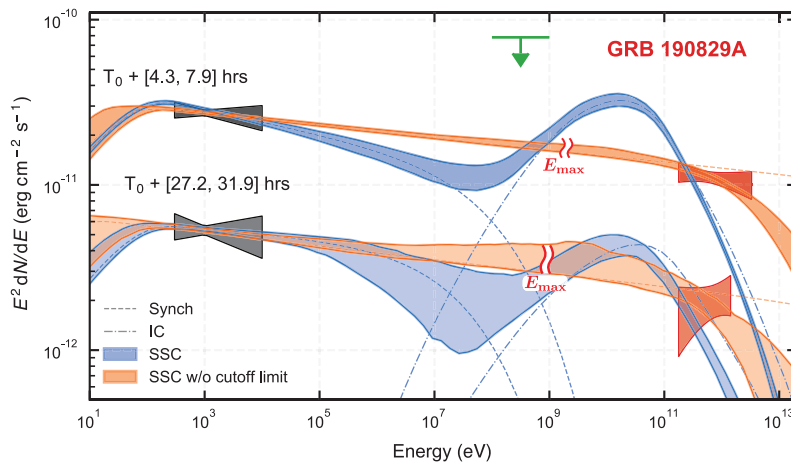


Fig. 4. Theoretical multiwavelength models of the first- and second-night data. The black region shows the spectrum and uncertainty of the *Swift*-XRT data, the green arrow upper limit is from *Fermi*-LAT [available only for the first night (19)], and the red region is the H.E.S.S. intrinsic spectrum and its uncertainty (statistical only). The shaded areas represent the 68% confidence intervals, determined from the posterior probability distributions of the MCMC parameter fitting for the standard SSC model (light blue) and the synchrotron-dominated model (orange); the latter model does not impose a synchrotron cut-off energy (labeled E_{max}) (16). The synchrotron components of the two SSC models are indicated by dashed curves, whereas the dashed-dotted curves show the inverse Compton components. These curves show the emission level when neglecting the internal gamma-gamma absorption. Two sets of data are shown: The upper set is for the first night, and the lower set is for the second night; both are labeled with the time periods. The best-fitting parameters are listed in tables S5 and S6.

To further investigate the emission origin, we searched for a theoretical instantaneous electron distribution such that the corresponding synchrotron and SSC emission can explain consistently both the x-ray and gamma-ray spectra. We performed a Markov Chain Monte Carlo (MCMC) exploration of the five-dimensional parameter space (the magnetic field strength and four parameters describing the broken power-law electron distribution) (16), with the results shown in Fig. 4. Additionally, we investigated whether including the optical data (14) affects these results and found that they remain unchanged (16).

The standard model in which the electron maximum energy is set by the energy-loss limit predicts a soft spectral index for the VHE emission. This is due to the combination of the accelerated electrons having a steep distribution (power-law index $\beta_2 \approx 3$) and the fact that in the VHE range, the photons are produced via inverse Compton scattering in the Klein-Nishina regime. Internal photon-photon absorption within the source makes the spectrum steeper. Such a spectrum is inconsistent with our observations.

For the alternative model with no limit placed on the maximum electron energy, the theoretical spectrum is dominated by a single synchrotron component covering a broad energy range from x-rays to VHE gamma rays (Fig. 4). The SSC component in this case is

three orders of magnitude weaker than the synchrotron component. In the VHE range covered by the H.E.S.S. observations, internal photon-photon absorption is non-negligible. A single synchrotron component provides a significantly ($>5\sigma$) better fit to the multiwavelength data. However, if particle acceleration and emission occur in a region where ideal magnetohydrodynamic conditions are satisfied, the synchrotron component should not extend beyond $E_{\text{max}} \approx 200D$ MeV (where D is the Doppler factor; $D \approx 2\Gamma$ for $\Gamma \gg 1$). Figure 4 shows that the synchrotron component would need to extend more than three orders of magnitude beyond the synchrotron limiting energy. This would require an unknown high-efficiency process to accelerate multi-PeV electrons in the magnetic fields (expected to be a few Gauss in strength) or a conventional acceleration mechanism in a medium with a large difference in the magnetic field strengths of the acceleration and radiation zones (24).

The spectral steepening predicted in the VHE range means we cannot reproduce the observations with a simple one-zone SSC model (Fig. 4). We discuss two ways to improve the agreement between the data and the models: (i) higher bulk Lorentz factor, and (ii) non-power law distributions of emitting particles.

The discrepancy between models and data could be removed if the Doppler factor at

4 hours after T_0 is increased to $\sim 10^2$. This assumption reduces the level of electron recoil in the inverse Compton scattering process, bringing the intrinsic VHE photon index closer to that measured in x-rays; the internal photon-photon absorption of the VHE emission is then reduced. However, the required value of the bulk Lorentz factor is inconsistent with predictions of the standard hydrodynamic model. The weak dependence of the Lorentz factor on the explosion energy and surrounding gas density makes it difficult to physically produce values of $\sim 10^2$ (16). If GRB 190829A was an off-axis explosion, with a large line-of-sight angle relative to the jetted outflow direction, then the bulk Lorentz factor could have been underestimated. Even in this case, the bulk Lorentz factor on the second night would have been smaller, which is inconsistent with the unchanged observed spectrum (16).

If the accelerated electrons instead had an additional hard energy distribution at high energies, then the synchrotron and inverse Compton components could potentially explain the x-ray and gamma-ray spectra recorded from GRB 190829A. However, this would require extreme assumptions regarding the properties of the circumburst medium. If inverse Compton losses are dominant, then the electrons that are cooled by inverse Compton losses follow an energy distribution that is harder than the injected distribution (16). This requires that the spectral energy distribution is strongly dominated by the inverse Compton component, which is inconsistent with the observed TeV flux and *Fermi*-LAT upper limit (Fig. 4).

In summary, we measured a hard intrinsic spectral index, $\gamma_{\text{VHE}}^{\text{int}} \approx 2$, over more than an order of magnitude in energy in the VHE band in the late time afterglow, at $T_0 + 4$ hours to $+56$ hours. The gamma-ray energy flux and spectral index are consistent with an extrapolation of the synchrotron spectrum observed in the x-ray band. This simple spectral behavior is difficult to describe with simple one-zone emission models.

REFERENCES AND NOTES

1. P. Mészáros, M. J. Rees, *Mon. Not. R. Astron. Soc.* **257**, 29P–31P (1992).
2. R. Sari, A. A. Esin, *Astrophys. J.* **548**, 787–799 (2001).
3. B. Zhang, P. Mészáros, *Astrophys. J.* **559**, 110–122 (2001).
4. MAGIC Collaboration, *Nature* **575**, 455–458 (2019).
5. P. Veres et al., *Nature* **575**, 459–463 (2019).
6. H. Abdalla et al., *Nature* **575**, 464–467 (2019).
7. Fermi GBM Team, *GRB Coordinates Network* 25551 (2019).
8. S. Dichiara et al., *GRB Coordinates Network* 25552 (2019).
9. D. A. Perley, A. M. Cockeram, *GRB Coordinates Network* 25623 (2019).
10. J. Bolmer, J. Greiner, T. W. Chen, *GRB Coordinates Network* 25651 (2019).
11. G. Terreran et al., *GRB Coordinates Network* 25664 (2019).
12. A. de Ugarte Postigo et al., *GRB Coordinates Network* 25677 (2019).
13. A. Volnova et al., *GRB Coordinates Network* 25682 (2019).
14. Y. D. Hu et al., *Astron. Astrophys.* **646**, A50 (2021).
15. J. P. Osborne et al., *GRB Coordinates Network* 25568 (2019).

16. Materials and methods are available as supplementary materials.
17. A. Franceschini, G. Rodighiero, M. Vaccari, *Astron. Astrophys.* **487**, 837–852 (2008).
18. S. Lesage et al., *GRB Coordinates Network* **25575** (2019).
19. M. Ajello et al., *Astrophys. J.* **863**, 138 (2018).
20. F. Piron et al., *GRB Coordinates Network* 25574 (2019).
21. P. A. Evans et al., *Mon. Not. R. Astron. Soc.* **444**, 250–267 (2014).
22. P. A. Evans et al., *Astron. Astrophys.* **519**, A102 (2010).
23. R. D. Blandford, C. F. McKee, *Phys. Fluids* **19**, 1130 (1976).
24. P. Kumar, R. A. Hernández, Ž. Bošnjak, R. Barniol Duran, *Mon. Not. R. Astron. Soc.* **427**, L40–L44 (2012).
25. A. Franceschini, G. Rodighiero, *Astron. Astrophys.* **603**, A34 (2017).
26. J. D. Finke, S. Razzaque, C. D. Dermer, *Astrophys. J.* **712**, 238–249 (2010).
27. A. Domínguez et al., *Mon. Not. R. Astron. Soc.* **410**, 2556–2578 (2011).
28. R. C. Gilmore, R. S. Somerville, J. R. Primack, A. Domínguez, *Mon. Not. R. Astron. Soc.* **422**, 3189–3207 (2012).

ACKNOWLEDGMENTS

We thank C. Arcaro, N. Zywuca, and H. Ashkar for discussions of the multiwavelength modeling and L. Mohrmann for guidance on the GAMMAPY analysis. We appreciate the work of the technical support staff in Berlin, Zeuthen, Heidelberg, Palaiseau, Paris, Saclay, Tübingen, and Namibia in the construction and operation of the H.E.S.S. equipment. This work benefited from services provided by the H.E.S.S. Virtual Organisation, supported by the national resource providers of the EGI Federation. **Funding:** This work was supported by the Max Planck Society (E.R.-V., C.R., and F.A.), the Dublin Institute for Advanced Studies (F.A.), the Helmholtz Association (A.M.T. and S.J.Z.), the Japanese Society for the Promotion of Science (D.K.), and the Commissariat à l'énergie atomique et aux énergies alternatives (F.S.). The H.E.S.S. collaboration acknowledges the support of the Namibian authorities and of the University of Namibia in facilitating the construction and operation of H.E.S.S., as well as support by the German Ministry for Education and Research (BMBF), the Max Planck Society, the German Research Foundation (DFG), the Helmholtz Association, the Alexander von Humboldt Foundation, the French Ministry of Higher Education, Research and Innovation, the Centre National de la Recherche Scientifique (CNRS/IN2P3 and CNRS/INSU), the Commissariat à l'énergie atomique et aux énergies alternatives (CEA), the UK Science and Technology Facilities Council (STFC), the Knut and Alice Wallenberg Foundation, the National Science Centre, Poland grant no. 2016/22/M/ST9/00382, the South African Department of Science and Technology and National Research Foundation, the University of Namibia, the National Commission on Research, Science and Technology of Namibia (NCRST), the Austrian Federal Ministry of Education, Science and Research and the Austrian Science Fund (FWF), the Australian Research Council (ARC), the Japan Society for the Promotion of Science, and the University of Amsterdam. **Author contributions:** E.R.-V. carried out the main H.E.S.S. data analysis, and F.S. provided the cross-check. S.J.Z. led the x-ray analysis and discussion. C.R., D.K., F.A., and A.M.T. performed modeling and interpretation. The manuscript was prepared by E.R.-V. (supervised by J. Hinton), S.J.Z., C.R., D.K., F.A., and A.M.T. S. Wagner is the collaboration spokesperson. Other H.E.S.S. collaboration authors contributed to the design, construction, and operation of H.E.S.S.; the development and maintenance of data handling; data reduction; and/or data analysis software. All authors meet the journal's authorship criteria and have reviewed, discussed, and commented on the results and the manuscript. **Competing interests:** We declare that we have no competing interests. **Data and materials availability:** The H.E.S.S. data are available at www.mpi-hd.mpg.de/hfm/HESS/pages/publications/auxiliary/GRB190829A/Auxiliary_Information_GRB190829A.html, including the spectral energy distribution data (Fig. 1), the light-curve (Fig. 2), the significance skymaps (fig. S1), and the code used for the MCMC modeling. Model output is listed in tables S5 and S6. The Swift-XRT data are available at www.swift.ac.uk/xrt_spectra/00922968/, and the files to reproduce our temporal analysis are available at the same URL as the H.E.S.S. data.

SUPPLEMENTARY MATERIALS

science.sciencemag.org/content/372/6546/1081/suppl/DC1
H.E.S.S. Collaboration Author and Affiliation List
Materials and Methods
Figs. S1 to S10
Tables S1 to S7
References (29–61)

18 September 2020; accepted 7 April 2021
10.1126/science.abe8560

GENETICS OF OBESITY

Extensive pleiotropism and allelic heterogeneity mediate metabolic effects of *IRX3* and *IRX5*

Débora R. Sobreira^{1*}, Amelia C. Joslin¹, Qi Zhang^{1,2}, Iain Williamson³, Grace T. Hansen¹, Kathryn M. Farris¹, Noboru J. Sakabe¹, Nasa Sinnott-Armstrong^{4,5}, Grazyna Bozek¹, Sharon O. Jensen-Cody⁶, Kyle H. Flippo⁶, Carole Ober¹, Wendy A. Bickmore³, Matthew Potthoff⁶, Mengjie Chen^{1,2}, Melina Claussnitzer^{5,7}, Ivy Aneas^{1*}, Marcelo A. Nóbrega^{1*}

Whereas coding variants often have pleiotropic effects across multiple tissues, noncoding variants are thought to mediate their phenotypic effects by specific tissue and temporal regulation of gene expression. Here, we investigated the genetic and functional architecture of a genomic region within the *FTO* gene that is strongly associated with obesity risk. We show that multiple variants on a common haplotype modify the regulatory properties of several enhancers targeting *IRX3* and *IRX5* from megabase distances. We demonstrate that these enhancers affect gene expression in multiple tissues, including adipose and brain, and impart regulatory effects during a restricted temporal window. Our data indicate that the genetic architecture of disease-associated loci may involve extensive pleiotropy, allelic heterogeneity, shared allelic effects across tissues, and temporally restricted effects.

Although genome-wide association studies (GWAS) have contributed extensively to complex disease mapping, our understanding of the genetic architecture and molecular mechanisms underlying most disease associations remains incomplete (1, 2). Recent studies suggest pervasive pleiotropy of regulatory variants modulating gene expression across multiple tissues, affecting seemingly disparate disease phenotypes (3, 4). We set out to determine the genetic architecture and phenotypic implications of a well-studied locus associated with human obesity. GWAS have identified common variants in the *FTO* gene as being the strongest genetic association with obesity in humans (5). Much effort has been directed toward identifying the causal variant, gene, and tissues underlying this association. The associated region is within a large topologically associated domain (TAD) of ~2 Mb encompassing *FTO*, *RPGRIPL*, and the *IRXB* cluster (including *IRX3*, *IRX5*, and *IRX6*) (6). As a consequence of this arrangement, the obesity-associated variants could affect the regulation of any or all of these genes. In fact, most of these genes have been independently implicated in body weight management phenotypes,

leading to additional controversy within the field as to which of these genes mediates the genetic association with obesity (7–10). In addition, whereas compelling evidence implicates a central nervous system (CNS) phenotype such as food preference and feeding behavior underlying the association with body mass index (BMI) (5, 11), alternative models involving altered thermogenesis, autonomous to adipose tissue, have also been put forth as putative mechanisms (7, 8). To address these discrepancies, we applied an integrated approach to mechanistically determine the genetic and functional architecture of the obesity GWAS signal emanating from the *FTO* locus.

To ascertain the pattern of long-range genomic interactions in the locus, we generated a comprehensive chromatin interaction map in cell types relevant to obesity. We performed in situ promoter capture Hi-C (PCHi-C) in human SGBS preadipocytes and in hypothalamic arcuate-like neurons derived from human induced pluripotent stem cells (hiPSCs). PCHi-C contact maps from both cell types, and additional 4C-sequencing (4C-seq) data, revealed long-range interactions between the obesity-associated locus and promoters of *IRX3* and *IRX5* but not those of *IRX6* or *FTO/RPGRIPL* (Fig. 1A and fig. S1A). Similar results were obtained from an enhancer capture Hi-C dataset in primary human preadipocytes (fig. S1B) (12). Because this locus is highly conserved between humans and mice (fig. S2A), we engineered a mouse model (mm*Fto*Δ20) harboring a 20,204-bp deletion spanning the orthologous obesity-associated interval in *Fto* (fig. S2B). Using fluorescence in situ hybridization (FISH) as an orthogonal assay to PCHi-C, we interrogated the three-dimensional (3D) organization of this region in vivo using brains from mm*Fto*Δ20-heterozygous mice. Designing

¹Department of Human Genetics, University of Chicago, Chicago, IL 60637, USA. ²Section of Genetic Medicine, Department of Medicine, University of Chicago, Chicago, IL 60637, USA. ³MRC Human Genetics Unit, Institute of Genetics and Molecular Medicine, University of Edinburgh, Edinburgh EH4 2XU, UK. ⁴Department of Genetics, Stanford University, Stanford 94305 CA, USA. ⁵Metabolism Program and Cardiovascular Disease Initiative, Broad Institute of Massachusetts Institute of Technology and Harvard University, Cambridge, MA 02142, USA. ⁶Department of Pharmacology, University of Iowa Carver College of Medicine, Iowa City, IA 52242, USA. ⁷Department of Medicine, Beth Israel Deaconess Medical Center, Boston, MA 02131, USA. *Corresponding author. Email: deborasobreira@gmail.com (D.R.S.); ianeas@bsd.uchicago.edu (I.A.); nobrega@uchicago.edu (M.A.N.)

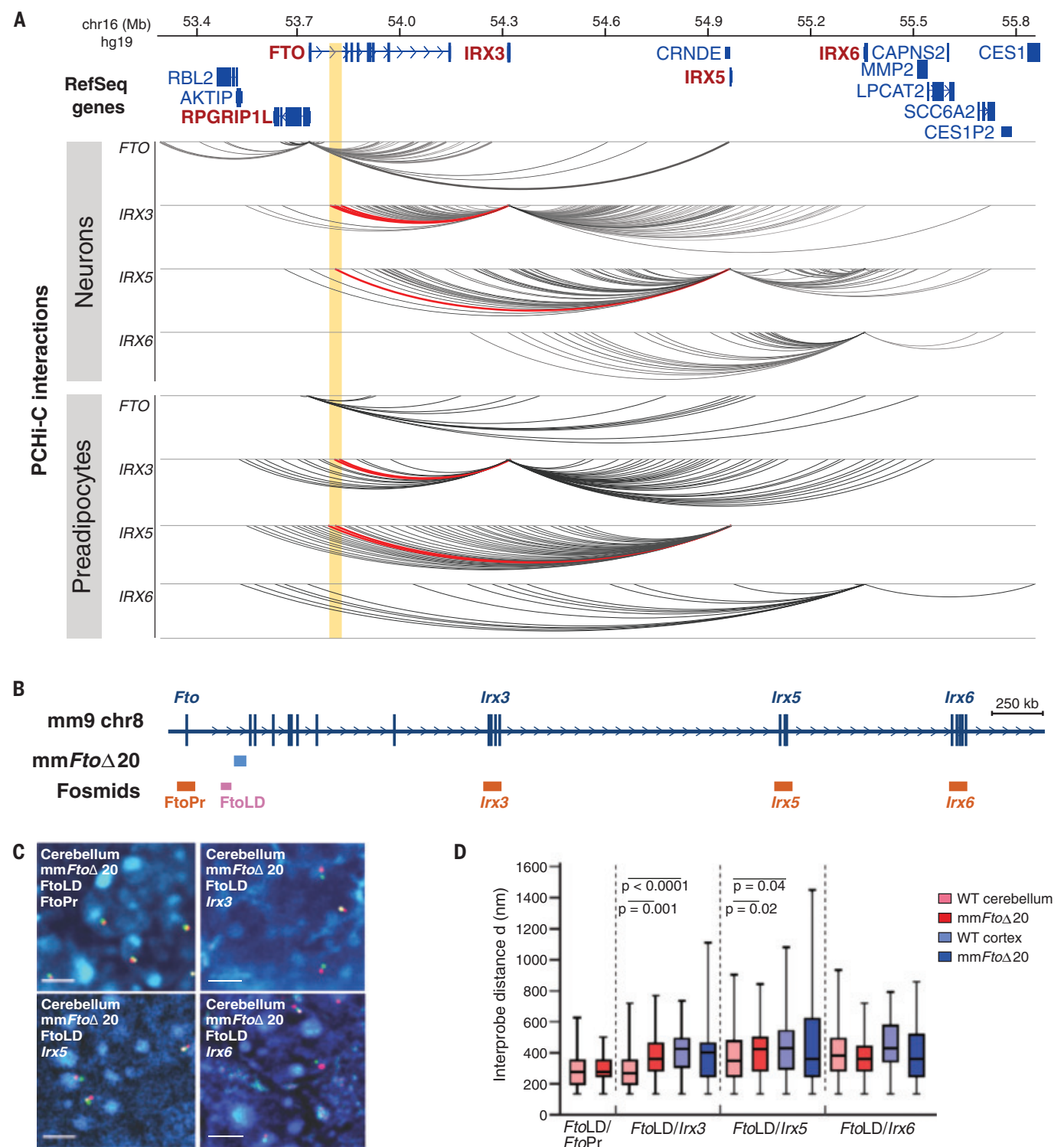


Fig. 1. Regulatory architecture of obesity-associated noncoding elements within *FTO*. (A) PChl-C interactions emanating from the *FTO*, *IRX3*, *IRX5*, and *IRX6* promoters in human Simpson-Golabi-Behmel syndrome cells (preadipocytes) and hiPSCs-derived hypothalamic arcuate-like neurons. The yellow strip highlights the obesity-associated interval. PChl-C interactions are presented as gray arcs. Red arcs highlight interactions of the *IRX3* and *IRX5* promoters with the obesity-associated region. (B) The 1.1-Mb region analyzed by FISH in mouse cerebellum encompassing the *Fto*, *Irx3*, *Irx5*, and *Irx6* genes. The fragment deleted in the mm*Fto*Δ20 mouse is indicated in blue. Fosmids used for analysis in (C) and (D) are

indicated in orange and light pink. (C) 3D-FISH with *Fto*, *Irx3*, *Irx5*, and *Irx6* probes (red) and directly distal *FTO* obesity-associated interval (green) counterstained with 4',6-diamidino-2-phenylindole (DAPI; blue). Scale bars, 5 μm. (D) Box plots represent the distribution of interprobe distances between different probe combinations in *Irx3*-expressing (cerebellum) and nonexpressing (cortex) brain tissue of mm*Fto*Δ20-heterozygous mice. Lines represent medians. The statistical significance of differences between datasets was determined using Mann-Whitney *U* tests. *n* = 50 to 60 WT and mm*Fto*Δ20 alleles each per slide. FtoLD, *FTO* obesity-associated interval; FtoPr, *Fto* promoter.

fosmid-based probes for regions encompassing the *Fto/Rpgrip1l*, *Irx3*, *Irx5*, and *Irx6* promoters and the *Fto* obesity-associated locus, as well as the region directly adjacent to the 20-kb deletion (Fig. 1B), we determined the pattern of interactions between the obesity-

associated region and genes in the *Fto-Irxb* locus. Consistent with our PChI-C and 4C-seq results, FISH data from wild-type (WT) alleles in cerebellum revealed increased colocalization (≤ 200 nm) of the *Irx3* and *Irx5* promoters with the *Fto* obesity-associated interval in WT

alleles compared with deletion alleles and cortex cells that do not express *Irx3* and *Irx5*. We obtained similar colocalization data in lung cells, supporting our previous observations that the obesity-associated interval harbors lung enhancers (7). Conversely, the

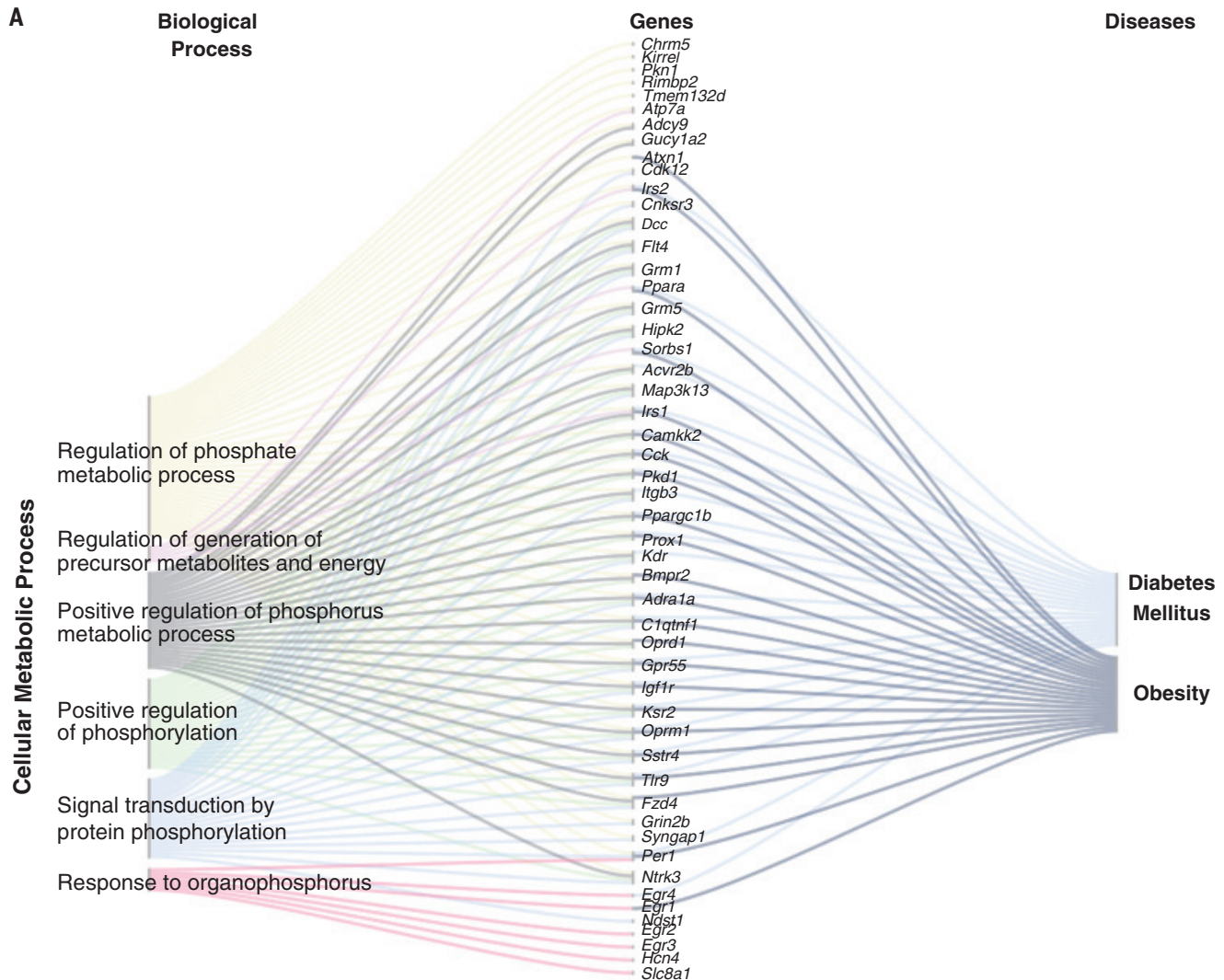


Fig. 2. *Irx3* acts in the brain to regulate metabolism and changes in macronutrient selection. (A) Expression analysis of differentially expressed genes between hypothalami of *Irx3*^{-/-} and WT mice using GO annotations. The Sankey flow diagram shows all genes up-regulated in the hypothalami from *Irx3*^{-/-} animals with high enrichment for cellular metabolic processes and the top-ranked diseases related to them. Gene symbols are shown. (B) Two-bottle choice experiment comparing *Irx3*^{-/-} and WT mice. Data are expressed as mean \pm SEM. * $P < 0.05$ compared with the WT group. (C) Regional association plot of the *FTO* locus. LocusZoom was used to plot the negative $\log_{10} P$ value of every SNP within ± 700 kb of rs1421085, the lead SNP in the locus.

20-kb deletion had no impact on the distance between the *Fto/RpgrilL* or *Irx6* promoters and the *Fto* obesity-associated interval (Fig. 1, C and D, and fig. S2C). These observations support a model of chromatin compaction at this locus, with the obesity-associated region

physically interacting with both *IRX3* and *IRX5* in humans and mice. We next explored the biological relevance of these observations in vivo. We genetically engineered germline-null (–/–) and germline-heterozygous (+/–) alleles for *Irx3*, *Irx5*, and

Irx6 in mice (fig. S3). At 20 weeks, *Irx3*^{–/–} animals displayed a 15 to 20% blunting in weight gain compared with their WT control littermates, as well as a reduction of total fat mass (10 to 15%), activation of molecular markers of browning in white adipose tissue (WAT),

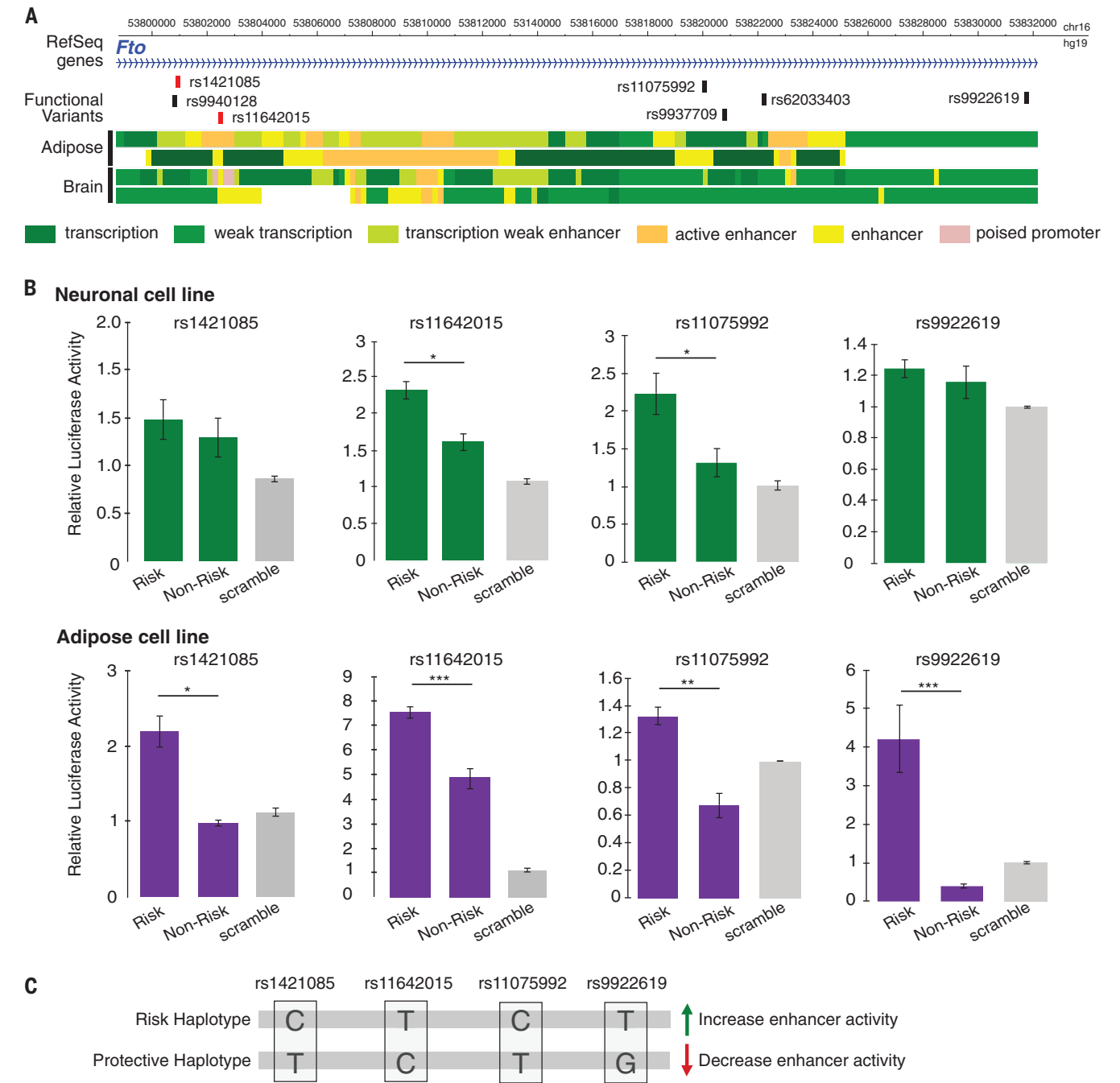


Fig. 3. Functional variants within the *FTO* association locus modulate enhancer activity in brain and adipose tissues. (A) Functional variants that showed allele-specific activity using massively parallel reporter assay (black boxes) and PMCA (red boxes). Colored bars indicate the chromatin state annotations from the Roadmap Epigenomics Project. Colored bars indicate chromatin state annotations from tissues profiled by the Roadmap Epigenomics

Project, including adipose tissue (epigenome identifiers E025 and E063), and brain (epigenome identifiers E071 and E081). (B) Comparison of allele-specific activity of four variants in the *FTO* obesity-associated interval using luciferase reporter assay. The plots show the mean \pm SEM from five triplicate experiments. * $P < 0.05$, ** $P < 0.01$, and *** $P < 0.001$. (C) Segregation of alleles by risk or nonrisk haplotype and effect on enhancer activity.

and improved glucose tolerance, mimicking phenotypes that we have previously shown (fig. S4) (7). Although the most notable feature of *Irx5*^{-/-} mice is early postnatal lethality, *Irx5*-heterozygous mice (*Irx5*^{+/-}) were viable and thrived. Similar to *Irx3*^{-/-}, *Irx5*^{+/-} mice exhibited an anti-obesity phenotype with 15 to 20% weight reduction, loss of body fat mass (5%), activation of browning in WAT, and improved glucose tolerance (fig. S5). *Irx6*-knockout (*Irx6*^{-/-}) mice showed none of these metabolic phenotypes (fig. S6). Altogether, our in vivo mouse models support our chromatin conformation data implicating *Irx3* and *Irx5*, but not *Irx6*, as potentially mediating the genetic association with obesity.

The phenotypic impact of *IRX3* and *IRX5* on adipocyte biology has been described previously (7, 8). Specifically, a single-nucleotide polymorphism (SNP) (rs1421085) modulates *IRX3* and *IRX5* expression in preadipocytes and regulates an adipose thermogenesis program (8). These data, however, do not provide an immediate explanation for the well-described association of variants within *FTO* with eating behavior and, more specifically, eating preferences such as increased caloric intake (5, 11, 13). Toward that end, we have previously shown that the hypothalamic expression of a dominant-negative *IRX3* isoform in mice phenocopies the organism-level metabolic phenotypes seen in germline *Irx3*-null mice (7). To investigate the impact of *Irx3* in molecular and physiological brain phenotypes associated with obesity, we performed transcriptomic analysis [RNA sequencing (RNA-seq)] on hypothalami from *Irx3*^{-/-} mice and WT littermates. Gene ontology (GO) enrichment analysis showed that, of the 359 up-regulated genes, at least 103 are involved in neurodevelopment and cellular processes such as cell communication and synaptic signaling, consistent with the well-known roles of *Irx3* in brain development (fig. S7A) (14–16). Using the ToppGene Suite database, we investigated GO categories for disease links and found that the top-ranked diseases associated with these differentially expressed genes are obesity, diabetes, and impaired glucose tolerance (Fig. 2A; fig. S7, A and B; and table S1), supporting the notion that *Irx3* expression in brain may coordinate a genetic program involved in metabolism. To determine whether *Irx3* plays a role in food intake or macronutrient preference, we subjected a cohort of adult *Irx3*^{-/-} and WT control littermates to a series of two-bottle choice experiments in which all mice were offered the choice between water and a range of nutritive and non-nutritive tastants (17). We found that obesity-resistant *Irx3*^{-/-} mice display a reduced preference for sucrose, but not lipid or protein, compared with WT animals (Fig. 2B and fig. S7C). Altered sweet preference has not been shown as a phenotype in

humans harboring risk alleles in the *FTO* obesity-associated region. To test this, we obtained GWAS summary statistics from 118,950 genotyped individuals responding to a sweet preference questionnaire from 23andMe (table S2). A GWAS of these data indicated that SNPs within the *FTO* obesity-associated region represent the second-strongest association with sweet preference in humans, with the C allele of rs1421085 associated with sweet food preference over salty (3.6×10^{-23} ; odds ratio = 1.1) (Fig. 2C). Taken together, our in vivo mouse data establish a CNS role of *Irx3* in the regulation of metabolism and feeding behavior analogous to phenotypes associated with allelic variants of obesity-associated SNPs within *FTO* in humans, including alterations in consummatory behavior. Previous work has described reciprocal counterregulatory mechanisms between peripheral energy expenditure and energy intake, with perturbations in diet and nutritional status inducing long-term changes in hypothalamic neurocircuit development (18). Future work should determine whether the alterations in feeding behavior in *Irx3*^{-/-} mice result from primary, autonomous dysfunction of regulatory circuits within the CNS, including the hypothalamus, or if they are secondary to peripheral effects through the intersection of neurohormonal cues from adipose and other peripheral tissues.

Having uncovered a CNS role of *Irx3* in metabolism and feeding behavior, we next sought to characterize the regulatory potential of obesity-associated SNPs within *FTO*. To functionally classify regulatory variants in neurons and adipocytes, thought to represent tissues that participate in the genetics of obesity in humans (19), we used orthogonal computational and experimental approaches. For computational regulatory variant predictions, we derived multiple variant features from sequence-based methods that harness cross-species functional sequence conservation and sequence-based regulatory evidence (20). Experimentally, we used a massively parallel reporter assay to identify variants located in enhancers in hippocampal (HT22) and preadipocyte (3T3-L1) mouse cell lines. We tested all 87 common (minor allele frequency $\geq 5\%$) variants in strong linkage disequilibrium ($r^2 > 0.8$) with the lead obesity GWAS-associated SNP rs1558902 (19). We found 21 SNPs in 3T3-L1 preadipocytes and 18 SNPs in HT22 neuronal cells located in enhancers in at least three replicates tested in each cell line (table S3). Of these, five SNPs displayed allelic-specific enhancer activities in preadipocyte and/or neuronal cells; each was located in independent enhancers spread over 31 kb (Fig. 3A, fig. S8, and tables S4 and S5). Using a luciferase reporter assay, we confirmed allele-specific enhancer properties and directional effects of four variants in preadipocytes, two of which

changed regulatory activity in neuronal cells as well (Fig. 3B). Three of the four SNPs mapped within accessible chromatin regions in human adipose and brain tissues, as assayed by the Roadmap Epigenomics Consortium (Fig. 3A). In addition, we confirmed that all accessible variants scored highest across multiple, orthogonal sequence-based computational metrics, including high functional conservation scores for the variant flanking the 120-bp regions evaluated with phylogenetic module complexity analysis (PMCA) (21) (table S6) and sequence-based predicted functional significance scores < 0.01 evaluated with DeepSEA (22) (table S7), and all four SNPs showed very consistent allele-specific chromatin accessibility with the Basset model when comparing the experimentally derived allelic activity in preadipocytes and hypothalamic neurons (table S8). All four SNPs are co-inherited as one common haplotype, with each allele in the obesity-risk haplotype associated with increased enhancer activity (Fig. 3C), suggesting that they may coordinately regulate target gene expression in the same direction (LDhap tool: <https://ldlink.nci.nih.gov>). Our data suggest that multiple genetic variants in this locus may regulate gene expression in both adipose and neuronal tissues. This supports a model in which GWAS signals may result from a complex genetic architecture whereby allelic heterogeneity of multiple regulatory variants in distinct regulatory elements imparts shared effects across tissues, regulating the quantitative and spatial expression of multiple genes (23). We next determined the impact of these enhancers on gene expression. Because all four regulatory regions with allele-specific enhancer properties mapped within the 20-kb region that we deleted in the mouse genome (fig. S2B), we used *mmFtoΔ20* mice to evaluate the impact, in vivo, of this deletion on the expression of neighboring genes in adipose and brain tissues. We initially assayed the expression of genes in the *Fto-Irxb* cluster during adipocyte differentiation. We isolated primary preadipocytes from *mmFtoΔ20* and WT mice and observed a decreased expression of *Irx3* and *Irx5* in *mmFtoΔ20*, but not of other genes in the locus (Fig. 4A). The impact of deleting these enhancers on the expression of *Irx3* and *Irx5* was restricted to preadipocytes, with no effect on expression in mature adipocytes, as previously described (8).

We next assayed the impact of the 20-kb deletion on gene expression in mouse hypothalamus during embryonic development [embryonic day 17 (E17)] as well as in adult mice (10 weeks). At E17, the 20-kb deletion leads to down-regulation of *Irx3* and *Irx5*, with no impact on the expression of *Fto* and *Irx6* (Fig. 4B). Similar to adipose tissue, this effect was restricted to embryonic development, with no

alterations in *Irx3* and *Irx5* expression in adult hypothalamus. To further explore the temporally restricted expression of *Irx3* and *Irx5* in the developing hypothalamus, we assessed single-cell gene expression across windows of mouse hypothalamic development in mice (24), and determined that the expression of *Irx3* and *Irx5* is highest at midgestation and decreases steadily afterward, being barely detectable in adult neurons (fig. S9). The expression of *Rpgrip1L* was also decreased in hypothalamus of *mmFtoΔ20* mice (Fig. 4B), raising the possibility that regulation of *Rpgrip1L* in the brain

may also contribute to obesity risk, as previously suggested (10).

Our data suggest that variants in multiple enhancers within the *FTO* obesity-associated region regulate the expression of multiple genes in at least two major obesity-relevant tissues, adipose and brain, in mice. Next, we tested the impact of the obesity-associated region on gene expression in human hypothalamic neuronal precursors. We first assayed the dynamic expression of *IRX3* and *IRX5* during differentiation of hiPSCs into hypothalamic neurons and observed that *IRX3* and *IRX5*

expression is highly correlated, peaks at an early stage of hypothalamic neuronal differentiation, and decreases at later developmental stages, paralleling the observations in mice (fig. S10, A and B). These data further support the possibility that some of the allelic effects of obesity-associated SNPs on gene expression may involve developmental phenotypes restricted to specific temporal windows and not detected in differentiated, adult tissues. A recent report uncovered evidence that the *FTO* locus variants have effects on BMI in early childhood (25), further raising the

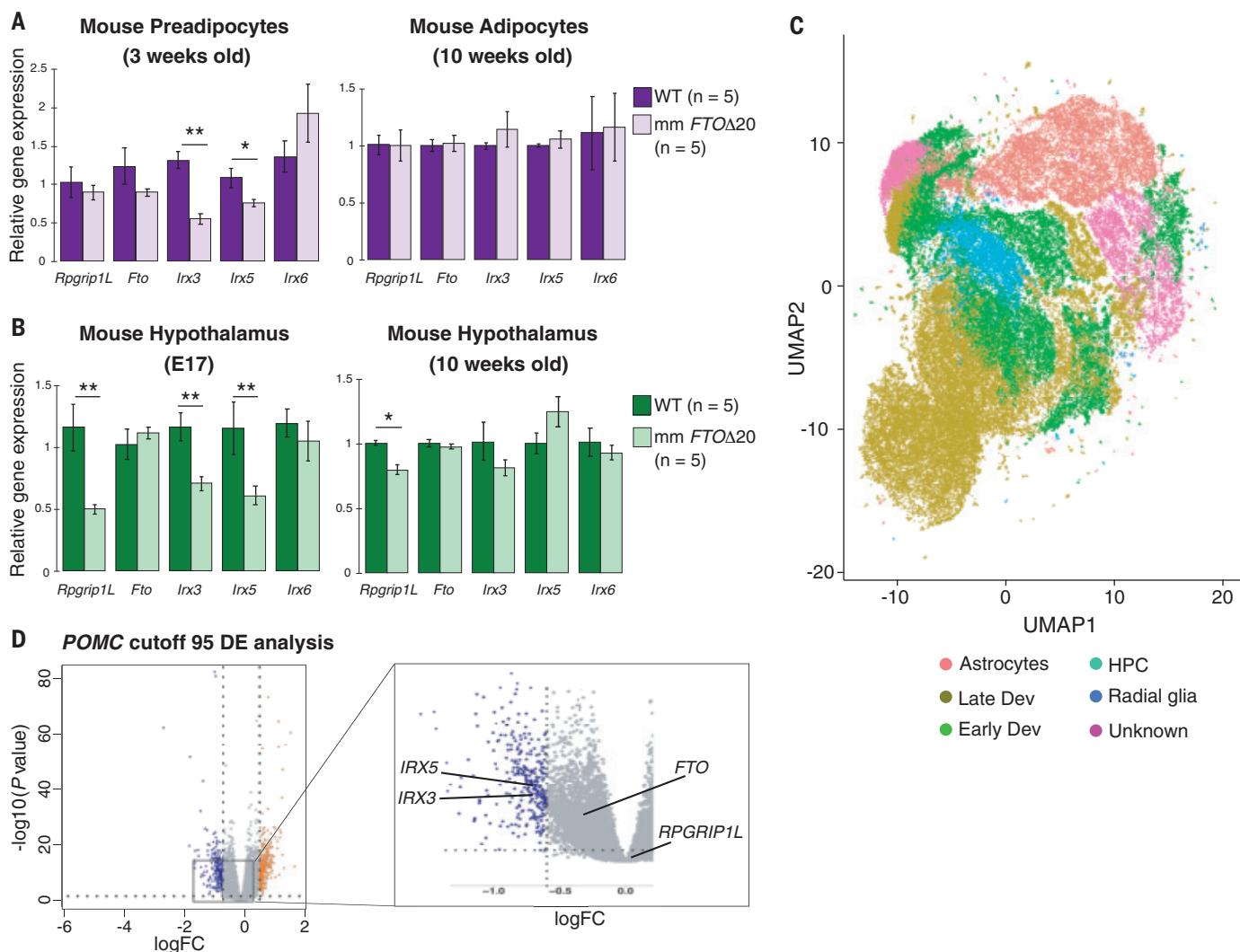


Fig. 4. Evaluation of enhancer activity in the *FTO* obesity-associated locus in neuronal and adipose tissues. (A and B) Relative expression of *Rpgrip1L*, *Fto*, *Irx3*, *Irx5*, and *Irx6* genes in mouse preadipocyte cells and adipose tissue (A) and hypothalamus (B). (C) Uniform manifold approximation and projection (UMAP) plot showing the different cell populations identified using single-cell sequencing. (D) Volcano plot of the differential gene expression (DE) analysis between WT and *mmFtoΔ20* hypothalamic precursor cells with POMC cutoff 95 (counts) and KNN K = 11. Gray dots represent genes that were not significantly changed. Blue and orange dots are genes significantly down-

and up-regulated, respectively. The log fold change (logFC) is shown on the x axis and the negative log₁₀ of the adjusted *P* value is shown on the y axis (logFC cutoff > 0.6 or < -0.6, and adjusted *P* value < 0.05 as significantly differentially expressed). *IRX3* and *IRX5* are significantly differentially expressed across two conditions with KNN K ranging from 10 to 13 (*IRX3*), from 11 to 13 (*IRX5*), and cutoff value >80 or 85 (counts). HPC, hypothalamic progenitor cells; Early Dev, hypothalamic neurons at an early development time point; Late Dev, hypothalamic neurons at a late development time point. For quantitative polymerase chain reaction analysis, data are expressed as mean ± SEM. **P* < 0.05 and ***P* < 0.01 compared with WT.

prospect that the association with BMI may involve a combination of developmental and growth phenotypes.

To test the effect of modulating these enhancers in a model of human hypothalamic neurons, we subsequently generated in human hiPSCs a genomic deletion of a 36,100-bp segment encompassing the *FTO* obesity-associated locus and corresponding to the deletion engineered in mm*Fto* Δ 20 mice. We differentiated WT and 36,100-bp deletion (hs*FTO* Δ 36) hiPSCs into hypothalamic arcuate-like neurons (fig. S10, C and D) (26–28). We performed single-cell RNA-seq (scRNA-seq) in 91,825 cells at the neuron progenitor stage to assess transcriptome differences between WT and hs*FTO* Δ 36 cells. Single-cell transcriptomic profiling identified distinct cell populations within the hypothalamic neuron precursor stage, grouped into distinct subtypes. We defined different developmental stages and cell types based on the expression of known neuronal markers (29, 30). Cell subtypes were designated as (i) hypothalamic neurons at a late development time point, (ii) hypothalamic neurons at an early developmental time point, (iii) hypothalamic progenitor cells, and (iv) radial glia, with all four subtypes together constituting the neurogenic lineage (Fig. 4C and table S9). We found *IRX3* and *IRX5* expressed in all hypothalamic cell subtypes. To assay for alterations in gene expression in cellular subgroups, we clustered cells based on the expression of eight major neural and hypothalamic markers, including *ARNT2*, *NES*, *NEUROD1*, *NHLH2*, *NKX2-1*, *NPY*, *OTP*, and *POMC* (fig. S11). We found that only in cells expressing *POMC*, which is critical in regulating normal feeding behavior and energy homeostasis, did the deletion of the 36-kb segment result in reduced expression of *IRX3* and *IRX5* compared with WT cells, supporting our findings in mouse hypothalami (Fig. 4D). No other gene in the locus was differentially expressed between the two groups in any other cell type cluster. Although we performed our analysis in hypothalamic cells, there currently is no clear delineation of the precise brain cell populations in which the expression of *IRX3* and *IRX5* is regulated by enhancers and allelic variants within these enhancers in the obesity-associated region. Future work addressing this outstanding question will be critical to determine the molecular, cellular, and organismal phenotypes involved in obesity susceptibility in this locus.

Our data highlight the complexities that arise during the functional determination of disease-associated loci in humans. Recent work has suggested extensive pleiotropy of loci, SNPs, and gene sets underlying associations with polygenic traits in humans (4). In addition, the Genotype-Tissue Expression (GTEx) project has shown that the regulatory effects of expressed quantitative trait loci tend to be highly shared

across tissues (31). Furthermore, the impact of regulatory variants on molecular phenotypes is often dependent on developmental context, with changes in gene expression restricted to specific temporal windows (32). Our findings support all of these observations, demonstrating how the collective effects of regulatory variants are integrated across tissues and developmental stages and result in a convergence of phenotypes reminiscent of homeostatic mechanisms governing complex physiological traits in vivo, such as body weight regulation.

There are important limitations to our study. The choice of immortalized cell lines for the reporter assays may mask allelic effects of SNPs that would be seen in primary cells. Also, the manipulation of candidate genes in mice may result in organismal phenotypes that are quantitatively and qualitatively different from the small-effect phenotypes elicited by allelic variants of SNPs associated with the human trait. Finally, the congruent macronutrient preference phenotypes that we describe between *Irx3*^{−/−} mice and humans represent but a subset of the feeding behavior phenotypes associated with this locus in humans. This may reflect species differences in the function of these genes but also that there are other functions associated with *IRX3*, *IRX5*, or other genes in the locus (*RPGRIP1L* or *FTO*) that contribute to the BMI association in humans.

Our work suggests that the genetic architecture of a disease-associated locus may include allelic heterogeneity, with multiple variants modifying the regulatory properties of distinct enhancers with broad tissue specificity and regulating multiple genes in limited temporal windows. These insights provide a mechanistic framework with which to explain the genetic and functional architecture of GWAS loci, predicting that it will often encompass multiple phenotypic mechanisms that ultimately converge to modulate disease susceptibility.

REFERENCES AND NOTES

- N. J. Timpson, C. M. T. Greenwood, N. Soranzo, D. J. Lawson, J. B. Richards, *Nat. Rev. Genet.* **19**, 110–124 (2018).
- P. M. Visscher et al., *Am. J. Hum. Genet.* **101**, 5–22 (2017).
- GTEx Consortium, *Science* **369**, 1318–1330 (2020).
- K. Watanabe et al., *Nat. Genet.* **51**, 1339–1348 (2019).
- J. E. Cecil, R. Tavendale, P. Watt, M. M. Hetherington, C. N. A. Palmer, *N. Engl. J. Med.* **359**, 2558–2566 (2008).
- J. R. Dixon et al., *Nature* **485**, 376–380 (2012).
- S. Smemo et al., *Nature* **507**, 371–375 (2014).
- M. Claussnitzer et al., *N. Engl. J. Med.* **373**, 895–907 (2015).
- J. Fischer et al., *Nature* **458**, 894–898 (2009).
- G. Stratigopoulos et al., *J. Clin. Invest.* **126**, 1897–1910 (2016).
- J. Wardle, C. Llewellyn, S. Sanderson, R. Plomin, *Int. J. Obes. (Lond.)* **33**, 42–45 (2009).
- J. G. S. Madsen et al., *Nat. Genet.* **52**, 1227–1238 (2020).
- L. M. Ranzienhofer et al., *Obesity (Silver Spring)* **27**, 1023–1029 (2019).

- J. L. Gómez-Skarmeta, R. Díez del Corral, E. de la Calle-Mustienes, D. Ferré-Marcó, J. Modolell, *Cell* **85**, 95–105 (1996).
- E. J. Bellefroid et al., *EMBO J.* **17**, 191–203 (1998).
- I. Anselme, C. Laclef, M. Lanaud, U. Rüther, S. Schneider-Maunoury, *Dev. Biol.* **304**, 208–220 (2007).
- S. von Holstein-Rathlou et al., *Cell Metab.* **23**, 335–343 (2016).
- M. C. Vogt et al., *Cell* **156**, 495–509 (2014).
- A. E. Locke et al., *Nature* **518**, 197–206 (2015).
- N. Sinnott-Armstrong et al., *Cell Metab.* **33**, 615–628.e13 (2021).
- M. Claussnitzer et al., *Cell* **156**, 343–358 (2014).
- J. Zhou, O. G. Troyanskaya, *Nat. Methods* **12**, 931–934 (2015).
- O. Corradin et al., *Genome Res.* **24**, 1–13 (2014).
- R. A. Romanov et al., *Nature* **582**, 246–252 (2020).
- Ø. Helgeland et al., *Nat. Commun.* **10**, 4448 (2019).
- L. Yao et al., *J. Neuroendocrinol.* **29**, (2017).
- F. T. Merkle et al., *Development* **142**, 633–643 (2015).
- L. Wang et al., *J. Clin. Invest.* **125**, 796–808 (2015).
- J. Shin et al., *Cell Stem Cell* **17**, 360–372 (2015).
- B. Artegiani et al., *Cell Rep.* **21**, 3271–3284 (2017).
- F. Aguet, A. N. Barbeira, R. Bonazzola, A. Brown, S. E. Castel, B. Jo, S. Kasela, S. Kim-Hellmuth, Y. Liang, M. Oliva, P. E. Parsana, E. Flynn, L. Fresard, E. R. Gaamzon, A. R. Hamel, Y. He, F. Hormozdizari, P. Mohammadi, M. Muñoz-Aguirre, Y. Park, A. Saha, A. V. Segré, B. J. Strober, X. Wen, V. Wucher, S. Das, D. Garrido-Martin, N. R. Gay, R. E. Handsaker, P. J. Hoffman, S. Kashin, A. Kwong, X. Li, D. MacArthur, J. M. Rouhana, M. Stephens, E. Todres, A. Viñuela, G. Wang, Y. Zou, The GTEx Consortium, C. D. Brown, N. Cox, E. Dermizakis, B. E. Engelhardt, G. Getz, R. Guigo, S. B. Montgomery, B. E. Stranger, H. K. Im, A. Battle, K. G. Ardlie, T. Lappalainen, The GTEx Consortium atlas of genetic regulatory effects across human tissues. bioRxiv 787903 [Preprint]. 3 October 2019. <https://doi.org/10.1101/787903>.
- B. J. Strober et al., *Science* **364**, 1287–1290 (2019).

ACKNOWLEDGMENTS

We thank R. Barrès, M. C. Ward, and X. Zhang for comments and valuable suggestions; J. Tena and J. Luis Gómez-Skarmeta for help with the 4C-seq analyses; S. Pott for assistance with the single-cell RNA-seq analysis; M. Wabitsch for his generous gift of the SGBS human preadipocyte cells; D. Schubert for the murine HT22 hippocampal neuronal cell line; and the customers of 23andMe, Inc. for answering surveys and participating in this research. **Funding:** This work was supported by the Novo Nordisk Foundation (challenge grant NNF18OC0033754 to M.A.N.); the National Institutes of Health (grants R01HL128075, R01HL119577, 5P30DK020595, and R01DK114661 to M.A.N.; grant R01HL085197 to C.O.; and grant R01DK106104 to M.J.P.); and the Department of Veterans Affairs (grant I01BX004634 to M.J.P.). I.W. and W.A.B. are supported by MRC University Unit program grant MC_UU_00007/2. **Author contributions:** M.A.N., D.R.S., and I.A. conceived and supervised the study. I.A. and D.R.S. designed the experiments. A.J. performed the massively parallel reporter assay. Q.Z. and M.C. performed the human hypothalamic single-cell analysis. I.W. and W.A.B. performed and analyzed the FISH experiment. G.T.H. performed the Hi-C analysis. N.J.S. performed the RNA-seq analysis. C.O. contributed reagent. K.M.F. and G.B. developed the methodology. S.O.J.-C., K.H.F., and M.P. performed the two-bottle experiment and the mouse single-cell RNA-seq analysis. N.A.S. and M.C. performed the DeepSEA, PMCA, and Basset analyses. M.A.N., I.A., and D.R.S. wrote the manuscript with comments from all authors. **Competing interests:** The authors declare no competing interests. **Data and materials availability:** RNA-seq (E-MTAB-10186), scRNA-seq (E-MTAB-10201), PCHI-C sequencing (E-MTAB-10200), ATAC-seq (E-MTAB-10257), and 4C-seq data (E-MTAB-10195) are deposited at <https://www.ebi.ac.uk/arrayexpress/>.

SUPPLEMENTARY MATERIALS

science.sciencemag.org/content/372/6546/1085/suppl/DC1
Materials and Methods
Figs. S1 to S11
Tables S1 to S17
References (33–55)
MDAR Reproducibility Checklist

23 October 2020; accepted 28 April 2021
10.1126/science.abf1008

CORONAVIRUS

Household COVID-19 risk and in-person schooling

Justin Lessler^{1*}, M. Kate Grabowski^{1,2}, Kyra H. Grantz¹, Elena Badillo-Goicoechea³,
C. Jessica E. Metcalf⁴, Carly Lupton-Smith⁵, Andrew S. Azman^{1,6}, Elizabeth A. Stuart^{3,5,7}

In-person schooling has proved contentious and difficult to study throughout the severe acute respiratory syndrome coronavirus 2 (SARS-CoV-2) pandemic. Data from a massive online survey in the United States indicate an increased risk of COVID-19–related outcomes among respondents living with a child attending school in person. School-based mitigation measures are associated with significant reductions in risk, particularly daily symptoms screens, teacher masking, and closure of extracurricular activities. A positive association between in-person schooling and COVID-19 outcomes persists at low levels of mitigation, but when seven or more mitigation measures are reported, a significant relationship is no longer observed. Among teachers, working outside the home was associated with an increase in COVID-19–related outcomes, but this association is similar to that observed in other occupations (e.g., health care or office work). Although in-person schooling is associated with household COVID-19 risk, this risk can likely be controlled with properly implemented school-based mitigation measures.

The role of schools in transmission—and the value of school closure—has been one of the most contentious issues of the COVID-19 pandemic. There is ongoing debate about exactly how much severe acute respiratory syndrome coronavirus 2 (SARS-CoV-2) risk is posed to individuals and communities by in-person schooling. Although there is general consensus that it should be possible to open schools safely with adequate mitigation

measures, there are few data and even less agreement as to what level of mitigation is needed.

Many ecological studies have shown an association between in-person schooling and the speed and extent of community SARS-CoV-2 transmission (1–3), though these results have not been uniform (4). Although there have been numerous outbreaks in schools and school-like settings (5–7), studies outside of outbreak settings have suggested that, when mitigation

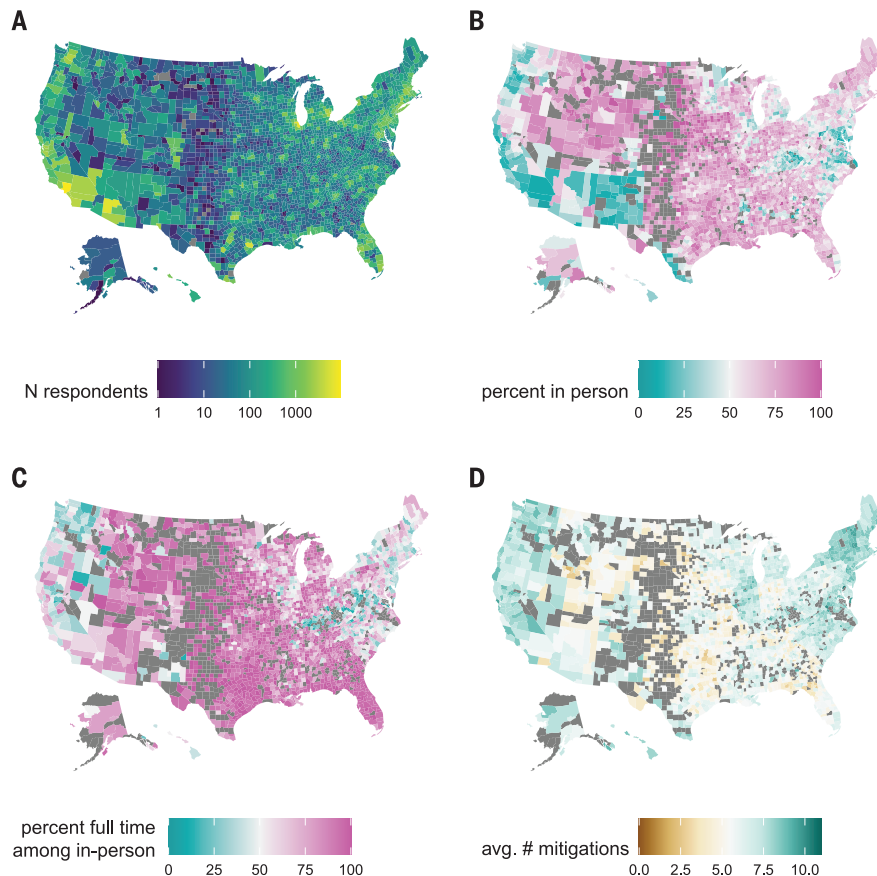
measures are in place, transmission within schools is limited and infection rates mirror those of the surrounding community (8, 9).

However, the ways in which in-person schooling influences community SARS-CoV-2 incidence are complex. Schools play a distinct role in the social fabric of the US and other countries and often create potential transmission connections between otherwise disparate communities. Even if transmission in classrooms is rare, activities surrounding in-person schooling, such as student pickup and drop-off, teacher interactions, and broader changes to behavior when school is in session, could lead to increases in community transmission.

There is also a growing body of evidence that younger children (e.g., those under 10 years of age) are less susceptible to infection when exposed (10); however, it is unclear whether

Fig. 1. Spatial distribution of survey responses.

(A) Number of survey respondents reporting a school-aged student in the household by county. **(B)** Percentage of households with school-aged children reporting any in-person schooling by county, excluding counties with fewer than 10 responses (excluded counties are shown in dark gray). **(C)** Percentage of households reporting a child in in-person schooling who report full-time in-person schooling, excluding counties with fewer than 10 reporting in-person schooling. **(D)** Average number of school-based mitigation measures reported for children with in-person schooling, excluding counties with fewer than 10 reporting in-person schooling.



¹Department of Epidemiology, Johns Hopkins Bloomberg School of Public Health, Baltimore, MD, USA. ²Department of Pathology, Johns Hopkins School of Medicine, Baltimore, MD, USA. ³Department of Mental Health, Johns Hopkins Bloomberg School of Public Health, Baltimore, MD, USA. ⁴Department of Ecology & Evolutionary Biology, Princeton University, Princeton, NJ, USA. ⁵Department of Biostatistics, Johns Hopkins Bloomberg School of Public Health, Baltimore, MD, USA. ⁶Institute of Global Health, Faculty of Medicine, University of Geneva, Geneva, Switzerland. ⁷Department of Health Policy and Management, Johns Hopkins Bloomberg School of Public Health, Baltimore, MD, USA.

*Corresponding author. Email: justin@jhu.edu

they are less likely to pass on the virus once infected (*11, 12*) or whether this reduced susceptibility is offset by increases in number of contacts during school (*13*). Even when school-aged children are infected, their risk of severe disease and death is low (*14*). This means that one of the main reasons for a focus on schools is not the risk to students, but the risk that in-person schooling poses to teachers and family members (*15*) and its impact on the overall

epidemic. Yet, few studies have focused on the risk that in-person school poses to household members (*15*).

Different interpretations of the evidence and local politics have led to massive heterogeneity in approaches to schooling across the US during the 2020 to 2021 school year (*16*)—running the gambit from complete cessation of in-person learning to opening completely with no mitigation measures. Most schools

that have opened have made some efforts to mitigate transmission, but there is much diversity in the approaches adopted.

This hodgepodge of approaches to schooling creates a natural experiment from which we can learn about what does and what does not work for controlling school-associated SARS-CoV-2 spread. However, there is no central repository of the measures implemented across the >130,000 schools in the US or the

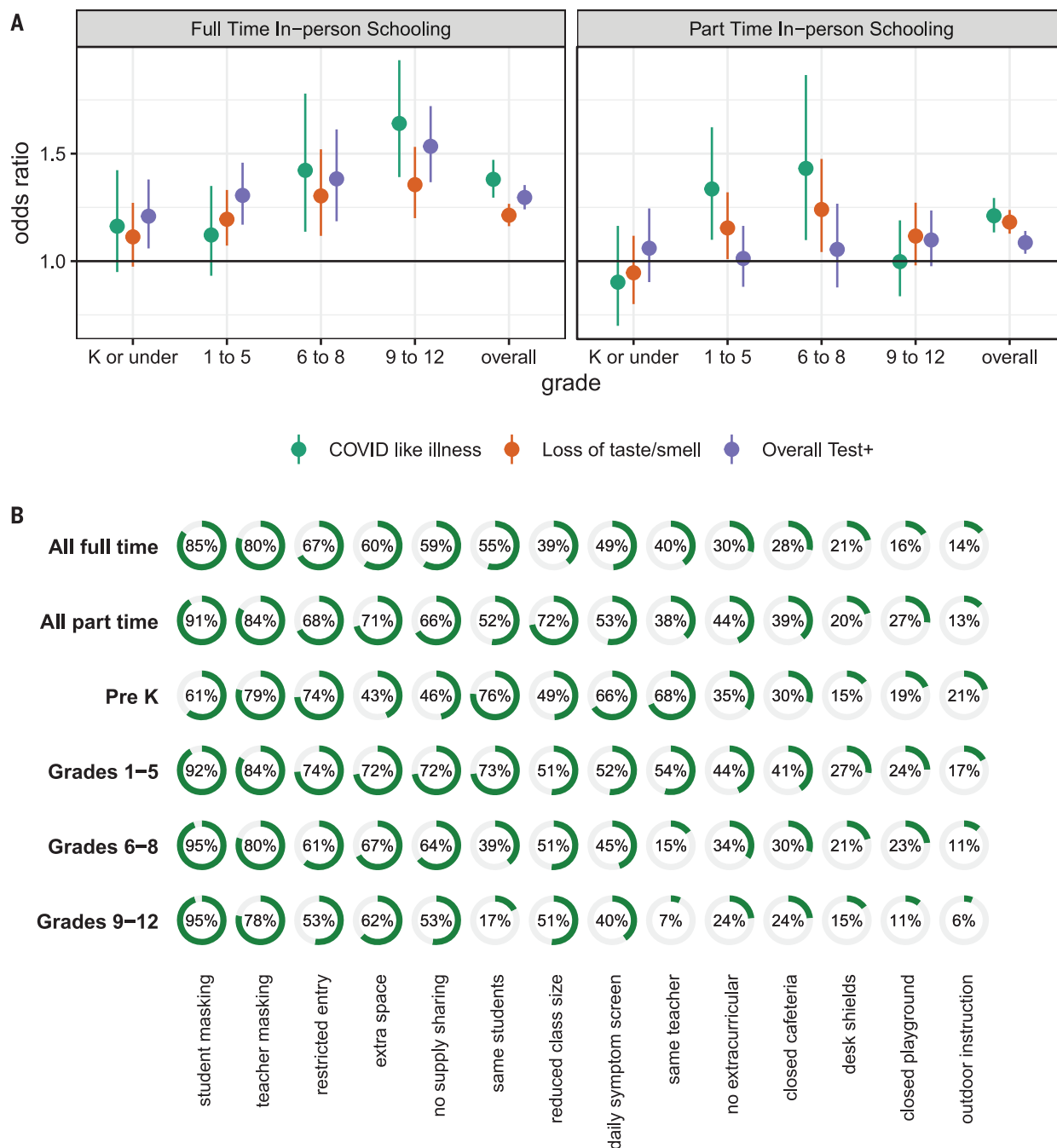


Fig. 2. Risk from in-person schooling and distribution of mitigation measures by grade. (A) Odds ratio of COVID-19-related outcomes associated with full- and part-time in-person schooling by outcome and grade level compared with individuals with children in their household not attending in-person schooling and adjusted for individual- and county-level covariates (but not number of mitigation measures), which indicates that the strength of the association increases with grade level. K, kindergarten. (B) Distribution of mitigation measures by grade level and full- versus part-time in-person status across all grades. Test+, positive SARS-CoV-2 test result.

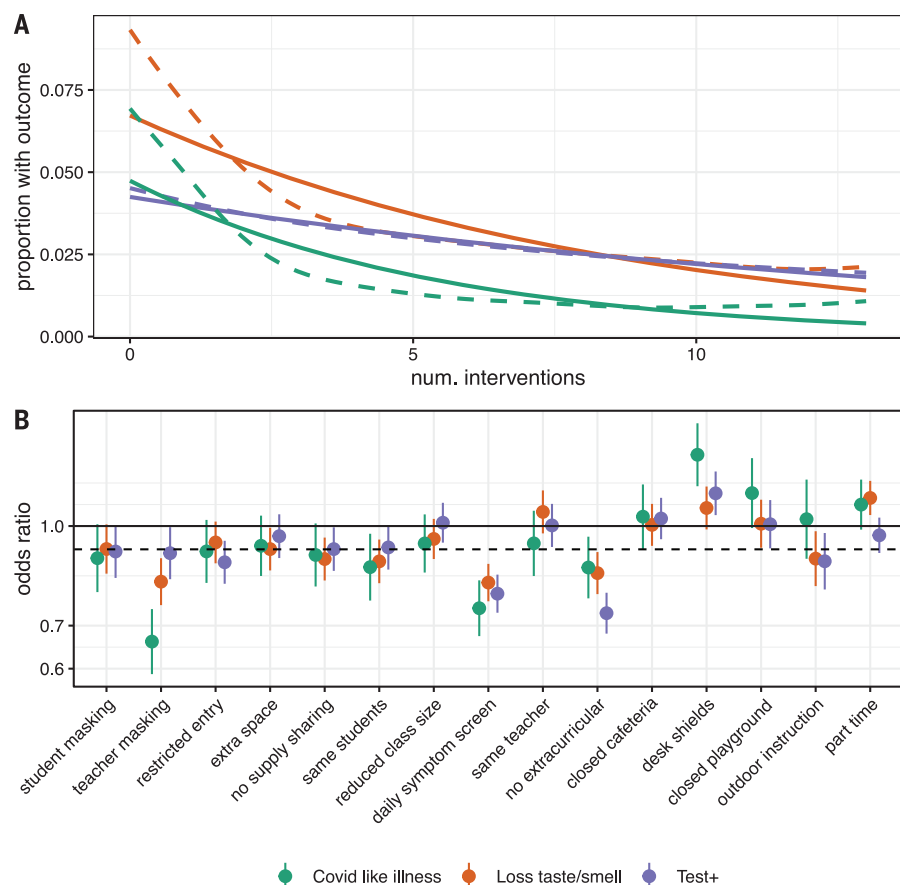


Fig. 3. Impact of individual mitigation measures. (A) Relationship between number of mitigation measures and percent reporting COVID-19–related outcomes using a log-linear (solid lines) and spline (dashed lines) model. (B) Odds ratio of COVID-19–related outcomes by mitigation measure in multivariable model including all measures versus the reduction resulting from a generic mitigation measure (dashed line).

health outcomes in these schools. Where data are available, they are often restricted to traditional public-school systems—though 28% of prekindergarten (pre-K) through 12th-grade students are in private or charter schools—and rarely can data be linked with individual- or household-level outcomes.

The COVID-19 Symptom Survey provides an opportunity to collect and analyze data on schooling behaviors and SARS-CoV-2–related outcomes from households throughout the US. This survey is administered through Facebook in partnership with Carnegie Mellon University and yields ~500,000 survey responses in the US weekly (17). It includes questions on symptoms related to COVID-19, testing, and, since late November 2020, the schooling experience of any children in the household [survey details and questionnaires are available at (18)]. Analysis weights adjust for non-response and coverage bias (see materials and methods).

We analyzed data collected over two time periods during the 2020 to 2021 school year (24 November 2020 to 23 December 2020

and 11 January 2021 to 10 February 2021). Of 2,142,887 total respondents in the 50 US states and Washington, DC, during this period, 576,051 (26.9%) reported at least one child in pre-K through high school living in their household (tables S1 and S2, Fig. 1A, and fig. S1). Although larger states have more responses, the per-capita response rate was fairly consistent across states (20 per 100,000; range, 10 to 29 per 100,000) and slightly higher in smaller states (fig. S2). Forty-nine percent (284,789 of 576,051) of these respondents reported a child living in the household engaged in either full- (68.8%) or part-time (46.0%) in-person schooling, with substantial variation both within and between states (Fig. 1 and table S3). Overall, in-person schooling increased between the two periods from 48 to 52%, although decreases were observed in some states (e.g., Arizona) (fig. S1 and table S3). Previous work has shown that household-reported rates of in-person schooling collected through the COVID-19 Symptom Survey track well with administrative data (19).

After adjusting for county-level incidence and other individual- and county-level factors

(but not school-based mitigation measures; tables S1 and S2 and fig. S3), living in a household with a child engaged in full-time in-person schooling is associated with a substantial increase in the odds [adjusted odds ratio (aOR), 1.38; 95% confidence interval (CI), 1.30 to 1.47] of reporting COVID-19–like illness [(CLI), defined as a fever of at least 100°F, along with cough, shortness of breath, or difficulty breathing], loss of taste or smell (aOR, 1.21; 95% CI, 1.16 to 1.27), or a positive SARS-CoV-2 test result within the previous 14 days (aOR, 1.30; 95% CI, 1.24 to 1.35) (Fig. 2A and table S4). Rates of reported COVID-19 outcomes were positively correlated with county-level confirmed SARS-CoV-2 incidence (figs. S4 and S5). When stratifying by grade level (restricted to households reporting children in a single grade strata), we find that the strength of the associations with full-time schooling increases with grade (Fig. 2A and table S4).

The association between COVID-19 outcomes and reporting a child in the household engaged in part-time in-person schooling is attenuated but still statistically significant for CLI (aOR, 1.21; 95% CI, 1.13 to 1.29), loss of taste or smell (aOR, 1.18; 95% CI, 1.13 to 1.24), and reporting a positive test (aOR, 1.09; 95% CI, 1.03 to 1.14). Among those reporting part-time schooling, the association between grade and COVID-19–related outcomes is less clear (Fig. 2A and table S4).

Respondents were asked to select all mitigation measures in place for any household child engaged in in-person schooling from a list of 14 measures (see materials and methods for wording). For students engaged in any form of in-person learning, the most common mitigation measure reported was student mask mandates (88%, unweighted), followed by teacher mask mandates (80%), restricted entry (e.g., no parents or caregivers allowed into school) (66%), and extra space between desks (63%) (see table S5 for survey-weighted rates). The distribution of mitigation measures reported was similar between those reporting full- and part-time in-person schooling, though most measures were slightly more likely to be reported in the part-time setting (Fig. 2B). Besides staying with the same teacher and staying with the same students throughout the day, we found minimal evidence of clustering of mitigation measures in principal components (table S6) or hierarchical clustering analyses (fig. S6). Student mask mandates were the only intervention reported alone.

Overall, respondents reporting a household child engaged in in-person school reported a mean of 6.7 [interquartile range (IQR), 4 to 9] mitigation measures in place at any school attended. Those reporting only children in part-time schooling reported more mitigation measures (mean, 7.0; IQR, 5 to 10) than those reporting only children in full-time schooling (mean, 6.4; IQR, 4 to 9). There is substantial

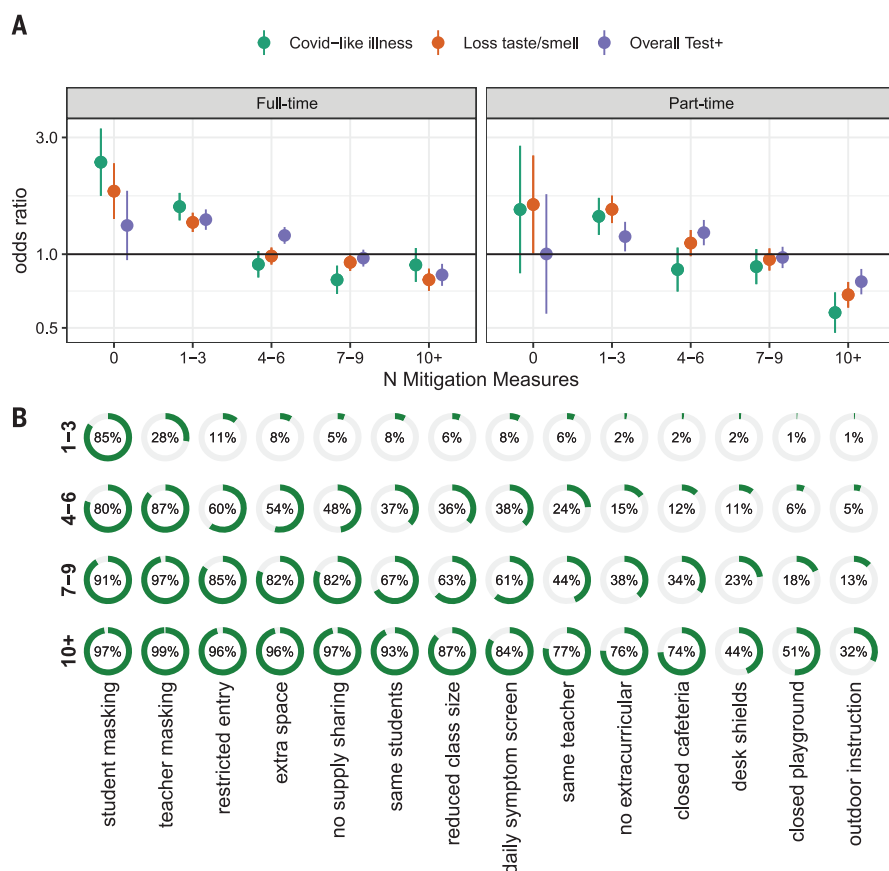


Fig. 4. Risk of in-person schooling by strata of number of reported mitigation measures.

(A) Estimated risk associated with full- and part-time in-person schooling by outcome and number of mitigation measures implemented, adjusted for individual- and county-level covariates. (B) Distribution of mitigation measures by total number of measures implemented.

geographic heterogeneity in the number of mitigation measures reported (Fig. 1D, fig. S7, and tables S5 and S7), with households in South Dakota reporting the least (mean, 4.6; IQR, 2 to 7) and households in Vermont reporting the most (mean, 8.9; IQR, 8 to 11).

We find a dose-response relationship with the number of mitigation measures implemented and the risk of COVID-19 outcomes among adult household members responding to the survey after adjustment for individual- and county-level factors. On average, each measure implemented is associated with a 9% decrease in the odds of CLI (aOR, 0.91; 95% CI, 0.89 to 0.92), an 8% decrease in the odds of loss of taste or smell (aOR, 0.92; 95% CI, 0.91 to 0.93), and a 7% decrease in the odds of a recent positive SARS-CoV-2 test (aOR, 0.93; 95% CI, 0.92 to 0.94) (table S8). Regression treating each individual mitigation measure as having an independent effect shows that daily symptom screening is clearly associated with greater risk reductions than the average measure (Fig. 3 and table S9), with some evidence that teacher mask mandates and cancelling extracurricular activities are also associated with

larger reductions than average. By contrast, closing cafeterias and playgrounds and the use of desk shields are associated with lower risk reductions (or even risk increases); however, this may reflect saturation effects because these are typically reported along with a high number of other measures. Notably, part-time in-person schooling is not associated with a decrease in the risk of COVID-19-related outcomes compared with full-time in-person schooling after accounting for other mitigation measures. Despite this heterogeneity in impact, we find that models including only the number of mitigation measures approximate well those where measures are modeled individually (fig. S8).

To explore what, if any, levels of mitigation are associated with elimination of the risk posed by in-person schooling, we conducted analyses where the in-person exposure groups were specific to whether 0, 1 to 3, 4 to 6, 7 to 9, or 10 or more mitigation measures were reported (Fig. 4, fig. S9, and tables S10 and S11). We found that when seven or more mitigation measures were in place, the positive association between in-person schooling and

COVID-19 outcomes disappeared. This result was robust to adjustment for the expected number of interventions (i.e., generalized propensity scores) on the basis of geographic- or individual-level covariates, but the result was less clear when propensity scores were based on both (fig. S10). Among those reporting seven or more mitigation measures, >80% reported student and teacher mask mandates, restricted entry, extra space between desks, and no supply sharing, and >50% reported student cohorting, reduced class size, and daily symptom screening.

The results presented here show a clear association between in-person schooling and the risk of COVID-19-related outcomes in adult household members and that this association disappears when more than seven school-based mitigation measures are reported. However, this association may not be causal, particularly given that in-person schooling and mitigation measures are not distributed randomly in the population (Fig. 1 and tables S1 to S3, S5, S7, S10, and S11). For example, households with a student attending in-person school tend to be in counties that are a higher percentage white (fig. S2) and contain respondents who are more likely to have recently eaten out or gone to a bar (table S2). Despite our best efforts to adjust for local incidence, individual behavior, and other potential confounders, it is possible that unmeasured factors drive the observed associations. Some subanalyses raise the possibility that complex interactions between geography and individual factors (but neither alone) may explain some of the observed results (fig. S10), although overadjustment is a concern in these models.

To address the possibility that the association with in-person schooling could be the result of differences between urban, suburban, and rural counties; local patterns of incidence; or other differences between those more and less likely to send children to school in person, we performed several stratified analyses (Fig. 5). When stratifying by propensity for in-person schooling and counties classified by size and metro status, or incidence, we found few systematic or statistically significant deviations from overall estimates, even if overall rates of outcomes differed (i.e., little evidence of effect modification by strata). We found similar results when stratifying counties by reported schooling behaviors, state, percent white, poverty, and access to broadband internet (figs. S11 to S14 and table S12). The notable exception is an apparent increase in the risk associated with in-person schooling in households with a higher propensity to have children attending in-person classes (Fig. 5C).

Although we were not able to specifically examine the relationship between in-person schooling, mitigation measures, and the risk to teachers, we were able to assess the risk

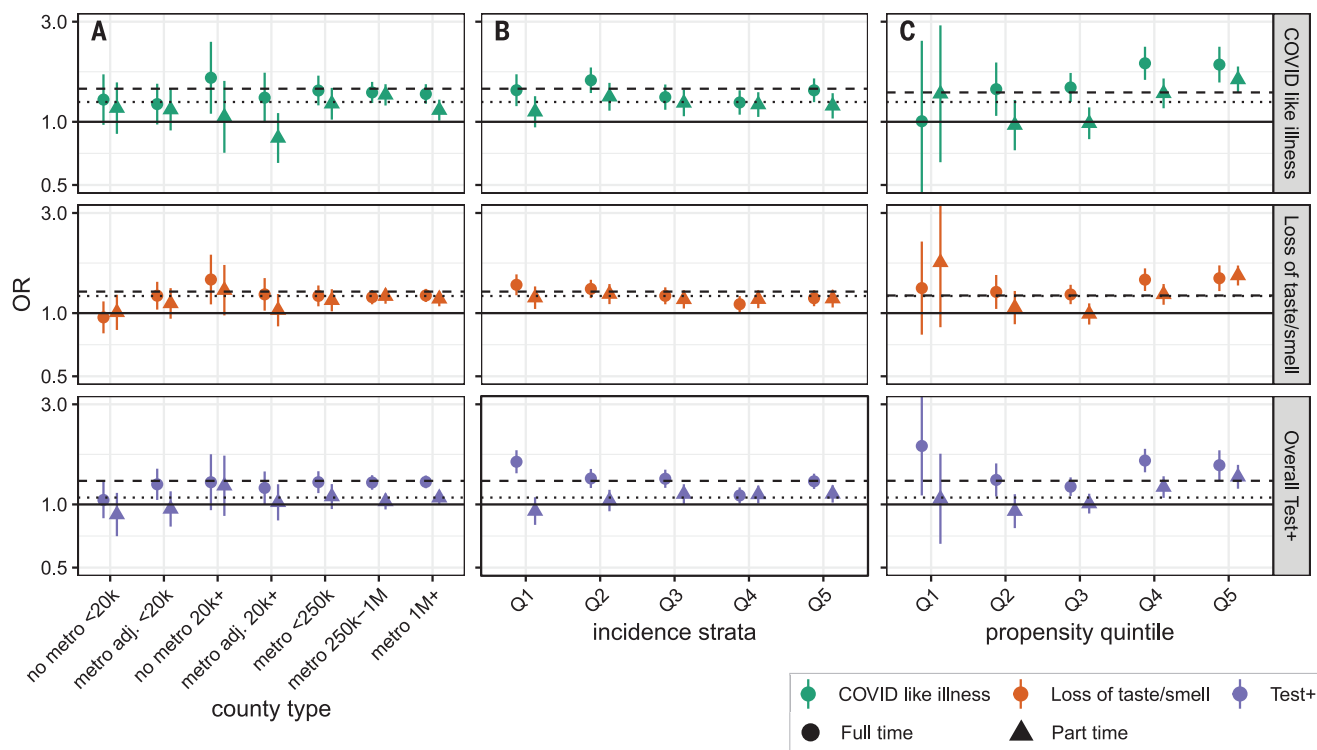


Fig. 5. Subgroup analysis of association between in-person schooling and COVID-19-related outcomes. (A to C) Estimated odds ratios (versus those in strata not reporting in-person schooling) of COVID-19-related outcomes from full-time (circles and dashed lines) and part-time (triangles and dotted lines) in-person schooling, when data are stratified by county population size and relation to

metropolitan areas (metropolitan area, nonmetropolitan area, or adjacent to metropolitan area) (A); quintile of incidence [quintile 1 (Q1) is lowest and Q5 is highest] (B); and propensity to report in-person schooling (Q5, most likely to have in-person schooling; Q1, least likely) (C). Horizontal dashed and dotted lines show overall point estimates for full-time and part-time in-person instruction, respectively.

associated with reporting paid work outside the home among pre-K through high school teachers. Teachers working outside the home were more likely to report COVID-19-related outcomes than those working at home (e.g., test positive; aOR, 1.8; 95% CI, 1.5 to 2.2; fig. S15 and table S13). The confidence interval summarizing the elevation of risk overlapped with corresponding intervals that are associated with working in health care (aOR, 1.7; 95% CI, 1.5 to 1.9) and office work (aOR, 1.6; 95% CI, 1.5 to 1.7).

The results presented here provide evidence that in-person schooling poses a risk to those living in the households of students but that this risk can be managed through commonly implemented school-based mitigation measures. This is consistent with findings from Sweden, where authors found risk to parents and teachers using a quasi-experimental approach (15). However, much remains unknown. We were unable to measure the risk posed by in-person schooling to the students themselves, nor were we able to specifically assess how different policies affect teachers and other school staff. Although the interplay between school policies and local incidence is complex and, possibly, multidirectional, we find substantial variation in SARS-CoV-2 incidence regardless of the mean number of mitigation

measures implemented within counties (figs. S8 and S15), and observed associations persist across study periods (figs. S17 to S19). This study also provides limited insight into the mechanisms by which in-person schooling increases risk, and it remains possible that classroom transmission plays a minor role and other school-related activities drive risk.

This study has limitations. Measures of association between COVID-19 outcomes and key exposures may be biased if confounding factors were not fully accounted for. Though we adjust for several county-level measures of socioeconomic status, these data were not available at the individual level and are known to be associated with COVID-19 risk and attitudes about in-person schooling. Analyses stratified on urbanization, background COVID-19 risk, and propensity for in-person schooling (table S5) did not reveal substantial sensitivity to the levels of factors investigated, nor did examining alternative measures of individual and household COVID-19 occurrence (figs. S20 to S22), which alleviates some of these concerns. Still, more formal studies that span schools with multiple policies and approaches would enhance insights into these questions.

Additionally, cross-sectional internet-based surveys have limitations and are subject to response biases. Although results are qualita-

tively consistent across COVID-19 outcomes [symptoms-based, test-based, and among those tested (figs. S20 to S22)], self-report has numerous limitations—for example, we cannot robustly assess asymptomatic spread. We were also unable to evaluate compliance with or investment in reported mitigation measures, and there is potential for mitigation measures to be reported inaccurately on the survey. Survey respondents may not be representative of the full US population, and although survey weights help account for nonresponse and coverage biases, weights calculated on the basis of the Facebook user base were adjusted for representativeness of the wider population on the basis of only age and gender—thus, these weights may not ensure representativeness across all covariates. However, the sample size of the survey and consistency of our findings across subanalyses allay some of these concerns, as does the assessment of non-COVID-19 outcomes (figs. S23 and S24). Further, any response biases would have to be differential based on schooling status to bias our results away from the null.

The debate around in-person schooling in the US has been intense and has exacerbated differences in approach between independent school systems and individual families nationally. This lack of coordination has

provided an opportunity to learn about the risks of in-person schooling and the degree to which mitigation measures may reduce risk. The results presented here provide one dimension of evidence for decision makers to consider in the context of a complex policy landscape, with many competing risks and priorities. Although online surveys have their specific limitations, the wide reach of the COVID-19 Symptom Survey has allowed us to gather data from households engaged in heterogeneous schooling activities throughout the country in a way that few other studies could. In analyzing these data, we find support for the idea that in-person schooling carries with it increased COVID-19 risk to household members, but we also find also evidence that common, low-cost mitigation measures can reduce this risk.

REFERENCES AND NOTES

1. Y. Li *et al.*, *Lancet Infect. Dis.* **21**, 193–202 (2021).
2. S. Flaxman *et al.*, *Nature* **584**, 257–261 (2020).
3. B. Yang *et al.*, UFGOVID Interventions Team, J. Lessler, C. D. Laird, D. A. T. Cummings, Effect of specific non-pharmaceutical intervention policies on SARS-CoV-2 transmission in the counties of the United States. medRxiv 2020.10.29.20221036 [Preprint]. 3 November 2020. <https://doi.org/10.1101/2020.10.29.20221036>.
4. D. N. Harris, E. Ziedan, S. Hassig, The Effects of School Reopenings on COVID-19 Hospitalizations [National Center for Research on Education Access and Choice (REACH), 2021]; www.reachcentered.org/publications/the-effects-of-school-reopenings-on-covid-19-hospitalizations.
5. C. Stein-Zamir *et al.*, *Euro Surveill.* **25**, 2001352 (2020).
6. A. S. Lopez *et al.*, *MMWR Morb. Mortal. Wkly. Rep.* **69**, 1319–1323 (2020).
7. C. M. Szablewski *et al.*, *MMWR Morb. Mortal. Wkly. Rep.* **69**, 1023–1025 (2020).
8. S. A. Ismail, V. Saliba, J. Lopez Bernal, M. E. Ramsay, S. N. Ladhani, *Lancet Infect. Dis.* **21**, 344–353 (2021).
9. A. Falk *et al.*, *MMWR Morb. Mortal. Wkly. Rep.* **70**, 136–140 (2021).
10. R. M. Viner *et al.*, *JAMA Pediatr.* **175**, 143–156 (2021).
11. S. Flasche, W. J. Edmunds, *Lancet Infect. Dis.* **21**, 298–299 (2021).
12. Q. Bi *et al.*, SEROCov-POP Study Group, Household Transmission of SARS-CoV-2: Insights from a Population-based Serological Survey. medRxiv 2020.11.04.20225573 [Preprint]. 16 January 2021. <https://doi.org/10.1101/2020.11.04.20225573>.
13. J. Zhang *et al.*, *Science* **368**, 1481–1486 (2020).
14. J. F. Ludvigsson, L. Engerström, C. Nordenhäll, E. Larsson, *N. Engl. J. Med.* **384**, 669–671 (2021).
15. J. Vlachos, E. Hertegård, H. B. Svaleryd, *Proc. Natl. Acad. Sci. USA* **118**, e2020834118 (2021).
16. Map: Where Has COVID-19 Closed Schools? Where Are They Open? (Education Week, 2020); www.edweek.org/leadership/map-where-are-schools-closed/2020/07.
17. F. Kreuter *et al.*, *Surv. Res. Methods* **14**, 159–163 (2020).
18. Symptom Surveys, Delphi Epidata API (2020); <https://cmu-delphi.github.io/delphi-epidata/api/covidcast-signals/fb-survey.html>.
19. C. Lupton-Smith *et al.*, Consistency between household and county measures of K-12 onsite schooling during the COVID-19 pandemic. arXiv:2103.13296 [stat.AP] (24 March 2021).
20. J. Lessler *et al.*, HopkinsIDD/inperson-schooling-covid-survey: second release with updated supplement, version v1.1, Zenodo (2021); <http://doi.org/10.5281/zenodo.4710757>.

ACKNOWLEDGMENTS

This research is partially based on survey results from Carnegie Mellon University's Delphi Group. **Funding:** This work was supported by the Johns Hopkins University Discovery Award (to E.B.-G., C.L.-S., and E.A.S.), the Johns Hopkins University COVID-19

Modeling and Policy Hub Award (to E.B.-G., C.L.-S., and E.A.S.), and the Department of Health and Human Services (to J.L. and M.K.G.). **Author contributions:** Conceptualization: J.L., M.K.G., C.J.E.M., A.S.A., and E.A.S. Methodology: J.L., M.K.G., and E.A.S. Investigation: J.L., M.K.G., E.B.-G., C.L.-S., and K.H.G. Visualization: J.L., M.K.G., and K.H.G. Funding acquisition: J.L. and E.A.S. Project administration: J.L. and E.A.S. Supervision: J.L., M.K.G., and E.A.S. Writing – original draft: J.L., M.K.G., K.H.G., E.B.-G., C.J.E.M., C.L.-S., A.S.A., and E.A.S. Writing – review and editing: J.L., M.K.G., K.H.G., E.B.-G., C.J.E.M., C.L.-S., A.S.A., and E.A.S. **Competing interests:** The authors declare that they have no competing interests. **Data and materials availability:** Data are freely available from the CMU Delphi Research Group to researchers at universities and non-profits, as detailed at Getting Data Access - Delphi Epidata API (<https://cmu-delphi.github.io/delphi-epidata/>). All analytic code with dummy datasets is available at <https://github.com/HopkinsIDD/inperson-schooling-covid-survey> (note, this code will not reproduce paper tables and figures without obtaining underlying data from CMU). Analytic code is available on Zenodo (20). This work is licensed under a Creative Commons Attribution 4.0 International (CC BY 4.0) license, which permits unrestricted use, distribution, and

reproduction in any medium, provided the original work is properly cited. To view a copy of this license, visit <https://creativecommons.org/licenses/by/4.0/>. This license does not apply to figures/photos/artwork or other content included in the article that is credited to a third party; obtain authorization from the rights holder before using such material.

SUPPLEMENTARY MATERIALS

science.sciencemag.org/content/372/6546/1092/suppl/DC1
Materials and Methods
Figs. S1 to S26
Tables S1 to S13
References (21–24)
MDAR Reproducibility Checklist
Data S1 to S3

27 February 2021; accepted 26 April 2021
Published online 29 April 2021
10.1126/science.abh2939

PALEOCLIMATE

Antarctic surface temperature and elevation during the Last Glacial Maximum

Christo Buizert^{1*}, T. J. Fudge², William H. G. Roberts³, Eric J. Steig², Sam Sherriff-Tadano⁴, Catherine Ritz⁵, Eric Lefebvre⁵, Jon Edwards¹, Kenji Kawamura^{6,7,8}, Ikumi Oyabu⁶, Hideaki Motoyama⁶, Emma C. Kahle², Tyler R. Jones⁹, Ayako Abe-Ouchi⁴, Takashi Obase⁴, Carlos Martin¹⁰, Hugh Corr¹⁰, Jeffrey P. Severinghaus¹¹, Ross Beaudette¹¹, Jenna A. Epifanio¹, Edward J. Brook¹, Kaden Martin¹, Jérôme Chappellaz⁵, Shuji Aoki¹², Takakiyo Nakazawa¹², Todd A. Sowers¹³, Richard B. Alley¹³, Jinho Ahn¹⁴, Michael Sigi¹⁵, Mirko Severi^{16,17}, Nelia W. Dunbar¹⁸, Anders Svensson¹⁹, John M. Fegyveresi²⁰, Chengfei He²¹, Zhengyu Liu²¹, Jiang Zhu²², Bette L. Otto-Bliesner²², Vladimir Y. Lipenkov²³, Masa Kageyama²⁴, Jakob Schwander¹⁵

Water-stable isotopes in polar ice cores are a widely used temperature proxy in paleoclimate reconstruction, yet calibration remains challenging in East Antarctica. Here, we reconstruct the magnitude and spatial pattern of Last Glacial Maximum surface cooling in Antarctica using borehole thermometry and firn properties in seven ice cores. West Antarctic sites cooled ~10°C relative to the preindustrial period. East Antarctic sites show a range from ~4° to ~7°C cooling, which is consistent with the results of global climate models when the effects of topographic changes indicated with ice core air-content data are included, but less than those indicated with the use of water-stable isotopes calibrated against modern spatial gradients. An altered Antarctic temperature inversion during the glacial reconciles our estimates with water-isotope observations.

Using oxygen and hydrogen isotope ratios in ancient polar ice as records of past site temperature requires a calibration (1). Surface temperature and the isotopic composition of precipitation correlate spatially in Antarctica, with a regression coefficient α_S (spatial slope) of 0.80 per mil per kelvin (‰K^{-1}) for $\delta^{18}\text{O}$ (the ratio of ^{18}O to ^{16}O) (2). Reconstructing past temperatures requires regression over time, and this temporal slope α_T may differ from α_S . In East Antarctica, where the longest continuous ice core records, going back to 800 thousand years before present (ka BP), have been extracted (3), independent temperature estimates are not available, and the spatial slope is commonly used to convert isotopic ratios to temperature (1); this approach gives a surface temperature differ-

ence ΔT_S of around ~9°C between the Last Glacial Maximum (LGM) (26 to 18 ka BP) and the preindustrial period (1, 4, 5).

Antarctic LGM-preindustrial isotope changes depend on many factors, including hemispheric sea surface temperatures (6), sea ice extent (7), ice sheet elevation (8), vapor origin and transport, precipitation seasonality, and post-depositional isotopic exchange (9). Isotope-enabled general circulation models seek to capture these physical processes, making them an invaluable tool for studying isotopic variations. Such models simulate LGM-preindustrial α_T ranging from 0.3 to 1.4 ‰K^{-1} in central East Antarctica (implied ΔT_S of ~4° to ~20°C), which implies that several aforementioned processes are poorly constrained (8, 10–12).

We distinguish three temperatures: (i) the climatic temperature T_{CLIM} at constant elevation (relative to the present-day geoid); (ii) the surface temperature T_s , which may differ from the climatic temperature because of changing ice sheet topography; and (iii) the vapor condensation temperature T_c , which is warmer than the surface because of the strong Antarctic inversion (2, 13).

In this study, we empirically reconstruct LGM surface temperature across Antarctica (Fig. 1) using two independent methods. We investigated five East Antarctic ice cores—EPICA (European Project for Ice Coring in Antarctica) Dome C (EDC), EPICA Dronning Maud Land (EDML), Dome Fuji (DF), Talos Dome (TAL), and South Pole (SP)—and two West Antarctic cores—West Antarctic Ice Sheet (WAIS) Divide (WD) and Siple Dome (SDM).

First, we estimated ΔT_s at EDC and DF from the measured borehole temperature profiles (Fig. 2) using a method similar to that used recently at WD (14). Owing to the downward ice flow and low thermal diffusivity, the ice sheet maintains an imprint of its past surface temperature history. The large ice sheet thickness at EDC and DF is favorable for preserving past temperatures, yet the low accumulation rate is not. Consequently, the relative uncertainty in the EDC and DF borehole reconstructions is larger than that at WD. To constrain the problem better, we used downward ice velocities measured by means of phase-sensitive radio-echo sounding (EDC only) and accurate age constraints derived through volcanic synchronization to the layer-counted WD time scale.

We forced a one-dimensional heat transport–ice flow model at the surface boundary with a temperature history that is based on the $\delta^{18}\text{O}$ record scaled with a constant α_T value (10). Applying traditional isotope scaling ($\alpha_T \approx 0.7 \text{ ‰ K}^{-1}$, yielding $\Delta T_s = -9^\circ\text{C}$ at EDC and -7.5°C at DF) simulates temperature profiles that do not fit the borehole observations at either site (Fig. 2). At EDC, the model-data fit is optimized for $\alpha_T = 1.14 \text{ ‰ K}^{-1}$, which is consistent with $\Delta T_s = -5.5^\circ\text{C}$ (95% confidence range is -6.9° to -3.1°C). At DF, the optimal ΔT_s is in the -2.0° to -5.4°C range; we provide a range without a best estimate because, at DF, there are no direct constraints on the down-

ward ice velocity. In Fig. 1, the WD, EDC, and DF borehole estimates are marked “BH.”

Second, we reconstructed past climate at all seven sites using the dependence of firm densification, the gradual transformation of polar snow to ice, on T_s and accumulation rate (A). Air bubbles are isolated from the atmosphere at the lock-in depth (50 to 120 m below the surface), an event preserved in two ice core signals (15): $\delta^{15}\text{N}$ of N_2 which records past firm column thickness by means of gravitational enrichment, and the gas age–ice age difference, or Δage . The $\delta^{15}\text{N}$ and Δage -isopleths are perpendicular in T_s - A space (Fig. 3A), meaning that if $\delta^{15}\text{N}$ and Δage are independently known, a distinctive climatic (T_s , A) solution exists (subject to the uncertainties of the firm model).

Synchronization using both volcanic deposits and globally synchronous abrupt atmospheric methane variations allowed us to estimate Δage empirically for the Antarctic ice cores (10, 16). We used an inverse dynamical firm

densification–heat transport model (17, 18) to reconstruct T_s and A histories that optimize the fit to Δage and $\delta^{15}\text{N}$ data (Fig. 3, B and C). Reconstructed accumulation rates agree (within uncertainty) with independent estimates (fig. S8). Methodological biases and uncertainties are estimated by using a Monte Carlo approach (10). The histograms in Fig. 1 give the ΔT_s distribution of the Δage -based reconstruction.

In East Antarctica, ΔT_s ranges from $-3.8^\circ \pm 2.0^\circ\text{C}$ (DF) to $-7.1^\circ \pm 1.7^\circ\text{C}$ (TAL); at DF, EDC, and EDML, ΔT_s is substantially lower than estimates from isotope scaling that use α_s . The two West Antarctic sites have similar ΔT_s of $-10.2^\circ \pm 2.4^\circ\text{C}$ (SDM) to $-10.3^\circ \pm 1.3^\circ\text{C}$ (WD). The Δage - and borehole-based reconstruction methods agree within uncertainty at all sites (Fig. 1). Allowing for more flank-like ice flow at EDC during the glacial period (which would occur if the divide position were different from that at present) improves the agreement by changing the borehole estimate

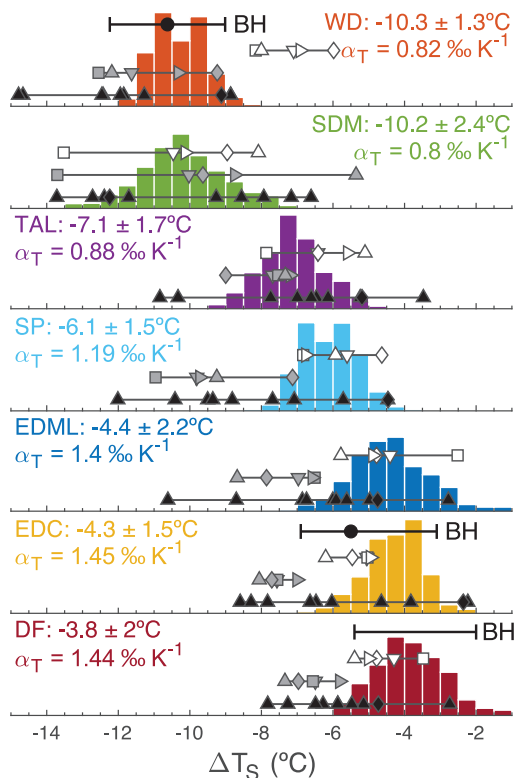


Fig. 1. Summary of Antarctic LGM cooling estimates. Black markers with horizontal error bars marked “BH” give borehole estimates; WD results are from (14). Histograms give distribution of Δage -based temperature reconstructions from a Monte Carlo sampling ($N = 1000$) of model parameters; listed are mean and 2σ standard deviation of the distribution, as well as the implied temporal isotope slope α_T . ΔT_s is the LGM (18 to 21.4 ka BP) minus preindustrial (0.5 to 2.5 ka BP) condition. White (MIROC), gray (HadCM3), and black (PMIP4) show AOGCM-simulated ΔT_s , with symbols denoting different LGM topography reconstructions (10): Pollard and Deconto (downward triangle) (32); Whitehouse *et al.* (square) (33); Glac-1D (diamond) (29); Gollledge *et al.* (rightward triangle) (34); and Ice-6G (upward triangle).

¹College of Earth Ocean and Atmospheric Sciences, Oregon State University, Corvallis, OR 97331, USA. ²Department of Earth and Space Science, University of Washington, Seattle, WA 98195, USA. ³Geographical and Environmental Sciences, Northumbria University, Newcastle, UK. ⁴Atmosphere and Ocean Research Institute, The University of Tokyo, Kashiwa 277-8568, Japan.

⁵Université Grenoble Alpes, CNRS, IRD, IGE, Grenoble, France. ⁶National Institute of Polar Research, Tachikawa, Tokyo, Japan. ⁷Department of Polar Science, The Graduate University of Advanced Studies (SOKENDAI), Tokyo, Japan. ⁸Japan Agency for Marine Science and Technology (JAMSTEC), Yokosuka, Japan. ⁹Institute of Arctic and Alpine Research, University of Colorado, Boulder, CO 80309, USA. ¹⁰British Antarctic Survey, Cambridge, UK. ¹¹Scripps Institution of Oceanography, University of California, San Diego, La Jolla, CA 92093, USA. ¹²Center for Atmospheric and Oceanic Studies, Graduate School of Science, Tohoku University, Sendai 980-8578, Japan. ¹³The Earth and Environmental Systems Institute, Pennsylvania State University, University Park, PA 16802, USA. ¹⁴School of Earth and Environmental Sciences, Seoul National University, Seoul 08826, South Korea. ¹⁵Climate and Environmental Physics, Physics Institute & Oeschger Center for Climate Change Research, University of Bern, 3012 Bern, Switzerland. ¹⁶Department of Chemistry “Ugo Schiff,” University of Florence, Florence, Italy. ¹⁷Institute of Polar Sciences, ISP-CNR, Venice-Mestre, Italy. ¹⁸New Mexico Bureau of Geology & Mineral Resources, Earth and Environmental Science Department, New Mexico Tech, Socorro, NM 87801, USA. ¹⁹Niels Bohr Institute, University of Copenhagen, Copenhagen, Denmark. ²⁰School of Earth and Sustainability, Northern Arizona University, Flagstaff, AZ 86011, USA. ²¹Department of Geography, Ohio State University, Columbus, OH 43210, USA. ²²National Center for Atmospheric Research, Boulder, CO 80307, USA. ²³Climate and Environmental Research Laboratory, Arctic and Antarctic Research Institute, St. Petersburg 199397, Russia. ²⁴Laboratoire des Sciences du Climat et de l’Environnement-IPSL, Université Paris-Saclay, Gif-sur-Yvette, France.

*Corresponding author. Email: christo.buizert@oregonstate.edu

to around -4.5°C (10); we choose to report the -5.5°C value to keep both methods independent. PMIP4 (Paleoclimate Modeling Intercomparison Project phase 4) simulations (19) find a seven-site-mean ΔT_s magnitude that is $1.2^{\circ} \pm 4.6^{\circ}\text{C}$ larger than our Δage -based reconstructions (mean and spread of 10 climate models; Fig. 1).

We emphasize that the firm method is primarily constrained by the empirical Δage es-

timates. Because T_s and A broadly covary via the saturation vapor pressure, the deglacial climatic changes run parallel to the $\delta^{15}\text{N}$ -isopleths (Fig. 3A). Therefore, $\delta^{15}\text{N}$ data alone do not constrain the magnitude of climate change meaningfully. The effects of T_s and A are additive in Δage , however, making Δage a sensitive proxy for climate change (Fig. 3D), as first noted by Schwander *et al.* (20). The empirical Δage at 24 ka BP is larger than

at 18 ka BP for all five cores where both are available, and coldest conditions in Antarctica occur ~ 27 to ~ 24 ka BP in our reconstructions (fig. S8h); this follows expectations from local insolation (21).

We propose that elevation changes explain the spatial differences in ΔT_s (8). Let Δz be the LGM elevation anomaly relative to the present. We present WD and DF total air-content data (fig. S12) and interpret them in terms of elevation change (22). These data suggest a 420-m (range, 280 to 590 m) contrast in Δz between WD and central East Antarctica (here, DF and EDC)—for example, $\Delta z = +300$ m at WAIS and $\Delta z = -120$ m in central East Antarctica (Fig. 4B). Our estimate is broadly in agreement with LGM ice sheet reconstructions that suggest a West-East Δz contrast between 160 and 560 m (10). Although the implied Δz at WAIS exceeds the observed highstand at ice margin nunataks (23), such data do not strongly constrain the elevation at WD more than 500 km away. The corresponding ΔT_s contrast (WD ΔT_s minus the average ΔT_s at DF and EDC) is $-6.2^{\circ} \pm 2.3^{\circ}\text{C}$ in the Δage -based reconstructions, $-6.0^{\circ} \pm 2.0^{\circ}\text{C}$ in the borehole reconstructions, and $-5.9^{\circ} \pm 2.7^{\circ}\text{C}$ in the PMIP4 model ensemble; the level of agreement suggests this is a robust feature of Antarctic LGM climate. This temperature contrast

Fig. 2. Borehole temperature reconstruction for EDC and DF.

(Left) Site borehole temperature observations at EDC (yellow) and DF (red). At both sites, the ice-bedrock interface is at the pressure melting point (-2.2°C). (Right) Model-data mismatch at EDC (yellow) and DF (red) for an ice flow-heat transport model forced by the optimized temperature histories (solid lines, ΔT_s of -5.5°C at EDC and -3.2°C at DF) and forced with water-isotope scaling of 0.7‰K^{-1} (dashed lines, ΔT_s of -9.0°C at EDC and -7.5°C at DF).

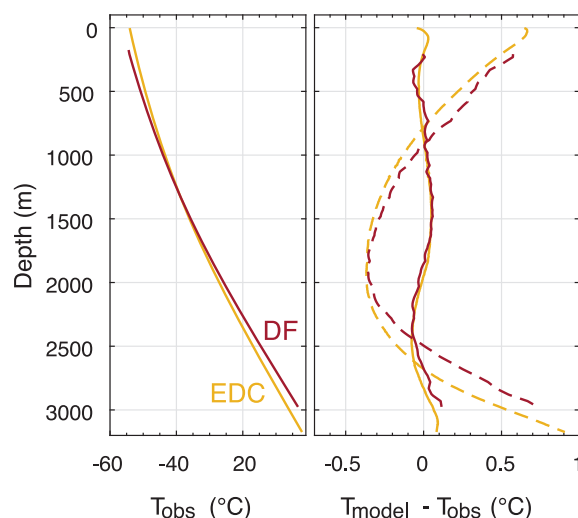
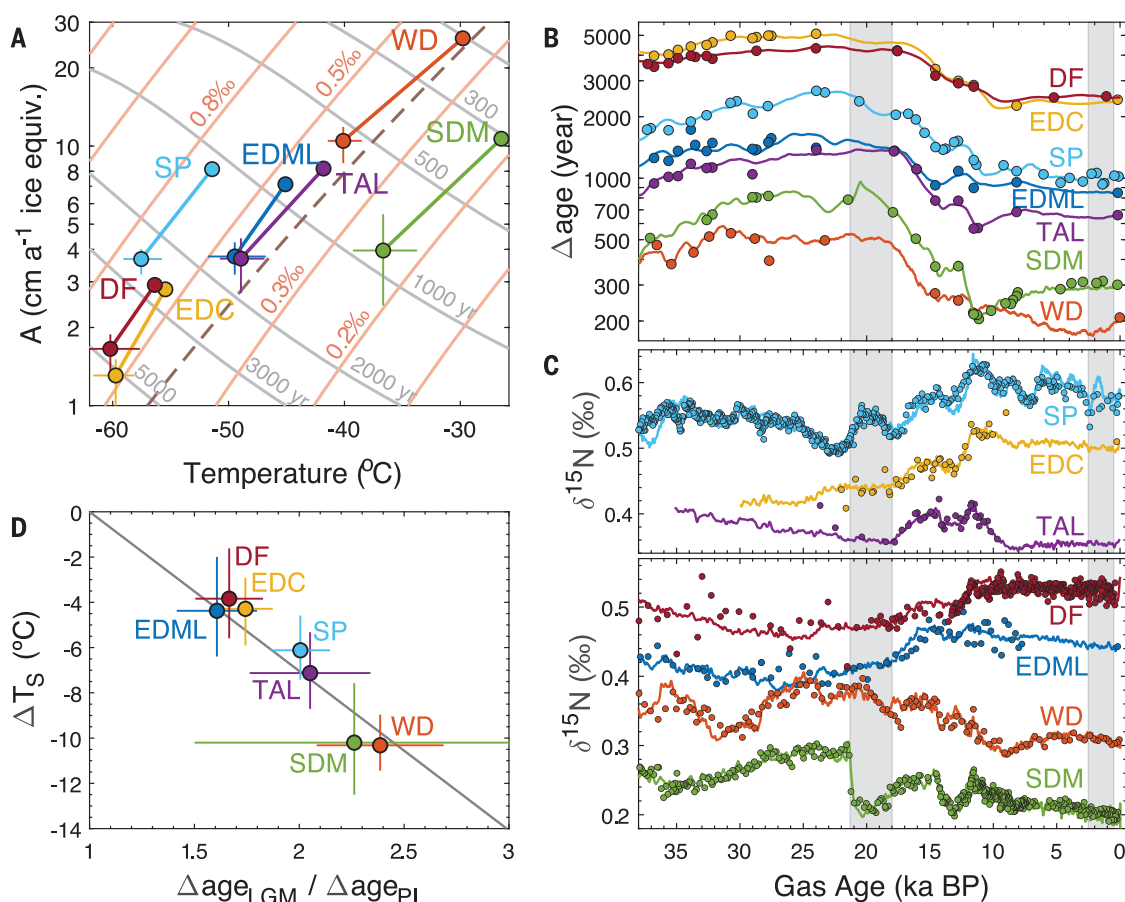


Fig. 3. Δage -based temperature reconstructions.

(A) Δage and $\delta^{15}\text{N}$ -isopleths (gray and salmon, respectively) in the steady-state Herron-Langway firn densification model as a function of T_s and A . The dashed line shows accumulation scaling by means of the saturation vapor pressure at the site (ignoring the atmospheric inversion). Reconstructed preindustrial and LGM conditions at the seven sites are indicated. (B) Model fit to empirical Δage constraints. Gray vertical bars denote the LGM (21.4 to 18 ka BP) and preindustrial (2.5 to 0.5 ka BP) periods. (C) Model fit to $\delta^{15}\text{N}$ data, divided over two panels to prevent overlapping curves. Data are shown on the WD2014 time scale (30, 31). (D) Reconstructed ΔT_s versus ratio of LGM Δage over preindustrial Δage (with linear fit) ($\Delta\text{age}_{\text{LGM}} / \Delta\text{age}_{\text{PI}}$), showing the utility of Δage as a climate proxy.



is thus plausibly linked to Δz through the (spatial) lapse rate in the interior of Antarctica of around $-12^{\circ}\text{C km}^{-1}$ (2, 24).

To further assess the elevation impact on ΔT_s , we perform an atmosphere-ocean general

circulation model (AOGCM) sensitivity study of Antarctic LGM climate using the MIROC (Model for Interdisciplinary Research on Climate) and HadCM3 (Hadley Centre Coupled Model version 3) models and a series of LGM

topographic reconstructions (10). We first estimated climatic LGM cooling using full LGM boundary conditions (including LGM albedo) but preindustrial Antarctic topography; this yielded a seven-site average ΔT_{CLIM} of -4.7°

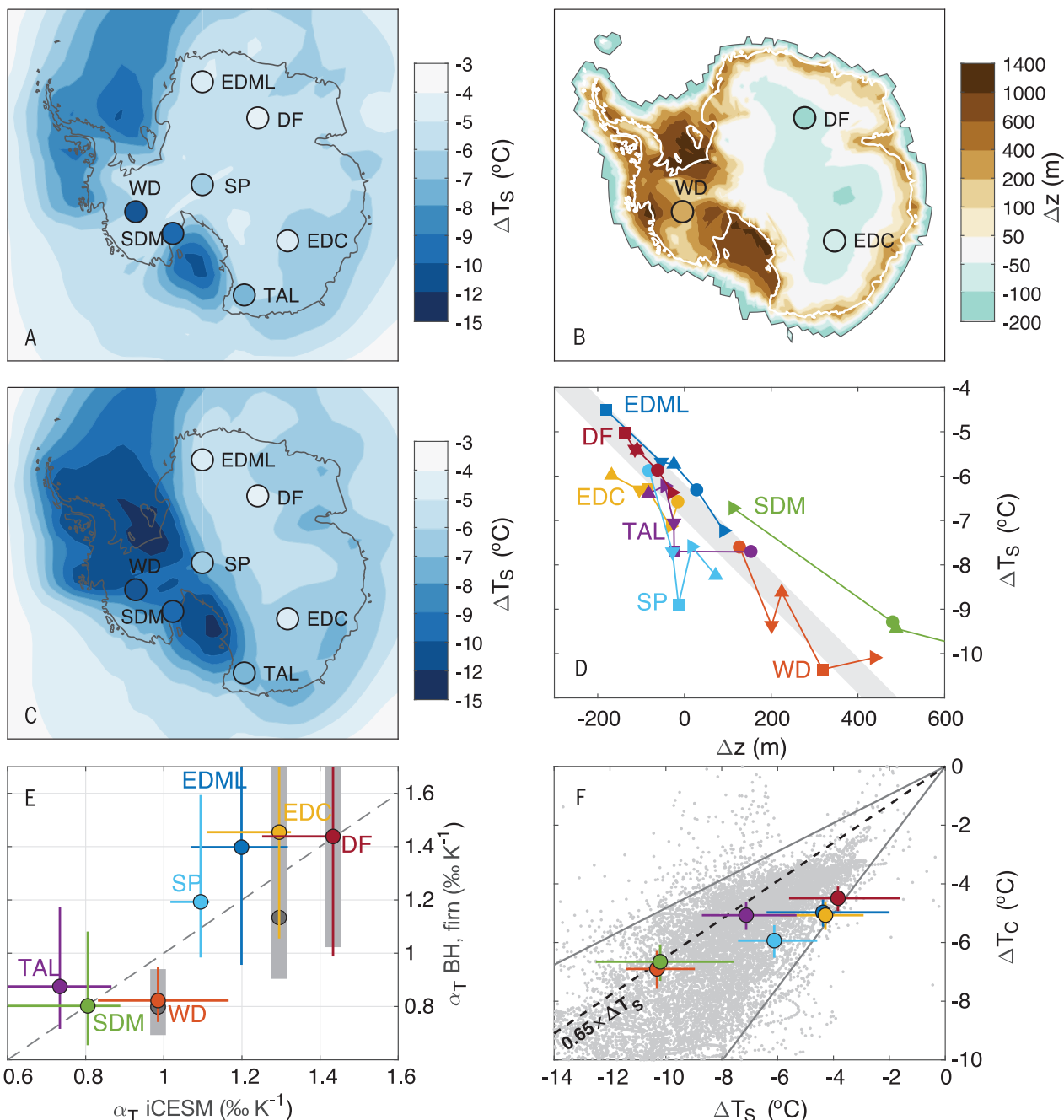


Fig. 4. Climate models and Antarctic topography. (A) AOGCM simulations of ΔT_s using preindustrial ice topography in Antarctica (average of MIROC and HadCM3 models), with Δz -based ΔT_s reconstructions for the seven sites. (B) Simulated LGM elevation anomaly (shaded, average of five topographies) with LGM elevation anomaly of +310, -80, and -140 m at WD, EDC, and DF (10). (C) As in (A), but using LGM ice topography in Antarctica (average of five LGM topographies and both MIROC and HadCM3 models). (D) Elevation change versus ΔT_s in the AOGCM simulations (average of MIROC and HadCM3 models); symbols denote the different LGM topographic reconstructions (see Fig. 1 caption for legend). The gray bar shows the dry adiabatic lapse rate. (E) Temporal isotope slope α_T from the iCESM model against

our reconstructions (borehole in gray, Δz -age-based in colors). (F) ΔT_s versus ΔT_c from Δz -age-based ΔT_s and isotope-based ΔT_c (large dots with error bars) and from LGM-preindustrial AOGCM simulations (small gray dots, gray lines enclose the central 95% of estimates); the black dashed line represents the modern spatial slope (2). Models plotted are PMIP3 [except for one model that simulates $\Delta T_s > 0^{\circ}\text{C}$], PMIP4 (all model output publicly available), and all iCESM, MIROC, and HadCM3 simulations used in this work; we show interior Antarctica (surface pressure < 800 hPa); T_c is taken to be the annual mean troposphere temperature maximum (typically ~ 500 hPa). The models have an average preindustrial spatial dT_c/dT_s of 0.68 (range, 0.31 to 0.89) in interior Antarctica.

and -7.0°C in the MIROC and HadCM3 models, respectively, but stronger albedo-driven cooling is found over the Ross and Weddell Seas due to ice growth onto the continental shelf (Fig. 4A). Simulated climatic ΔT_{CLIM} is similar in interior West and East Antarctica in the absence of topographic change.

Next, we performed climate simulations with five Antarctic LGM topographic reconstructions. These reconstructions suggest Δz of +100 to +600 m in interior WAIS and down to -250 m in interior East Antarctica (Fig. 4B). These changes result in greater ΔT_{S} in West than in central East Antarctica (Fig. 4C), in agreement with our reconstructions. By comparing the various topographic reconstructions, we find that ΔT_{S} is closely linked to Δz in both models through the dry adiabatic lapse rate of $-9.8^{\circ}\text{C km}^{-1}$ (Fig. 4D). Also, a fraction of the variance is due to the topography altering the atmospheric circulation around Antarctica, rather than the direct lapse-rate effect. We find a correlation $r = 0.96$ between the reconstructed and the simulated site ΔT_{S} pattern (averaged across the five topographic reconstructions and both models); for the PMIP4 multimodel mean, this correlation is $r = 0.95$. We conclude that changes in LGM ice sheet topography plausibly explain the ΔT_{S} spatial variability in our reconstruction (8).

Our findings have implications for the interpretation of water isotopes in Antarctic ice cores. We found α_{T} in the range of 0.9 to 1.4‰K^{-1} in East Antarctica and, therefore, $\alpha_{\text{T}} > \alpha_{\text{S}}$, opposite to Greenland, where $\alpha_{\text{T}} < \alpha_{\text{S}}$ (17, 25). We compared our α_{T} with those from LGM and preindustrial simulations using the latest-generation isotope-enabled Community Earth System Model (iCESM) (Fig. 4E). The good agreement ($r = 0.91$; 0.06‰K^{-1} mean offset) demonstrates that our reconstructed α_{T} are consistent with isotope physics, yet the large intermodel spread in simulated α_{T} [see section S3.5 in (10) for a review] prevents us from claiming that it validates our results. Although the α_{T} agree well, iCESM simulated a ΔT_{S} and LGM-preindustrial $\delta^{18}\text{O}$ change that are both too large (compared with our reconstructions and ice core data, respectively).

Last, we investigated changes to the strong surface-based inversion in the Antarctic boundary layer (Fig. 4F). The condensation temperature T_{C} is higher than T_{S} , and they correlate spatially with a slope $dT_{\text{C}}/dT_{\text{S}}$ in the 0.63 to 0.67 range (2, 13, 26). T_{C} controls precipitation $\delta^{18}\text{O}$, with a present-day spatial sensitivity of $d\delta^{18}\text{O}/dT_{\text{C}} = d\delta^{18}\text{O}/dT_{\text{S}} \times dT_{\text{S}}/dT_{\text{C}} \approx 0.80/0.65 = 1.23\text{‰K}^{-1}$. We now assume that, unlike ΔT_{S} , the LGM-preindustrial change ΔT_{C} can be estimated by using this spatial slope via $\Delta T_{\text{C}} = \Delta\delta^{18}\text{O}/1.23$ (Fig. 4F). At WD and SDM, the $\alpha_{\text{T}} \approx \alpha_{\text{S}}$ assumption holds, suggesting that the ratio $\Delta T_{\text{C}}/\Delta T_{\text{S}}$ is close to the present-day ratio of 0.65; in central East Antarctica, the

ratio $\Delta T_{\text{C}}/\Delta T_{\text{S}}$ exceeds 0.65, which is consistent with $\alpha_{\text{T}} > \alpha_{\text{S}}$. We plotted simulated ΔT_{S} versus ΔT_{C} across interior Antarctica from a wide range of AOGCMs and topographies; we found that the ratio $\Delta T_{\text{C}}/\Delta T_{\text{S}}$ ranges from 0.48 to 1.3 (95% interval, gray lines), with our empirical reconstructions falling within the model data cloud (Fig. 4F). In aggregate, these simulations find that $\Delta T_{\text{C}}/\Delta T_{\text{S}}$ tends to exceed the present-day ratio of 0.65 ($\sim 79\%$ of model data points); such a change to the inversion structure would result in $\alpha_{\text{T}} > \alpha_{\text{S}}$ for ΔT_{S} . In the iCESM simulations, the $\Delta T_{\text{C}}/\Delta T_{\text{S}}$ and α_{T} fields look similar, with the $\Delta T_{\text{C}}/\Delta T_{\text{S}} = 0.65$ contour line broadly aligning with the $\alpha_{\text{T}} = 0.8\text{‰K}^{-1}$ contour line (fig. S11). We conclude that physically plausible changes to the inversion (27, 28) may reconcile our reconstructions with previous work on Antarctic LGM water isotopes.

Our reconstructions improve the LGM Antarctic temperature estimation and provide a benchmark for testing the ability of (isotope-enabled) climate models to simulate climate states radically different from the late Holocene. For surface temperature, the spatial isotopic slope is not always a good approximation of the temporal slope, challenging the prevalent interpretation of ice core water isotopes in Antarctica.

REFERENCES AND NOTES

- J. Jouzel et al., *J. Geophys. Res.* **108**, 4361 (2003).
- V. Masson-Delmotte et al., *J. Clim.* **21**, 3359–3387 (2008).
- L. Augustin et al., *Nature* **429**, 623–628 (2004).
- V. Masson-Delmotte et al., *Quat. Sci. Rev.* **29**, 113–128 (2010).
- J. Jouzel et al., *Science* **317**, 793–796 (2007).
- C. Risi, S. Bony, F. Vimeux, J. Jouzel, *J. Geophys. Res.* **115**, D12118 (2010).
- D. Noone, I. Simmonds, *J. Geophys. Res.* **109**, D07105 (2004).
- M. Werner, J. Jouzel, V. Masson-Delmotte, G. Lohmann, *Nat. Commun.* **9**, 3537 (2018).
- M. Casado et al., *Cryosphere* **12**, 1745–1766 (2018).
- Materials and methods are available as supplementary materials.
- J.-E. Lee, I. Fung, D. J. DePaolo, B. Otto-Bliesner, *J. Geophys. Res.* **113**, D19109 (2008).
- G. Hoffmann, J. Jouzel, V. Masson, *Hydrol. Processes* **14**, 1385–1406 (2000).
- J. Jouzel, L. Merlivat, *J. Geophys. Res.* **89**, 11749–11757 (1984).
- K. M. Cuffey et al., *Proc. Natl. Acad. Sci. U.S.A.* **113**, 14249–14254 (2016).
- T. Sowers, M. Bender, D. Raynaud, Y. S. Korotkevich, *J. Geophys. Res.* **97**, 15683–15697 (1992).
- J. A. Epifanio et al., *Clim. Past* **16**, 2431–2444 (2020).
- C. Buizert et al., *Science* **345**, 1177–1180 (2014).
- M. M. Herron, C. C. Langway, *J. Glaciol.* **25**, 373–385 (1980).
- M. Kageyama et al., *Geosci. Model Dev.* **10**, 4035–4055 (2017).
- J. Schwander et al., *J. Geophys. Res.* **102**, 19483–19493 (1997).
- P. Huybers, G. Denton, *Nat. Geosci.* **1**, 787–792 (2008).
- D. Raynaud et al., *Earth Planet. Sci. Lett.* **261**, 337–349 (2007).
- P. Spector, J. Stone, B. Goehring, *Cryosphere* **13**, 3061–3075 (2019).
- J. Fortuin, J. Oerlemans, *Ann. Glaciol.* **14**, 78–84 (1990).
- K. M. Cuffey et al., *Science* **270**, 455–458 (1995).
- W. Connolley, *Int. J. Climatol.* **16**, 1333–1342 (1996).
- G. Kriinner, C. Genthon, *Clim. Dyn.* **14**, 741–758 (1998).
- N. P. M. Van Lipzig, E. Van Meijgaard, J. Oerlemans, *J. Glaciol.* **48**, 611–621 (2002).
- L. Tarasov, A. S. Dyke, R. M. Neal, W. R. Peltier, *Earth Planet. Sci. Lett.* **315–316**, 30–40 (2012).
- C. Buizert et al., *Clim. Past* **11**, 153–173 (2015).
- M. Sigl et al., *Clim. Past* **12**, 769–786 (2016).
- D. Pollard, R. M. DeConto, *Nature* **458**, 329–332 (2009).
- P. L. Whitehouse, M. J. Bentley, A. M. Le Brocq, *Quat. Sci. Rev.* **32**, 1–24 (2012).
- N. R. Golledge et al., *Nat. Commun.* **5**, 5107 (2014).
- Computational and Information Systems Lab, Cheyenne: HPE/SGI ICE XA System (University Community Computing) (National Center for Atmospheric Research, 2019); <https://doi.org/10.5065/D6RX99HX>.

ACKNOWLEDGMENTS

The idea of weak East Antarctic LGM cooling was suggested a decade ago by S. J. Johnsen (1940–2013) and J. Schwander but never published. We thank E. Capron and A. Landais for help in gathering $\delta^{25}\text{N}$ data; T. Hondoh and T. Kameda for support in Dome Fuji air-content analyses; C. Bréant for sharing model output; V. Gkinis for useful discussions; W.-L. Chan for assistance with model analysis; J.-Y. Peterschmitt for compiling PMIP4 model data and all PMIP4 groups for sharing model output; and C. Adams of Corvidopolis for providing a toddler-free work space during the COVID-19 pandemic. **Funding:** This work was supported by the US National Science Foundation (NSF) (grants 1643394 to C.B.; 1643355 to T.J.F. and E.J.S.; 1602435, 1443105, 1141839, 1043092, 0537930, and 1443105 to E.J.S.; 1443472 and 1643722 to E.J.B.; and 1738934 to R.B.A.); the University of Washington Royalty Research Fund (to T.J.F.); MEXT and the Japan Society for the Promotion of Science KAKENHI (grant numbers 18749002, 26241011, 15K10027, 17H06316, and 20H00639 to K.K.; 20H04327 to I.O.; 22310003 to T.N.; and 15J12515, 17H06104, 17H06323, and 20K14552 to A.A.-O.); the National Research Foundation of Korea (NRF) (grants NRF-2018R1A2B3003256 and NRF-2018R1A5A1024958 to J.A.); the European Research Council (ERC) under the European Union's Horizon 2020 research and innovation program (grant agreement no. 820047 to M.Si.); IT-MIUR-PNRA (Italian Antarctic Research Program) through the BE-OI (PNRA16_00124) project (to M.Se.); the Villum Investigator Project IceFlow (NR. 16572 to A.S.); Beyond EPICA - Oldest Ice Core EU Coordination and Support Action; measurements at EDC (Concordia Station) were supported by the French Polar Institute (IPEV, prog. 902) and the Italian Antarctic Program (PNRA and ENEA). The Talos Dome Ice core Project (TALDICE), a joint European program, is funded by national contributions from Italy, France, Germany, Switzerland, and the United Kingdom. Primary logistical support was provided by PNRA at Talos Dome. This is TALDICE publication no. 59. The CESM project is supported primarily by the NSF. This material is based upon work supported by the National Center for Atmospheric Research (NCAR), which is a major facility sponsored by the NSF under cooperative agreement no. 1852977 (B.L.O.-B.). Computing and data storage resources, including the Cheyenne supercomputer (35), were provided by the Computational and Information Systems Laboratory at NCAR (Z.L., C.H., and B.L.O.-B.). **Author contributions:** C.B., E.J.S., and W.H.G.R. conceived of the study; Δz -based reconstructions were by C.B.; ice flow and borehole temperature modeling were by T.J.F. and C.R.; GCM modeling was by W.H.G.R., S.S.-T., T.O., A.A.-O., C.H., Z.L., J.Z., and B.L.O.-B.; PMIP4 model compilation was by M.K.; methane data were by E.J.B., J.E., J.A., K.M., J.C., T.A.S., K.K., S.A., and T.N.; $\delta^{15}\text{N}-\text{N}_2$ data were by I.O., K.K., R.B., J.P.S., S.A., and T.N.; borehole thermometry data were by C.R., E.L., and H.M.; ApRES data were by C.M. and H.C.; SP isotope data were by E.J.S., E.C.K., and T.R.J.; air-content data and corrections were by J.E., K.K., V.L., J.M.F., and R.B.A.; SDM chronology was by T.J.F. and C.B.; SDM tephra matches were by N.W.D.; volcanic matching was by M.Si., M.Se., A.S., T.J.F., and C.B.; J.S. independently performed a similar study that reached the same conclusion around a decade ago; all authors contributed toward the final manuscript. **Competing interests:** The authors declare no competing interests. **Data and materials availability:** All new ice core data from this study are available in the supplementary materials as Data S1 and online at www.ncdc.noaa.gov/paleo/study/32632; previously published data are available with their original publications and/or in publicly accessible online data archives. Climate model output is available at <http://dods.lscce.ipsl.fr/pmip4/db/> or upon request from the corresponding author.

SUPPLEMENTARY MATERIALS

science.sciencemag.org/content/372/6546/1097/suppl/DC1
Materials and Methods
Figs. S1 to S12
Tables S1 to S7
References (36–160)
Data S1

18 June 2020; accepted 29 April 2021
10.1126/science.abd2897

IMMUNOLOGY

Antibody fucosylation predicts disease severity in secondary dengue infection

Stylianos Bournazos¹, Hoa Thi My Vo², Veasna Duong³, Heidi Auerswald³, Sowath Ly⁴, Anavaj Sakuntabhai^{5,6}, Philippe Dussart³, Tineke Cantaert^{2†*}, Jeffrey V. Ravetch^{1†*}

Although antiviral antibodies generally confer protective functions, antibodies against dengue virus (DENV) are associated with enhanced disease susceptibility. Antibodies can mediate DENV infection of leukocytes via Fc γ receptors, likely contributing to dengue disease pathogenesis. To determine if this mechanism accounts for variable disease severity, we examined Fab and Fc structures of anti-DENV antibodies from patients before and after infection and with variable disease outcomes. Neither antibody titers nor neutralizing activity correlated with disease severity in DENV-infected populations. Rather, DENV infection induced a specific increase in immunoglobulin G1 (IgG1) afucosylation, and the levels of afucosylated IgG1 were predictive of dengue disease severity. Thus, the IgG1 fucosylation status represents a robust prognostic tool for dengue disease, highlighting the key role of the Fc glycan structure in dengue pathogenesis.

Immune status to dengue virus (DENV) currently represents the greatest risk factor for hospitalization after a bite from a DENV-infected mosquito (1). Depending on the infecting DENV serotype, primary infection commonly leads to inapparent infection, but secondary infection can produce life-threatening symptoms (2, 3). A mismatch between the infecting serotype and the memory adaptive immunity is hypothesized to lead to exacerbated immune responses. Disease enhancement has been proposed to be mediated by preexisting DENV-reactive immunoglobulin G (IgG) antibodies, which at subneutralizing levels promote infection of leukocytes. This phenomenon, termed antibody-dependent enhancement (ADE), is dependent on the interactions of the IgG Fc domain with Fc γ receptors (Fc γ R) expressed on leukocytes (4).

Consistent with a pathogenic role for IgG antibodies in dengue, epidemiologic studies support that preexisting anti-DENV titers are a key determinant for susceptibility to symptomatic disease (5, 6). Additional susceptibility factors likely exist, because <5% of patients with preexisting anti-DENV IgGs develop severe disease. Given the dependence of DENV ADE on Fc-Fc γ R interactions, disease susceptibility may be determined by the affinity of these antibodies for specific Fc γ Rs, the abundance

of Fc γ R⁺-leukocytes, Fc γ R expression levels on leukocytes, and Fc γ R alleles (7–9). The affinity of the IgG molecule for the various Fc γ R types is dynamically regulated during an immune response and determined by the Fc domain protein sequence and the composition of the Fc-associated glycan (10) (Fig. 1A). Severe dengue patients are characterized by

an increased abundance of afucosylated IgG1 glycoforms, which exhibit higher affinity for the activating Fc γ RIIIa (11). However, whether afucosylated anti-DENV IgGs are the result of secondary DENV infection or whether their increased abundance truly represents a prognostic factor for susceptibility to severe dengue disease remains unknown.

To investigate the contribution of immune status and IgG Fc glycoforms to the development of severe disease, we analyzed the distribution of IgG subclasses and Fc-associated glycoforms from individuals with variable dengue disease severity (Fig. 1, fig. S1, and table S1). Hospitalized cases exhibited a global increase in plasma levels of afucosylated IgG1 Fc glycoforms for both antigen-specific (anti-DENV E) and total IgGs (Fig. 1, B to D). Increased levels of IgG1 afucosylation were also observed in hospitalized patients at the time of admission, confirming that these effects were not related to differences in sample timing and not induced in response to clinical management (fig. S1A). No differences in afucosylated Fc levels were observed for the other IgG subclasses, suggesting the existence of subclass-specific regulatory mechanisms for Fc fucosylation, likely associated with the conditions that drive IgG class switch (Fig. 1, B and C). Hospitalized

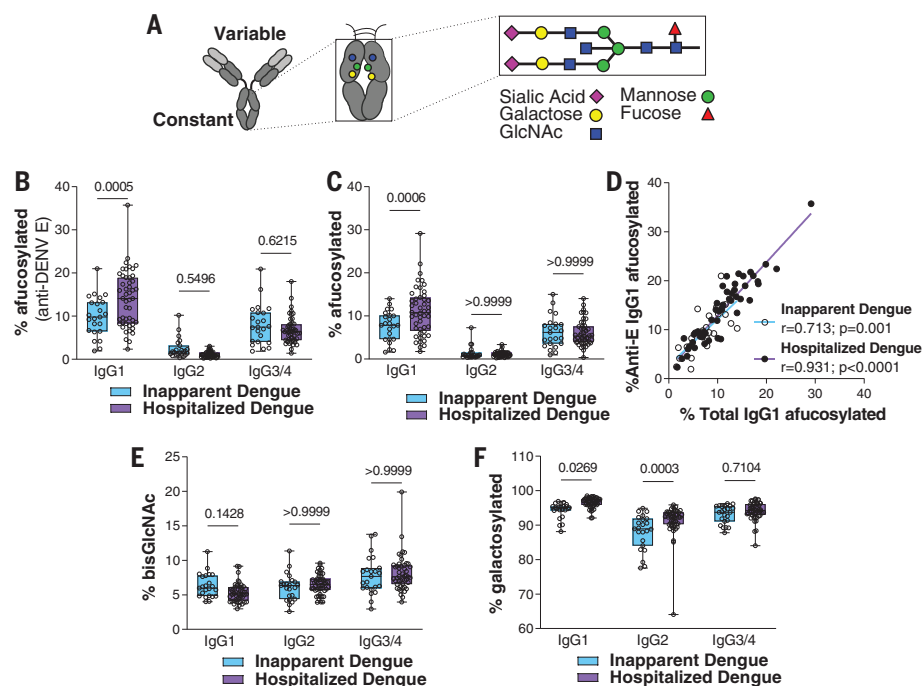


Fig. 1. Hospitalized dengue disease cases exhibit increased levels of afucosylated IgG1 glycoforms.

(A) Overview of the Fc-associated glycan. GlcNAc, N-acetylglucosamine. (B and C) Analysis of the levels of afucosylated IgG1 glycoforms for (B) anti-DENV E-specific and (C) total IgGs from inapparent and hospitalized cases. (D) Correlation of the abundance of afucosylated IgG1 levels of total with DENV E-specific IgGs. r , correlation coefficient. (E and F) Analysis of (E) bisecting GlcNAc and (F) galactosylated Fc glycoforms of IgGs from inapparent and hospitalized cases. One-way analysis of variance (ANOVA) with Bonferroni post hoc test was used for (B), (C), (E), and (F); Pearson correlation analysis was used for (D). For (B), (C), (E), and (F), boxes and whiskers represent the median, quartiles, and range (minimum to maximum); numbers above the boxes indicate p values.

¹Laboratory of Molecular Genetics and Immunology, The Rockefeller University, New York, NY, USA. ²Immunology Unit, Institut Pasteur du Cambodge, Institut Pasteur International Network, Phnom Penh, Cambodia. ³Virology Unit, Institut Pasteur du Cambodge, Institut Pasteur International Network, Phnom Penh, Cambodia. ⁴Epidemiology and Public Health Unit, Institut Pasteur du Cambodge, Institut Pasteur International Network, Phnom Penh, Cambodia. ⁵Functional Genetics of Infectious Diseases Unit, Department of Global Health, Institut Pasteur, Paris Cedex 15, France. ⁶Centre National de la Recherche Scientifique (CNRS), UMR2000, Paris Cedex 15, France.

*Corresponding author. Email: ravetch@rockefeller.edu (J.V.R.); tcantaert@pasteur-kh.org (T.C.)

†These authors contributed equally to this work.

cases also exhibited increased levels of IgG1 and IgG2 galactosylation (Fig. 1, E and F), which are expected to have limited biological importance (12). The global increase in IgG1 afucosylation raises the possibility of competition effects by non-antigen-specific IgGs, which may limit the Fc function of anti-DENV IgGs. However, such effects are expected to be minimal, because FcγRIIIa has low affinity for monomeric IgG1 (10). Indeed, in a model of monoclonal antibody (mAb)-mediated thrombocytopenia, the presence of excess, non-antigen-specific afucosylated IgG had no impact on cytotoxic anti-platelet mAb activity (fig. S2).

Hospitalized cases exhibited differential platelet and hematocrit (Hct) levels (Fig. 2, A and B) and were classified according to disease severity (13). Compared with dengue fever (DF), dengue hemorrhagic fever (DHF) and dengue shock syndrome (DSS) cases exhibited increased levels of afucosylated IgG1 glycoforms (Fig. 2C), but no major differences were noted in the abundance of other Fc glycoforms (fig. S1, B to I). Among all hospitalized cases, the abundance of afucosylated IgG1 levels correlated with platelet levels and Hct (Fig. 2, D and E). To determine whether the increase in afucosylation truly represents a prognostic factor of disease severity or whether it is the outcome of severe disease, we analyzed IgG samples from hospitalized patients obtained at the time of admission. Patients that developed DHF or DSS had significantly higher levels of afucosylated IgG1 glycoforms at admission compared with DF patients (Fig. 2F). Receiver operating characteristic (ROC) analysis also confirmed that IgG1 afucosylation levels at hospital admission are predictive of severe dengue disease (Fig. 2G).

Consistent with prior reports (6, 14), we also observed increased anti-DENV IgG levels (Fig. 3A) and frequency of secondary DENV infection (Fig. 3B) in hospitalized cases compared with inapparent cases. When patients were stratified based on immune history, the increased anti-DENV titers of hospitalized cases were found to be due to the higher frequency of secondary DENV infection in these patients. Secondary DENV infection was characterized by comparable anti-DENV IgG titers between inapparent and hospitalized cases, suggesting that neither the anti-DENV IgG titers nor the immune history alone can sufficiently predict dengue disease susceptibility (Fig. 3C). By contrast, IgG1 afucosylation was specifically increased in hospitalized, but not in inapparent, cases with prior history of DENV infection (Fig. 3D and fig. S3, A to C). Likewise, IgG1 afucosylation among hospitalized patients was associated with platelet levels and Hct (Fig. 2, D and E), but no such association was observed for anti-DENV IgG titers (Fig. 3, E and F). Thus, IgG1 afucosylation, when combined with DENV immune status, represents a more sensitive and

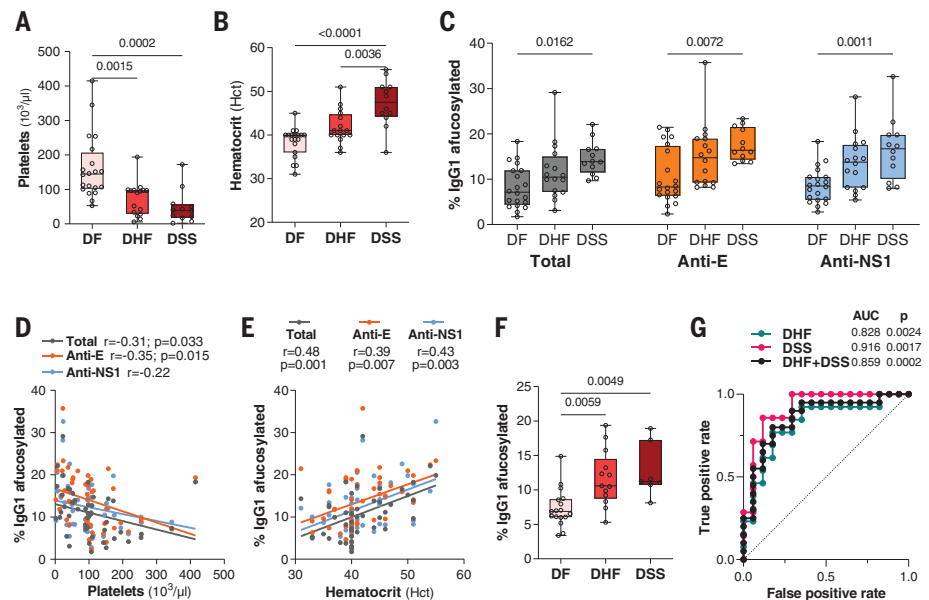


Fig. 2. Afucosylation is associated with dengue disease severity and correlates with biological features of severe disease. (A and B) Analysis of (A) platelet counts and (B) Hct in hospitalized dengue patients with variable clinical classification. (C) Afucosylation levels for total, anti-E, and anti-NS1 IgG1 from dengue patients with variable disease severity. (D and E) Correlation of afucosylated IgG1 levels with platelets and Hct among hospitalized cases. (F) Abundance of afucosylated IgG1 glycoforms in plasma samples from hospitalized patients obtained at the time of admission. (G) ROC analysis assessing the predictive value of the levels of IgG1 afucosylation at admission for severe dengue disease. AUC, area under curve. One-way ANOVA with Bonferroni post hoc test was used for (A) to (C) and (F); Pearson correlation analysis was used for (D) and (E). For (A) to (C) and (F), boxes and whiskers represent the median, quartiles, and range (minimum to maximum); numbers above the boxes indicate *p* values.

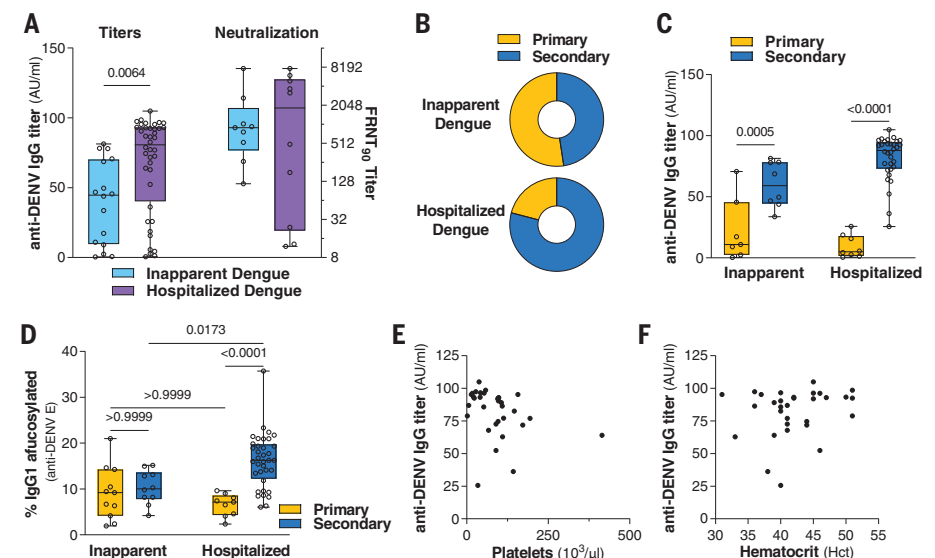


Fig. 3. Afucosylation, but not preexisting IgG titers, is associated with dengue disease susceptibility and severity. (A and B) Analysis of (A) anti-DENV binding and neutralizing titers (against DENV-1 and DENV-2) and (B) DENV immune status of inapparent and hospitalized dengue cases. Unpaired two-tailed Student's *t* test was used. AU, arbitrary units; FRNT, foci reduction neutralization titer. (C and D) Analysis of (C) anti-DENV IgG titers and (D) abundance of afucosylated anti-DENV E IgG1 in dengue cases stratified based on DENV immune status. One-way ANOVA with Bonferroni post hoc test was used. (E and F) Correlation of anti-DENV IgG titers with (E) platelet levels and (F) Hct. For (A), (C), and (D), boxes and whiskers represent the median, quartiles, and range (minimum to maximum); numbers above the boxes indicate *p* values.

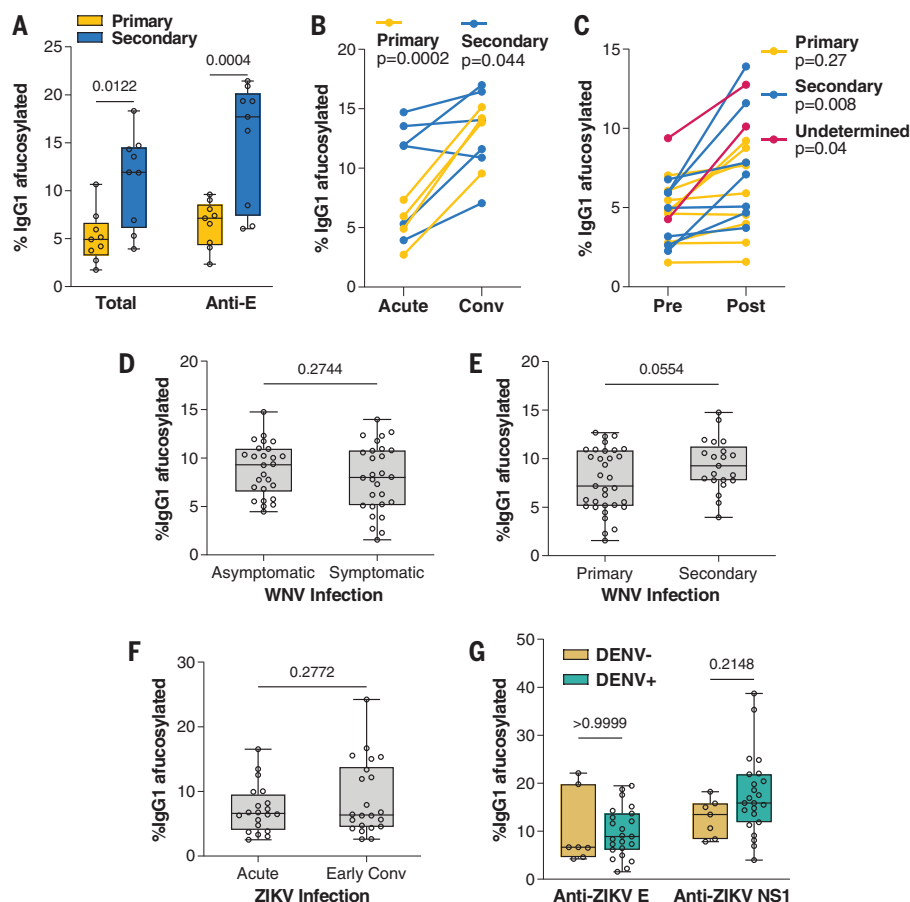


Fig. 4. DENV infection specifically modulates IgG Fc fucosylation. (A) Abundance of afucosylated IgG1 glycoforms in patients with identical disease classification (DF). (B) Levels of IgG1 afucosylation in DF patients during acute infection and at convalescence. (C) Afucosylation of total IgG1 in matched plasma samples (pre- and post-DENV infection). Patients were stratified based on DENV immune status. (D and E) Afucosylated IgG1 levels in WNV-infected patients with differential (D) disease severity and (E) WNV immune status. (F) Analysis of IgG1 afucosylation in ZIKV-infected patients at the acute phase of infection or at early convalescence. (G) Levels of afucosylated IgG1 glycoforms of anti-ZIKV E and anti-ZIKV NS1 IgGs in ZIKV-infected patients with differential DENV immune history. One-way ANOVA with Bonferroni post hoc test was used for (A) and (G); two-tailed Student's *t* test was used for (B) and (C) (paired) and for (D) to (F) (unpaired). For (A) and (D) to (G), boxes and whiskers represent the median, quartiles, and range (minimum to maximum); numbers above the boxes indicate *p* values.

accurate determinant for dengue disease susceptibility and is associated with clinical severity of symptomatic dengue disease.

To assess whether it is the severity of the disease that is inducing higher afucosylation or whether afucosylated IgG antibodies are elicited upon secondary DENV exposure, we compared the levels of IgG1 afucosylation among patients with identical clinical classification (DF) but differential DENV immune history. DF patients with prior DENV exposure exhibited increased IgG1 afucosylation levels, suggesting that immune history, rather than disease severity, determines the IgG1 fucosylation status (Fig. 4A). Likewise, primary DF cases exhibited increased levels of afucosylated IgG1 glycoforms at convalescence compared

with the acute phase of infection. This effect was not observed in secondary cases, which had persistently high levels of IgG1 afucosylation both at the acute and at the convalescent phase (Fig. 4B and fig. S3D).

Although the determinants that regulate Fc fucosylation are poorly characterized, the observed increase in the levels of IgG1 afucosylation in secondary cases may reflect specific modulation by DENV infection of the pathways that regulate Fc fucosylation. We therefore included in our study individuals with matched blood samples obtained before and after DENV infection (table S1). We observed that DENV infection specifically induced an increase in IgG1 afucosylation (Fig. 4C). By contrast, no changes were noted in the levels

of afucosylation of other IgG subclasses or in levels of other glycan modifications (fig. S3, E to L). To determine whether these effects on IgG1 afucosylation extend to other flaviviruses, we analyzed the Fc glycan of IgGs from asymptomatic or symptomatic West Nile virus (WNV)-infected patients with differential immune status (fig. S4, A to D, and table S2). In contrast to DENV-infected patients, no differences in IgG1 afucosylation levels were observed among WNV-infected patients with different disease severity (Fig. 4D) or immune status (Fig. 4E). We also assessed the IgG Fc glycan in plasma samples obtained from Zika virus (ZIKV)-infected patients at the acute infection phase and at early convalescence (table S3). Comparable IgG1 afucosylation levels were observed at the acute phase and convalescence, suggesting that in contrast to DENV infection, ZIKV infection has no impact on Fc fucosylation (Fig. 4F and fig. S4, E to H).

Because ZIKV and DENV cocirculate in endemic areas, dysregulated IgG1 afucosylation induced upon DENV exposure might result in a higher abundance of afucosylated Fc glycoforms. To investigate the impact of preexisting anti-DENV immunity on the Fc glycosylation of IgGs elicited upon ZIKV infection, we analyzed the Fc glycan structure of ZIKV-infected patients with differential DENV immune history of DENV infection (table S4). Anti-ZIKV E and NS1 IgGs from DENV-naïve or -experienced ZIKV patients exhibited comparable levels of afucosylated IgG1 (Fig. 4G) and other Fc glycoforms (fig. S5, A to D).

As recently demonstrated for other enveloped viruses (15), DENV can modulate IgG1 afucosylation either by eliciting distinctive inflammatory cues to B cells (16) or through direct infection of B cells (17, 18). This may modulate Fc fucosylation through inappropriate activation of cellular antiviral responses and/or dysregulated B cell function. Irrespective of the mechanism, we observed persistently high levels of IgG1 afucosylation at convalescence, suggesting that DENV infection has lasting consequences on the IgG Fc glycan structure. Given the well-established link between autoimmunity and Fc afucosylation (19), this may put dengue patients at risk for developing autoimmune pathologies, as has been observed in population-wide studies (20, 21).

Although substantial evidence supports ADE mechanisms in dengue disease pathogenesis, the role of preexisting IgG is less clear in shaping disease susceptibility to other flaviviruses like WNV or ZIKV (22, 23). Increased IgG1 afucosylation was evident only in DENV-infected, but not in ZIKV- or WNV-infected, patients, suggesting that aberrant Fc fucosylation likely represents an immune evasion mechanism that specifically drives dengue disease pathogenesis through modulation of the anti-DENV IgG-FcγRIIIa interaction.

Our findings support that DENV infection causes a specific increase in afucosylated IgG1 glycoforms. In contrast to DENV immune status, IgG1 afucosylation levels not only are associated with susceptibility to symptomatic disease but also correlate with the specific clinical manifestations of severe dengue disease. Thus, the IgG1 afucosylation status represents a robust prognostic tool to predict susceptibility to symptomatic dengue disease, confirming the role of Fc-FcγR interactions in mediating ADE of dengue disease.

REFERENCES AND NOTES

1. S. Bhatt *et al.*, *Nature* **496**, 504–507 (2013).
2. D. W. Vaughn *et al.*, *J. Infect. Dis.* **181**, 2–9 (2000).
3. S. B. Halstead, S. Nimmannitya, S. N. Cohen, *Yale J. Biol. Med.* **42**, 311–328 (1970).
4. S. Bournazos, A. Gupta, J. V. Ravetch, *Nat. Rev. Immunol.* **20**, 633–643 (2020).
5. H. Salje *et al.*, *Nature* **557**, 719–723 (2018).
6. L. C. Katzelnick *et al.*, *Science* **358**, 929–932 (2017).
7. J. A. Aguilar-Briseño *et al.*, *Nat. Commun.* **11**, 3177 (2020).
8. C. A. Noecker, I. Y. Amaya-Larios, M. Galeana-Hernández, J. Ramos-Castañeda, R. A. Martínez-Vega, *Acta Trop.* **138**, 15–22 (2014).
9. S. N. Mohsin *et al.*, *Am. J. Trop. Med. Hyg.* **93**, 691–696 (2015).
10. S. Bournazos, T. T. Wang, R. Dahan, J. Maamary, J. V. Ravetch, *Annu. Rev. Immunol.* **35**, 285–311 (2017).
11. T. T. Wang *et al.*, *Science* **355**, 395–398 (2017).
12. S. Borghi *et al.*, *Proc. Natl. Acad. Sci. U.S.A.* **117**, 12943–12951 (2020).
13. World Health Organization, *Dengue Haemorrhagic Fever: Diagnosis, Treatment, Prevention and Control* (World Health Organization, ed. 2, 1997).
14. E. Simon-Lorière *et al.*, *Sci. Transl. Med.* **9**, eaal5088 (2017).
15. M. D. Larsen *et al.*, *Science* **371**, eaac8378 (2021).
16. V. Upasani *et al.*, *Front. Immunol.* **10**, 2500 (2019).
17. F. Zanini *et al.*, *Proc. Natl. Acad. Sci. U.S.A.* **115**, E12363–E12369 (2018).
18. V. Upasani *et al.*, *Front. Immunol.* **11**, 594813 (2021).
19. T. T. Wang, *Curr. Top. Microbiol. Immunol.* **423**, 63–75 (2019).
20. H. M. Li, Y. K. Huang, Y. C. Su, C. H. Kao, *J. Infect.* **77**, 212–219 (2018).
21. H. T. M. Vo *et al.*, *Pathogens* **9**, 1060 (2020).
22. P. Pantoja *et al.*, *Nat. Commun.* **8**, 15674 (2017).
23. A. C. B. Terzian *et al.*, *Clin. Infect. Dis.* **65**, 1260–1265 (2017).

ACKNOWLEDGMENTS

We thank the participating patients and the doctors and nurses of the three hospitals in Kampong Cham province for patient enrollment and sample collection and H. Rekol from the National Dengue Control Program. Plasma samples from ZIKV- and WNV-infected individuals were obtained from BEI Resources and the National Heart, Lung, and Blood Institute (NHLBI) Biologic Specimen and Data Repository Information Coordinating Center, respectively. We thank E. Lam, R. Francis (Rockefeller University), and R. Sherwood (Cornell University) for excellent technical support. **Funding:** We acknowledge support from the Howard Hughes Medical Institute (HHMI)–Wellcome Trust (208710/Z/17/Z to T.C.), the National Institute of Allergy and Infectious Diseases (NIAD) (R01AI137276 to S.B.; U19AI111825 to J.V.R.), and the Rockefeller University. Sample collection from DENV patients was supported by the EU Seventh Framework Programme (FP7/2007–2011). This manuscript was prepared using samples from ZIKV-infected individuals provided by Blood Systems Research Institute (BSRI) from studies funded in whole or in part by NHLBI (HHSN2682011000011); Roche Molecular Systems, Inc.; and the Department of Health and Human Services, Biomedical Advanced Research and Development Authority (HHSO100201600010C). The content is solely the responsibility of the authors and does not necessarily represent the official views of BSRI or the NIH. **Author**

contributions: S.B., T.C., and J.V.R. designed the study. S.B., H.T.M.V., T.C., and J.V.R. wrote the manuscript. S.B., H.T.M.V., and H.A. performed experiments, collected, and/or analyzed data. P.D., T.C., and J.V.R. supervised the experiments. V.D., S.L., and A.S. were responsible for the DENV cohort collections. T.C. and P.D. selected the patient samples and revised World Health Organization (WHO) classifications. **Competing interests:** The Rockefeller University has filed a provisional patent application that covers the diagnosis and treatment of DENV infection described in the manuscript. **Data and materials availability:** All data are available in the main text or the supplementary materials. All materials, except for clinical specimens, are available on request after completion of a materials transfer agreement with The Rockefeller University.

SUPPLEMENTARY MATERIALS

science.sciencemag.org/content/372/6546/1102/suppl/DC1
Materials and Methods
Figs. S1 to S5
Tables S1 to S4
References (24–34)
MDAR Reproducibility Checklist

10 May 2020; resubmitted 19 January 2021
Accepted 14 April 2021
10.1126/science.abc7303

PALEONTOLOGY

An early Miocene extinction in pelagic sharks

Elizabeth C. Sibert^{1,2,3*} and Leah D. Rubin⁴

Shark populations have been decimated in recent decades because of overfishing and other anthropogenic stressors; however, the long-term impacts of such changes in marine predator abundance and diversity are poorly constrained. We present evidence for a previously unknown major extinction event in sharks that occurred in the early Miocene, ~19 million years ago. During this interval, sharks virtually disappeared from open-ocean sediments, declining in abundance by >90% and morphological diversity by >70%, an event from which they never recovered. This abrupt extinction occurred independently from any known global climate event and ~2 million to 5 million years before diversifications in the highly migratory, large-bodied predators that dominate pelagic ecosystems today, indicating that the early Miocene was a period of rapid, transformative change for open-ocean ecosystems.

Using isolated shark dermal denticles from two red-clay deep-sea sediment cores with well-developed age models, Deep Sea Drilling Project (DSDP) Site 596 (1) in the South Pacific gyre and Ocean Drilling Program (ODP) Site 886 (2) in the North Pacific gyre, we found that a major, previously undescribed shark extinction event occurred in the open ocean during the early Miocene epoch, around 19 million years ago (Ma) (Fig. 1). The extinction is marked by a notable decrease in the ratio of shark to fish fossils in open-ocean sediments from 1 shark fossil per 5 fish fossils pre-extinction to 1 shark fossil per 100 fish fossils post-extinction, the only such shift since the Cretaceous-Paleogene (K/Pg) mass extinction event 66 Ma (3). Fish teeth and elasmobranch denticles are composed of the same material (bioapatite), and visual inspection of the samples pre- and post-extinction revealed no signs of dissolution or other taphonomic changes in either group. All pre-extinction samples had abundant denticles and teeth. The post-extinction samples had abundant fish teeth, but only a third of the samples had even a single denticle (3). When normalized to sediment accumulation rate

(Fig. 1), post-extinction tooth abundances are comparable to those in the Paleogene, whereas denticle abundances are reduced by >90% (3). This event fundamentally altered the structure of pelagic fish and shark communities, disrupting more than 40 million years of stability (3).

We quantified the morphological variation of shark denticles preserved in our samples and classified 798 denticles from the South Pacific and 465 denticles from the North Pacific (a total of 1263 fossil denticles) into 85 explicit morphological types, with three additional “catch-all” categories for incomplete denticles (figs. S1 and S2). We applied the same morphological scheme to a comprehensive literature review of modern elasmobranch skin images by assigning denticle morphotypes from published skin sample images of 152 species of extant sharks, skates, and rays (4–9). Most species in the modern denticle diversity catalog have only one or two denticle morphotypes, and most denticle morphotypes matched to one or two families (fig. S3). Several generic denticle morphotypes were found across multiple orders (fig. S3 and table S3), and most surviving denticle morphotypes fell into this category. Although not all denticle morphotypes are diagnostic for a specific taxonomic entity, denticle morphotype richness provides a reasonable indicator of overall shark diversity (fig. S3).

We observed a >70% extinction of denticle morphotypes in the early Miocene, with >90% of denticle morphotypes disappearing from

¹Harvard Society of Fellows, Harvard University, Cambridge, MA 02138, USA. ²Department of Organismic and Evolutionary Biology, Harvard University, Cambridge, MA 02138, USA. ³Department of Earth and Planetary Sciences, Yale University, New Haven, CT 06511, USA. ⁴College of the Atlantic, Bar Harbor, ME 04609, USA.

*Corresponding author. Email: elizabeth.sibert@yale.edu

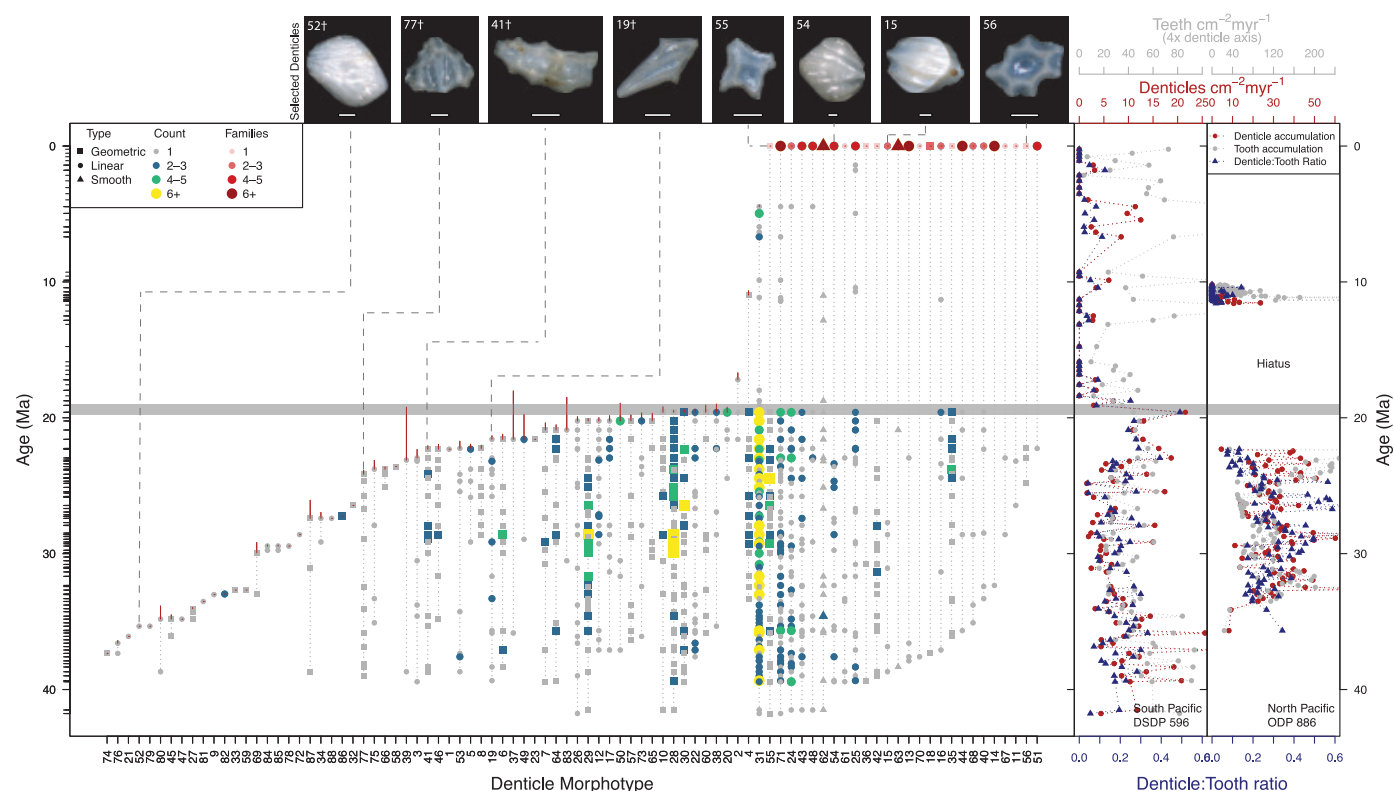


Fig. 1. A range chart showing the combined occurrences of denticle morphotypes from DSDP Site 596 and ODP Site 886, along with modern analogs. Denticle morphotypes are indicated by numbers on the x axis. A key matching the morphotype number to denticle morphotype is available in table S1. The gray box represents the 95% confidence interval of the extinction horizon, which was estimated by using the 20% range extensions method (12), red lines are the calculated range extensions. The colors demark

raw abundance counts of each morphotype in an individual sediment sample. The shades of red in the top row indicate the number of extant families with that morphotype. The y-axis ticks indicate all sediment samples inspected, including those with teeth but no denticles. Right panels show the denticle (red circles) and tooth (gray circles) accumulation rate and relative abundance compared with teeth (blue triangles) for DSDP Site 596 and ODP Site 886, first reported in (3). myr, million years.

the open-ocean fossil record; the remaining 20% of surviving denticle types are found only in the modern catalog (Fig. 1 and fig. S8). No new denticle morphotypes appear in the post-extinction sedimentary record, which suggests a failure to rediversify after the extinction event. This >70% extinction is substantially greater than the 30 to 40% shark extinction at the K/Pg mass extinction event (10). The disappearance of a few less-common denticle types just before 19 Ma is best explained by the Signor-Lipps effect (17), and range extension estimates restrict the extinction horizon to between 19 and 19.75 Ma (12). There is additional uncertainty in the precision of the cobalt-based age model of DSDP Site 596, although biostratigraphy at the site restricts the event to the middle of the early Miocene (1).

We identified two broad types of denticles: linear denticles, the typical parallel-ridged denticles found on most extant shark species, and geometric denticles, characterized by intricate, interlacing ridge systems (Fig. 2 and table S3). Also, smooth denticles exist that lack charac-

teristic ridges and are found on many groups of sharks (4). Most modern sharks have linear denticles (8), which may improve swimming efficiency over long-distance migrations. By contrast, the extant geometric denticles are found mostly on small, sit-and-wait ambush predators that live in the deep sea, including the cookiecutter shark (*Isistius brasiliensis*) and the lantern shark (*Etmopterus perryi*) (13).

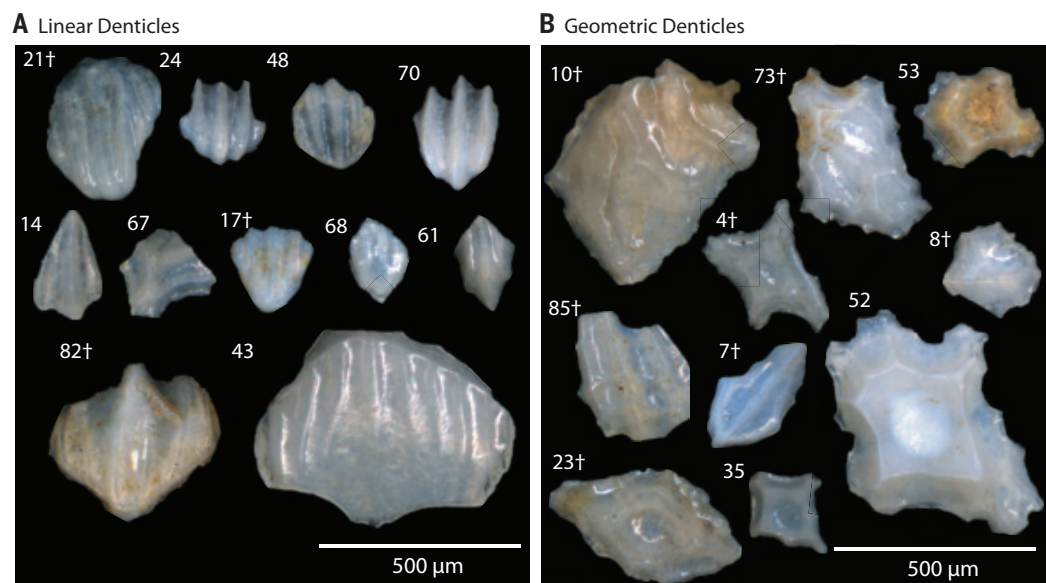
In our samples, 6 of the 33 geometric morphotypes found in the Paleogene and earliest Miocene persist to the present day with a single post-extinction fossil representative (82% extinction), and 18 of the 53 linear morphotypes found in the Paleogene are known today, including six post-extinction fossil representatives (66% extinction). Geometric denticles decline in relative abundance from 35% of pre-extinction denticle assemblages to just 3% post-extinction, which is a significant difference (chi-square test, $P < 0.01$). Although the number of denticles in the post-extinction samples is lower than those pre-extinction, a rarefaction analysis demonstrates that morphotype diver-

sity post-extinction is significantly lower than pre-extinction (fig. S6). The reduced abundance and diversity across denticle types suggest that this event affected all sharks; however, the higher level of extinction of geometric denticle morphotypes and their decline in relative abundance post-extinction suggest that this early Miocene event may have selectively extirpated sharks restricted to the pelagic realm while allowing at least some migratory lineages to survive.

There is no clear environmental driver for this substantial decline in pelagic sharks. The early Miocene does not stand out in terms of global climate (14–16), as it falls nearly 15 million years after the Eocene-Oligocene transition (17) and several million years before the relative warmth of the mid-Miocene Climate Optimum (18). The Paleogene-Neogene boundary occurred ~4 million years before this event (19). Mixed evidence exists for an increase in diatom diversity beginning around this interval (20), along with an increase in benthic foraminifera associated with high

Fig. 2. Examples of some distinctive linear and geometric denticle types observed in this study. (A) Linear denticles. (B) Geometric denticles.

Numbers correspond to the x axis in Fig. 1, and denticles marked with the † symbol are extinct. Full plates of all denticle morphotypes identified in this study are in figs. S1 and S2.



productivity (21). However, this interval has few well-studied or well-preserved deep-ocean sediment records. Only ~10% of ocean drilling sites that extend deeper than the early Miocene have a potentially continuous early Miocene section, which suggests a substantial disruption to sediment accumulation around this interval (fig. S13).

Pelagic sharks were not gradually driven to extinction by the evolution of modern pelagic top predator groups. Rather, the abrupt shark extinction appears to have occurred several million years before radiations in tunas and billfish (22), seabirds (23), beaked whales (24), baleen whales (25), and even migratory sharks (26). A gap in whale fossilization that spans the early Miocene shark extinction is associated with a shift in the trajectory of baleen whale evolution and a subsequent appearance of crown filter-feeding whales. (27). It is possible that these new, large migratory marine vertebrates contributed to the suppression of pelagic sharks in the aftermath of the extinction, as denticle abundance and morphotype diversity never recovered.

Before this early Miocene extinction, sharks played a much larger role in the open-ocean ecosystem than they do today. The transition was geologically abrupt, likely occurring in <100,000 years (1), and featured a >70% extinction in open-ocean sharks, followed by a permanent evolutionary and ecological suppression of the group to the present day. This previously undocumented extinction marked a tipping point for pelagic marine vertebrate communities, setting the stage for middle-Miocene radiations in the large, migratory pelagic lineages now dominant in the modern open ocean and fundamentally changing pelagic vertebrate predator ecology. Anthro-

pogenic stressors are rapidly decimating populations of sharks, whales, and other large marine predators, a trend that could upset the system established after this similar, geologically rapid extinction in pelagic predators nearly 19 Ma.

REFERENCES AND NOTES

1. L. Zhou, F. T. Kyte, *Paleoceanography* **7**, 441–465 (1992).
2. H. Snoeckx, D. Rea, C. Jones, B. Ingram, in *Proceedings of the Ocean Drilling Program Scientific Results*, vol. 145, D. Rea, I. Basov, D. Scholl, J. Allan, Eds. (Ocean Drilling Program, 1995), pp. 219–230.
3. E. Sibert, R. Norris, J. Cuevas, L. Graves, Eighty-five million years of Pacific Ocean gyre ecosystem structure: long-term stability marked by punctuated change. *Proc. Biol. Sci.* **283**, 20160189 (2016).
4. M. V. Ankhelyi, D. K. Wainwright, G. V. Lauder, *J. Morphol.* **279**, 1132–1154 (2018).
5. A. D. Marshall, L. J. Compagno, M. B. Bennett, *Zootaxa* **2301**, 1–28 (2009).
6. R. Gravendeel, W. Van Neer, D. Brinkhuizen, *Int. J. Osteoarchaeol.* **12**, 420–441 (2002).
7. B. Serra-Pereira, I. Figueiredo, I. Farias, T. Moura, L. Gordo, *ICES J. Mar. Sci.* **65**, 1701–1709 (2008).
8. J. I. Castro, *The Sharks of North America* (Oxford Univ. Press, 2010).
9. W.-E. Reif, *Squamation and Ecology of Sharks* (Senckenbergische Naturforschende Gesellschaft, 1985).
10. J. Kriwet, M. J. Benton, *Palaeogeogr. Palaeoclimatol. Palaeoecol.* **214**, 181–194 (2004).
11. P. W. Signor, J. H. Lipps, *Spec. Pap. Geol. Soc. Am.* **190**, 291–296 (1982).
12. S. C. Wang, C. R. Marshall, *Paleobiology* **30**, 5–18 (2004).
13. Y. P. Papastamatiou, B. M. Wetherbee, J. O'Sullivan, G. D. Goodmanlowe, C. G. Lowe, *Environ. Biol. Fishes* **88**, 361–368 (2010).
14. J. Zachos, M. Pagani, L. Sloan, E. Thomas, K. Billups, *Science* **292**, 686–693 (2001).
15. B. S. Cramer, K. G. Miller, P. J. Barrett, J. D. Wright, *J. Geophys. Res. Oceans* **116** (C12), C12023 (2011).
16. B. S. Cramer, J. R. Toggweiler, J. D. Wright, M. E. Katz, K. G. Miller, *Paleoceanography* **24**, PA4216 (2009).
17. A. Goldner, N. Herold, M. Huber, *Nature* **511**, 574–577 (2014).
18. A. Holbourn, W. Kuhnt, K. G. Kochhann, N. Andersen, K. Sebastian Meier, *Geology* **43**, 123–126 (2015).
19. B. S. Wade, P. N. Pearson, W. A. Berggren, H. Pälike, *Earth Sci. Rev.* **104**, 111–142 (2011).
20. D. Lazarus, J. Barron, J. Renaudie, P. Diver, A. Türke, *PLoS ONE* **9**, e84857 (2014).
21. C. W. Smart, A. T. S. Ramsay, *J. Geol. Soc. London* **152**, 735–738 (1995).
22. M. Miya et al., *PLoS ONE* **8**, e73535 (2013).
23. T. Park, E. M. Fitzgerald, S. J. Gallagher, E. Tomkins, T. Allan, *PLoS ONE* **11**, e0153915 (2016).
24. O. Lambert et al., *Proc. Biol. Sci.* **282**, 20151530 (2015).
25. F. G. Marx, R. E. Fordyce, *R. Soc. Open Sci.* **2**, 140434 (2015).
26. S. Corrigan, L. B. Beheregaray, *Mol. Phylogenet. Evol.* **52**, 205–216 (2009).
27. F. G. Marx, E. M. Fitzgerald, R. E. Fordyce, *Acta Palaeontol. Pol.* **64**, 231–238 (2019).
28. E. C. Sibert, L. D. Rubin, *Dryad* (2021); doi:10.5061/dryad.tlg1jw0n.
29. E. C. Sibert, L. D. Rubin, *Zenodo* (2021); doi:10.5281/zenodo.4684080.

ACKNOWLEDGMENTS

We thank P. Dayton, A. Freibott, A. Knoll, P. Hull, and three anonymous reviewers for helpful discussion regarding this manuscript. This research uses samples collected by the IODP. Images were taken on the Hull Lab Imaging System at Yale University and in the Harvard University Museum of Comparative Zoology's Digital Imaging Facility. **Funding:** This work was supported by the William F. Milton Fund to E.C.S., the Harvard Society of Fellows, and a Hutchinson Fellowship from the Yale Institute of Biospheric Sciences to E.C.S. **Author contributions:** Conceptualization: E.C.S.; Methodology: E.C.S. and L.D.R.; Investigation: L.D.R.; Formal Analyses: E.C.S.; Visualization: E.C.S. and L.D.R.; Writing—Original Draft: E.C.S.; Writing—Editing and Revision: L.D.R. and E.C.S.; Supervision, Project Administration, and Funding Acquisition: E.C.S. **Competing interests:** The authors declare no competing interests. **Data and materials availability:** Images of all denticles included in this study are archived on Dryad (28). The R Code and data used in this study are available at <https://github.com/esibert/EarlyMioceneDenticles> and archived on Zenodo (29).

SUPPLEMENTARY MATERIALS

science.sciencemag.org/content/372/6546/1105/suppl/DC1
Figs. S1 to S13
Tables S1 to S5
References (30–51)
Data Files S1 to S3

2 September 2019; resubmitted 21 August 2020
Accepted 21 April 2021
10.1126/science.aaz3549

CORONAVIRUS

Prevalent, protective, and convergent IgG recognition of SARS-CoV-2 non-RBD spike epitopes

William N. Voss¹, Yixuan J. Hou^{2,†}, Nicole V. Johnson^{1,†}, George Delidakis³, Jin Eyun Kim⁴, Kamyab Javanmardi¹, Andrew P. Horton¹, Foteini Bartzoka¹, Chelsea J. Paresi⁵, Yuri Tanno³, Chia-Wei Chou¹, Shawn A. Abbasi⁶, Whitney Pickens¹, Katia George¹, Daniel R. Boutz^{1,7}, Dalton M. Towers³, Jonathan R. McDaniel⁸, Daniel Billick¹, Jule Goike¹, Lori Rowe^{9,10}, Dhvani Batra⁹, Jan Pohl⁹, Justin Lee⁹, Shivaprakash Gangappa¹¹, Suryaprakash Sambhara¹¹, Michelle Gadush¹², Nianshuang Wang¹, Maria D. Person¹², Brent L. Iverson⁵, Jimmy D. Gollihar^{1,7,13}, John M. Dye⁶, Andrew S. Herbert⁶, Ilya J. Finkelstein¹, Ralph S. Baric^{2,14}, Jason S. McLellan¹, George Georgiou^{1,3,4,15}, Jason J. Lavinder^{1,3,*}, Gregory C. Ippolito^{1,13,15*}

The molecular composition and binding epitopes of the immunoglobulin G (IgG) antibodies that circulate in blood plasma after severe acute respiratory syndrome coronavirus 2 (SARS-CoV-2) infection are unknown. Proteomic deconvolution of the IgG repertoire to the spike glycoprotein in convalescent subjects revealed that the response is directed predominantly (>80%) against epitopes residing outside the receptor binding domain (RBD). In one subject, just four IgG lineages accounted for 93.5% of the response, including an amino (N)-terminal domain (NTD)-directed antibody that was protective against lethal viral challenge. Genetic, structural, and functional characterization of a multidonor class of “public” antibodies revealed an NTD epitope that is recurrently mutated among emerging SARS-CoV-2 variants of concern. These data show that “public” NTD-directed and other non-RBD plasma antibodies are prevalent and have implications for SARS-CoV-2 protection and antibody escape.

The severe acute respiratory syndrome coronavirus 2 (SARS-CoV-2) spike ectodomain (S-ECD) folds into a multidomain architecture (1, 2) and includes the receptor binding domain (RBD), which is essential for viral infectivity, and the structurally adjacent amino (N)-terminal domain (NTD), which plays an uncertain role. Humoral immunity to the spike (S) surface glycoprotein can correlate with protection (3), and it is the primary antigenic target for most vaccines and monoclonal antibodies (mAbs). That the B cell repertoire can recognize multiple spike epitopes is supported by extensive single-cell cloning campaigns (4–9). However, the identity, abundance, and clonality of the immunoglobulin G (IgG) plasma antibody repertoire and the epitopes it may target are not known (10–12). Divergence between the two repertoires is biologically plausible (13–17), and the evidence in COVID-19 includes a paradoxical disconnect between virus-neutralizing IgG titers and RBD-specific B cell immunity (6, 11, 18, 19).

To analyze the IgG repertoire, we collected blood during early convalescence from four seroconverted study subjects (P1 to P4) who

experienced mild COVID-19 disease that manifested with plasma virus-neutralization titers in the lowest quartile (P1 and P3), the second highest quartile (P2), or the highest quartile (P4) compared to a larger cohort (table S1 and fig. S1). The lineage composition and relative abundance of constituent IgG antibodies comprising the plasma response to either intact stabilized S-ECD (S-2P (1)) or RBD was determined using the Ig-Seq pipeline (13, 14, 20) that integrates analytical proteomics of affinity-purified IgG fractions with peripheral B cell antibody variable region repertoires (BCR-Seq).

IgG lineages detected by Ig-Seq in the S-ECD fraction but absent from the RBD fraction were deemed to be reactive with spike epitopes outside the RBD. In subject P3, we detected six IgG lineages that bound to S-ECD (Fig. 1A). Four of these (Lin.1 to Lin.4) accounted for 93.5% abundance of the total plasma IgG S-ECD response and exhibited extensive intralinear diversity (fig. S2) indicative of clonal expansion and selection. Notably, the top three lineages (Lin.1 to Lin.3; >85% abundance) all bound to non-RBD epitopes (S2 subunit or NTD). Bulk serology enzyme-linked immunosorbent assays (ELISAs) recapitulated the Ig-Seq result and

demonstrated similarly high levels of non-RBD-binding IgG ($P > 0.05$) (Fig. 1B), confirming that RBD-binding plasma antibodies constitute only a minor proportion of all spike-binding IgG in naturally infected individuals (21). In all four subjects, the detected plasma IgG repertoire to S-ECD was oligoclonal, comprising only 6 to 22 lineages, with the top-ranked lineage constituting 15 to 50% of the total abundance. On average, 84% of the anti-S-ECD plasma IgG repertoire bound to epitopes outside the RBD (Fig. 1C), a finding consistent with data from single B cell analyses (22), and the most abundant plasma IgG lineage in all donors recognized a non-RBD epitope (Figs. 1A and 2A and fig. S3).

Binding analysis of P3 mAbs CM29 to CM32 representing the most expanded clones within each of lineages Lin.1 to Lin.4 showed that CM29 (Lin.1) recognizes the S2 subunit [dissociation constant (K_D) = 6.6 nM], CM30 and CM31 (Lin.2 and Lin.3 with K_D = 0.8 and 37.7 nM, respectively) were specific for the NTD, and CM32 (Lin.4) bound the RBD (K_D = 6.0 nM), as expected from the Ig-Seq differential affinity purifications (Fig. 1A and table S2). CM30 potentially neutralized authentic SARS-CoV-2 in vitro [median inhibitory concentration (IC_{50}) = 0.83 μ g/ml] and CM32 was slightly less potent (2.1 μ g/ml), whereas CM29 and CM31 showed minimal neutralization activity (Fig. 1D).

We then determined the capacity of mAbs CM29 to CM32, singly and in combination, to confer prophylactic protection in vivo to virus challenge using the MA10 mouse model of SARS-CoV-2 infection (23, 24). Even though the RBD-directed mAb CM32 could neutralize authentic virus in vitro and had relatively high antibody-dependent cellular phagocytosis (ADCP) activity (fig. S4), it did not protect in vivo (fig. S5), possibly because of amino acid changes in the MA10 virus. Similarly, no protection was observed for the non-neutralizing S2-directed mAb CM29 or non-neutralizing NTD-directed mAb CM31. The neutralizing mAb CM30, derived from the top-ranking NTD-targeting IgG lineage (21% abundance), was the sole plasma antibody that conferred complete protection to MA10 viral challenge (Fig. 1, E and F, and fig. S5). Administration of a cocktail comprising the top non-RBD plasma mAbs CM29 to CM31 (>85% of the IgG plasma lineages to S-ECD; Fig. 1A) showed the most

¹Department of Molecular Biosciences, The University of Texas at Austin, Austin, TX, USA. ²Department of Epidemiology, University of North Carolina at Chapel Hill, Chapel Hill, NC, USA.

³Department of Chemical Engineering, The University of Texas at Austin, Austin, TX, USA. ⁴Department of Biomedical Engineering, The University of Texas at Austin, Austin, TX, USA.

⁵Department of Chemistry, The University of Texas at Austin, Austin, TX, USA. ⁶U.S. Army Medical Research Institute of Infectious Diseases, Frederick, MD, USA. ⁷CCDC Army Research

Laboratory-South, The University of Texas at Austin, Austin, TX, USA. ⁸Biomedicine Design, Pfizer, Cambridge, MA, USA. ⁹Biotechnology Core Facility Branch, Division of Scientific Resources,

National Center for Emerging and Zoonotic Infectious Diseases, Centers for Disease Control and Prevention, Atlanta, GA, USA. ¹⁰Tulane National Primate Research Center Department of

Microbiology 18703 Three Rivers Road Covington, LA, USA. ¹¹Immunology and Pathogenesis Branch, Influenza Division, National Center for Immunization and Respiratory Diseases, Centers for

Disease Control and Prevention, Atlanta, GA, USA. ¹²Center for Biomedical Research Support, The University of Texas at Austin, Austin, TX, USA. ¹³Department of Pathology and Genomic

Medicine, Houston Methodist Research Institute, Houston Methodist Hospital, Houston, TX, USA. ¹⁴Department of Microbiology and Immunology, University of North Carolina at Chapel Hill,

Chapel Hill, NC, USA. ¹⁵Department of Oncology, Dell Medical School, The University of Texas at Austin, Austin, TX, USA.

*Corresponding author. Email: jlavinder@utexas.edu (J.J.L.); gci@utexas.edu (G.C.I.)

†These authors contributed equally to this work.

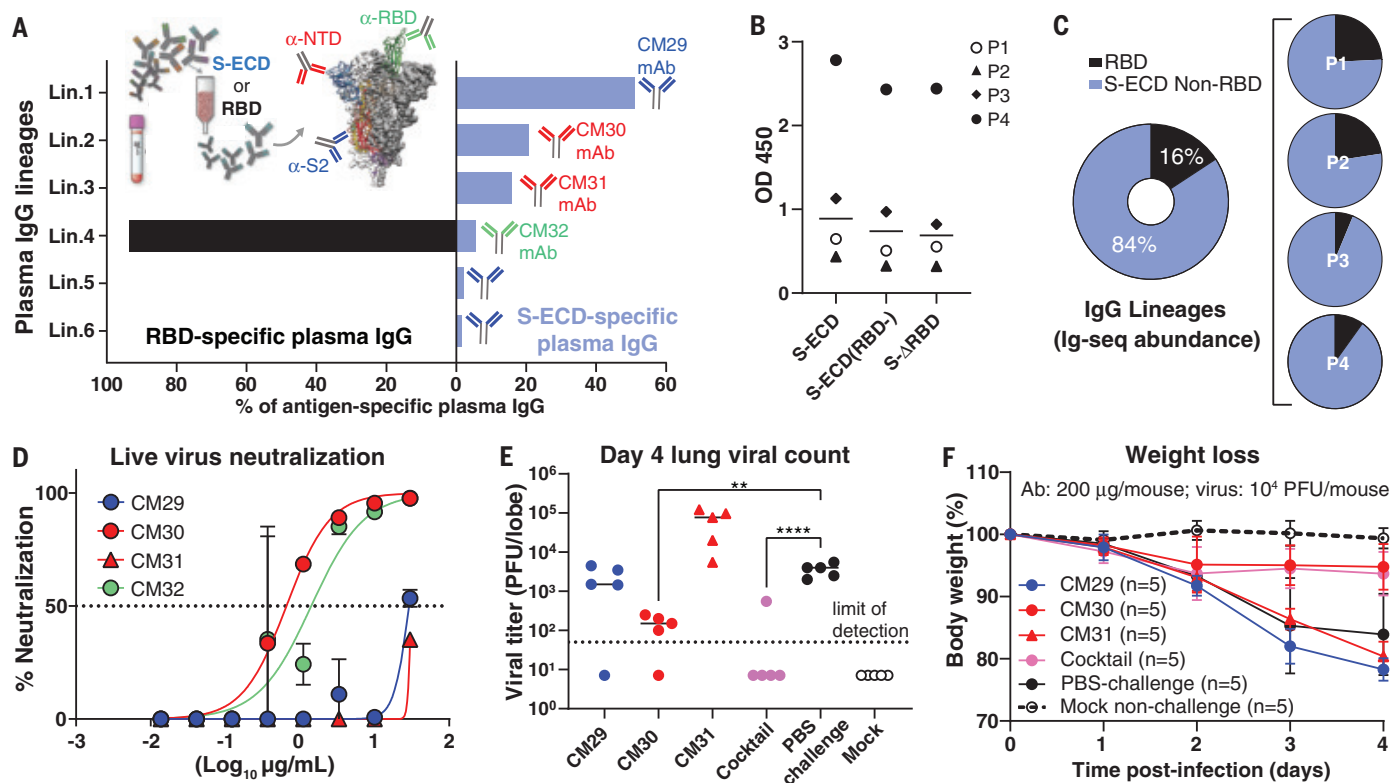


Fig. 1. Most plasma IgG antibodies bind non-RBD spike epitopes such as the NTD. **(A)** Affinity purification using spike S-ECD (I) or RBD for subject P3. Plasma IgG lineage identities, binding specificity, and relative abundance were mapped by means of Ig-seq proteomics (14), facilitating recombinant plasma mAb characterization; anti-RBD (green); anti-S2 (blue); and anti-NTD (red). **(B)** IgG ELISA binding (1:150 plasma dilution) to S-ECD alone or in the presence of RBD (50 μ g/ml) [S-ECD(RBD-)] or S- Δ RBD deletion mutant. **(C)** Quantitative Ig-seq determination of anti-RBD and non-RBD IgG mAb abundance in early convalescent

plasmas across four subjects. **(D)** Authentic virus neutralization (in duplicate) of the four most abundant plasma IgGs (CM29, CM30, CM31, CM32) from plasma lineages Lin.1, Lin.2, Lin.3, and Lin.4 in subject P3. **(E and F)** Prophylactic protection of 12-month-old BALB/c mice ($n = 5$ per group) against lethal challenge with a high dose (10^4 PFU) of mouse-adapted (MA10) SARS-CoV-2. Cocktail of non-RBD mAbs (200 μ g per mouse) at 2:1:1 ratio reflecting their relative plasma abundance. ** $P < 0.005$; **** $P < 0.0001$, determined by one-way analysis of variance (ANOVA) with Dunnett's multiple comparisons test.

robust protection and lung viral titers below the limit of detection in high-viral load challenge [10^4 plaque-forming units (PFU)].

Subject P2, with ~ 10 -fold higher neutralizing titer compared with subject P3 (fig. S1 and table S1), displayed a more polyclonal IgG response (Fig. 2A), with 12 out of 15 lineages ($>80\%$ total abundance) in the anti-S-ECD repertoire recognizing non-RBD epitopes. Conspicuously, as with P3, the most abundant S-ECD-directed plasma antibodies target the S2 subunit, with the four topmost lineages (68% total abundance) binding to S2. mAbs CM25 and CM17, representative of two NTD-targeting lineages each constituting $\sim 2.5\%$ of the response at day 56 (Ig-Seq Lin.6 and Lin.9) (Fig. 2A), were both encoded by unmutated or near-germline immunoglobulin G heavy-chain variable region 1-24 (IGHV1-24). We found an additional NTD-targeting unmutated IGHV1-24 plasma mAb (CM58) in subject P4. CM17, CM25, and CM58 bound S-ECD with similar single-digit nanomolar affinity (Fig. 2B and table S2), and all three potentially neutralized SARS-CoV-2 virus, with IC_{50} values of 0.01

to 0.81 μ g/ml comparable to those of S309 anti-RBD control (25) (Fig. 2C, fig. S6, and table S2). For all three mAbs, preadministration in the MA10 mouse model resulted in significantly reduced lung viral titers after infection with 10^5 PFU (Fig. 2D; $P < 0.001$), resulting in 100% survival, compared with just 40% in the control group (Fig. 2E). CM17- and CM25-treated cohorts exhibited only minimal weight loss (Fig. 2F). Thus, IGHV1-24 is intrinsically suited for potent and protective targeting of the NTD.

B cell expression of IGHV1-24 in COVID-19 (~ 5 to 8%) (5, 7, 26) is ~ 10 -fold higher than in healthy individuals (0.4 to 0.8%) (27). Moreover, we could detect IGHV1-24 plasma antibodies only in S-ECD fractions (mean 3.7%) but not among anti-RBD IgGs (Fig. 3, A and B). Alignment of CM17, CM25, and CM58 with four neutralizing IGHV1-24 anti-NTD mAbs cloned from peripheral B cells [4A8 (4), 1-68 (5), 1-87 (5), COVA2-37 (7)] and an additional antibody [COV2-2199 (8)] identified a class of convergent heavy-chain variable (V_H) immune receptor sequences (Fig. 3C). In

all cases, three glutamate (Glu) residues (Glu³⁶, Glu⁵⁹, and Glu⁸⁰) located in complementarity-determining region-H1 (CDR-H1), CDR-H2, and framework H3 (FWR-H3), respectively, as well as a phenylalanine (Phe) residue (Phe⁵⁶) in CDR-H2, were invariably unmutated and are specific to the electronegative IGHV1-24 [isoelectric point (pI) = 4.6]. The convergent V_H genes paired promiscuously with six distinct light-chain variable (V_L) genes, yet CDR-H3 peptide lengths were restricted (14 or 21 amino acids) (table S3). A “checkerboard” binding-competition experiment (Fig. 3D) indicated the presence of at least two epitope clusters on the NTD, including one targeted by all of the tested IGHV1-24 mAbs (4A8, CM25, CM17, CM58, and 1-68) and the IGHV3-11 mAb CM30. Another NTD epitope was identified by CM31 (IGHV2-5, 6.4% mutation), which overlapped with CM30 (IGHV3-11; 3.1% mutation), CM58, and 1-68 but did not compete with the other three IGHV1-24 NTD mAbs.

To better understand the IGHV1-24 interactions with the spike NTD, we determined a cryo-electron microscopy (EM) structure of

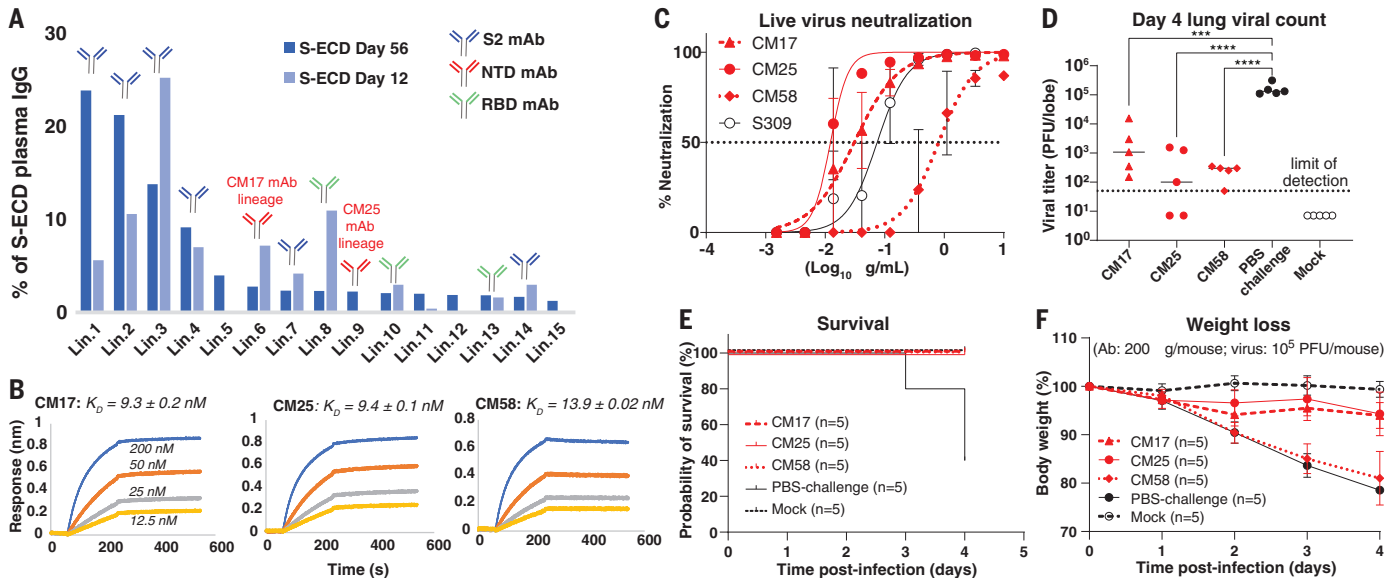


Fig. 2. Protective spike NTD-targeting antibodies are prevalent in COVID-19 convalescent plasma. (A) Temporal Ig-seq dynamics of the anti-S-ECD IgG repertoire at days 12 and 56 after symptom onset. (B) Biolayer interferometry (BLI) sensorgrams to S-ECD ligand of anti-NTD mAbs CM17, CM25 (subject P2), and CM58 (subject P4). (C) In vitro live virus neutralization (performed in duplicate). (D to F) In vivo prophylactic protection of 12-month-old BALB/c mice ($n = 5$ per group) against high-dose intranasal challenge (10^5 PFU) of mouse-adapted (MA10) SARS-CoV-2. *** $P < 0.0007$; **** $P < 0.0001$, determined by one-way ANOVA with Dunnett's multiple comparisons test.

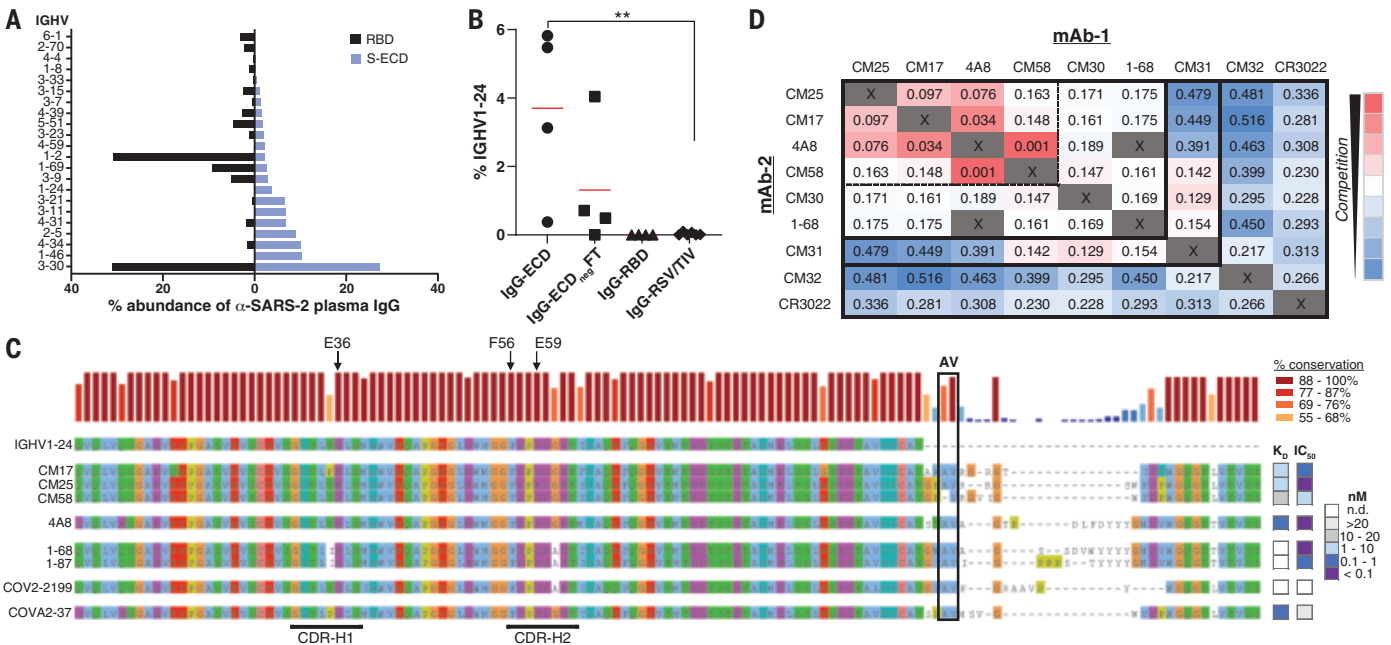


Fig. 3. Genetic basis of a shared, or public, class of IGHV1-24 plasma antibodies targeting the spike NTD. (A) IGHV usage of plasma antibodies in all subjects ($n = 4$). (B) Comparative IGHV1-24 usage of anti-S-ECD (IgG-ECD) and anti-RBD (IgG-RBD) plasma antibodies, or in depleted S-ECD affinity column flow-through (IgG-ECD_{neg}FT) in all subjects ($n = 4$). IgG-RSV/TIV: IgG specific to respiratory syncytial virus (RSV) or trivalent influenza vaccine hemagglutinin HA1 (TIV) in healthy controls after vaccination ($n = 6$). ** $P < 0.01$, determined by Mann-Whitney U test. (C) Sequence alignment of IGHV1-24 neutralizing anti-NTD IgGs from plasma (CM17, CM25, and CM58) or from peripheral B cells [4A8 (4), 1-68 and 1-87 from a subject with ARDS (5), COV2-2199 (13), and COVA2-37 (mild disease subject)] (7). Arrows point to

specific IGHV1-24 residues. Heatmap shows recombinant mAb affinity (K_D) and live-virus neutralization (IC_{50}) for individual antibodies. (D) Competitive BLI binding assay ("checkerboard competition") of NTD-binding mAbs found in this study (CM17, CM25, CM58, CM30, and CM31) and others (4A8 and 1-68). RBD-binding mAbs CM32 and CR3022 included for comparison. Numbers refer to the shift, in nanometers, after second mAb binding to the preformed mAb-NTD complex. Dashed box drawn to highlight strong competition (<0.1 nm shift) among 4A8 and three IGHV1-24 mAbs examined in this study. Abbreviations for the amino acid residues are as follows: A, Ala; C, Cys; D, Asp; E, Glu; F, Phe; G, Gly; H, His; I, Ile; K, Lys; L, Leu; M, Met; N, Asn; P, Pro; Q, Gln; R, Arg; S, Ser; T, Thr; V, Val; W, Trp; and Y, Tyr.

CM25 Fabs bound to trimeric S-ECD (Fig. 4A and figs. S7 and S8). Focused refinement of the CM25-NTD interface resulted in a 3.5-Å reconstruction that revealed a heavy-chain-dominant mode of binding, with substantial contacts mediated by interactions among the three CDRs and the N3 and N5 loops of the NTD (Fig. 4B). The light chain contributes only 11% (86 Å²) of the total CM25 binding

interface, mainly through a stacked hydrophobic interaction between CDR-L2 Tyr⁵⁵ and Pro²⁵¹ within the N5 loop. Distinctive germline IGHV1-24 residues contribute 20% (149 Å²) of the total binding interface. CDR-H1 interacts extensively through hydrogen bonds and contacts between hydrophobic residues, including a salt bridge formed between the conserved Glu³⁶ residue and the N5 loop residue Arg²⁴⁶

(Fig. 4C). The common IGHV1-24 Phe⁵⁶ residue in CDR-H2 forms a pi-cation interaction with Lys¹⁴⁷ in the N3 loop (Fig. 4C). CM25 contains a 14-amino acid CDR-H3 loop that contributes 35% (261 Å²) of the total interface, including the AV aliphatic motif found in all but one of the convergent IGHV1-24 NTD-binding mAbs. Ala¹⁰⁹ and Val¹¹⁰ are buried at the interface in a binding pocket framed by the N3 and N5 loops. A comparison of CM25 with an extant structure of an IGHV1-24 NTD-binding antibody isolated by B cell cloning, 4A8 (4), revealed that the AV dipeptide interaction is structurally conserved, and the 21-amino acid CDR-H3 of 4A8 extends along the outside of the NTD, contributing three additional contacts and 46% (415 Å²) of the total binding interface (Fig. 4D). Both structures show extensive contacts between the heavy chain of the Fabs and the NTD N3 and N5 loops. The Glu³⁶-Arg²⁴⁶ salt bridge and an identical CDR-H2 contact between Phe⁵⁶ and Lys¹⁴⁷ are conserved in the 4A8-NTD interface.

SARS-CoV-2 variants of concern contain mutations in the NTD N3 and N5 loops, including Y144/Y145Δ and K147E (UK lineage B.1.1.7), W152C (California B.1.429), and 242-244Δ or R246I (South Africa B.1.351). Alanine substitutions at several of these positions ablated binding or reduced affinity more than five-fold by public IGHV1-24 antibodies, as exemplified by 4A8, CM17, and CM25 (Fig. 4E and fig. S9), a result consistent with the CM25-NTD and 4A8-NTD structures. Additionally, we confirmed that an engineered N3-N5 double mutant and native B.1.351 (28) both evade neutralization by mAbs CM25 and 4A8 (Fig. 4F). Thus, mutations in SARS-CoV-2 variants confer escape from public neutralizing anti-NTD antibodies.

In conclusion, we find that the convalescent plasma IgG response to SARS-CoV-2 is oligoclonal and directed overwhelmingly toward non-RBD epitopes in the S-ECD. This includes public, near-germline, and potentially neutralizing antibodies against the NTD. The extent to which public anti-NTD antibodies contribute to protection is likely related to their relative concentrations in plasma, which can be dominant in some individuals. Our finding that mutations present in circulating SARS-CoV-2 variants can impair or ablate binding and neutralization by public anti-NTD antibodies may constitute a mechanism of viral escape in a subset of the population. Numerous other NTD mutations—which overlap with the structural epitope recognized by the public IGHV1-24 antibody class—have been described in additional circulating variants, in laboratory escape mutants, and in immunocompromised patients (12, 29–33).

REFERENCES AND NOTES

1. D. Wrapp et al., *Science* **367**, 1260–1263 (2020).
2. A. C. Walls et al., *Cell* **181**, 281–292.e6 (2020).
3. K. McMahan et al., *Nature* **590**, 630–634 (2021).

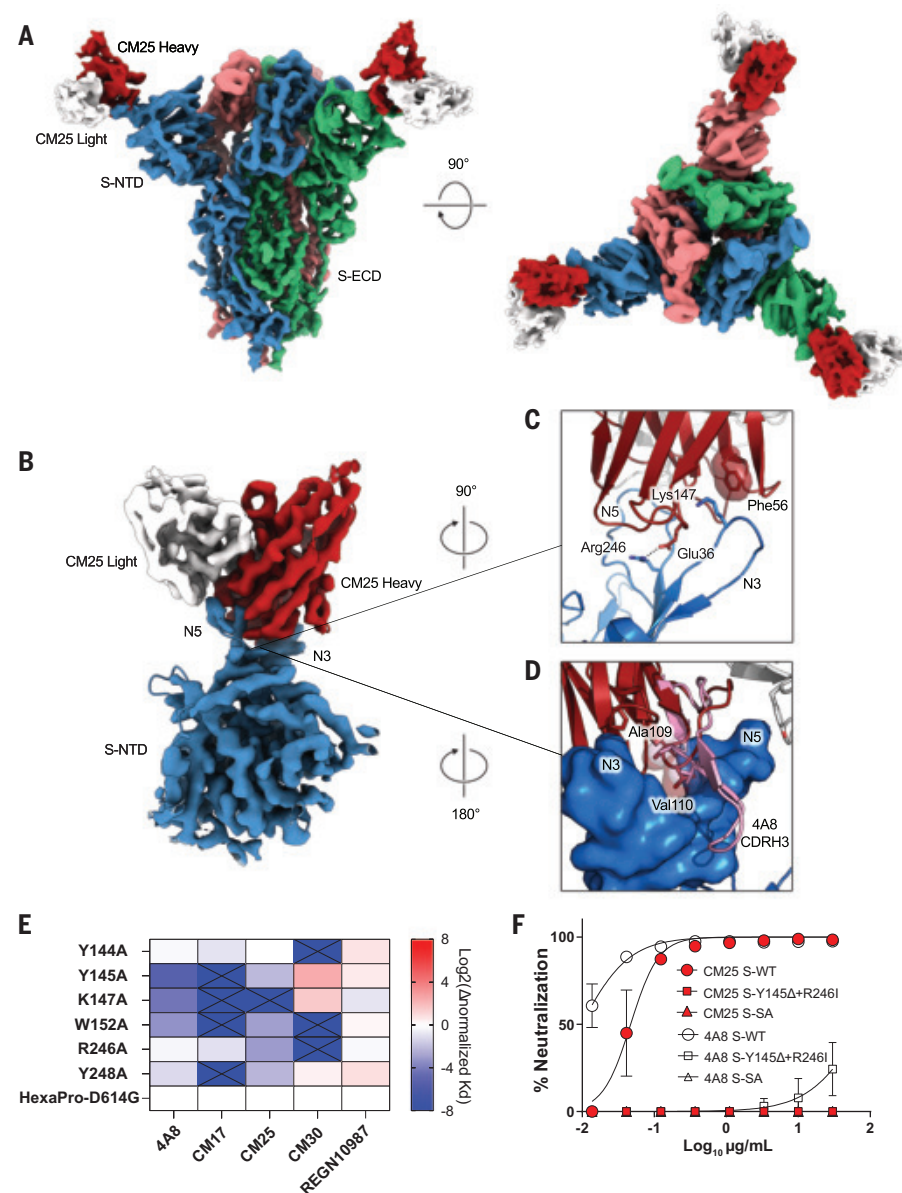


Fig. 4. Structural basis of public IGHV1-24 plasma antibodies, NTD mutations, and antibody escape.

(A) Side and top views of the structure of CM25 Fab bound to S-ECD shown as cryo-EM density. (B) Focused refinement density revealing a V_H-dominant mode of binding, with substantial contacts mediated by interactions among the three CDRs and the N3 and N5 loops of the NTD. (C) CDR-H1 interaction includes a salt bridge formed between the distinctive encoded Glu³⁶ residue and the N5 loop residue Arg²⁴⁶, the distinctive Phe⁵⁶ residue in CDR-H2 forms a pi-cation interaction with Lys¹⁴⁷ in the N3 loop. (D) The AV dipeptide interaction with the N3 and N5 loops of the NTD is structurally conserved between mAbs CM25 (red) and 4A8 (pink). (E) Normalized shift (log₂) in binding K_D , as measured by differential BLI affinities for single Ala mutants and parental D614G spike protein. (F) Authentic virus neutralization of CM25 and 4A8 against wild-type (WT), double S-N3/N5 loop mutants, and South Africa (SA) B.1.351 viral variant.

4. X. Chi *et al.*, *Science* **369**, 650–655 (2020).
5. L. Liu *et al.*, *Nature* **584**, 450–456 (2020).
6. D. F. Robbani *et al.*, *Nature* **584**, 437–442 (2020).
7. P. J. M. Brouwer *et al.*, *Science* **369**, 643–650 (2020).
8. S. J. Zost *et al.*, *Nature* **584**, 443–449 (2020).
9. A. Z. Wec *et al.*, *Science* **369**, 731–736 (2020).
10. T. J. Ripberger *et al.*, *Immunity* **53**, 925–933.e4 (2020).
11. J. A. Juno *et al.*, *Nat. Med.* **26**, 1428–1434 (2020).
12. Y. Weisblum *et al.*, *eLife* **9**, e61312 (2020).
13. J. J. Lavinder *et al.*, *Proc. Natl. Acad. Sci. U.S.A.* **111**, 2259–2264 (2014).
14. J. J. Lavinder, A. P. Horton, G. Georgiou, G. C. Ippolito, *Curr. Opin. Chem. Biol.* **24**, 112–120 (2015).
15. W. E. Purtha, T. F. Tedder, S. Johnson, D. Bhattacharya, M. S. Diamond, *J. Exp. Med.* **208**, 2599–2606 (2011).
16. K. G. Smith, A. Light, G. J. Nossal, D. M. Tarlinton, *EMBO J.* **16**, 2996–3006 (1997).
17. C. O. Barnes *et al.*, *Cell* **182**, 828–842.e16 (2020).
18. L. L. Luchsinger *et al.*, *J. Clin. Microbiol.* **58**, e02005-20 (2020).
19. F. Wu *et al.*, *JAMA Intern. Med.* **180**, 1356–1362 (2020).
20. B. J. DeKosky *et al.*, *Nat. Med.* **21**, 86–91 (2015).
21. A. J. Greaney *et al.*, *Cell Host Microbe* **29**, 463–476.e6 (2021).
22. T. F. Rogers *et al.*, *Science* **369**, 956–963 (2020).
23. S. R. Leist *et al.*, *Cell* **183**, 1070–1085.e12 (2020).
24. K. H. Dinnon 3rd *et al.*, *Nature* **586**, 560–566 (2020).
25. D. Pinto *et al.*, *Nature* **583**, 290–295 (2020).
26. S. C. A. Nielsen *et al.*, *Cell Host Microbe* **28**, 516–525.e5 (2020).
27. S. D. Boyd *et al.*, *J. Immunol.* **184**, 6986–6992 (2010).
28. H. Tegally *et al.*, *Nature* **592**, 438–443 (2021).
29. K. R. McCarthy *et al.*, *Science* **371**, 1139–1142 (2021).
30. B. Choi *et al.*, *N. Engl. J. Med.* **383**, 2291–2293 (2020).
31. V. A. Avanzato *et al.*, *Cell* **183**, 1901–1912.e9 (2020).
32. P. C. Resende *et al.*, The ongoing evolution of variants of concern and interest of SARS-CoV-2 in Brazil revealed by convergent indels in the amino (N)-terminal domain of the Spike protein. *medRxiv* 2021.03.19.21253946 [Preprint]. 20 March 2021. <https://doi.org/10.1101/2021.03.19.21253946>.
33. E. Andreano *et al.*, SARS-CoV-2 escape in vitro from a highly neutralizing COVID-19 convalescent plasma. *bioRxiv* 2020.12.28.424451 [Preprint]. 28 December 2020. <https://doi.org/10.1101/2020.12.28.424451>.

ACKNOWLEDGMENTS

We are indebted to our study subjects for providing the blood samples required for this study. We thank G. Fennes, D. Jaffee, and A. Matouschek for their support. The authors are grateful for the administrative expertise of E. K. Miller, to The LaMontagne Center for Infectious Disease, for the university's core facilities, and to C.-L. Hsieh for providing reagents and advice. **Funding:** Funding for USAMRIID was provided through the CARES Act with programmatic oversight from the Military Infectious Diseases Research Program—project 14066041. Opinions, conclusions, interpretations, and recommendations are those of the authors and are not necessarily endorsed by the U.S. Army. The mention of trade names or commercial products does not constitute endorsement or recommendation for use by the Department of the Army or the Department of Defense. The findings and conclusions in this report are those of the authors and do not necessarily represent the views of Centers for Disease Control and Prevention. Molecular graphics and analyses performed with UCSF Chimera, developed by the Resource for Biocomputing, Visualization, and Informatics at the University of California, San Francisco, with support from NIH P41-GM103311. The Sauer Structural Biology Laboratory is supported by the University of Texas College of Natural Sciences and by award RR160023 from the Cancer Prevention and Research Institute of Texas (CPRIT). This research was funded in part by the Clayton Foundation (C.J.P., B.L.I., G.G.) and a National Institutes of Health (NIH)—National Institute of Allergy and Infectious Diseases (NIAID) grant awarded to J.S.M. (R01-AI127521), as well as by Welch Foundation grant nos. F-0003-19620604 (J.S.M.) and F-1016 (I.J.F.); NIH NCI COVID-19 SeroNet grant U54-CA260543 (R.S.B.); UT System Proteomics Network pilot funding (J.J.L., M.D.P.); and in part with federal funds under a contract from the NIH NIAID, contract no. 75N93019C00050 (G.G., J.J.L., G.C.I.). **Author contributions:** Conceptualization: W.N.V., G.G., J.J.L. and G.C.I.; Methodology: W.N.V., Y.J.H., N.V.J., J.E.K., G.D., A.P.H., B.L.I., M.D.P., J.D., A.H., R.S.B., J.S.M., G.G., J.J.L., and G.C.I.; Investigation: W.N.V., Y.J.H., N.V.J., J.E.K., G.D., A.P.H., F.B., C.P., Y.T., S.A.A., W.P., K.G., D.R.B., D.M.T., J.G., D.B., M.G., J.J.L., and G.C.I.; Data Analysis and Interpretation: W.N.V., Y.J.H., N.V.J., J.E.K., G.D., A.P.H., S.A.A., W.P., D.R.B., J.R.M., L.R., D.B., J.L., J.P., S.G., S.S., A.H., J.D.G., R.S.B., J.S.M., G.G., J.J.L., and G.C.I.; Data Curation: W.N.V., J.Y.H., N.V.J., J.E.K., G.D., J.J.L., and G.C.I.;

Writing: Original Draft, W.N.V., N.J.V., J.J.L., and G.C.I.; Writing: Review & Editing: W.N.V., Y.J.H., N.J.V., B.L.I., R.S.B., J.S.M., G.G., J.J.L., and G.C.I.; Funding: J.D.G., R.S.B., J.S.M., G.G., and G.C.I. **Competing interests:** A patent application submitted by The University of Texas Board of Regents is pending for anti-SARS-CoV-2 monoclonal antibodies described in the manuscript (W.N.V., J.D.G., J.S.M., G.G., J.J.L., and G.C.I.). **Data and materials availability:** FASTQ VH and VH-VL sequence files have been deposited in the NCBI Sequence Read Archive with accession numbers PRJNA729513. The monoclonal antibodies have been deposited in GenBank (www.ncbi.nlm.nih.gov/genbank/) with accession numbers MZ049539 to MZ049552. Coordinates for the CM25 Fab in complex with trimeric spike ectodomain have been deposited to the Protein Data Bank as PDBID:7M8J. Cryo-EM maps have been deposited to the Electron Microscopy Data Bank under accession code EMD-23717. These structural data are presented in Fig. 4, table S4, and figs. S7 and S8. All other data are available in the main text or the supplementary materials. This work is licensed under a Creative Commons Attribution 4.0 International (CC BY 4.0) license, which permits unrestricted use, distribution, and reproduction in any medium, provided the original work is properly cited. To view a copy of this license, visit <https://creativecommons.org/licenses/by/4.0/>. This license does not apply to figures/photos/artwork or other content included in the article that is credited to a third party; obtain authorization from the rights holder before using such material.

SUPPLEMENTARY MATERIALS

science.sciencemag.org/content/372/6546/1108/suppl/DC1
Materials and Methods
Figs. S1 to S9
Tables S1 to S5
References (34–54)
MDAR Reproducibility Checklist

12 January 2021; accepted 29 April 2021
Published online 4 May 2021
10.1126/science.abg5268



Plastic Discs and Annular Absorbers

Employing precision-moulding and die-cutting processes, Porvair Sciences can efficiently convert hydrophilic Vycon porous plastic into discs and annular-shaped parts to tightly tolerated specifications. These versatile approaches enable Porvair to offer high-performing, precisely manufactured products in diameters ranging from 3 mm to 1 m using any of its hydrophilic Vycon materials options, up to 4.75 mm thick. Hydrophilically treated Vycon materials have exceptional absorption and fluid-transfer properties and therefore, can be implemented as an efficient absorber with their instantaneous wetting properties. Due to the tortuous path of its porous structure, hydrophilic Vycon can efficiently filter and trap contaminants while allowing for effective delivery of drugs in various forms, such as solutions, suspensions, and emulsions. It has been tested to the most rigorous of United States Pharmacopeia classes and certified with a Class VI approval.

Porvair Sciences

For info: +44-(0)-1978-661144

www.vyconporousplastics.com/material-treatments

High-Performance Beam Collimators

Optical Surfaces announces a new series of high-performance beam collimators designed for modulation transfer function testing of optical systems. LW-series beam collimators incorporate a low-expansion off-axis parabolic mirror manufactured to better than $\lambda/10$ p-v surface accuracy. The optics within the collimators are secured by the use of stress-free mounts and come prealigned for optimum performance. Their off-axis design produces no central obscuration, ensuring highly efficient transmission. The all-reflecting design of LW-series beam collimators is achromatic, and their aluminium/magnesium fluoride coatings enable them to operate from the UV to the infrared without adjustment. Using low-expansion glass mirror substrates, these collimators provide high operational stability and performance. Each system has an output port datum plane, giving a defined distance to the focus. Each system is also supplied with an easy-to-use alignment aid to identify the center of the focal plane. All LW-series beam collimators provide a 20-mm field, ensuring full compatibility with standard black bodies.

Optical Surfaces

For info: +44-(0)-208-668-6126

www.optisurf.com

Biotinylated Heparan Sulfate Antibodies

AMS Biotechnology has launched two new biotinylated formats of the heparan sulfate 10E4 antibody (high and low biotin) along with a starter pack, to allow scientists to test both formats at a reduced cost. Heparan sulfate (HS) is a highly sulfated linear polysaccharide that is attached to a core protein to form HS proteoglycans on the cell membrane or in the extracellular matrix. In particular, HS has emerged as a key factor in infection by the SARS-CoV-2 virus, which is the cause of the COVID-19 coronavirus pandemic. Biotinylated antibodies are often used for the detection of low-abundance proteins. The process of biotin labeling is also frequently used as a nonradiative labeling method for proteins and as a protein purification technique. Biotin conjugation of the heparan sulfate 10E4 antibody confers many advantages by removing the need for conjugated secondary antibodies to quantify

the level of detection/binding in immunological assays.

AMS Biotechnology

For info: +44-(0)-1235-828200

www.amsbio.com

Automated Protein Purification

Automate your protein purification while maintaining sample integrity using the Thermo Fisher Scientific KingFisher Apex instrument. It automates protein isolation at low sample input volumes and produces yields high enough for LC-MS and Western downstream applications. The flexible design supports common applications as well as custom magnetic-based biomolecular separation—all with little hands-on time. It comes with user-defined, controlled cooling and heating options to maintain sample integrity. You can create and modify protocols to optimize the isolation of difficult-to-express proteins. KingFisher Apex supports 24- and 96-well plate formats for high-throughput processing. It produces consistent yields for downstream applications, such as immunoprecipitation, phage display, peptide mapping, and quantitation.

Thermo Fisher Scientific

For info: 800-955-6288

www.thermofisher.com/us/en/home

Nasal Swab for COVID-19 Testing

Melbourne-based Rhinomed Limited has provided evidence that its Rhinoswab provides superior performance for COVID-19 testing as well as making nasal sampling easier and more comfortable for users. Dual-nostril Rhinoswab has been developed to provide more comfortable, accurate, and standardized nasal sample collection that people can do themselves. Rhinoswab offers significant potential community benefits, including lessening the burden and risk to health care workers. In December 2020, the company established that Rhinoswab was comparable to existing standard-of-care nasal swabs in detecting the SARS-CoV-2 virus using RT-PCR testing, through testing at the Victorian Infectious Diseases Reference Laboratory (Peter Doherty Institute). Rhinomed has further refined the swab technology by improving the nylon flock used on the swab. Rhinoswab has recently been approved for sale in the Australian market, is listed on the Australian Register of Therapeutic Goods, and has class 1 registration with the U.S. Food and Drug Administration.

Rhinomed Limited

For info: 866-316-0671

www.rhinomed.global/about-rhino-med/sample-collection

Hyperspectral Sensor Chlorophyll Fluorescence Measurements

The Hyperspec Solar Induced Fluorescence (SIF) imaging sensor from Analytik is ideal for remote sensing, particularly in plant and crop photosynthesis and climatology applications where high-resolution chlorophyll fluorescence measurements are vital. Its pushbroom sensor collects hyperspectral image data with 1,600 spatial pixels per line at extremely high spectral resolution (0.1 nm–0.2 nm full width at half maximum) across the chlorophyll fluorescence emission spectrum from 671 nm to 780 nm. This allows both the important oxygen-A and oxygen-B bands (O2-A and O2-B) to be exploited for more accurate insight into photosynthetic processes. With this data, environmental scientists can gain a better understanding of plant physiology and stress. The Hyperspec SIF imaging sensor is purpose-built for deployment on manned aircraft or for field-based work, such as measurements from environmental observation towers.

Analytik

For info: +44-(0)-1954-232-776

analytik.co.uk

Electronically submit your new product description or product literature information! Go to www.sciencemag.org/about/new-products-section for more information.

Newly offered instrumentation, apparatus, and laboratory materials of interest to researchers in all disciplines in academic, industrial, and governmental organizations are featured in this space. Emphasis is given to purpose, chief characteristics, and availability of products and materials. Endorsement by *Science* or AAAS of any products or materials mentioned is not implied. Additional information may be obtained from the manufacturer or supplier.

ScienceCareers

FROM THE JOURNAL SCIENCE  AAAS

Confused about your next career move?



**Download Free Career
Advice Booklets!**

ScienceCareers.org/booklets





香港城市大學
City University of Hong Kong

#48

World
University

#4

World's top 50
Universities
under age 50

#1

World's Most
International Universities

#1

Engineering/Technology/
Computer Sciences
in Hong Kong

#1

Business School
in Asia



Global Scholar Recruitment Campaign

City University of Hong Kong (CityU) is one of the world's leading universities, known for innovation, creativity and research. We are now seeking exceptional scholars to join us as Assistant Professors/Associate Professors/Professors/Chair Professors (on substantiation-track) in all academic fields with special focuses on **One Health, Digital Society, Smart City, Matter, Brain**, and related interdisciplinary areas. Research fields of particular interest include, but not limited to:



- biomedical science and engineering
- computer science and data science
- neuroscience and neural engineering
- bio-statistics and AI-healthcare
- smart/semi-conductor manufacturing
- AI/robotics/autonomous systems
- aerospace and microelectronics engineering
- energy generation and storage
- digital business and innovation management
- fintech and business analytics
- computational social sciences
- digital humanities
- digital and new media
- law and technology
- private law
- healthy, smart and sustainable cities


Successful candidates should have a demonstrated ability to build a world-class research programme related to CityU's strategic research areas, plus a commitment to education and student mentorship. Candidates must possess a doctorate in their respective field by the time of appointment.

To apply, please submit your curriculum vitae through the website:
<https://www.cityu.edu.hk/provost/global-recruiting>



City University of Hong Kong is an equal opportunity employer. We are committed to the principle of diversity. Personal data provided by applicants will be used for recruitment and other employment-related purposes.

Worldwide recognition ranking #48, and #4 among top 50 universities under age 50 (QS survey 2021); #1 in the World's Most International Universities (THE survey 2020); #1 in Engineering/Technology/Computer Sciences in Hong Kong (ARWU survey 2016); and #1 Business School in Asia-Pacific region (UT Dallas survey 2019).

A man with short dark hair, wearing a white lab coat over a light blue button-down shirt, and clear safety goggles. He is smiling slightly and looking towards the camera. His arms are crossed, and he is wearing a blue nitrile glove on his left hand. The background is a blurred laboratory setting with shelves containing various bottles and equipment.

YOU'D SMILE TOO IF YOU JUST ADVANCED YOUR CAREER.



Find your next job at [ScienceCareers.org](https://www.sciencecareers.org)

There's scientific proof that when you're happy with what you do, you're better at what you do. Access career opportunities, see who's hiring and take advantage of our proprietary career-search tools. Get tailored job alerts, post your resume and manage your applications all in one place: [sciencecareers.org](https://www.sciencecareers.org)

ScienceCareers

FROM THE JOURNAL SCIENCE  AAAS

Who's the top employer for 2020?

Science Careers' annual survey reveals the top companies in biotech & pharma voted on by Science readers.

Read the article and employer profiles at sciencecareers.org/topemployers



**Science 2020
TOP EMPLOYER**



Shenzhen Institute of
Advanced Technology
Chinese Academy of Sciences



Established in partnership between the Chinese Academy of Sciences and the Shenzhen Municipal Government, the Shenzhen Institute of Advanced Technology (SIAT) is a newly-created university with an objective to become the world's preeminent institute for emerging science and engineering programs. SIAT is equipped with state-of-art teaching and research facilities and is dedicated to cultivating international, visionary, and interdisciplinary talents while delivering research support to pursue innovation-driven development.

SIAT is located in Shenzhen, also known as the "Silicon Valley of China," a modern, clean, and green city, well-known for its stunning architecture, vibrant economy, and its status as a leading global technology hub. SIAT is seeking applications for faculty positions of all ranks in the following academic programs: Computer Science and Engineering, Bioinformatics, Robotics, Life Sciences, Material Science and Engineering, Bio-medical Engineering, Pharmaceutical Sciences, Synthetic Biology, Neurosciences, etc. SIAT seeks individuals with a strong record of scholarship who possess the ability to develop and lead high-quality teaching and research programs. SIAT offers a comprehensive benefits package and is committed to faculty success throughout the academic career trajectory, providing support for ambitious and world-class research projects and innovative, interactive teaching methods.

Further information:

<http://english.siat.cas.cn/DP/Va/>

**myIDP: A career plan customized
for you, by you.**



For your career in science, there's only one

Science

Features in myIDP include:

- Exercises to help you examine your skills, interests, and values.
- A list of 20 scientific career paths with a prediction of which ones best fit your skills and interests.



Visit the website and start planning today!
myIDP.sciencecareers.org

ScienceCareers | AAAS In partnership with:



By Natalia Aristizábal

Seeing beyond a test

The third time I took the Graduate Record Examination (GRE) was going to be my last, regardless of how I scored. I had long harbored dreams of pursuing a Ph.D., and I wanted to do well because the exam is key for admission to many U.S. graduate programs. But I couldn't afford to retake it, emotionally or financially. I was unemployed at the time and my partner and I were trying to get by on his postdoc salary. I'd taken the exam 7 years earlier, but my scores were so low I didn't even bother applying to Ph.D. programs. Now, I was giving it one more shot.

I didn't know what standardized tests were until high school, when I immigrated from Colombia to the United States. I wanted to attend college so I took the American College Testing exam. Fortunately, my high school offered a free prep course and I managed to achieve good enough scores to get into college with financial aid.

During my first year, I told my biology professor I was passionate about studying and protecting nature. He offered me a position in his lab, which taught me how to conduct research and what a career in academia looks like. Then, in my third year I was selected for a program that prepares undergraduate students from underrepresented groups for doctoral studies. As I neared graduation, applying to grad school felt like a natural next step.

But then I took the GRE and bombed, testing below average in all sections. I couldn't afford to enroll in a prep course, which cost upward of \$3000. Instead, I had studied using a \$40 test prep book. As a native Spanish speaker, I found the verbal section demoralizing. But what was even more daunting was the way the test was administered: Correct answers were followed by harder questions. That affected me psychologically: When easier questions appeared, I assumed I'd gotten the previous question wrong.

Convinced I would perform better and manage my test anxiety with more preparation, I took time off after graduation to study full time. But my scores didn't improve on my second try. My hopes of becoming a scientist vanished.

Over the next few years, I took a series of temporary jobs. I worked in a molecular biology lab troubleshooting protocols. Then I moved to Brazil—a place I'd always wanted to live—and found jobs studying birds in the Amazon rainforest and curating specimens in a natural history museum. That connected me with professors in Brazil, where I was accepted into a master's program.

After I defended my master's thesis, a paper on which I was



“I wonder what I’d be doing if the admissions committee had not overlooked my GRE scores.”

the lead author—my first—was accepted for publication. Slowly, I began to see myself as a scientist. I wanted to continue down the academic path. So after my partner and I moved to Boston for his postdoc, I summoned the courage to give the GRE one last try. I studied for weeks and paid \$205 to book an appointment.

I remember how anxious I was as I walked into the windowless, dimly lit exam center, aware my performance that day could make or break my dream of pursuing a Ph.D. As the test proceeded, I thought it was going OK. But when my score appeared on screen immediately afterward, my stomach dropped. I'd scored even lower than my first two attempts. I felt defeated.

Afterward, I reached out to a professor who I'd been in contact with

before my exam appointment. I felt insecure and embarrassed about my scores, but our conversation left me reassured. He told me about research suggesting the GRE is a better measure of race, ethnicity, and income than academic ability, and he ended by saying, “I will go to battle for you in front of the admissions committee.” His confidence in my potential encouraged me to continue applying.

Weeks later, when I received an offer from his university, I felt a mixture of excitement and disbelief. I was filled with joy, but I also couldn't believe how much time, energy, and expense it had taken to get into a Ph.D. program.

Now in my third year, I have no doubt I am where I need to be. Still, I wonder what I'd be doing if the admissions committee had not overlooked my GRE scores. It pains me to think how many people are kept out of science not for a lack of talent, but because they didn't excel at a standardized test. Many graduate programs, including my own, have decided to drop the GRE requirement in recent years—and I hope many others will follow. ■

Natalia Aristizábal is a Ph.D. candidate at the University of Vermont.

CALL FOR PAPERS

BioDesign Research

 OPEN ACCESS

BioDesign Research is a Science Partner Journal published in affiliation with **Nanjing Agricultural University (NAU)** and distributed by the **American Association for the Advancement of Science (AAAS)**. *BioDesign Research* publishes high quality breakthrough research, reviews, editorials, and perspectives focusing on in silico biosystems design, genetic or epigenetic modifications, and genome writing or rewriting in any organism.

Submit your research to *BioDesign Research* today!

Learn more at spj.sciencemag.org/bdr

The Science Partner Journals (SPJ) program was established by the American Association for the Advancement of Science (AAAS), the non-profit publisher of the *Science* family of journals. The SPJ program features high quality, online-only, editorially independent open-access publications produced in collaboration with international research institutions, foundations, funders and societies. Through these collaborations, AAAS expands its efforts to communicate science broadly and for the benefit of all people by providing a top-tier international research organization with the technology, visibility, and publishing expertise that AAAS is uniquely positioned to offer as the world's largest general science membership society.

Learn more at spj.sciencemag.org



@SPJournals

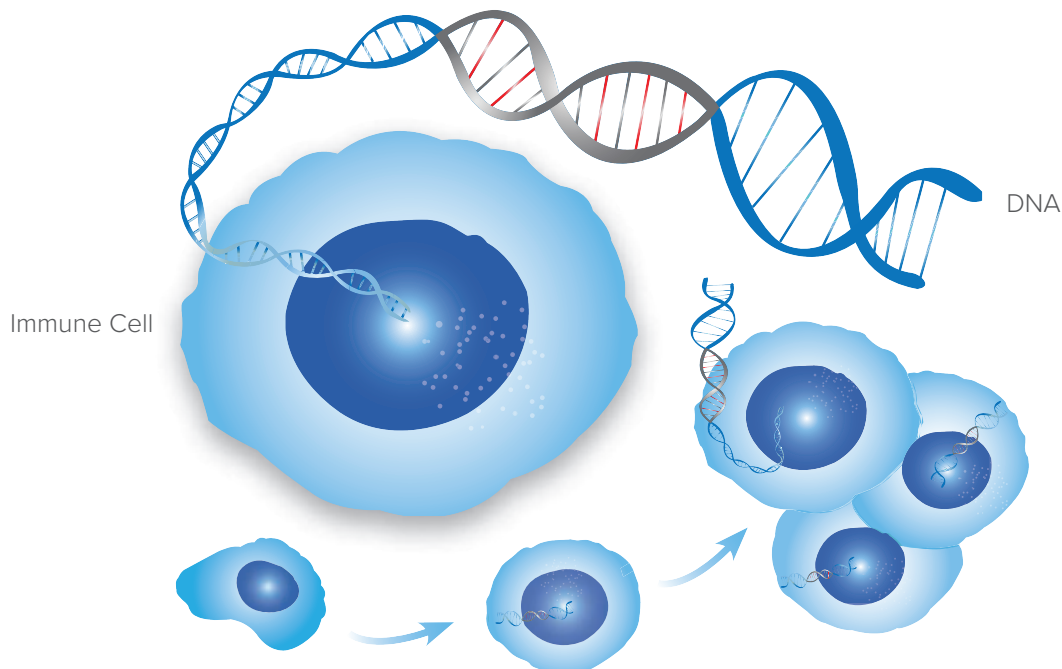


@SPJournals

ARTICLE PROCESSING CHARGES WAIVED UNTIL 2022

Immune Cell Engineering

Modifying Cells for Immunology & Cell Therapy Research

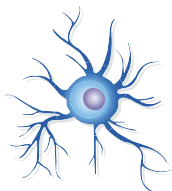


The ability to genetically modify immune cells provides a powerful tool to sense and treat diseases that our natural immune system cannot normally handle. ProMab's established CAR-T CRO platform allows us to work not only with T cells but also advance research in other immune cell types by utilizing highly capable cellular engineering techniques such as gene editing, viral transduction, setting up model cell systems, or performing detailed cell-based assays.

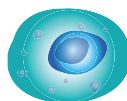
Types of Cells:



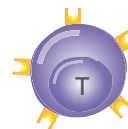
Macrophage



Dendritic cell



Natural Killer cell



γδ T cell



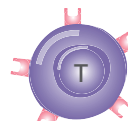
Erythrocyte



B cell



Monocyte



T cell

All products are for research only

Discover more | www.promab.com

